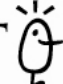


VNIVERSITAT  VALÈNCIA

 **Facultat de Química**



**HIGH ACCESSIBILITY AND CHEMICAL
HOMOGENEITY IN MESOPOROUS MATERIALS:
SILICAS, GOLD-CONTAINING COMPOSITES AND
PHOSPHATES**

Alaina María Moragues Bartolomé

Valencia, 2015



PhD Program

3056 Química

 **Facultat de Química**

Title of the Thesis

**HIGH ACCESSIBILITY AND CHEMICAL HOMOGENEITY IN
MESOPOROUS MATERIALS: SILICAS, GOLD-CONTAINING
COMPOSITES AND PHOSPHATES**

PhD Thesis submitted by

Alaina María Moragues Bartolomé

PhD Supervisor

To obtain the degree

Pedro José Amorós del Toro

International Doctor in Chemistry

Valencia, 2015



VNIVERSITAT
DE VALÈNCIA



D. Pedro José Amorós del Toro, Catedrático del Departamento de Química Inorgánica de la Facultad de Química de la Universidad de Valencia.

CERTIFICA:

Que el trabajo que presenta D. Alaina María Moragues Bartolomé en esta memoria, bajo el título “High Accessibility And Chemical Homogeneity In Mesoporous Materials: Silicas, Gold-Containing Composites And Phosphates” ha sido realizado bajo su dirección en el Institut de Ciència dels Materials de la Universitat de València.

Y para que así conste, a efectos de su presentación para optar al Grado de Doctora Internacional en Química, expide la presente, que firma en Paterna a de
de 2015.

Dr. Pedro J. Amorós del Toro

A los míos

Agradecimientos

Me gustaría en primer lugar agradecer a mi director de tesis por su ayuda inestimable y por haber hecho en estos cinco años que me sintiera una más de esta familia que es el ICMUV. Este agradecimiento debe extenderse sin duda al resto de componentes del instituto: Aurelio, Carmen, Julio, Daniel, Fernando, Eduardo, Sonia, Clara, Ana,... A Adela, por ser mi nexo con la química analítica. Y por supuesto a M^a Ángeles, Toni, Julián, Pilar y David Vie por su contante ayuda.

A mis compañeros, tanto a los que siguen aquí como a los que andan ya investigando por otros países, ya que son ellos los que han compartido mi día a día en el laboratorio: Jamal, Mario, David, Paula, Regina, Andrés, Toni. A los compis de comida por hacerme desconectar cuando era necesario y ser capaces de dar siempre otras perspectivas: Abel, Carlos, Guillermo, Raúl, Raquel. Y a todos los que han pasado por aquí durante estos años, ya que todos ellos han aportado algo a esta experiencia.

Al grupo del profesor Pârvulescu por su amabilidad durante mi estancia en Bucarest y por acercarme al mundo de la catálisis.

Por último quiero agradecer a mi familia y a mis amigos por haber estado ahí en todo momento, entender los altibajos emocionales que este proceso conlleva e intentar siempre sacarme una sonrisa. A mis quimiquillos, porque entramos juntos en este mundo y nos hemos visto crecer, siempre ahí para felicitarnos por ese nuevo artículo o quitarnos las preocupaciones con unas risas. A Sara, Sandra y Paula, sois mi retiro espiritual. En estos momentos de “reflexión” una se da cuenta de toda la gente que en cierta manera ha participado en esto: animándome a embarcarme en este proyecto, interesándose constantemente por la evolución o sufriendo mis nervios y ayudándome a desconectar. Gracias a todos por vuestro granito de arena. Y por último a mis grandes pilares, mis padres y mi hermana, que han tenido que soportar oír y leer sobre mesoporosos aún sin saber bien lo que era. Creo que nunca os lo agradeceré lo suficiente.

Resumen

El trabajo recopilado en esta tesis está basado en la formación de materiales mesoporosos y sus posibles usos como catalizadores. Este trabajo se ha estructurado en cuatro partes diferenciadas. En primer lugar se presenta una breve introducción a los materiales mesoporosos revisando su evolución en la historia, los diferentes métodos de síntesis, su versatilidad en cuanto a funcionalización y aplicaciones y acabando con un repaso al trabajo realizado en el grupo de investigación.

El segundo capítulo está centrado en el mejor conocimiento de la sílice UVM-7, un material mesoporoso de carácter bimodal desarrollado por el grupo. En primer lugar se estudia en detalle la estructura del material para confirmar la interconexión en tres dimensiones de los mesoporos. Esto se consigue a través de medidas de tomografía electrónica, combinadas con la formación de réplicas de carbono y la preparación de composites con oro y el posterior estudio microscópico de su dispersión en el material. Una vez conocida al detalle su estructura, se trabaja en la expansión de los mesoporos utilizando alcanos como agentes expansores, suponiendo que, dado su carácter hidrofóbico, estos se alojarán en el interior de las micelas de surfactante. En este trabajo se estudia la cantidad real de alcano alojada en las micelas a través de medidas espectrofotométricas y se trata de explicar los resultados obtenidos en base a estudios coloidales. Finalmente, para poner en valor la expansión obtenida se inmovilizan enzimas e ibuprofeno en los materiales con mayor expansión.

El tercer capítulo recoge dos trabajos en los que se ha colaborado con diferentes grupos de catálisis. Se forman composites de sílice con diferentes dominios oxídicos utilizando dos estrategias diferentes. En el primer caso, se forman composites tipo UVM-7 con Ni/Sn/Ce utilizando una síntesis en “one-pot”, siguiendo del método de los atranos. En el segundo caso, se impregna el material UVM-7 para formar óxidos cristalinos de TiO_2 , ZrO_2 y CeO_2 en su superficie. Posteriormente se depositan partículas de Au sobre los materiales y se prueban en la catálisis de la condensación selectiva de benzilamina a N-benzilidenbenzilamina y en la oxidación de CO a CO_2 respectivamente. El trabajo realizado por nuestra parte recoge la síntesis y

caracterización de los soportes, así como la comprensión de los resultados catalíticos en base a la estructura de los distintos materiales.

Por último se incluye un capítulo sobre materiales mesoporos no silíceos en el que se estudia la formación de un fosfato de hierro mesoporoso así como de fosfonatos de hierro. Para ello se utiliza un surfactante como agente director estructural, igual que en el caso de la UVM-7. Se caracterizan los materiales con diferentes técnicas y se propone una estructura.

Resum

El treball recopilat en aquesta tesi està basat en la formació de materials mesoporosos i la seua possible aplicació en catàlisi. Aquest treball està estructurat en quatre parts ben diferenciades. En primer lloc es presenta una breu introducció als materials mesoporosos, revisant la seua evolució en la història, els diferents mètodes de síntesi, la seua versatilitat en quant a funcionalització i aplicacions i acabant amb un repàs al treball realitzat al grup d'investigació.

El segon capítol està centrat en un millor coneixement del material UVM-7, un material mesoporós de caràcter bimodal desenvolupat per el grup. En primer lloc s'estudia en detall l'estructura del material per a confirmar la interconnexió en tres dimensions del mesopors. S'aconsegueix amb mesures de tomografia electrònica, combinades amb la formació de rèpliques de carbó i la preparació de composites amb or i el posterior estudi microscòpic de la seua dispersió al material. Una volta coneguda al detall la seua estructura, es treballa en la expansió dels mesopors utilitzant alcans com a agents expandors suposant que, per el seu caràcter hidròfob, s'acomodaran a l'interior de les micel·les de surfactant. En aquest treball s'estudia la quantitat d'alcà allotjada a les micel·les a través d'estudis espectrofotomètrics i es tracta d'explicar els resultats obtinguts mitjançant estudis col·loïdals. Finalment, per a posar en valor la expansió aconseguida s'immobilitzen micel·les i ibuprofè als materials amb major grau d'expansió.

El tercer capítol recull dos treballs en els que s'ha col·laborat amb diferents grups de catàlisi. Es formen composites de sílice amb diversos dominis oxidics fent servir dos estratègies diferents. En el primer cas es formen composites de tipus UVM-7 amb Ni/Sn/Ce utilitzant una síntesi en "one-pot", seguint el mètode dels atrans. En el segon cas s'impregna el material UVM-7 per a formar òxids cristal·lins de TiO_2 , ZrO_2 y CeO_2 a la seua superfície. Posteriorment es depositen partícules d'or sobre els materials i s'utilitzen en la oxidació selectiva de benzilamina a N-benzilidenbenzilamina i en la oxidació de CO a CO_2 respectivament. El treball realitzat per la nostra part recull

la síntesi i caracterització dels materials, així como la comprensió dels resultats catalítics en base a la estructura dels diferents materials.

Per últim, s'inclou un capítol sobre materials mesoporosos no silícis en el que s'estudia la formació d'un fosfat de ferro mesoporós així com de fosfonats de ferro. Per a aconseguir la seua formació s'utilitza un surfactant com a agent director estructural, com en el cas de la UVM-7. Estos materials es caracteritzen utilitzant diferents tècniques i es proposa una estructura.

The content on this Thesis has generated the following scientific publications:

1. Perez-Cabero, M.; Hungria, A. B.; Morales, J. M.; Tortajada, M.; Ramon, D.; **Moragues, A.**; El Haskouri, J.; Beltran, A.; Beltran, D.; Amoros, P., Interconnected mesopores and high accessibility in UVM-7-like silicas. *Journal of Nanoparticle Research* **2012**, *14*, 1045-1057.
2. El Haskouri, J.; **Moragues, A.**; Beltran, A.; Murcia-Mascaros, S.; Plazaola, F.; Legarra, E.; Mauri-Aucejo, A.; Brotons-Gisbert, M.; Sanchez-Royo, J. F.; Beltran, D.; Amoros, P., Mesoporous iron phosphate/phosphonate hybrid materials. *Microporous and Mesoporous Materials* **2014**, *187*, 14-22.
3. Opreș, C. M.; Pavel, O. D.; **Moragues, A.**; El Haskouri, J.; Beltrán, D.; Amorós, P.; Marcos, M. D.; Stofleae, L. E.; Parvulescu, V. I., New multicomponent catalysts for the selective aerobic oxidative condensation of benzylamine to N-benzylidenebenzylamine *Catalysis Science & Technology* **2014**, *4*, 4340-4355.
4. Puértolas, B.; Mayoral, Á.; Arenal, R.; Solsona, B.; **Moragues, A.**; Murcia-Mascaros, S.; Amorós, P.; Hungría, A. B.; Taylor, S. H.; García, T., High-Temperature Stable Gold Nanoparticle Catalysts for Application under Severe Conditions: The Role of TiO₂ Nanodomains in Structure and Activity. *ACS Catalysis* **2015**, *5*, 1078-1086.
5. **Moragues, A.**; Guillem, C.; Mauri-Aucejo, A.; Tortajada, M.; Beltran, A.; Beltran, D.; Amoros, P., Enlarged pore size in nanoparticulated bimodal porous silicas by using alkanes as swelling agents. Submitted to *Microporous and Mesoporous Materials*.

As well as some papers in progress:

1. **Moragues, A.**; Neatu, F.; Pârvulescu, V.; Michelet, V.; Amorós, P., Heterogeneous gold catalysts efficient for addition of boronic acids to 2-cyclohexen-1-one.
2. **Moragues, A.**; Guillem, C.; Mauri-Aucejo, A.; Beltran, A.; Beltran, D.; Amorós, P., From nanoparticulated to core-shell mesoporous materials.
3. Puértolas, B.; **Moragues, A.**; Mayoral, Á.; Arenal, R.; Solsona, B.; Murcia-Mascaros, S.; Amorós, P.; Hungría, A. B.; Taylor, S. H.; García, T., Binary silica-based porous composites as support for gold nanoparticles: influence of the preparative route on structural and catalytic properties.

Other publications:

1. **Moragues-Bartolome, A. M.**; Jones, W.; Cruz-Cabeza, A. J., Synthon preferences in cocrystals of cis-carboxamides: carboxylic acids. *Crystengcomm* **2012**, *14*, 2552-2559.
2. Puertolas, B.; Smith, A.; Vazquez, I.; Dejoz, A.; **Moragues, A.**; Garcia, T.; Solsona, B., The different catalytic behaviour in the propane total oxidation of cobalt and manganese oxides prepared by a wet combustion procedure. *Chemical Engineering Journal* **2013**, *229*, 547-558.
3. Morales, J. M.; **Moragues, A.**; El Haskouri, J.; Guillem, C.; Latorre, J.; Murcia-Mascaros, S.; Beltrán, A.; Beltrán, D.; Amorós, P., Low-Cost Synthesis of Bimodal Mesoporous Silica-Based Materials by Pseudomorphic Transformation. *ChemPlusChem* **2015**, *80*, 1014-1028.

Table of Contents

1. General Introduction	1
1.1 - Mesoporous silica discovery and background	3
1.2 - Evolution and applications of mesoporous silica	6
1.3 - Synthetic methods.....	9
1.3.1 - Soft-templating	9
1.3.2 - Hard-templating.....	16
1.4 - Functionalization	19
1.5 - Accessibility	23
1.6 - Previous work by the group and motivation.....	24
References	30
2. Mesoporous silicas with enhanced accessibility	41
2.1 - Overview.....	43
2.1.1 - Reduction of particle size.....	44
2.1.2 - Pore hierarchy.....	46
2.1.3 - Pore expansion	49
2.2 - UVM-7.....	50
2.3 - Drug delivery	51
2.4 - Enzyme immobilization	51
2.4.1 - Immobilization methods.....	52
2.4.2 - Enzymes used.....	55
2.5 - Objectives	56
References	57

Interconnected mesopores and high accessibility in UVM-7-like silicas	61
Enlarged pore size in nanoparticulated bimodal porous silicas: improving accessibility	85

3. Gold mesoporous silica nano-composites used in catalytic

<i>applications</i>.....	131
3.1 - Overview.....	133
3.2 - Particle size	135
3.3 - Nanoparticle formation	137
3.4 - Catalysis	139
3.4.1 - Homogeneous catalysis	140
3.4.2 - Supported (heterogeneous catalysis).....	141
3.4.2.1 - Anchoring	142
3.4.2.2 - Anchoring methods.....	143
3.4.2.3 - Mesoporous silica.....	145
3.5 - Objectives	147
References	149

New multicomponent catalysts for the selective aerobic oxidative condensation of benzylamine to N-benzylidenebenzylamine.....	155
--	------------

High Temperature Stable Gold Nanoparticle Catalysts for Application under Severe Conditions: The Role of TiO₂ Nanodomains on Structure and Activity	207
---	------------

4. Non-silica mesoporous materials: new iron phosphates and hybrid phosphonates.....

4.1 - Overview.....	249
4.2 - Non-silica oxides.....	252

4.2.1 - Alumina	252
4.2.2 - Transition metal oxides.....	254
4.2.2.1 - Titania.....	254
4.2.2.2 - Zirconia	255
4.2.2.3 - Other metal oxides.....	255
4.3 - Carbon	257
4.4 - Chalcogenide	262
4.5 - Nitrides	263
4.5.1 - Silicon nitrides.....	263
4.5.2 - Carbon nitrides	264
4.5.3 - Metal nitrides.....	265
4.6 - Metals.....	265
4.7 - Phosphates	267
4.7.1 - Zirconium and titanium phosphates.....	269
4.7.2 - Other compositions	269
4.7.3 - Phosphonates	270
4.8 - Objectives	270
References	272
Mesoporous iron phosphate/phosphonate hybrid materials	285
5. Conclusions and perspectives.....	319

1. General Introduction

1.1 - Mesoporous silica discovery and background

Zeolites are a family of microporous crystalline solids with well-defined structures. These structures involve silicon, aluminium and oxygen atoms, including cations, water and other molecules inside the pore system ($M_{2/n}O, Al_2O_3, xSiO_2, yH_2O$). Zeolites are used in a wide range of applications, the most important being the catalysis of petrochemical processes, ion exchange (water purification) and separation and elimination of solvents and gases.

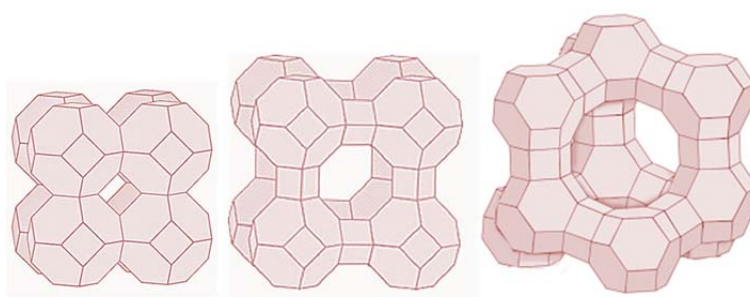


Figure 1. Topology of sodalite, zeolite A and faujasite.

One of the main features of zeolites is that they consist of a tridimensional network of TO_4 tetrahedron (where $T = Si$ or Al and every oxygen connects two different tetrahedron) resulting in a variety of structures where cages, canals or cavities are formed in which small molecules *ca.* 1 nm can be introduced. Great effort has been made in order to avoid diffusion limitations in zeolites, creating large pore zeolites, smaller zeolite particles or mesopores in the particles^{1,2}.

In 1992, during the study on new zeolites that could selectively process petroleum based molecules with high molecular weight, researchers from the Mobil Oil Corporation developed a family of materials named M41S³⁻⁶. These are mesoporous silicas with uniform pore sizes. During the second half of the 1980s they were trying to create large pore zeolites (to escape from the “1 nm prison”) by investigating pillared layered materials. The advantage of these materials was that

pore size and other variables could be modulated. However, they did not have enough thermal and hydrothermal stability to be used in petroleum processes⁷.

The next step in their study, at the end of the 1980s, was to combine both pillared layered materials and zeolite formation concepts, considering that some zeolites were formed through layered intermediates. In fact, they had previously discovered the zeolite MCM-22, with the ability of produce a lamellar precursor (MCM-22P)⁸. Their idea was to delaminate crystalline layers of MCM-22 and alternate them with an alkyltrimethylammonium compound⁹ and, afterwards, insert inorganic pillars using tetraethyl orthosilicate as the silica source.

But MCM-22 delamination was a challenge and, as an approximation, they decided to interrupt zeolite synthesis, isolate layered precursors and use those crystalline layers as the reagent. At that point, high concentrations of an alkyltrimethylammonium salt were added to the reaction media, working at a high pH and under hydrothermal treatment. They obtained a product with an empty X-ray diffraction pattern, with the exception of a broad peak at $2^\circ 2\theta$. They expected to find the same pattern as for the original zeolite, but apparently the new reaction conditions inhibited its formation. This product also presents a BET surface area of $1000 \text{ m}^2/\text{g}$ and a high adsorption capacity. These results were intriguing for the researchers, as they were not those expected for the synthesized material. To identify the nature and structure of the material, they observed it by TEM and found traces of a hexagonal pore structure; this new material was named MCM-41 (Mobil Crystalline Material).

The synthesis conditions were basic pH, high surfactant concentration and a silica source. After months of study, they also reported on two different structures, MCM-48 (cubic) and MCM-50 (laminar), as a result of a study on the surfactant concentration⁹. These three materials made up the M41S family, all of them being mesoporous materials with narrow pore size distribution. Shown in Figure 2 are their diffraction patterns and structures.

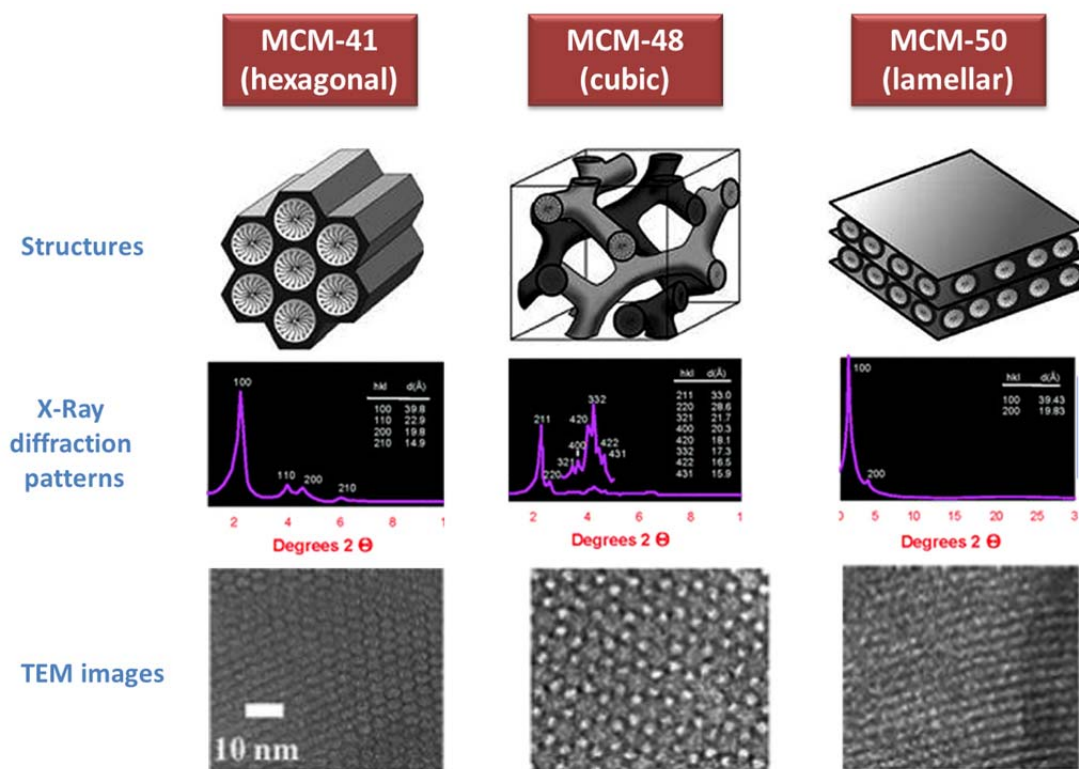


Figure 2. Structure, diffraction pattern and TEM image of M41S family.

The formation processes for these materials were described with the liquid-crystal templating mechanism (LCT)¹⁰, assuming that the silica precursor forms inorganic walls covering surfactant micelles. This mechanism will be explained in detail in a subsequent section.

There are two cases that might be considered as precedents to this discovery. The first one is a 1971 patent¹¹ of a material obtained by the reaction of tetraethyl orthosilicate and a cetyltrimethylammonium surfactant. At that time, characterization techniques were not yet developed enough, so it was reported with limited characterization and the outstanding features of this material were not identified. In 1997, after the discovery of M41S, the synthesis was repeated and the material was considered to be an ordered mesoporous material.

The second case is contemporaneous to Mobil's discovery. In 1989 Kuroda et al. studied kanemite expansion with an alkyltrimethylammonium surfactant at basic pH^{12,13}. They propose the Folding Sheet Mechanism (FSM)¹², schematized in Figure 3:

kanemite layers can wrap alkyltrimethylammonium ions, resulting in silanol condensation in the adjacent kanemite layers. This mechanism could explain the formation of hexagonal material, but not the entire M41S family.

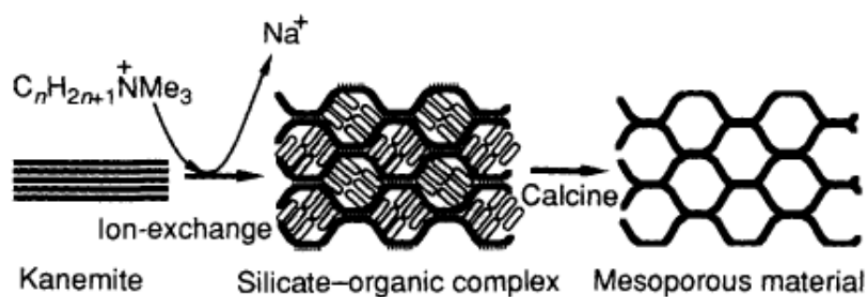


Figure 3. Folding Sheet Mechanism, from reference 12.

1.2 - Evolution and applications of mesoporous silica

After the discovery of the M41S family, the number of reports related to mesoporous materials exponentially increased (Figure 4). It was such a promising area that in 1998 a specialized journal, *Microporous and Mesoporous Materials*, was created.

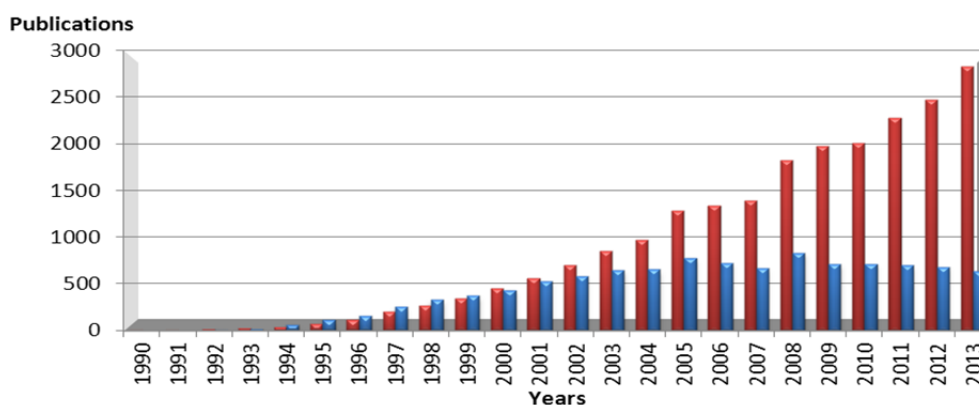


Figure 4. Number of publications on mesoporous materials (red) and citations of the initial Kresge et al. Nature paper (blue); data from Web of Science.

However, the expectations about these materials outweighed reality. In the beginning, mesoporous materials were expected to act as large pore zeolites. However, due to their amorphous nature, they are not stable enough at the pressure and temperatures needed for their application in petrochemistry, the main application field of zeolites. As a result, their catalytic activity is much lower. On the other hand, the production cost for these materials is higher due to the use of surfactants and the need for more synthesis steps (Table 1). These factors, added to the cost of their implementation in industry, make them non-suitable for these processes.

Table 1. Examples of template price, from reference 14.

Template	Price (€/kg)	wt.% of final material	Template price (€/kg _{final material})
CTMABr	530	73	387
P123	100	55	55
TPAOH	2610	44	1148
Carbon nanofibres	2520	72	1814
Carbon particles	6150	74	4550

The only known application of mesostructured silica in petrochemistry is a mesostructured Y Zeolite¹⁵ obtained by a post-synthetic surfactant-templated process. This material shows excellent hydrothermal stability and improved selectivity. Moreover, MCM-41 added to a FCC catalyst¹⁶ has been evaluated and it is capable of cracking heavy oil feedstock, decreasing secondary reactions with enhanced diffusion.

Mesoporous silicas have other possible applications. They are stable at low pressures and temperatures, so they can be used in catalytic procedures under soft conditions as well as in fine chemistry processes (cosmetics, pharmacy, fragrances, agrochemical, etc.). Some applications are listed in Table 2.

Table 2. Applications of mesoporous materials, adapted from reference 17.

Field	Type of properties	Name of the material	Applications	Ref.
Adsorption	Biomolecular adsorption properties	MCM-41, MCM-48, SBA-15, CMK-3, CMK-1, OMS	Separation of biochemicals, adsorption of amino acid, vitamins, proteins, CO ₂	18-20
	Toxic ion adsorption properties	Mesoporous alumina, PMO, titanium-silico phosphate	Fluoride, As(III/V), Cd(II), Hg(II), Fe(III), Cu(II), Zn(II) etc. adsorption to purify water	21,22
	Gas adsorption properties	Mesoporous polymers, Organically functionalized silica	N ₂ , H ₂ , CO ₂ gas adsorption and storage	23-26
	Adsorption and release properties	Mesoporous SiO ₂ -ZrO ₂ , silica nanoparticles, calcium phosphate, Au capped silica	Drug delivery of bisphosphonate, adsorption and desorption of DNA, dyes and drugs in human cell	27-30
Catalysis	Redox properties	Mesoporous titanium–phosphorous mixed oxide, Ti-Al-SBA-15, mesoporous mixed oxides	Partial oxidation of styrene, oxidation of cyclohexene to adipic acid, reduction of nitroarenes	31,21,32
	Acid-base properties	Mesoporous zinc-titanate, Zn doped silica, -COOH functionalized SBA-15, zirconium phosphate	Friedel-Crafts benzylation, esterification, transesterification, base catalyzed Knoevenagel condensation, Xanthenes preparation, biofuel production via esterification	33-37
	Other synthetic name reactions	Mesoporous NiO-ZrO ₂ , Pd doped porous polymer, polyoxometalate doped silica, Fe ₃ O ₄ @silica	C-S cross coupling, C-C cross coupling, Mannich reaction, Biginelli condensation reaction	38-41
	Photocatalytic properties	Mesoporous TiO ₂ , ZnO-CeO ₂ binary oxide, tantalum oxide	Photodegradation of dye, decomposition of dye, photosplitting of water	42-44
Optics, electricity, magnetism	Magnetic property	Mesoporous Fe ₃ O ₄	Ferromagnetism	45
	Optical properties	Luminescent PMO, rare earth doped silica, tungsten oxide	Chemosensing	46-48
	Electrical properties	Nanostructured SnO ₂	Dielectric effect	49
	Optoelectronics	Mesoporous TiO ₂ , ZnO, TiO ₂ nanoparticles	Photocurrent enhancement on dye doping, DSSC	50,51
Sensing	Gas sensing property	Mesoporous SnO ₂ , TiO ₂ materials, ordered mesoporous ZnO, In ₂ O ₃ , WO ₃	CO, NH ₃ , H ₂ , NO ₂ , CH ₄ etc. gas sensing,	52-54
	Ion sensing property	Azo compound functionalized organosilica, fluorescent grafted silica, dye doped silica, porous carbon nitride	Optical and electro-chemical sensing of cations like Fe(III), Zn(II), Cu(II), -NH ₂ gr. etc. and anions like -CN, citrate, borate, carboxylate etc.	55-60
	Biosensing property	Mesoporous titania MSN, organically functionalized silica	Detection and sensing of glucose oxidase, protein, glucose etc.	61,62
	pH sensing role	Functionalized silica	pH sensor of a particular medium	58,63

1.3 - Synthetic methods

In the 22 years since the discovery of the M41S family, the number of modifications proposed with respect to the initial preparative procedure has been very high. This has resulted in a wide variety of mesoporous materials. Schematized in Figure 5 are examples of these materials. The common step for all these syntheses is precursor condensation in the presence of a structure-directing agent; this is organized in supramolecular structures around which the inorganic structure condenses. This condensation can occur via two different paths: soft templating and hard templating.

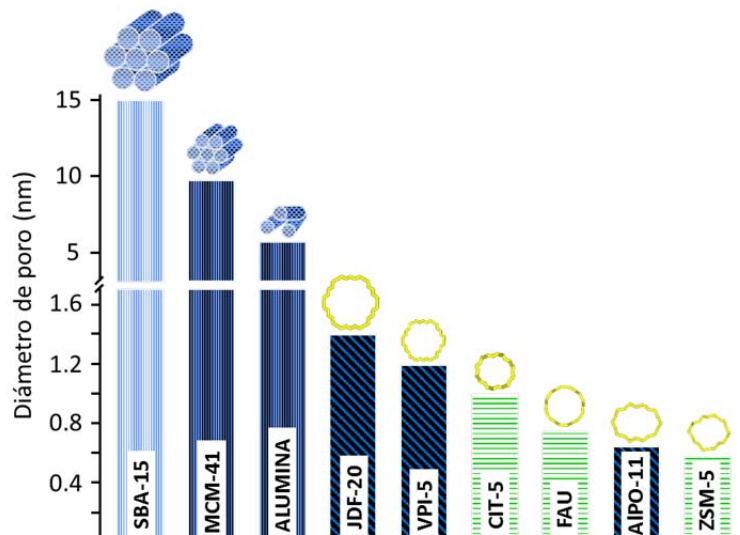


Figure 5. Schematic representation of the pore size ranges of microporous and mesoporous solids.

1.3.1 - Soft-templating

Soft templating syntheses are based on self-assembly of surfactant molecules with the precursor (and solvent). Surfactants are amphiphilic molecules with a hydrophilic head and a hydrophobic tail, which prefer non-polar solvents. Due to the hydrophobic effect, when they are in solution, surfactants form aggregates called micelles (Figure 6). Micelle formation is controlled by two main factors: the Kraft temperature, or critical micelle temperature (CMT), which is the temperature below

which the surfactant is not dissolved, and the critical micelle concentration (CMC) which is the surfactant concentration from which micelles start to form; above CMC all the surfactant added to the solution will be incorporated in micelles.

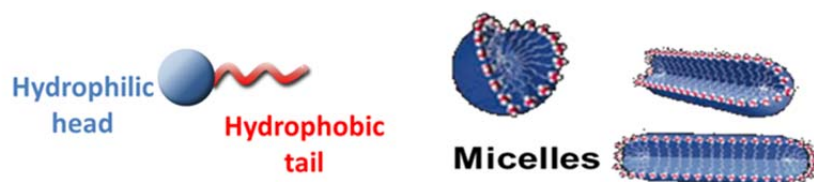


Figure 6. Scheme of a surfactant and different micelle arrangements.

The form of the micelles depends on the surfactant structure. There is a factor known as the packing parameter (g) that permits an explanation of the forms that are adopted in solution. The packing parameter definition is $g = v_o / (a_e l_o)$, where v_o is the hydrophobic chain effective volume, a_e is the equilibrium area of the surfactant head and l_o is the chain length. Low g values imply a highly curved surface between micelle and solution, while an increase in the g value reduces the curvature. Shown in table 3 and Figure 7 are the possible micellar structures formed, depending on g value. The variables in the definition of the packing parameter are not constant for a given surfactant, but depend on solution conditions. When the surfactant concentration increases, a phase transition can occur.

Table 3. Packing parameter (g) of different micellar structures.

$g = v_o / (a_e l_o)$	Structures	Examples
$g < 0.33$	Spherical micelles	Single chain lipids with a large polar head (soaps or ionic detergents)
$g = 0.33-0.5$	Cylindrical micelles	Single chain lipids with a small polar head (soaps or ionic detergents in concentrated electrolyte solutions)
$g = 0.5-2$	Bilayer (vesicles or membranes)	Double-chain lipids
$g = 2-3$	Inverse cylindrical micelles	Double-chain lipids and a small polar head
$g > 3$	Inverse spherical micelles	Water in oil systems

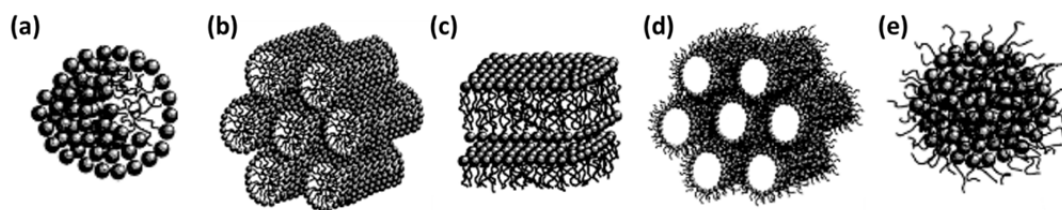


Figure 7. Scheme of different micellar structures: (a) spherical micelle; (b) cylindrical micelle; (c) bilayer; (d) inverse cylindrical micelle; and (e) inverse spherical micelle.

The soft templating route is rather flexible; variations regarding precursor and/or surfactant used, synthesis conditions or structure of the final material (pore size, connectivity) can be introduced by adjusting the method. There are three different groups of surfactants depending on the charge of the hydrophilic head in neutral pH: cationic, anionic and nonionic.

Cationic surfactants, such as those used in Mobil's first studies, are formed by at least one amine group, which acts as a hydrophilic head, and a hydrophobic tail. They are highly soluble in aqueous solutions, have high CMC and can be used in both acid and basic media. Their main problem is that they are expensive and toxic. Quaternary ammonium cationic surfactants ($C_nH_{2n+1}N(CH_3)_3Br$ ($n=8-22$)), such as CTMABr, are those most commonly used in the preparation of mesoporous materials, but other examples such as gemini, bolaform, multi-head group and cationic fluorinated surfactants have been also studied (Figure 8). On the other hand, there is a wide variety of anionic surfactants with hydrophilic groups (such as sulphates, sulphonates, carboxylates and phosphates) joined to a hydrophobic tail.

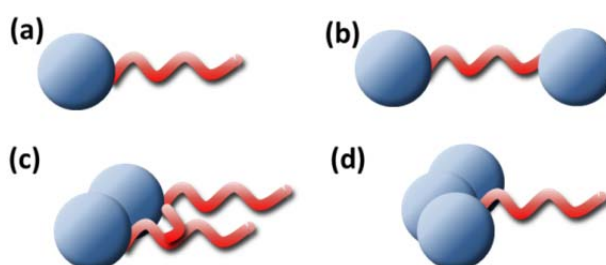


Figure 8. Schematic illustrations of various types of surfactants: (a) quaternary surfactants; (b) bolaform surfactants; (c) gemini surfactants; and (d) multi-headed surfactants.

Ionic surfactants interact with the precursors via electrostatic interactions. In the simplest case, the charges of the surfactant (S) and the ionic specie (I) are opposite under the synthesis conditions, generating S^+I^- and S^-I^{+65} interactions. Moreover, using a bridging counter ion, it is also possible to have interactions between species with the same charge, what is known as indirect synthesis. In acid media this happens through halides S^+X^- ($X = Cl^-, Br^-$) and in basic media through alkaline cations S^-M^+ ($M^+ = Na^+, K^+$).

Nonionic surfactants have very diverse structures, from linear chains to block copolymers. Self-assembly processes for this kind of surfactants basically consist of van der Waals interactions and hydrogen bonds. They are widely used because of their low cost, biodegradability and non-toxicity. They are available in a wide variety of chemical structures (Figure 9). Some examples are Pluronic, Triton, Tween, etc.

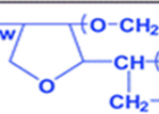
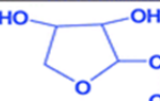
Poly (alkylene-oxide) block copolymers Oligomeric alkyl poly(ethylene oxide)	$HO(CH_2-CH_2-O)_n(\overset{CH_3}{ }CH-CH_2-O)_m(CH_2-CH_2-O)_nH$	Pluronic PEO-PPO-PEO
	$HO(\overset{CH_3}{ }CH-CH_2-O)_n(CH_2-CH_2-O)_m(\overset{CH_3}{ }CH_2-CH-O)_nH$	Pluronic R PPO-PEO-PPO
	$HO(CH_2-CH_2-O)_n(\overset{CH_2-CH_3}{ }CH-CH_2-O)_m(CH_2-CH_2-O)_nH$	PEO-PBO-PEO
	$CH_3(CH_2)_n(O-CH_2-CH_2)_mOH$	Brij
	$CH_3-\overset{CH_3}{ }CH-\overset{CH_3}{ }CH-CH_2-CH_2-CH-\overset{CH_3}{ }(O-CH_2-CH_2)_xOH$	Tergitol
Alkyl-phenol poly (ethylene oxide)	$CH_3-\overset{CH_3}{ }C-\overset{CH_3}{ }CH_2-\overset{CH_3}{ }C-\overset{CH=CH}{ }C-\overset{CH-CH}{ }C-(O-CH_2-CH_2)_xOH$	Triton
Sorbitan esters	$HO(CH_2-CH_2-O)_w$  $(O-CH_2-CH_2)_xOH$ $CH-(O-CH_2-CH_2)_yOH$ $CH_2-O-(CH_2-CH_2-O)_zC(=O)R$ <p>$x+y+z+w=20$</p>	Tween
	 $CH-CH_2-O-C(=O)-(CH_2)_nCH_3$	Span

Figure 9. Classical nonionic surfactants.

Table 4. Possible pathways for the synthesis of mesoporous materials, from reference 64.

Template	Interaction		Synt. conditions	Examples
Ionic surfactant	Direct interaction (ionic)	I^-S^+	Basic	MCM-41, MCM-48, MCM-50, FSM-16 (aluminium, iron, lead oxides, etc) AMS
		I^+S^-	Neutral-basic	
	Intermediated interaction (ionic)	$I^+X^-S^+$	Acidic	SBA-1, SBA-2, SBA-3, HMS, TLCT (aluminium, zinc oxides, etc)
		$I^-M^+S^-$	Basic	
Nonionic surfactant	Van der Waals or hydrogen bonds	I^0S^0	Acidic	HMS
		I^0N^0		MSU, SBA-15, TLCT
Copolymer (ligand assisted)	Covalent bonding	$I-S$		Nb-TMS, Ta-TMS
Nanocasting				CMK-n

Precursor addition to a surfactant solution can cause substantial changes in the self-assembly process as a result of the interactions between precursor, surfactant and solvent. In the paragraphs below the possible mechanisms are explained.

- **Cooperative assembly**

In many cases, formation of the mesostructure happens by a simultaneous assembly of the precursor and the surfactant⁶⁶. Small clusters of surfactant and precursor are initially developed in solution. Afterwards, they are held together via electrostatic interactions and keep growing into larger structures.

This has been explained on the basis of the formation of a lamellar phase^{67,68}, favoured by electrostatic interactions between precursor and surfactant. Once the condensation has started, the negative charge density diminishes, resulting in an increase of the optimum surface per polar group. For this reason, the precursor/surfactant molar ratio must increase to maintain electro-neutrality. As a consequence, the interface adopts a major curvature.

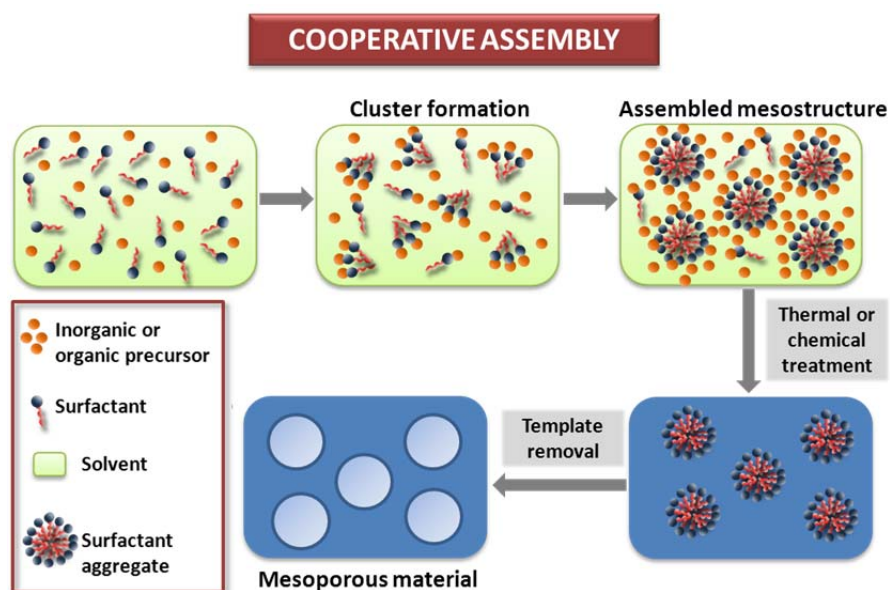


Figure 10. Scheme of cooperative assembly process.

- **Liquid crystal templating (LCT)**

In this type of process, the resulting mesostructure mainly depends on the surfactant concentration in the media. A liquid crystal phase is formed prior to the inorganic network condensation around the aggregates.

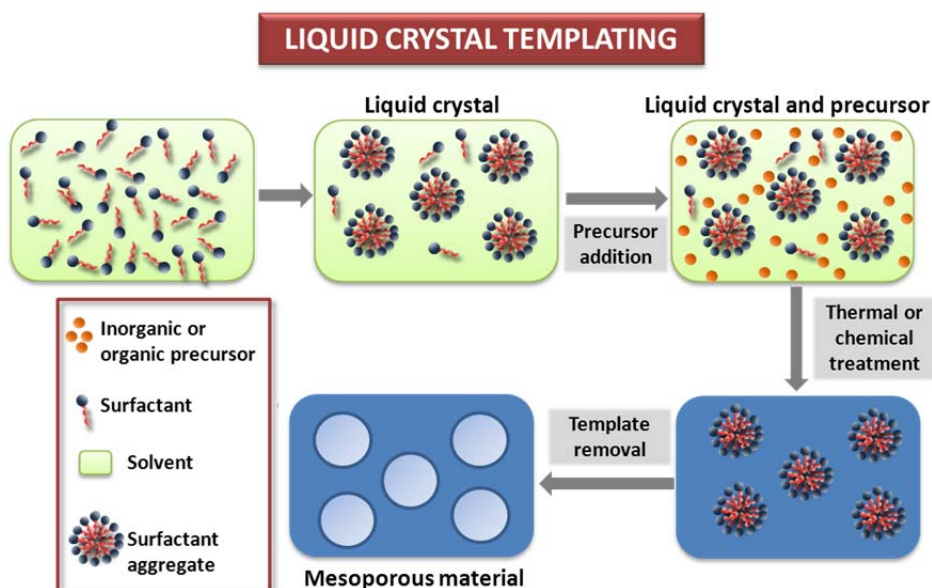


Figure 11. Scheme of liquid crystal templating process.

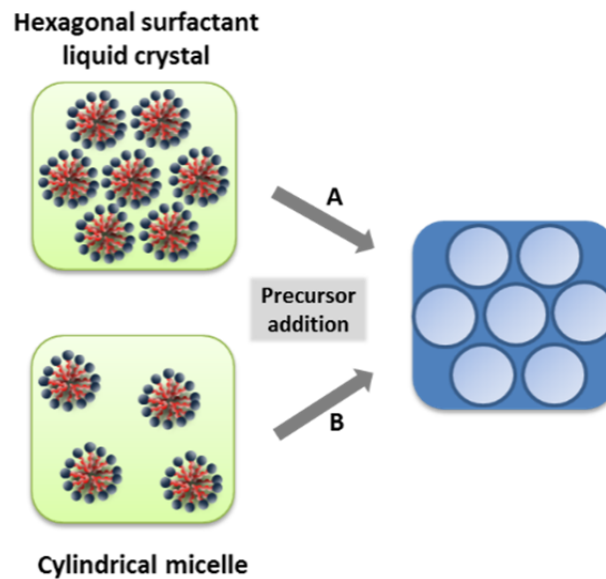


Figure 12. Different pathways for the liquid crystal templating mechanism.

The analogy with liquid crystal mesophases allows for the suggestion of two different mechanisms⁵. In the first one, silica precursors fill the water rich spaces of a hexagonal preformed phase, condensing on the polar heads. In the second, the inorganic precursor directs the surfactant self-assembly, forming rod like isolated micelles. In both cases, the inorganic phase interaction occurs through the polar heads of the surfactant.

- **Evaporation-induced self-assembly (EISA)**

A diluted solution containing the precursor, the surfactant and a volatile solvent are used in this method.

The solution is extended over a large area and allowed to evaporate. During evaporation, the solution concentration increases, reaching the CMC value. At this point, the water content is in equilibrium with the atmosphere and a crystalline phase is formed⁶⁹. Some precursors are not fully condensed in this step and relative humidity of the surroundings can affect the mesostructure; this is known as the tunable steady state⁷⁰. This method is widely used for the preparation of thin films.

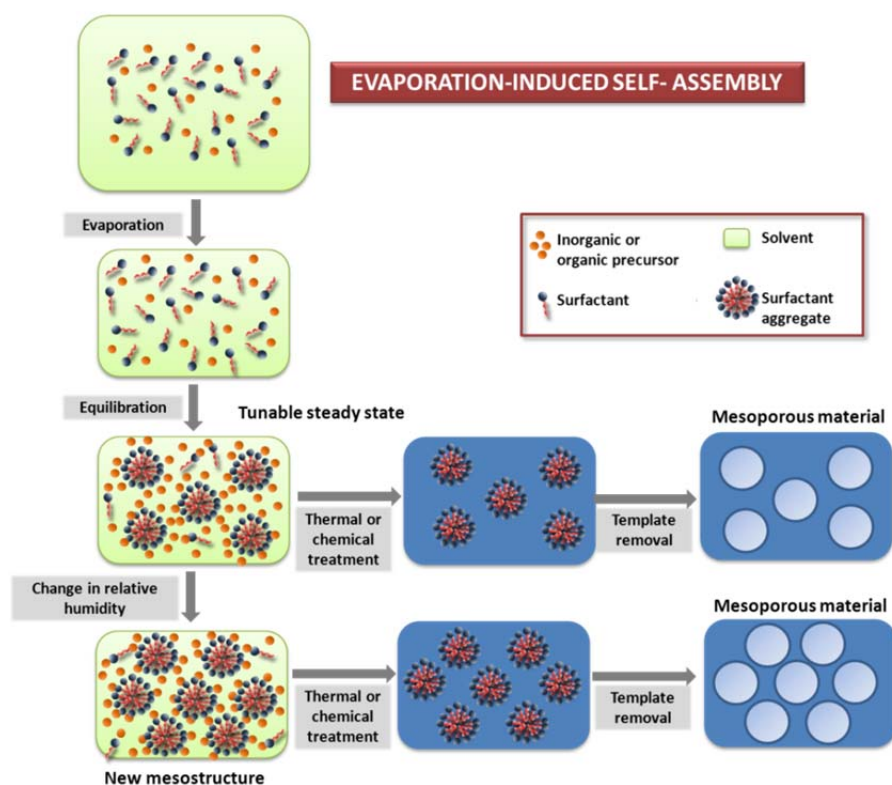


Figure 13. Scheme of evaporation-induced self-assembly process.

In all three cases, additional thermal or chemical treatment is needed to favour condensation. Afterwards, surfactant must be removed by ion exchange or calcination.

1.3.2 - Hard-templating

The hard-templating method is mainly used in the preparation of mesoporous materials that are difficult to synthesize via conventional processes. This concept was proposed by the groups of Ryoo⁷¹ and Hyeon⁷². It can be explained by the analogy of the template and the replica, although under experimental conditions the replica is not always an exact negative of the template.

Rigid structures with features in the micrometre or nanometre scale are used as templates. They are usually classified into three groups: macroscopic structures, in situ templates and discrete particles.

Examples of macroscopic structures are films, fibres, powders and monolithic objects with dimensions greater than 1 nm. In any case, the templates do not need to be formed before the synthesis. In fact, a precursor can become a template through a chemical process inducing physical or chemical transformations, which transform the compound into a solid template. Some examples are salts, carbon and ice crystals. Porous materials generated with an in situ template usually have monolithic structure. Furthermore, colloidal particles (less than 10 μm) such as polymers or SiO_2 spheres are common templates in the synthesis of hollow spheres. Other particles such as metallic oxides (in the range of micrometres or nanometres) can also be used as templates.

Mesoporous silica is usually used as the template, but other mesoporous materials, including carbon, can also be applied. For the selection of the template, two main points have to be considered. The first one is that mesopores have to be interconnected in order to keep the mesostructure after template removal (Figure 14). The other is that the template needs to be easily removed without affecting the final material.

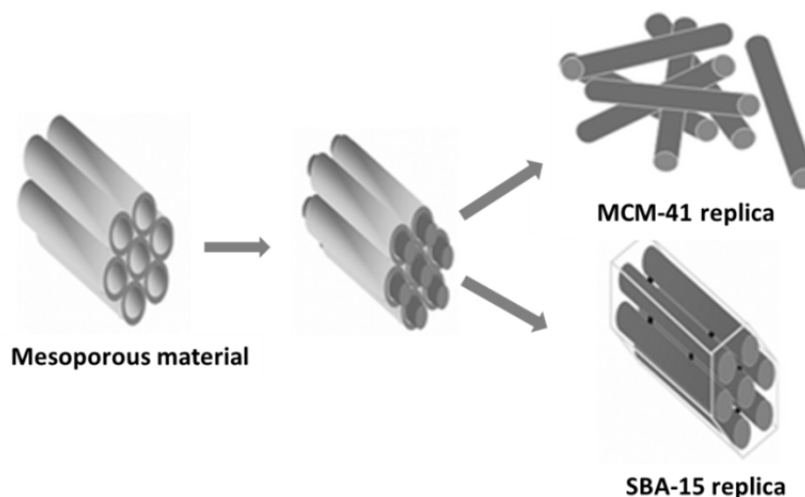


Figure 14. Synthetic procedure for the hard-templating method, from reference 73.

The synthesis of porous materials following hard templating methods involves four general steps. The first one is the formation of a precursor solution. The second

step consists of the infiltration or coating of the template with the precursor. This can be done by filling the gaps in the structure by capillarity, or immersing the template in the precursor solution (Figure 15).

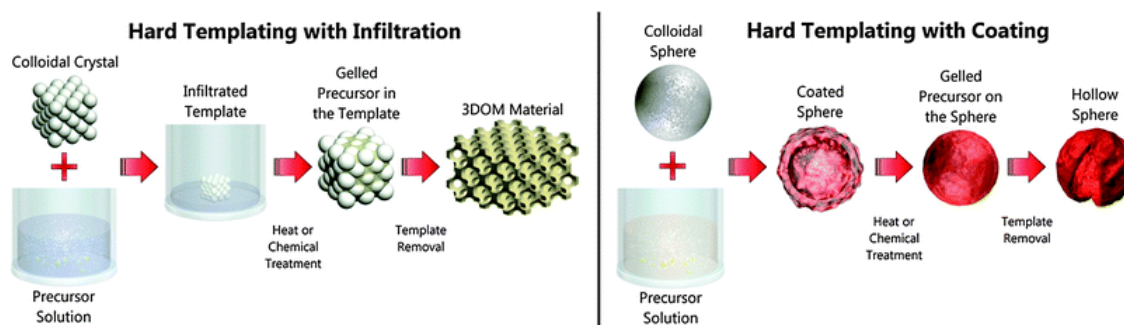


Figure 15. Hard templating synthesis using infiltration process (left) and via a coating process (right), from reference 74.

Uniform distribution of the precursor inside the template is critical in these syntheses. To obtain a good result, both template and precursor must have similar polarities and low viscosity. This step is avoided when using in situ templates. Once impregnated or coated with the precursor, the latter has to become a solid material. In this step, chemical or thermal treatments are used to induce hydrolysis and condensation of the salt or alkoxide. It is important to avoid quick gelation or uncontrolled precipitation; for this reason, the synthesis conditions might need some changes depending on the precursor. The last step is the removal of the template. Oxides can be removed via acid or basic etching and polymeric templates can be eliminated with organic solvents or by calcination. With etching it is hard to achieve complete removal of the template and several cycles might be necessary. Besides, the resistance of the resulting structure to a specific solvent needs to be tested before its use. Calcination is very effective, but temperature ramps have to be carefully selected to avoid heat focus that can affect the structure.

1.4 - Functionalization

One of the main advantages of mesoporous materials over zeolites is their great versatility with regard to functionalization. It is known that applications of pure silica are limited because of its catalytically inactive nature. However, acid and redox properties can be “added” to the material via silica substitution, or doping with different metals or organic moieties. With a good choice of the functional groups, monofunctional or multifunctional materials can be obtained, with the desired morphology, pore size, structure and surface area. This can extend applications of molecular sieves to relatively larger molecules, and it is the basis of their use in areas such as remediation, sensors^{75,76}, nanomedicine, energy, etc.

Mesoporous material functionalization is achieved with the introduction of functional groups on their internal or external surface. This can be achieved by two main approaches: in situ functionalization (via co-condensation) or post-synthetic grafting^{77,78}. The former is based on co-condensation of the alkoxysilane and an organic/inorganic precursor in a surfactant containing solution, while the latter is based on the silylation of organoalkoxysilane with silanol groups at the surface. The main advantages and disadvantages of these methods are summarized in Table 5. In both cases, the interacting moieties are preferentially located on the surface, possibly due to the occlusion caused by the surfactant micelles in the hydrophobic interior of the mesopores. In contrast, periodic mesoporous organosilica (PMOs) are materials synthesized by condensation of bridged organosilane compounds ($Z_3Si-R-SiZ_3$) around a soft template. This method of synthesis allows the integration of organic species into the walls. As a result, the organofunctionalized materials combine the functional variations of organic chemistry with the advantages of a stable inorganic support. Schematized in Figure 16 are the three functionalization methods.

Table 5. Advantages and disadvantages of the two commonly adopted but different synthetic methods to functionalize mesoporous silica.

Method	Advantages	Disadvantages
Grafting synthesis	<p>Mesostructures and mesoporosity of parent MSNs basically remained</p> <p>Grafting of the organic groups effectively performed on the available surfaces on the MSNs</p>	<p>Nonselective deposition of functional groups on the inner and outer surfaces of MSNs</p> <p>Inhomogeneous distribution of the functional groups with usually higher density at the pore mouths and on external surface of the MSNs</p>
Co-condensation synthesis	<p>A direct synthesis of MSNs with functional groups at the same time as the orderly mesostructures with certain morphology formed</p> <p>The synthesized periodic mesoporous organosilica was chemically diversified by the insertion of non-hydrolyzable Si-C covalent bonds</p>	<p>Simultaneous addition of functional molecules co-condensed with the mesophase of template-silicate aggregates, affecting the structural features of resultant MSNs</p> <p>Only organic extraction adopted as a post-synthetic treatment of functionalized MSNs to remove the templating surfactant</p>

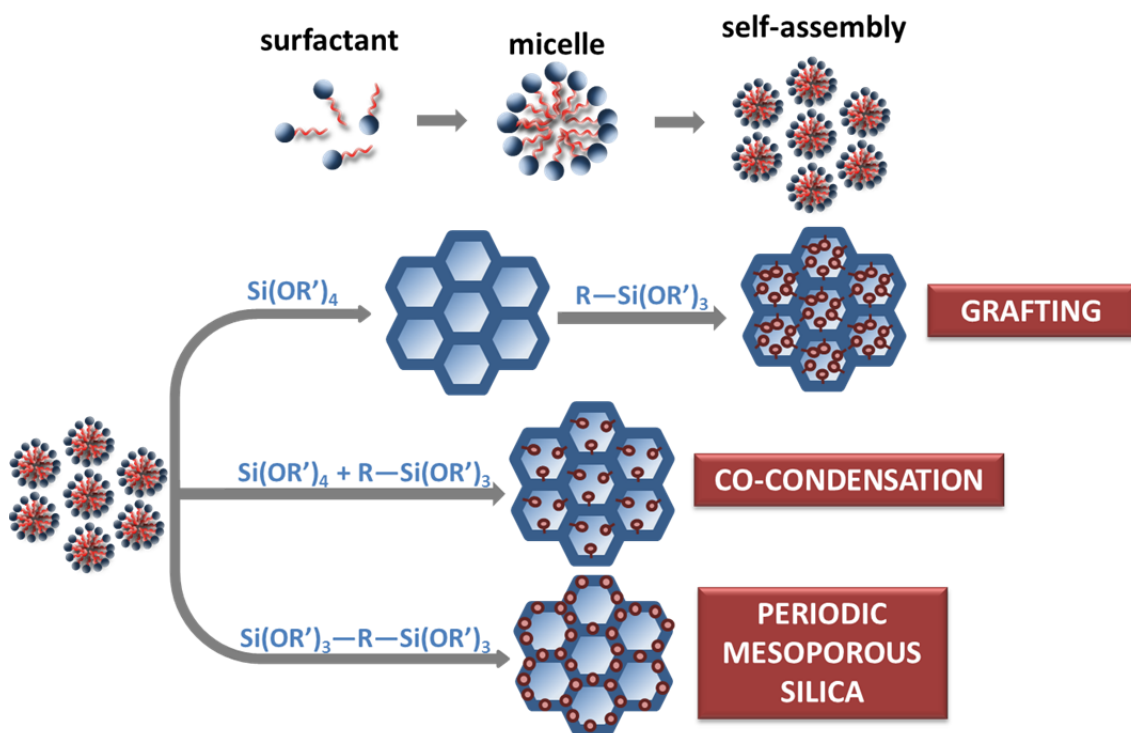


Figure 16. Synthetic pathways of organic-inorganic hybrid mesoporous silica.

The functionalization of mesoporous silica with amino groups⁷⁹ permits their use as an adsorbent, drug delivery system and solid-base catalyst. Some specific examples are the adsorption of carbon dioxide^{80,81}, heavy metals^{82,83} and oxoanions⁸⁴⁻⁸⁶, the heterogeneous catalysis of epoxidation reactions and the formation of carbon-carbon bonds^{75,87,88}, and the delivery of salicylic acid⁸⁹, among others. Thiol groups (-SH) show a great affinity with mercurium(II). Some silicas have been functionalized with thiol, thiourea or thioether, and show a large Hg²⁺ adsorption capacity and good selectivity^{90,91}.

Table 6. Pharmacology, adsorption and release mechanism of different model drugs, adapted from reference 97.

Model drug	Pharmacology	Carrier	Adsorption mechanism	Release mechanism	Ref.
Doxorubicin	Anticancer drug	1. Rattle-type Fe ₃ O ₄ @mSiO ₂	Electrostatic interaction	Dissolution-diffusion controlled mechanism	98
		2. β-CD capped MSNs	Electrostatic interaction	pH responsive release	99
Ibuprofen	Anti-inflammatory/analgesic	1. Fe ₃ O ₄ functionalized SBA-15	Physical adsorption and hydrogen bond	Diffusion controlled mechanism	100
		2. Hollow MSNs capped with PAH/PSS multilayers	Simple impregnation	pH responsive release	101
Aspirin	Anti-inflammatory/analgesic	Rattle-type Fe ₃ O ₄ @mSiO ₂	Physical adsorption and hydrogen bond	Fickian diffusion mechanism	102
Gentamycin	Antibiotic	Hollow MSNs capped with PAH/PSS multilayers	Simple impregnation	pH responsive release	103
Vancomycin	Antibiotic	CdS NPs capped MCM-41	Impregnation	Reducing agents responsive release	104
Lysozyme (Enzyme)	—	CaWO ₄ :Tb ³⁺ functionalized SBA-15	Electrostatic interaction	Diffusion controlled mechanism	105
Vitamine-B2 (Nutriment)	—	Polyamines capped MCM-41	Simple impregnation	pH and anion responsive release	106
Insulin	—	Enzyme multilayers capped MSNs	Simple impregnation	Glucose responsive release	107
Adenosine triphosphate	—	CdS NPs capped MCM-41	Simple impregnation	Reducing agents responsive release	104

Functionalization is very helpful for drug delivery applications. A chemical modification of the carrier with groups that interact with biologically active molecules allows for a better control over the drug diffusion kinetics^{92,93}. Besides, it is possible to guide the drug to the desired location and remove it after therapy⁹⁴ using multifunctional mesoporous silica composites with magnetic⁹⁵ or luminescent⁹⁶ properties. Some examples of drug delivery are summarized in Table 6.

Another important application for functionalized materials is pollutant removal¹⁰⁸; the pollutants mostly targeted are heavy metals ions and metalloids, inorganic anions, phenolic compounds, polyaromatic hydrocarbons, pesticides, and dyes.

Mesoporous silica can also be modified with the addition of inorganic groups such as metal oxides, complexes and nanoparticles, or more complex systems such as clusters, polymers or enzymes.

The first metal included in the framework of an MCM-41 silica was aluminium. After this, some others (Ti, Co, Ni, etc.) were incorporated. In the case of nanoparticles, noble metals are often deposited on silicas for catalytic applications. As for organo-functionalization, this can be done by both co-condensation or grafting processes. The main drawbacks of grafting processes are the poor dispersion of the functionalities in the material obtained, partial blocking of the porosity and weak interactions between the support and the grafted particle, leading to agglomeration and leaching. For in situ or co-condensation methods, although it is still difficult to know where the functionalities are located, the distribution within the silica is more homogeneous. Besides, trapping the moieties in the walls limits their mobility, reducing the leaching and agglomeration.

1.5 - Accessibility

A frequent objective in different syntheses of porous materials has been the search for symmetry in pore distribution. However, it has been argued that a periodic and unimodal mesoporous structure does not offer advantages for some applications. In fact, pore-blocking might be an impediment for accessibility¹⁰⁹. In practice, open structures and good accessibility to the active centres are desirable characteristics of mesoporous supports¹¹⁰.

In order to deal with accessibility problems different strategies have been adopted. One of them is the formation of nanoparticles; this implies the shortening of the pore length and the generation of inter-particle porosity through nanoparticle packing¹¹¹. This strategy offers the possibility of combining enhanced accessibility to the functional active groups (across large pores) with the conservation of high surface area and pore volume^{112,113}. The first nano-sized mesoporous silicas were synthesized by the groups of Cai¹¹⁴, Mann¹¹⁵ and Ostafin¹¹⁶ and the term MSN was popularized by Lin¹⁰⁴ to refer to mesoporous silica nanospheres.

Another approach was the creation of hierarchic pore systems, using in the synthesis as many templates as desired pore sizes⁷⁴. By the combination of soft and hard-templating methods, any number of hard templates can be coated or filled with a surfactant containing precursor solution.

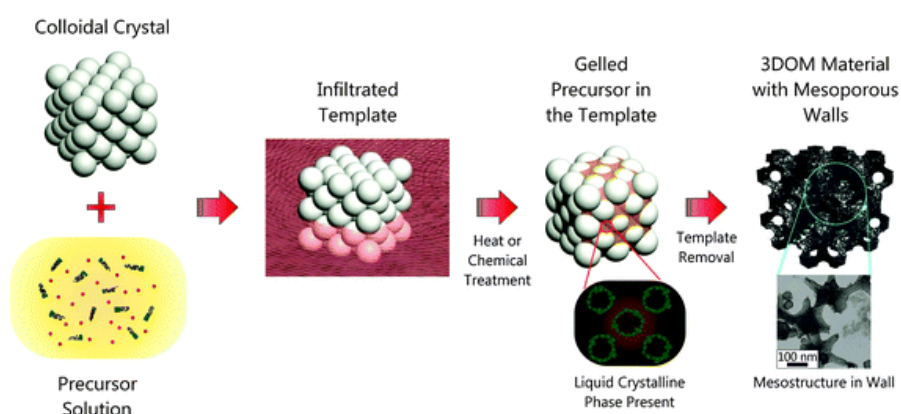


Figure 17. Multiple templating approach.

Different combinations of soft and hard templating can induce some changes in the mesostructure. As an example, figure 17 shows the combination of colloidal crystal templating and surfactant templating.

A common point for both approaches is that the diffusion through the pore system is enhanced. For applications such as catalysis or medicine, one of the main points is the control of the diffusion of reactants and products.

1.6 - Previous work by the group and motivation

In 2002, the Nanostructured Materials Group from the Institut de Ciència dels Materials of the University of Valencia (ICMUV) developed a new mesoporous silica material, UVM-7, a nanoparticulated material with a bimodal pore system.

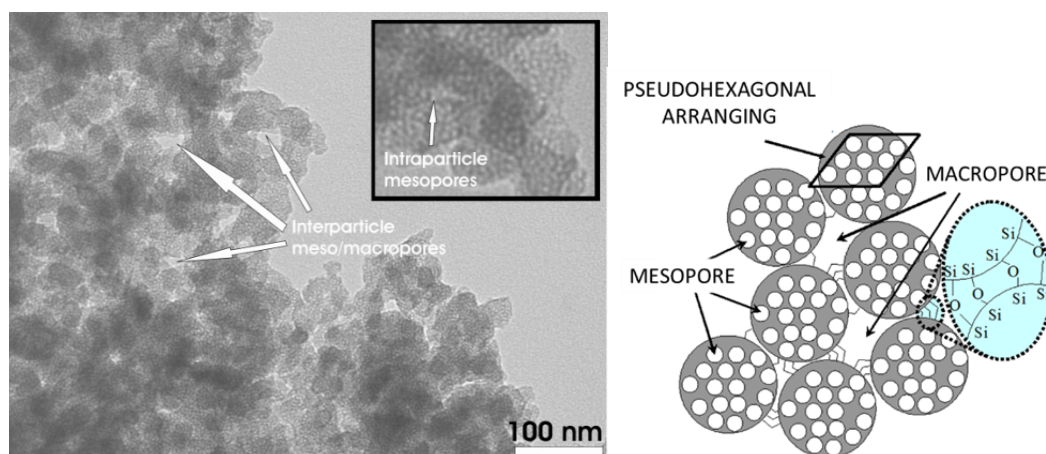


Figure 18. TEM image and scheme of UVM-7 .

The main difference between this material and MCM-41 is derived from how it is prepared. Thus, in the case of MCM-41, because of the NaOH addition the pH is close to 11. This pH guarantees an Ostwald growth of the particles, obtaining a large, compact mesostructure. In the case of UVM-7, the working pH is close to 9. Under these conditions, redissolution is not favoured and the system evolves into randomly

aggregated nanoparticles. Once the surfactant is removed, this aggregation leads to a bimodal pore system. As previously explained, the accessibility of the material was enhanced in comparison with MCM-41. The porosity of this material is high and comparable to that of MCM-41, but an X-Ray diffractogram shows less order in the structure due to worse stacking of pores in the nanoparticles (disordered hexagonal packing). Moreover, inter-particle pores are not reflected in the X-Ray diffractogram because of the lack of periodicity.

The inorganic precursor in UVM-7 synthesis is an atrane complex; a complex formed by transesterification of an alkoxide in non-aqueous solvent. Metallic alkoxides are thermodynamically unstable in water solution; they easily react with water to form a precipitate. In order to moderate this reactivity some metallic complexes are used, providing major inertia when increasing both the size of the organic groups in ligands (steric effect), and the number of hydroxyl groups (chelate effect). For these reasons, polyalcoholic complexes are considered good candidates for their use as precursors.

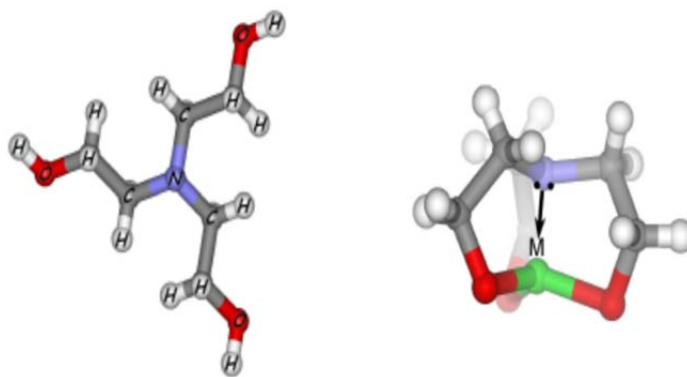


Figure 19. Structural model of triethanolamine molecule (left) and an atrane complex (right).

In the above mentioned case, triethanolamine (2,2',2''-nitrietriethanol, TEA) was selected due to its nature, physical properties and availability. It is a tertiary amine with three ethanol substituents. It forms thermodynamically reactive but kinetically inert complexes with a diversity of metals, and in the absence of water TEA acts as a tripod ligand¹¹⁷.

The use of atrane complexes instead of alkoxides has a number of advantages: it acts as a buffering agent, keeping basic pH (pH=8-9) implies a high degree of hydrolysis and condensation with minimum re-dissolution which favours the formation of aggregates of nanoparticles. Also, the presence of TEA helps to harmonize the rates of the hydrolytic processes involving different metallic centres (while alkoxides have a very different reactivity), which is very useful for the preparation of mixed oxides: atrane complexes are water miscible so hydrolysis and condensation happen in an homogenous phase in the whole system, not only at the interface.

Using the atrane method, the group has worked on mesoporous materials with different compositions. Some previous publications from the group on different porous materials and their applications are shown in Table 7. Mesoporous silica, alumina and titania¹¹⁸, as well as modified silica with different metals (Ti, V, Al, Zr, Co)^{111,119,120} or organically modified¹²¹ are some of the materials previously studied. Intra-particle pore size has been modulated by using different surfactants (C_xTMABr, x=10-18), while inter-particle pore size has been controlled by modifying the dielectric constant of the media with ethanol¹²².

With regard to applications, thiol modified UVM-7 has been used in Hg²⁺ detection¹²³; as chemosensors when amino modified¹²⁴; and Ti-UVM-7 has been used to improve epoxide production¹²⁵. Moreover, in collaboration with external groups, different mesoporous materials have been tested as catalysts¹²⁶⁻¹²⁹, drug carriers¹³⁰, adsorbents¹³¹, etc.

Table 7. Previous work from the group.

Year	Material	Objective	Pore size / BET surface area	Ref.
1999	ICMUV-3 (aluminophosphates)	Tune the pore size by adjusting P/Al molar ratio (0.12-1.5)	1,3-3,7 nm 480-650 m ² /g	132
1999	alumina	Tune pore size by changing water/TEA molar ratio (7.4-44.5)	3,3-6,0 nm 250-340 m ² /g	133
2000	ICMUV-4 (mesoporous TiO ₂)	Preparation of thermally stable and high surface area mesoporous titania	3,5 nm 606 m ² /g	134
2000	AIO (ICMUV-1), TiO (ICMUV-4). SiO, doped silica (Si/M), ALPO/SAPO	Use of a hydrolysis retarding agent to obtain diverse mesoporous materials	-	118
2001	ICMUV-6 (N-containing silicas)	Preparation of ordered mesoporous N-containing silicas (N % 6,9-12,9)	1,7-2,0 nm 882-1095 m ² /g	135
2002	UVM-7, M-UVM-7 (M=Al, Ti, V, Zr)	Preparation of bimodal silicas (powders and monoliths) and doping with different elements	2,6-3,2 nm 924-1095 m ² /g	111
2002	Organosilicas (bis(triethoxysilyl)ethane, methyltriethoxysilane)	Preparation of bimodal organosilicas (0-100 % BTE, 0-50 % MTMS)	2,69-3,38 nm 7125-1095 m ² /g	121
2002	Ti-UVM-7	Use of Ti-UVM-7 as catalyst in olefin epoxidation Si/Ti 10-80	2,83-3,17 nm 1045-1125 m ² /g	125
2002	MCM-41	Grafting of aminoanthracene onto mesoporous silica and use as anion sensor		124
2003	UVM-7 like	Preparation of silica-based monoliths with a trimodal pore system (UVM-7 nanoparticles and polyurethane foams)		136
2004	Co-MCM-41	Preparation in one-pot of Co-MCM-41 (Si/Co 20-50)	2,47-2,50 nm 479-909 m ² /g	119
2004	UVM-9 (Aluminophosphonates and diphosphonates)	Preparation of mesoporous aluminium phosphonates and diphosphonates	2,69-3,32 nm 633-793 m ² /g	137
2004	UVM-10 (mesoporous silica), Al-UVM-10, Ti-UVM-10	Use of low-cost precursors (sodium silicate) for the synthesis of mesoporous silica	2,71-3,11 nm 481-839 m ² /g	138
2005	UVM-7	Immobilization of lysozyme and α -L-arabinofuranosidase in UVM-7		139
2006	UVM-7	Formation of nanoparticulated bimodal silicas	2,91 nm 1073 m ² /g	140

Year	Material	Objective	Pore size / BET surface area	Ref.
2006	Zr-UVM-7	Synthesis of mesoporous silica doped with Zr (Si/Zr 5-50)	2,70-2,99 nm 846-1146 m ² /g	120
2007	UVM-7 covered ceramic foam	Preparation of trimodal silicas with UVM-7 nanoparticles and ceramic foams	3,12 nm /50 nm 44-140 m ² /g	141
2008	UVM-7	Control of the pore size by changing surfactant chain and control of aggregation with ethanol	1,8-3,4 nm 1050-1279 m ² /g	122
2008	ZnO nanoparticles in MCM-41	Preparation of ZnO nanoparticles embedded in the wall of MCM-41 (Si/Zn 5-50)	2,09-2,26 nm 440-1114 m ² /g	142
2008	UVM-7-SH	Preparation of UVM-7-SH materials and use in detection and adsorption of Hg ²⁺	2,37 nm 596 m ² /g	123
2009		Use of chitosan to promote silica formation and aggregation as happens in diatoms	-	143
2009	Zn-UVM-7	Synthesis of ZnO nanoparticles embedded in UVM-7 (Si/Zn 5-30)	2,63-2,80 nm 756-1061 m ² /g	144
2009	phosphite	Preparation of mesoporous materials containing phosphite anions (50-100 % phosphorous acid solution)	2,53-2,71 nm 432-510 m ² /g	145
2010	Au/Co-UVM-7	Deposition of gold nanoparticles on metal nanodomains embedded in UVM-7 silica (Si/Co 10-45)	636-1002 m ² /g	146
2012	Au/Co-UVM-7	Preparation of catalysts containing both, gold and cobalt, supported on a mesoporous UVM-7 (Si/Co 10-45) and use in propane and toluene oxidation	549-1099 m ² /g	147
2012	UVM-7	Ibuprofen storage in UVM-7 and delivery	-	148
2014	UVM-10, M-UVM-10	Preparation of low-cost mesoporous silica and doping with metals		149

In this doctoral thesis, the study of the UVM-7 silica is perfected by establishing the interconnected nature of the UVM-7 intra-particle mesopore. Moreover, the expansion of the mesopore system using swelling agents is dealt with. This expansion serves a dual purpose: the introduction of larger molecules in the mesopore and the increase in the loading capability of the support.

Once the atrane route re-examination has been concluded, mixed silica and metal-oxide systems are studied for their use in catalysis. Mixed oxides of Si/Ni/Ce(Sn) and SiO₂/TiO₂(ZrO₂) nanocomposites have been prepared. In both cases, gold nanoparticles are deposited on the materials and the solid is used as a catalyst in different reactions.

Last but not least, following the studies of the group on non-silica mesoporous materials (titania, alumina, aluminium phosphates), mesoporous iron phosphate mixed oxides have been explored.

References

1. Smith, J. V. *Chemical Reviews* **1988**, *88*, 149-182.
2. van Donk, S.; Broersma, A.; Gijzeman, O. L. J.; van Bokhoven, J. A.; Bitter, J. H.; de Jong, K. P. *Journal of Catalysis* **2001**, *204*, 272-280.
3. Kresge, C. T.; Leonowicz, M. E.; Roth, W. J.; Vartuli, J. C.; Beck, J. S. *Nature* **1992**, *359*, 710-712.
4. Kresge, C. T.; Roth, W. J. *Chemical Society Reviews* **2013**, *42*, 3663-3670.
5. Beck, J. S.; Vartuli, J. C.; Roth, W. J.; Leonowicz, M. E.; Kresge, C. T.; Schmitt, K. D.; Chu, C. T. W.; Olson, D. H.; Sheppard, E. W.; McCullen, S. B.; Higgins, J. B.; Schlenker, J. L. *Journal of the American Chemical Society* **1992**, *114*, 10834-10843.
6. Kresge, C. T.; Leonowicz, M. E.; Roth, W. J.; Schmitt, K. D.; Vartuli, J. C. In *Google patents*, 1993.
7. Landis, M. E.; Aufdembrink, B. A.; Chu, P.; Johnson, I. D.; Kirker, G. W.; Rubin, M. K. *Journal of the American Chemical Society* **1991**, *113*, 3189-3190.
8. Leonowicz, M. E.; Lawton, J. A.; Lawton, S. L.; Rubin, M. K. *Science* **1994**, *264*, 1910-1913.
9. Vartuli, J. C.; Schmitt, K. D.; Kresge, C. T.; Roth, W. J.; Leonowicz, M. E.; McCullen, S. B.; Hellring, S. D.; Beck, J. S.; Schlenker, J. L.; Olson, D. H.; Sheppard, E. W. *Chemistry of Materials* **1994**, *6*, 2317-2326.
10. Tiddy, G. J. T. *Physics Reports-Review Section of Physics Letters* **1980**, *57*, 1-46.
11. Chiola, V.; Ritsko, J. E.; Vanderpool, C. D.; Office, U. S. P. Ed., 1971.
12. Inagaki, S.; Fukushima, Y.; Kuroda, K. *Journal of the Chemical Society-Chemical Communications* **1993**, 680-682.
13. Yanagisawa, T.; Shimizu, T.; Kuroda, K.; Kato, C. *Bulletin of the Chemical Society of Japan* **1990**, *63*, 988-992.
14. Perego, C.; Millini, R. *Chemical Society Reviews* **2013**, *42*, 3956-3976.
15. Garcia-Martinez, J.; Li, K.; Krishnaiah, G. *Chemical Communications* **2012**, *48*, 11841-11843.
16. Da, J.-W.; Song, C.-M.; Qian, L.; Su, J.-M.; Xu, X.-Z. *Journal of Porous Materials* **2008**, *15*, 189-197.
17. Pal, N.; Bhaumik, A. *Advances in Colloid and Interface Science* **2013**, *189*, 21-41.

18. Hartmann, M.; Vinu, A.; Chandrasekar, G. *Chemistry of Materials* **2005**, *17*, 829-833.
19. Vinu, A.; Hossain, K. Z.; Kumar, G. S.; Sivamurugan, V.; Ariga, K. *Nanoporous Materials Iv* **2005**, *156*, 631-636.
20. Chew, T.-L.; Ahmad, A. L.; Bhatia, S. *Advances in Colloid and Interface Science* **2010**, *153*, 43-57.
21. Salinas, A. J.; Shruti, S.; Malavasi, G.; Menabue, L.; Vallet-Regi, M. *Acta Biomaterialia* **2011**, *7*, 3452-3458.
22. Paul, M.; Pal, N.; Rajamohanan, P. R.; Rana, B. S.; Sinha, A. K.; Bhaumik, A. *Physical Chemistry Chemical Physics* **2010**, *12*, 9389-9394.
23. Nandi, M.; Sarkar, M.; Sarkar, K.; Bhaumik, A. *Journal of Physical Chemistry C* **2009**, *113*, 6839-6844.
24. Choi, S.; Drese, J. H.; Jones, C. W. *Chemsuschem* **2009**, *2*, 796-854.
25. Volkov, V. V.; Lebedeva, V. I.; Petrova, I. V.; Bobyl, A. V.; Konnikov, S. G.; Roldughin, V. I.; van Erkel, J.; Tereshchenko, G. F. *Advances in Colloid and Interface Science* **2011**, *164*, 144-155.
26. Vaidhyanathan, R.; Iremonger, S. S.; Shimizu, G. K. H.; Boyd, P. G.; Alavi, S.; Woo, T. K. *Science* **2010**, *330*, 650-653.
27. Colilla, M.; Izquierdo-Barba, I.; Sanchez-Salcedo, S.; Fierro, J. L. G.; Hueso, J. L.; Vallet-Regi, M. *Chemistry of Materials* **2010**, *22*, 6459-6466.
28. Li, X.; Zhang, J.; Gu, H. *Langmuir* **2011**, *27*, 6099-6106.
29. Min, K. H.; Lee, H. J.; Kim, K.; Kwon, I. C.; Jeong, S. Y.; Lee, S. C. *Biomaterials* **2012**, *33*, 5788-5797.
30. Vivero-Escoto, J. L.; Slowing, I. I.; Wu, C.-W.; Lin, V. S. Y. *Journal of the American Chemical Society* **2009**, *131*, 3462-+.
31. Lapisardi, G.; Chiker, F.; Launay, F.; Nogier, J. P.; Bonardet, J. L. *Catalysis Communications* **2004**, *5*, 277-281.
32. Sayari, A.; Liu, P. *Microporous Materials* **1997**, *12*, 149-177.
33. Pal, N.; Paul, M.; Bera, A.; Basak, D.; Bhaumik, A. *Analytica Chimica Acta* **2010**, *674*, 96-101.
34. Knoefel, C.; Lutecki, M.; Martin, C.; Mertens, M.; Hornebecq, V.; Llewellyn, P. L. *Microporous and Mesoporous Materials* **2010**, *128*, 26-33.
35. Guidotti, M.; Gavrilova, E.; Galarneau, A.; Coq, B.; Psaroa, R.; Ravasio, N. *Green Chemistry* **2011**, *13*, 1806-1811.
36. Pal, N.; Paul, M.; Bhaumik, A. *Applied Catalysis a-General* **2011**, *393*, 153-160.

37. Diaz, U.; Garcia, T.; Velty, A.; Corma, A. *Chemistry-a European Journal* **2012**, *18*, 8659-8672.
38. Sun, S.; Wang, W.; Shang, M.; Ren, J.; Zhang, L. *Journal of Molecular Catalysis a-Chemical* **2010**, *320*, 72-78.
39. Modak, A.; Mondal, J.; Sasidharan, M.; Bhaumik, A. *Green Chemistry* **2011**, *13*, 1317-1331.
40. Rafiee, E.; Eavani, S. *Green Chemistry* **2011**, *13*, 2116-2122.
41. Mondal, J.; Sen, T.; Bhaumik, A. *Dalton Transactions* **2012**, *41*, 6173-6181.
42. Ma, T.-Y.; Yuan, Z.-Y.; Cao, J.-L. *European Journal of Inorganic Chemistry* **2010**, 716-724.
43. Noda, Y.; Lee, B.; Domen, K.; Kondo, J. N. *Chemistry of Materials* **2008**, *20*, 5361-5367.
44. Groves, J. A.; Miller, S. R.; Warrender, S. J.; Mellot-Draznieks, C.; Lightfoot, P.; Wright, P. A. *Chemical Communications* **2006**, 3305-3307.
45. Huang, Z. B.; Tang, F. Q. *Journal of Colloid and Interface Science* **2005**, *281*, 432-436.
46. Muralidharan, M. N.; Rasmitha, C. A.; Ratheesh, R. *Journal of Porous Materials* **2009**, *16*, 635-640.
47. Ozkan, E.; Lee, S. H.; Liu, P.; Tracy, C. E.; Tepehan, F. Z.; Pitts, J. R.; Deb, S. K. *Solid State Ionics* **2002**, *149*, 139-146.
48. Chandra, D.; Yokoi, T.; Tatsumi, T.; Bhaumik, A. *Chemistry of Materials* **2007**, *19*, 5347-5354.
49. Chandra, D.; Mukherjee, N.; Mondal, A.; Bhaumik, A. *Journal of Physical Chemistry C* **2008**, *112*, 8668-8674.
50. Prado, A. G. S.; Airoidi, C. *Journal of Materials Chemistry* **2002**, *12*, 3823-3826.
51. Chandra, D.; Mridha, S.; Basak, D.; Bhaumik, A. *Chemical Communications* **2009**, 2384-2386.
52. Waitz, T.; Wagner, T.; Sauerwald, T.; Kohl, C.-D.; Tiemann, M. *Advanced Functional Materials* **2009**, *19*, 653-661.
53. Teoh, L. G.; Hung, I. M.; Shieh, J.; Lai, W. H.; Hon, M. H. *Electrochemical and Solid State Letters* **2003**, *6*, G108-G111.
54. Wagner, T.; Kohl, C. D.; Froba, M.; Tiemann, M. *Sensors* **2006**, *6*, 318-323.
55. Sarkar, K.; Dhara, K.; Nandi, M.; Roy, P.; Bhaumik, A.; Banerjee, P. *Advanced Functional Materials* **2009**, *19*, 223-234.

56. Wang, J.-Q.; Huang, L.; Xue, M.; Wang, Y.; Gao, L.; Zhu, J. H.; Zou, Z. *Journal of Physical Chemistry C* **2008**, *112*, 5014-5022.
57. Descalzo, A. B.; Rurack, K.; Weisshoff, H.; Martinez-Manez, R.; Marcos, M. D.; Amoros, P.; Hoffmann, K.; Soto, J. *Journal of the American Chemical Society* **2005**, *127*, 184-200.
58. Melde, B. J.; Johnson, B. J.; Charles, P. T. *Sensors* **2008**, *8*, 5202-5228.
59. Lee, E. Z.; Lee, S. U.; Heo, N.-S.; Stucky, G. D.; Jun, Y.-S.; Hong, W. H. *Chemical Communications* **2012**, *48*, 3942-3944.
60. Martinez-Manez, R.; Sancenon, F. *Coordination Chemistry Reviews* **2006**, *250*, 3081-3093.
61. Melde, B. J.; Johnson, B. J. *Analytical and Bioanalytical Chemistry* **2010**, *398*, 1565-1573.
62. Slowing, I. I.; Trewyn, B. G.; Giri, S.; Lin, V. S. Y. *Advanced Functional Materials* **2007**, *17*, 1225-1236.
63. Li, L.-L.; Sun, H.; Fang, C.-J.; Xu, J.; Jin, J.-Y.; Yan, C.-H. *Journal of Materials Chemistry* **2007**, *17*, 4492-4498.
64. Taguchi, A.; Schuth, F. *Microporous and Mesoporous Materials* **2005**, *77*, 1-45.
65. Huo, Q. S.; Margolese, D. I.; Ciesla, U.; Feng, P. Y.; Gier, T. E.; Sieger, P.; Leon, R.; Petroff, P. M.; Schuth, F.; Stucky, G. D. *Nature* **1994**, *368*, 317-321.
66. Fan, W.; Snyder, M. A.; Kumar, S.; Lee, P.-S.; Yoo, W. C.; McCormick, A. V.; Penn, R. L.; Stein, A.; Tsapatsis, M. *Nature Materials* **2008**, *7*, 984-991.
67. Stucky, G. D.; Monnier, A.; Schuth, F.; Huo, Q.; Margolese, D.; Kumar, D.; Krishnamurty, M.; Petroff, P.; Firouzi, A.; Janicke, M.; Chmelka, B. F. *Molecular Crystals and Liquid Crystals Science and Technology Section a-Molecular Crystals and Liquid Crystals* **1994**, *240*, 187-200.
68. Monnier, A.; Schuth, F.; Huo, Q.; Kumar, D.; Margolese, D.; Maxwell, R. S.; Stucky, G. D.; Krishnamurty, M.; Petroff, P.; Firouzi, A.; Janicke, M.; Chmelka, B. F. *Science* **1993**, *261*, 1299-1303.
69. Soler-Illia, G. J. A. A.; Azzaroni, O. *Chemical Society Reviews* **2011**, *40*, 1107-1150.
70. Soler-illia, G. J. D.; Sanchez, C.; Lebeau, B.; Patarin, J. *Chemical Reviews* **2002**, *102*, 4093-4138.
71. Ryoo, R.; Joo, S. H.; Jun, S. *Journal of Physical Chemistry B* **1999**, *103*, 7743-7746.

72. Lee, J.; Yoon, S.; Hyeon, T.; Oh, S. M.; Kim, K. B. *Chemical Communications* **1999**, 2177-2178.
73. Van der Voort, P.; Vercaemst, C.; Schaubroeck, D.; Verpoort, F. *Physical Chemistry Chemical Physics* **2008**, *10*, 347-360.
74. Petkovich, N. D.; Stein, A. *Chemical Society Reviews* **2013**, *42*, 3721-3739.
75. Davis, M. E. *Nature* **2002**, *417*, 813-821.
76. Wagner, T.; Haffer, S.; Weinberger, C.; Klaus, D.; Tiemann, M. *Chemical Society Reviews* **2013**, *42*, 4036-4053.
77. Sayari, A.; Hamoudi, S. *Chemistry of Materials* **2001**, *13*, 3151-3168.
78. Stein, A.; Melde, B. J.; Schroden, R. C. *Advanced Materials* **2000**, *12*, 1403-1419.
79. Yokoi, T.; Kubota, Y.; Tatsumi, T. *Applied Catalysis a-General* **2012**, 421.
80. Serna-Guerrero, R.; Sayari, A. *Chemical Engineering Journal* **2010**, 161.
81. Yue, M. B.; Sun, L. B.; Cao, Y.; Wang, Y.; Wang, Z. J.; Zhu, J. H. *Chemistry-a European Journal* **2008**, *14*.
82. Antochshuk, V.; Jaroniec, M. *Chemical Communications* **2002**, 258-259.
83. Mercier, L.; Pinnavaia, T. J. *Environmental Science & Technology* **1998**, *32*, 2749-2754.
84. Yoshitake, H.; Yokoi, T.; Tatsumi, T. *Chemistry Letters* **2002**, 586-587.
85. Peak, D.; Sparks, D. L. *Environmental Science & Technology* **2002**, *36*, 1460-1466.
86. Nickson, R.; McArthur, J.; Burgess, W.; Ahmed, K. M.; Ravenscroft, P.; Rahman, M. *Nature* **1998**, *395*, 338-338.
87. Ying, J. Y.; Mehnert, C. P.; Wong, M. S. *Angewandte Chemie-International Edition* **1999**, *38*, 56-77.
88. Wight, A. P.; Davis, M. E. *Chemical Reviews* **2002**, *102*, 3589-3613.
89. Rosenholm, J. M.; Linden, M. *Journal of Controlled Release* **2008**, *128*, 157-164.
90. Feng, X.; Fryxell, G. E.; Wang, L. Q.; Kim, A. Y.; Liu, J.; Kemner, K. M. *Science* **1997**, *276*, 923-926.
91. Antochshuk, V.; Olkhovyk, O.; Jaroniec, M.; Park, I. S.; Ryoo, R. *Langmuir* **2003**, *19*, 3031-3034.
92. Vallet-Regi, M. *Chemistry-a European Journal* **2006**, *12*, 5934-5943.
93. Balas, F.; Manzano, M.; Horcajada, P.; Vallet-Regi, M. *Journal of the American Chemical Society* **2006**, *128*, 8116-8117.

94. Akerman, M. E.; Chan, W. C. W.; Laakkonen, P.; Bhatia, S. N.; Ruoslahti, E. *Proceedings of the National Academy of Sciences of the United States of America* **2002**, *99*, 12617-12621.
95. Zhang, L.; Qiao, S.; Jin, Y.; Chen, Z.; Gu, H.; Lu, G. Q. *Advanced Materials* **2008**, *20*, 805-+.
96. Insin, N.; Tracy, J. B.; Lee, H.; Zimmer, J. P.; Westervelt, R. M.; Bawendi, M. G. *Acs Nano* **2008**, *2*, 197-202.
97. Yang, P.; Gai, S.; Lin, J. *Chemical Society Reviews* **2012**, *41*, 3679-3698.
98. Liu, Y.; Zhang, W. Z.; Pinnavaia, T. J. *Angewandte Chemie-International Edition* **2001**, *40*, 1255-+.
99. Meng, H.; Xue, M.; Xia, T.; Zhao, Y.-L.; Tamanoi, F.; Stoddart, J. F.; Zink, J. I.; Nel, A. E. *Journal of the American Chemical Society* **2010**, *132*, 12690-12697.
100. Huang, S.; Yang, P.; Cheng, Z.; Li, C.; Fan, Y.; Kong, D.; Lin, J. *Journal of Physical Chemistry C* **2008**, *112*, 7130-7137.
101. Zhu, Y. F.; Shi, J. L.; Shen, W. H.; Dong, X. P.; Feng, J. W.; Ruan, M. L.; Li, Y. S. *Angewandte Chemie-International Edition* **2005**, *44*, 5083-5087.
102. Zhu, Y.; Kockrick, E.; Ikoma, T.; Hanagata, N.; Kaskel, S. *Chemistry of Materials* **2009**, *21*, 2547-2553.
103. Zhu, Y.; Shi, J. *Microporous and Mesoporous Materials* **2007**, *103*, 243-249.
104. Lai, C. Y.; Trewyn, B. G.; Jęftinija, D. M.; Jęftinija, K.; Xu, S.; Jęftinija, S.; Lin, V. S. Y. *Journal of the American Chemical Society* **2003**, *125*, 4451-4459.
105. Huang, S.; Li, C.; Yang, P.; Zhang, C.; Cheng, Z.; Fan, Y.; Lin, J. *European Journal of Inorganic Chemistry* **2010**, 2655-2662.
106. Bernardos, A.; Aznar, E.; Coll, C.; Martinez-Manez, R.; Manuel Barat, J.; Dolores Marcos, M.; Sancenon, F.; Benito, A.; Soto, J. *Journal of Controlled Release* **2008**, *131*, 181-189.
107. Zhao, W.; Zhang, H.; He, Q.; Li, Y.; Gu, J.; Li, L.; Li, H.; Shi, J. *Chemical Communications* **2011**, *47*, 9459-9461.
108. Walcarius, A.; Mercier, L. *Journal of Materials Chemistry* **2010**, *20*, 4478-4511.
109. Rolison, D. R. *Science* **2003**, *299*, 1698-1701.
110. Zurner, A.; Kirstein, J.; Doblinger, M.; Brauchle, C.; Bein, T. *Nature* **2007**, *450*, 705-+.
111. El Haskouri, J.; de Zarate, D. O.; Guillem, C.; Latorre, J.; Caldes, M.; Beltran, A.; Beltran, D.; Descalzo, A. B.; Rodriguez-Lopez, G.; Martinez-Manez, R.; Marcos, M. D.; Amoros, P. *Chemical Communications* **2002**, 330-331.

112. Antonietti, M.; Ozin, G. A. *Chemistry-a European Journal* **2004**, *10*, 29-41.
113. Yuan, Z. Y.; Su, B. L. *Journal of Materials Chemistry* **2006**, *16*, 663-677.
114. Cai, Q.; Luo, Z. S.; Pang, W. Q.; Fan, Y. W.; Chen, X. H.; Cui, F. Z. *Chemistry of Materials* **2001**, *13*, 258-263.
115. Fowler, C. E.; Khushalani, D.; Lebeau, B.; Mann, S. *Advanced Materials* **2001**, *13*, 649-652.
116. Nooney, R. I.; Thirunavukkarasu, D.; Chen, Y. M.; Josephs, R.; Ostafin, A. E. *Chemistry of Materials* **2002**, *14*, 4721-4728.
117. Voronkov, M. G. *Pure and Applied Chemistry* **1966**, *13*, 35-60.
118. Cabrera, S.; El Haskouri, J.; Guillem, C.; Latorre, J.; Beltran-Porter, A.; Beltran-Porter, D.; Marcos, M. D.; Amoros, P. *Solid State Sciences* **2000**, *2*, 405-420.
119. El Haskouri, J.; Cabrera, S.; Gomez-Garcia, C. J.; Guillem, C.; Latorre, J.; Beltran, A.; Beltran, D.; Marcos, M. D.; Amoros, P. *Chemistry of Materials* **2004**, *16*, 2805-2813.
120. de Zarate, D. O.; Gomez-Moratalla, A.; Guillem, C.; Beltran, A.; Latorre, J.; Beltran, D.; Amoros, P. *European Journal of Inorganic Chemistry* **2006**, 2572-2581.
121. El Haskouri, J.; de Zarate, D. O.; Guillem, C.; Beltran-Porter, A.; Caldes, M.; Marcos, M. D.; Beltran-Porter, D.; Latorre, J.; Amoros, P. *Chemistry of Materials* **2002**, *14*, 4502-4504.
122. El Haskouri, J.; Manuel Morales, J.; Ortiz de Zarate, D.; Fernandez, L.; Latorre, J.; Guillem, C.; Beltran, A.; Beltran, D.; Amoros, P. *Inorganic Chemistry* **2008**, *47*, 8267-8277.
123. Ros-Lis, J. V.; Casasus, R.; Comes, M.; Coll, C.; Marcos, M. D.; Martinez-Manez, R.; Sancenon, F.; Soto, J.; Amoros, P.; El Haskouri, J.; Garro, N.; Rurack, K. *Chemistry-a European Journal* **2008**, *14*, 8267-8278.
124. Descalzo, A. B.; Jimenez, D.; Marcos, M. D.; Martinez-Manez, R.; Soto, J.; El Haskouri, J.; Guillem, C.; Beltran, D.; Amoros, P.; Borrachero, M. V. *Advanced Materials* **2002**, *14*.
125. El Haskouri, J.; de Zarate, D. O.; Perez-Pla, F.; Cervilla, A.; Guillem, C.; Latorre, J.; Marcos, M. D.; Beltran, A.; Beltran, D.; Amoros, P. *New Journal of Chemistry* **2002**, *26*.
126. Candu, N.; Ciobanu, M.; Filip, P.; El Haskouri, J.; Guillem, C.; Amoros, P.; Beltran, D.; Coman, S. M.; Parvulescu, V. I. *Journal of Catalysis* **2012**, *287*, 76-85.
127. Candu, N.; Musteata, M.; Coman, S. M.; Parvulescu, V. I.; El Haskouri, J.; Amoros, P.; Beltran, D. *Chemical Engineering Journal* **2010**, *161*, 363-370.

128. Coman, S. M.; Pop, G.; Stere, C.; Parvulescu, V. I.; El Haskouri, J.; Beltran, D.; Amoros, P. *Journal of Catalysis* **2007**, *251*, 388-399.
129. Parvulescu, V. I.; Coman, S. M.; Candu, N.; El Haskouri, J.; Beltran, D.; Amoros, P. *Journal of Materials Science* **2009**, *44*, 6693-6700.
130. de la Torre, C.; Mondragon, L.; Coll, C.; Sancenon, F.; Marcos, M. D.; Martinez-Manez, R.; Amoros, P.; Perez-Paya, E.; Orzaez, M. *Chemistry-a European Journal* **2014**, *20*, 15309-15314.
131. Sanfeliu, C.; Martinez-Manez, R.; Sancenon, F.; Soto, J.; Puchol, V.; Amoros, P.; Dolores Marcos, M. *Journal of Materials Chemistry* **2012**, *22*, 25362-25372.
132. Cabrera, S.; El Haskouri, J.; Guillem, C.; Beltran-Porter, A.; Beltran-Porter, D.; Mendioroz, S.; Marcos, M. D.; Amoros, P. *Chemical Communications* **1999**, 333-334.
133. Cabrera, S.; El Haskouri, J.; Alamo, J.; Beltran, A.; Beltran, D.; Mendioroz, S.; Marcos, M. D.; Amoros, P. *Advanced Materials* **1999**, *11*, 379-381.
134. Cabrera, S.; El Haskouri, J.; Beltran-Porter, A.; Beltran-Porter, D.; Marcos, M. D.; Amoros, P. *Solid State Sciences* **2000**, *2*, 513-518.
135. El Haskouri, J.; Cabrera, S.; Sapina, F.; Latorre, J.; Guillem, C.; Beltran-Porter, A.; Beltran-Porter, D.; Marcos, M. D.; Amoros, P. *Advanced Materials* **2001**, *13*, 192-195.
136. Huerta, L.; Guillem, C.; Latorre, J.; Beltran, A.; Beltran, D.; Amoros, P. *Chemical Communications* **2003**, 1448-1449.
137. El Haskouri, J.; Guillem, C.; Latorre, J.; Beltran, A.; Beltran, D.; Amoros, P. *Chemistry of Materials* **2004**, *16*, 4359-4372.
138. Morales, J. M.; Latorre, J.; Guillem, C.; Beltran-Porter, A.; Beltran-Porter, D.; Amoros, P. *Solid State Sciences* **2005**, *7*, 415-421.
139. Tortajada, M.; Ramon, N.; Beltran, D.; Amoros, P. *Journal of Materials Chemistry* **2005**, *15*, 3859-3868.
140. Huerta, L.; Guillem, C.; Latorre, J.; Beltran, A.; Martinez-Manez, R.; Marcos, M. D.; Beltran, D.; Amoros, P. *Solid State Sciences* **2006**, *8*, 940-951.
141. Huerta, L.; El Haskouri, J.; Vie, D.; Comes, M.; Latorre, J.; Guillem, C.; Marcos, M. D.; Martinez-Manez, R.; Beltran, A.; Beltran, D.; Amoros, P. *Chemistry of Materials* **2007**, *19*, 1082-1088.
142. Fernandez, L.; Garro, N.; El Haskouri, J.; Perez-Cabero, M.; Alvarez-Rodriguez, J.; Latorre, J.; Guillem, C.; Beltran, A.; Beltran, D.; Amoros, P. *Nanotechnology* **2008**, *19*.

143. Puchol, V.; El Haskouri, J.; Latorre, J.; Guillem, C.; Beltran, A.; Beltran, D.; Amoros, P. *Chemical Communications* **2009**, 2694-2696.
144. El Haskouri, J.; Dallali, L.; Fernandez, L.; Garro, N.; Jaziri, S.; Latorre, J.; Guillem, C.; Beltran, A.; Beltran, D.; Amoros, P. *Physica E-Low-Dimensional Systems & Nanostructures* **2009**, *42*, 25-31.
145. El Haskouri, J.; Perez-Cabero, M.; Guillem, C.; Latorre, J.; Beltran, A.; Beltran, D.; Amoros, P. *Journal of Solid State Chemistry* **2009**, *182*, 2122-2129.
146. Perez-Cabero, M.; El Haskouri, J.; Solsona, B.; Vazquez, I.; Dejoz, A.; Garcia, T.; Alvarez-Rodriguez, J.; Beltran, A.; Beltran, D.; Amoros, P. *Journal of Materials Chemistry* **2010**, *20*, 6780-6788.
147. Solsona, B.; Perez-Cabero, M.; Vazquez, I.; Dejoz, A.; Garcia, T.; Alvarez-Rodriguez, J.; El-Haskouri, J.; Beltran, D.; Amoros, P. *Chemical Engineering Journal* **2012**, *187*, 391-400.
148. Burguete, P.; Beltran, A.; Guillem, C.; Latorre, J.; Perez-Pla, F.; Beltran, D.; Amoros, P. *Chempluschem* **2012**, *77*, 817-831.
149. Morales, J. M.; Moragues, A.; El Haskouri, J.; Guillem, C.; Latorre, J.; Murcia-Mascarós, S.; Beltrán, A.; Beltrán, D.; Amorós, P. *ChemPlusChem* **2015**, *80*, 1014-1028.

2. Mesoporous silicas with enhanced accessibility

2.1 - Overview

Symmetry can be found everywhere, from artistic objects to microscopic algae such as diatoms. In our research area, symmetry can also be found in the pore distribution of materials such as MCM-41, MCM-48 or SBA-15. The appeal of symmetry cannot be denied but, does it provide materials with any additional advantage?

In 2003, Debra Rolison¹ published an eye-opening work where the preponderance of accessibility over periodicity was claimed, emphasizing the critical role of the transport paths for applications such as catalysis, sensing, energy storage or synthesis among others. She pointed out plumbing problems as a serious drawback for mesoporous materials; when porosity is one-dimensional, an obstruction in the pore causes necks or even blockages in the system as shown in Figure 1.

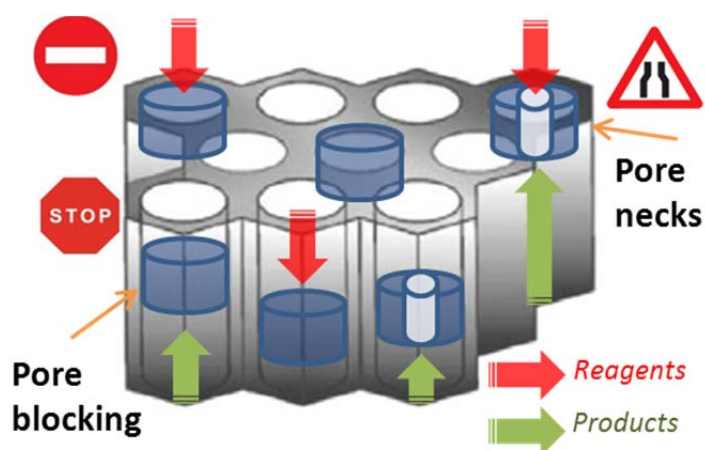


Figure 1. Scheme of plumbing problems in mesoporous materials.

Different strategies (such as the formation of small particles, the insertion of larger pores into the structure or the pore expansion) have been explored in order to enhance the accessibility to the active sites (Figure 2). In the following sections these methods will be briefly described.

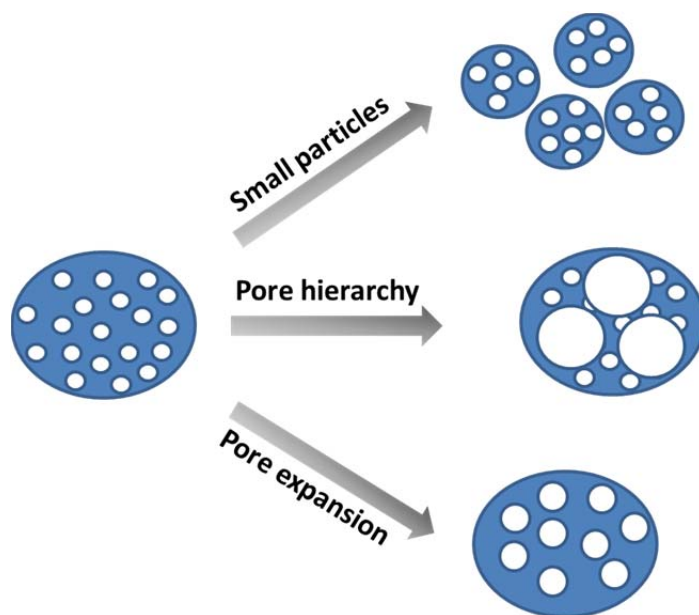


Figure 2. Scheme of different strategies to enhance accessibility.

2.1.1 - Reduction of particle size

The formation of mesoporous nanoparticles reduces pore blocking problems. Insofar as pore length is necessarily shortened, the loss of active surface in the case of an obstruction is minor. This idea is closely related to zeolite delamination², where zeolite layers are separated in order to increase accessibility to their active sites. Nano-sized mesoporous silicas were first reported by the groups of Cai³, Mann⁴ and Ostafin⁵. Since then, other groups have explored this type of material.

Control of the nucleation and growth mechanisms is basic in the synthesis of nanoparticles. Nucleation and growth steps need to be separated in order to obtain a narrow size distribution. In addition, aggregation of nanoparticles is also a variable which needs to be controlled.

This process is general for nanoparticle formation, but mesostructured silica building blocks are more complex (organic templates and silica species) and other experimental factors have to be considered to control template-silica interactions, silica condensation and growth and nucleation rates. Many synthesis of mesoporous silica nanoparticles are based on the Stöber method⁶, developed in 1968 for the synthesis of monodispersed silica particles. It consists of performing the hydrolysis of

tetraalkyl silicates in a mixture of alcohol and water, using ammonia as a catalyst. An adaptation of the Stöber method (with the introduction of a surfactant) has been used for the formation of mesoporous spherical particles.

The charge of the silica species is influenced by the pH of the solution⁷. When the pH is above the isoelectric point (2.0) the silica species are negatively charged. When the pH is between 2.0-7.0, negatively charged silicates interact with the surfactant via electrostatic and hydrogen-bonding interactions. At a higher pH, they interact with the cationic surfactants via strong electrostatic interactions⁸.

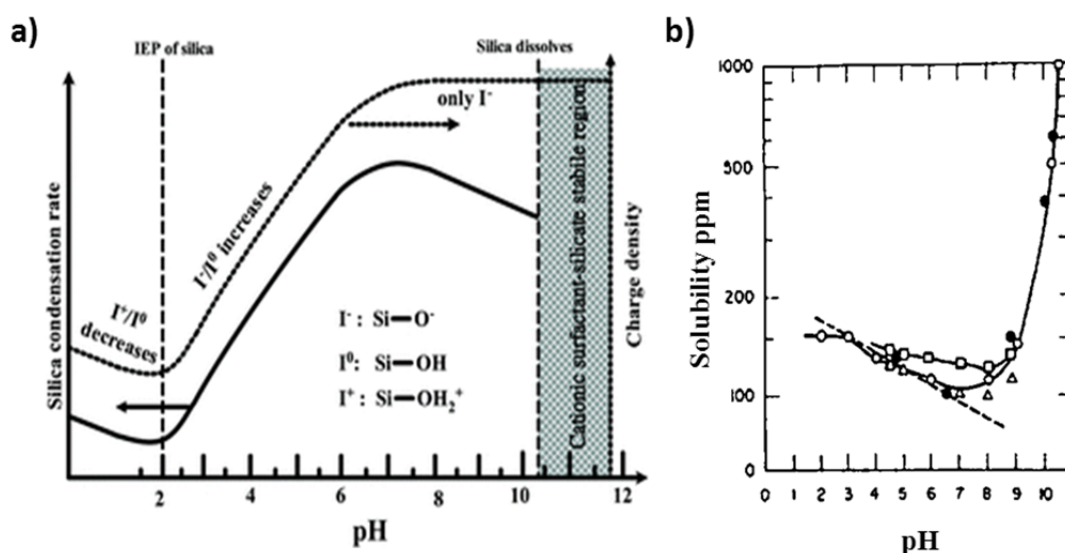


Figure 3. Effects of pH value on the: a) silica condensation rate, charge properties and charge density on the surface of the silica species, from reference 9; b) Redisolution of silica, from reference 7.

As shown in Figure 3a, the maximum condensation rate is around pH 7.5 and it then decreases until pH 10.5, where silicate dissolves. Another factor to take into account is re-dissolution of small particles to form larger ones (Ostwald ripening). Figure 3b shows that minimum silica solubility is at a pH around 8-9. Most syntheses of silica mesoporous nanoparticles are performed above pH 10.5; the strong interactions between silica and the surfactant stabilize the composites and permit their existence at such high pH levels. However, the groups of Mann and Lin used a fast pH-changing method; they pre-hydrolyze silica at a pH around the isoelectric point (to form silica

nuclei without precipitation) and then increase the pH to 6.0-9.0 (to quickly induce the growth of nanoparticles). Particle size can be tuned by changing the reactant concentrations.

In order to keep a small particle size, aggregation of the nanoparticles must be controlled. When silanols at the surface are active, there is a tendency to form Si-O-Si bridging bonds between particles. High dilution methods can be applied^{4,10}. When it is complicated to work under these conditions, direct contact of silanols could be prevented with the use of a binary surfactant mixture (Figure 4), using a cationic surfactant as the directing agent and a nonionic polymeric triblock¹¹ to protect the surface. Other compounds as PEG¹² or TEA¹³ can also be used as protecting agents.

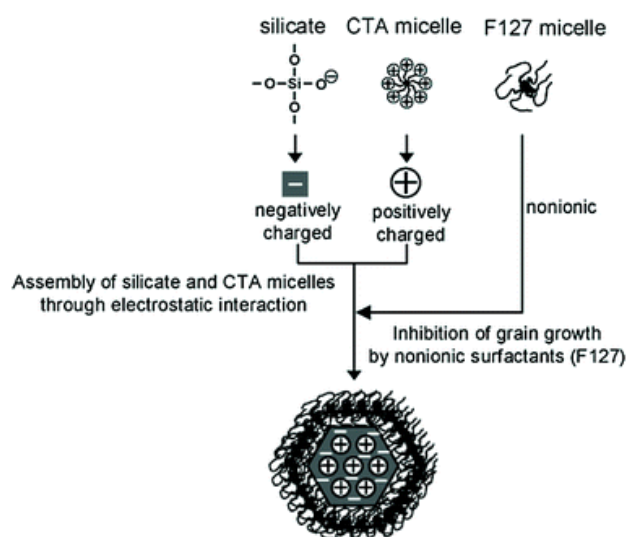


Figure 4. Schematic representation of the functions of two surfactants for assembly of the mesostructure, from reference 9.

2.1.2 - Pore hierarchy

High accessibility and an open architecture can be achieved with hierarchical pore systems. This means the integration of at least two levels of porosity in the material, combining the advantages associated with each level. For example, the presence of mesopores provides large surface areas, while macropores improve transport properties. Hierarchically structured materials have been studied, and three

different pore combinations have been described: micro-mesoporous, micro-macroporous and micro-meso-macroporous structured materials. The most efficient method to obtain these solids consists of the use of several structure directing agents, including soft and hard templates. These syntheses are similar to those with a single hard template, but additional steps may be necessary depending on the soft templating route. In these syntheses, the number of pore systems obtained is the same as the number of templates used; this can be a drawback since the price of the material increases with the number of templates.

Systems with microporosity always involve zeolitic crystals and a larger template. Interconnected pore systems can overcome mass transport problems in zeolites. Materials with meso and macroporosity are usually prepared using CTMABr and a second template which can be a larger neutral surfactant, biological (unicellular organisms, complex tissues and biomolecules¹⁴), colloidal crystals, three-dimensionally ordered macroporous structures (3DOM)¹⁵, latex spheres¹⁶ or foams¹⁷⁻¹⁹, among others. The morphology of these materials is usually hard to predict, as interactions between the components of the precursor and the template can modify the obtained structure.

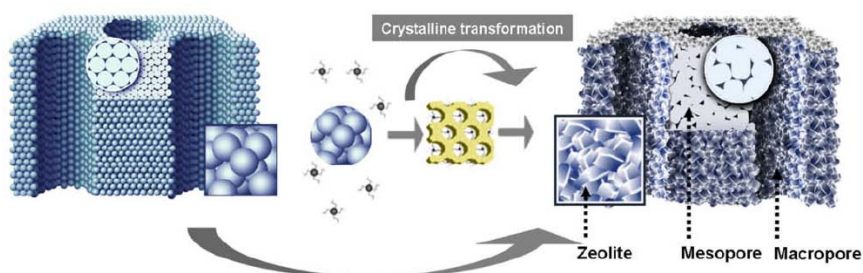


Figure 5. Schematic representation of micro-meso-macroporous materials, from reference 20.

The generation of hierarchical pores can also be achieved by etching processes (Figure 6). Dealumination or desilication of a zeolite can result in amorphous areas in the framework using such a destructive process, which means sacrificing part of the typical zeolite to generate larger cavities. Alternatively, the aggregation of zeolite

nanoparticles has also been employed to add mesopores to the structure²¹; the addition of an interconnected secondary pore system enhances mass transport.

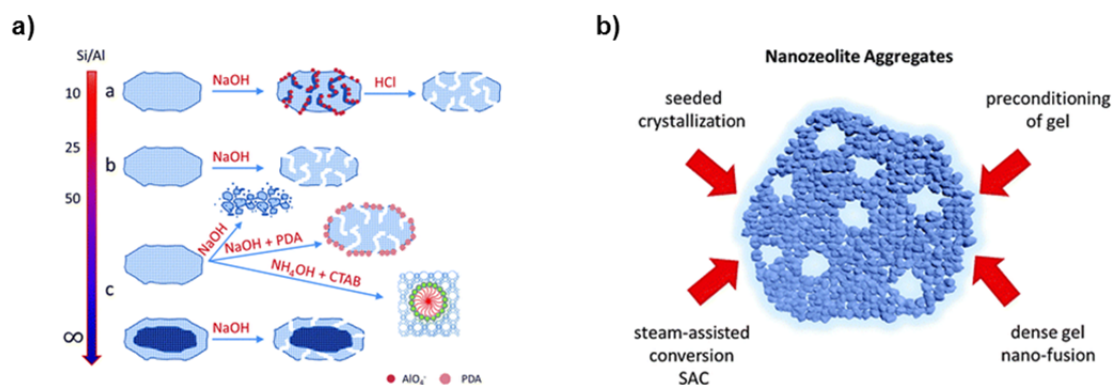


Figure 6. a) Desilication processes used for different Si/Al ratios; b) Synthetic routes to form mesoporous zeolites through nanozeolite assembly, from reference 22.

Hierarchy can be seen from two different perspectives. There are materials where access to the mesopore is through macropores, such as the ones mentioned above. But the opposite way is also possible, as happens in hollow spheres, where access to the inner macropore is through mesopores. The preferred strategy depends on the desired applications.

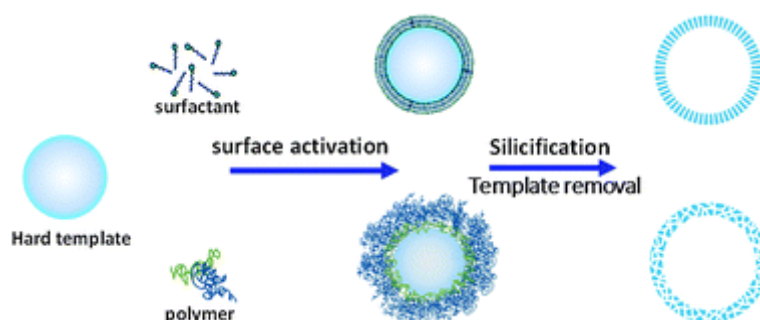


Figure 7. Synthesis of hollow spheres by hard-templating method, from reference 9.

Hollow mesoporous silica nanoparticles have a high load capacity. This is interesting in biomedical applications (drug storage and release), and encapsulation of

photoactive agents. Also, magnetic or catalytic properties can confer interest to many of these materials from the applied point of view.

They have been prepared from many soft (micelles²³, microemulsion droplets²⁴ or vesicular structures²⁵) and hard templates (polymer beads, metal or metal oxide nanoparticles).

2.1.3 - Pore expansion

Many applications, such as carrying protein or nucleic acids, require large pore sizes^{26,27} (in the 4-8 nm range). When dealing with silicas prepared using cetyltrimethylammonium surfactants, the pore size is restricted to around 3 nm^{28,29}. An evident solution would lie in the use of mesoporous materials with larger pores, such as SBA-15. However, these materials are more difficult to isolate in the form of nanoparticles, due to the acidic synthesis conditions. Insofar as the particle size is a critical factor in applications in biocatalysts or biosensors, it is mandatory to redesign the synthetic strategies to obtain nanoparticles.

Different strategies can be followed in order to control the pore size while keeping structural properties. One of them is the use of surfactants with different alkyl chain lengths³⁰ (C_xTMABr). The pore size increases from 1.81 to 3.41 nm when changing x from 10 to 16. It is also possible to use a mixture of surfactants with different alkyl chain lengths³¹ to obtain a uniform pore size between the expected sizes for each surfactant.

Another effective way is the use of swelling agents. Swelling agents are hydrophobic compounds that are assumed to be located inside the micelle, increasing the pore size in the product. Different hydrophobic compounds such as aromatic hydrocarbons, long-chain alkanes and alkylamines have been used for this purpose. In 1992, at the beginning of silica mesoporous materials, Beck et al.³² had already used 1,3,5-trimethylbenzene (TMB) as an expanding agent to obtain MCM-41 materials with pores sizes up to 7 nm. However, it was observed that these materials presented very broad pore size distributions. Other groups also used TMB or 1,3,5-triisopropylbenzene

as swelling agents³³. Pore size expansion has also been explored using alkanes with different chain lengths³⁴ (Figure 8) and by varying the alkane/surfactant molar ratio³⁵ or combining alkanes and TMB³⁶. In 2013, Mou's group³⁷ reported on the pore expansion of silica nanoparticles using alkanes and ethanol.

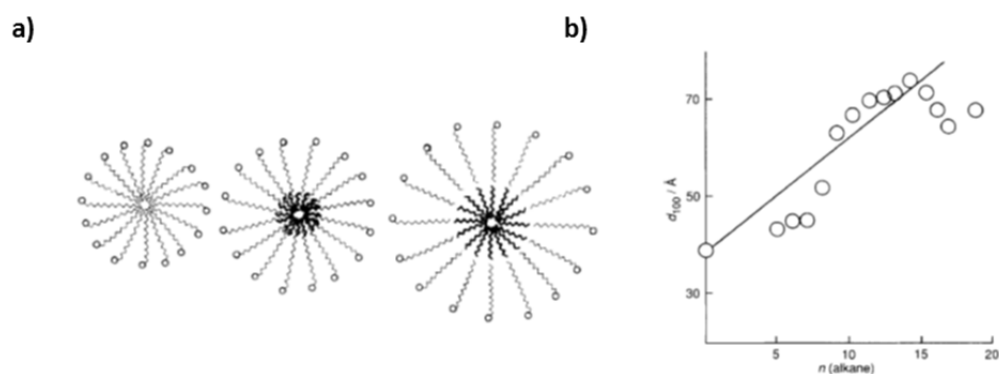


Figure 8. **a)** Scheme of a micelle in absence and presence of alkanes; **b)** Pore size evolution with chain longitude of the alkane, from reference 34.

2.2 - UVM-7

A combination of the above mentioned features leads to the formation of a material with improved accessibility to the active centres. An example is UVM-7 (Chapter 1), a nanoparticulated material with hierarchical porosity. It combines short pore length with a bimodal pore system consisting of intra-particle mesopores (porogen effect of the surfactant) and inter-particle macropores (formed by the aggregation of the particles). Diffusion to the mesopores is eased by the macropores.

In order to increase the accessibility in this material even more, pore size expansion can also be explored, which might, in turn, expand applications. As an example, pore size is a key factor in theranostic applications.

2.3 - Drug delivery

As already mentioned in Chapter 1, mesoporous silicas can be used as carriers for drug uptake and delivery due to their textural properties and easy functionalization. The first report on drug delivery using a MCM-41 like mesoporous silica material as the carrier³⁸ comes from 2001. Because of their size, nanoparticles can penetrate deep into tissues and the cell can generally take them efficiently.

Drug molecules are usually loaded in mesoporous silicas through weak interactions such as hydrogen bonds, physical adsorption, electrostatic interactions and π - π stacking³⁹. Introduction of functional groups can induce attractive interactions allowing control of the release rate⁴⁰. Also, magnetic or luminescent properties can be induced in the materials in order to facilitate their monitoring and elimination⁴¹.

Ibuprofen has been used as a model drug^{38,42-44} for drug uptake because of its low solubility in water and its relatively small molecular size. Diverse mesoporous materials have been used as supports for ibuprofen, and different aspects such as pore size or functionalization of silica have been studied. Most of the studies are focused on unimodal porous silicas such as MCM-41 or SBA-15; however, it seems reasonable to think that hierarchical porosity and short pore lengths could favour higher uptake levels^{44,45}.

2.4 - Enzyme immobilization

Enzymes are proteins folded into a three dimensional structure. They are biological catalysts with high selectivity, capable of regulating chemical processes in living matter. The reaction happens in a specific part of the enzyme called the active site. Enzyme-catalysed processes are interesting due to enzyme chemo-, stereo- and regioselectivity. Nevertheless, their commercial use is restricted due to some limitations such as high cost, low stability and difficult recovery. Their immobilization

provides enhanced stability, easy separation (and reuse) and the ability to use the enzyme in solutions in which they are insoluble.

In 1916, Nelson's group⁴⁶ reported the first enzyme immobilization of invertase adsorbed on charcoal. Almost one hundred years later, immobilized enzymes are used in applications such as biocatalysis, biosensors and biofuel cells, and in many industrial processes. Different supports for enzyme immobilization have been studied (such as sol-gels, polymers, porous and non-porous inorganic materials). Among them, mesoporous silicas are good candidates due to their high surface areas, narrow and tailorable pore size distribution, thermal and mechanical stability and low toxicity. Furthermore, silicas can be functionalized with organic groups to favour immobilization.

2.4.1 - Immobilization methods

The aim of immobilization is to confine the enzyme on a surface that does not alter their catalytic activity and improves their stability and recovery. There is no universal approach to immobilize enzymes; a specific immobilisation process is required depending on the enzyme and the support used. Three main strategies are typically used: physical adsorption, covalent binding and cross-linking.

- **Physical adsorption**

This method is based on the physical interaction between the solid surface and enzyme chains, including hydrophobic, hydrogen bonding, van der Waals and electrostatic forces. As the interaction with the surface is weak, the native structure and catalytic activity of the enzyme is not considerably affected. As a weakness of this method we can point out that minor changes in the reaction conditions can cause leaching from the support. To avoid this leaching, enzyme-support interactions can be reinforced, using, for example, glycosylated enzymes, or electrostatic interactions can be enhanced working at a pH where the silica possess a negative charge and the

enzyme is positively charged (i.e. at pH values below the isoelectric point of the enzyme). The interactions with the silica will be stronger as the positive charge of the enzyme increases. The pH value needs to be kept constant during application to avoid leaching. Another solution is enzyme encapsulation after the physical adsorption by adding bulky functional groups to reduce the pore size⁴⁷; for example silanation and coating with organic layers have been used. The problem with this solution is that enzyme activity may be reduced after silica modification and the diffusion rate through the pore system could be affected.

- **Covalent binding**

Covalent immobilization of the enzymes requires chemical modification of the silica surface. Organosilane species (such as alkoxy silanes, chlorosilanes or methyl silanes) are condensed with silanol groups on the surface. These species are able to covalently bond with enzymes. With this method, enzyme leaching is decreased, thus minimizing enzyme contamination of the product. Organic moieties can be added to the silica via co-condensation or grafting, as explained in the previous chapter. The most common functionalization is with amino groups followed by reaction with glutaraldehyde. Aldehyde groups on the surface could then react with amino groups of the enzyme.

Covalent binding permits the use of the catalyst in polar solvents without leaching, and their use at high reaction temperatures. However, the specific activity of the enzyme can be affected by conformational changes caused in the attachment.

- **Cross-linking**

Originally, cross-linking is the covalent bond between enzymes to create enzyme aggregates. These aggregates can be prepared by a two-step process. First of all, the enzyme is precipitated (with salts or organic solvents) to form aggregates that are stabilized by addition of a cross-linking agent (which reacts with the amino groups

of the enzymes). This immobilization strategy was adapted for incorporation in porous materials and usually the enzymes are adsorbed on a porous material, aggregated and then cross-linked.

In comparison with carrier free cross-linked enzymes, no precipitant is needed to form aggregates. With this method enzymes retain their catalytic activity.

Table 1 shows the advantages and disadvantages of each method.

Table 1. Advantages and disadvantages of the different immobilization methods, from reference 48 .

Immobilization method	Advantages	Disadvantages
Physical adsorption	Cheap, simple and rapid experimental procedure No functionalization of support is required No toxic solvents are required No conformational changes of the enzyme No destruction of the active site of the enzyme	Leaching of enzymes from the support during the catalytic reaction due to changes in reaction conditions or through mechanical shear forces
Covalent binding	No leaching of enzymes from the support Tight binding of the enzyme to the support Wide choice of organic linkers available Established methods of functionalization of supports	Most complicated and expensive immobilization method Functionalization of the support is necessary Use of toxic chemicals Reduction or loss of catalytic activity resulting from conformational changes of the enzyme
Cross-linking	Stabilization of multimeric enzymes Stabilization towards harsh reaction conditions (e.g. extreme pH) High purity of enzyme is not required No leaching from the support Different enzymes can be co-immobilized (tandem-system) No or minimal conformational changes of the enzyme Size of the aggregates is restricted by the cage size	Complicated experimental process (more than two steps are necessary) Use of toxic chemicals Decreased diffusion rate of substrates/products due to reduced pore volume

Enzymes differ amongst themselves, with variations in size, shape, isoelectric point or catalytic performance among others. So, support properties have to be

considered (pore size, particle size and morphology, surface area, charge density, hydrophobicity). Not every porous material is capable of retaining enzymes. When pore size is not large enough, enzymes are adsorbed onto the external surface (where they are not protected from the environment). In addition, a pore much bigger than the enzyme facilitates the leaching processes. It is important to study the size of the pore and the enzyme to obtain high loading and high enzymatic activity. For example, materials such as UVM-7 or MCM-41 are restricted to small sized enzymes.

Particle size can also affect enzyme loading and catalytic activity. Small particle sizes imply that the number of pore entrances increases; so, pore blocking is minimized and diffusion of the substrate to the enzyme is improved.

2.4.2 - Enzymes used

- **Lysozyme**

Lysozyme or muramidase is a glycoside hydrolase that degrades bacteria cell walls. It is abundant in secretions such as tears, saliva, human milk and mucus and large amounts can be found in hen egg white.

The isoelectric point of lysozyme is 11.3, the molecular weight is 14.3 kDa and the hydrodynamic diameter is 4.0 nm.

- **Trypsin**

Trypsin is an important enzyme in the metabolic process. It is a serine protease, also called peptidase, that catalyses the hydrolysis of peptide bonds at the carboxyl side of the amino acids lysine and arginine. It is used in detergents, waste management, food, diagnostics and in the pharmaceutical industry.

The isoelectric point of trypsin is 10.5, the molecular weight is 23.4 kDa and the hydrodynamic diameter is 3.8 nm.

2.5 - Objectives

The objective of this chapter is to complete previous work done by the group on UVM-7 with a better comprehension of its structure. In the first paper, the nature of UVM-7 pore system was studied by different methods: carbon replicas have been prepared to prove its interconnected structure; Au particles have been deposited into the silica and materials were studied by tomography studies; and to finish lysozyme has been loaded into the material.

In the second paper, expansion of mesopores with alkanes as swelling agents has been studied. Alkanes from hexane to hexadecane have been tested as swelling agents for calcined and extracted silicas. The amount of alkane incorporated into the micelle has been analysed in order to understand the swelling effect and expansion has been tested by the adsorption of lysozyme and trypsin in the porous structure, as well as with ibuprofen loading.

References

1. Rolison, D. R. *Science* **2003**, *299*, 1698-1701.
2. Corma, A.; Fornes, V.; Pergher, S. B.; Maesen, T. L. M.; Buglass, J. G. *Nature* **1998**, *396*, 353-356.
3. Cai, Q.; Luo, Z. S.; Pang, W. Q.; Fan, Y. W.; Chen, X. H.; Cui, F. Z. *Chemistry of Materials* **2001**, *13*, 258-263.
4. Fowler, C. E.; Khushalani, D.; Lebeau, B.; Mann, S. *Advanced Materials* **2001**, *13*, 649-652.
5. Nooney, R. I.; Thirunavukkarasu, D.; Chen, Y. M.; Josephs, R.; Ostafin, A. E. *Chemistry of Materials* **2002**, *14*, 4721-4728.
6. Stober, W.; Fink, A.; Bohn, E. *Journal of Colloid and Interface Science* **1968**, *26*, 62-&.
7. Iler, R. K. *The Chemistry of Silica*; John Wiley & Sons, Inc., 1979.
8. Lin, H. P.; Mou, C. Y. *Accounts of Chemical Research* **2002**, *35*, 927-935.
9. Wu, S.-H.; Mou, C.-Y.; Lin, H.-P. *Chemical Society Reviews* **2013**, *42*, 3862-3875.
10. Shi, Y.-T.; Cheng, H.-Y.; Geng, Y.; Nan, H.-M.; Chen, W.; Cai, Q.; Chen, B.-H.; Sun, X.-D.; Yao, Y.-W.; Li, H.-D. *Materials Chemistry and Physics* **2010**, *120*, 193-198.
11. Ikari, K.; Suzuki, K.; Imai, H. *Langmuir* **2006**, *22*, 802-806.
12. Lin, Y.-S.; Haynes, C. L. *Chemistry of Materials* **2009**, *21*, 3979-3986.
13. Moeller, K.; Kobler, J.; Bein, T. *Advanced Functional Materials* **2007**, *17*, 605-612.
14. Caruso, R. A. *Colloid Chemistry 1* **2003**, *226*, 91-118.
15. Mandlmeier, B.; Szeifert, J. M.; Fattakhova-Rohlfing, D.; Amenitsch, H.; Bein, T. *Journal of the American Chemical Society* **2011**, *133*, 17274-17282.
16. Danumah, C.; Vaudreuil, S.; Bonneviot, L.; Bousmina, M.; Giasson, S.; Kaliaguine, S. *Microporous and Mesoporous Materials* **2001**, *44*, 241-247.
17. Huerta, L.; Guillem, C.; Latorre, J.; Beltran, A.; Beltran, D.; Amoros, P. *Chemical Communications* **2003**, 1448-1449.
18. Huerta, L.; El Haskouri, J.; Vie, D.; Comes, M.; Latorre, J.; Guillem, C.; Marcos, M. D.; Martinez-Manez, R.; Beltran, A.; Beltran, D.; Amoros, P. *Chemistry of Materials* **2007**, *19*, 1082-1088.
19. Bagshaw, S. A. *Chemical Communications* **1999**, 767-768.
20. Chen, L.-H.; Li, X.-Y.; Rooke, J. C.; Zhang, Y.-H.; Yang, X.-Y.; Tang, Y.; Xiao, F.-S.; Su, B.-L. *Journal of Materials Chemistry* **2012**, *22*, 17381-17403.
21. Na, K.; Choi, M.; Ryoo, R. *Journal of Materials Chemistry* **2009**, *19*, 6713-6719.
22. Moeller, K.; Bein, T. *Chemical Society Reviews* **2013**, *42*, 3689-3707.
23. Liu, J.; Yang, Q.; Zhang, L.; Yang, H.; Gao, J.; Li, C. *Chemistry of Materials* **2008**, *20*, 4268-4275.

24. Yi, D. K.; Lee, S. S.; Papaefthymiou, G. C.; Ying, J. Y. *Chemistry of Materials* **2006**, *18*, 614-619.
25. Yeh, Y. Q.; Chen, B. C.; Lin, H. P.; Tang, C. Y. *Langmuir* **2006**, *22*, 6-9.
26. Ashley, C. E.; Carnes, E. C.; Epler, K. E.; Padilla, D. P.; Phillips, G. K.; Castillo, R. E.; Wilkinson, D. C.; Wilkinson, B. S.; Burgard, C. A.; Kalinich, R. M.; Townson, J. L.; Chackerian, B.; Willman, C. L.; Peabody, D. S.; Wharton, W.; Brinker, C. J. *ACS Nano* **2012**, *6*, 2174-2188.
27. Slowing, I. I.; Trewyn, B. G.; Lin, V. S. Y. *Journal of the American Chemical Society* **2007**, *129*, 8845-8849.
28. Lin, Y. S.; Tsai, C. P.; Huang, H. Y.; Kuo, C. T.; Hung, Y.; Huang, D. M.; Chen, Y. C.; Mou, C. Y. *Chemistry of Materials* **2005**, *17*, 4570-4573.
29. Lai, C. Y.; Trewyn, B. G.; Jeftinija, D. M.; Jeftinija, K.; Xu, S.; Jeftinija, S.; Lin, V. S. Y. *Journal of the American Chemical Society* **2003**, *125*, 4451-4459.
30. El Haskouri, J.; Morales, J. M.; de Zarate, D. O.; Fernandez, L.; Latorre, J.; Guillem, C.; Beltran, A.; Beltran, D.; Amoros, P. *Inorganic Chemistry* **2008**, *47*, 8267-8277.
31. Jana, S. K.; Nishida, R.; Shindo, K.; Kugita, T.; Namba, S. *Microporous and Mesoporous Materials* **2004**, *68*.
32. Beck, J. S.; Vartuli, J. C.; Roth, W. J.; Leonowicz, M. E.; Kresge, C. T.; Schmitt, K. D.; Chu, C. T. W.; Olson, D. H.; Sheppard, E. W.; McCullen, S. B.; Higgins, J. B.; Schlenker, J. L. *Journal of the American Chemical Society* **1992**, *114*, 10834-10843.
33. Lindlar, B.; Kogelbauer, A.; Kooyman, P. J.; Prins, R. *Microporous and Mesoporous Materials* **2001**, *44*, 89-94.
34. Ulagappan, N.; Rao, C. N. R. *Chemical Communications* **1996**.
35. Blin, J. L.; Otjacques, C.; Herrier, G.; Su, B. L. *Langmuir* **2000**, *16*.
36. Lefevre, B.; Galarneau, A.; Iapichella, J.; Petitto, C.; Di Renzo, F.; Fajula, F.; Bayram-Hahn, Z.; Skudas, R.; Unger, K. *Chemistry of Materials* **2005**, *17*, 601-607.
37. Kao, K.-C.; Mou, C.-Y. *Microporous and Mesoporous Materials* **2013**, *169*, 7-15.
38. Vallet-Regi, M.; Ramila, A.; del Real, R. P.; Perez-Pariente, J. *Chemistry of Materials* **2001**, *13*, 308-311.
39. Tang, S.; Huang, X.; Chen, X.; Zheng, N. *Advanced Functional Materials* **2010**, *20*, 2442-2447.
40. Song, S. W.; Hidajat, K.; Kawi, S. *Langmuir* **2005**, *21*, 9568-9575.
41. Akerman, M. E.; Chan, W. C. W.; Laakkonen, P.; Bhatia, S. N.; Ruoslahti, E. *Proceedings of the National Academy of Sciences of the United States of America* **2002**, *99*, 12617-12621.
42. He, Q.; Shi, J. *Journal of Materials Chemistry* **2011**, *21*, 5845-5855.
43. Wang, S. *Microporous and Mesoporous Materials* **2009**, *117*, 1-9.

44. Burguete, P.; Beltran, A.; Guillem, C.; Latorre, J.; Perez-Pla, F.; Beltran, D.; Amoros, P. *Chempluschem* **2012**, *77*, 817-831.
45. Gao, L.; Sun, J.; Li, Y. *Journal of Solid State Chemistry* **2011**, *184*, 1909-1914.
46. Nelson, J. M.; Griffin, E. G. *Journal of the American Chemical Society* **1916**, *38*, 1109-1115.
47. Yiu, H. H. P.; Wright, P. A. *Journal of Materials Chemistry* **2005**, *15*, 3690-3700.
48. Hartmann, M.; Kostrov, X. *Chemical Society Reviews* **2013**, *42*, 6277-6289.

Interconnected mesopores and high accessibility in UVM-7-like silicas

Mónica Pérez-Cabero^a, Ana B. Hungría^b, José Manuel Morales^a, Marta Tortajada^c, Daniel Ramón^c, Alaina Moragues^a, Jamal El Haskouri^{a,d}, Aurelio Beltrán^a, Daniel Beltrán^a and Pedro Amorós^a

^a Institut de Ciència dels Materials, Universitat de València, 46071 Valencia, Spain

^b Departamento de Ciencia de Materiales, Ingeniería Metalúrgica y Química Inorgánica, Universidad de Cádiz, 11510 Puerto Real, Cádiz, Spain

^c Biópolis S. L., 46980 Paterna, Valencia, Spain

^d Fundació General, Universitat de València, 46071 Valencia, Spain

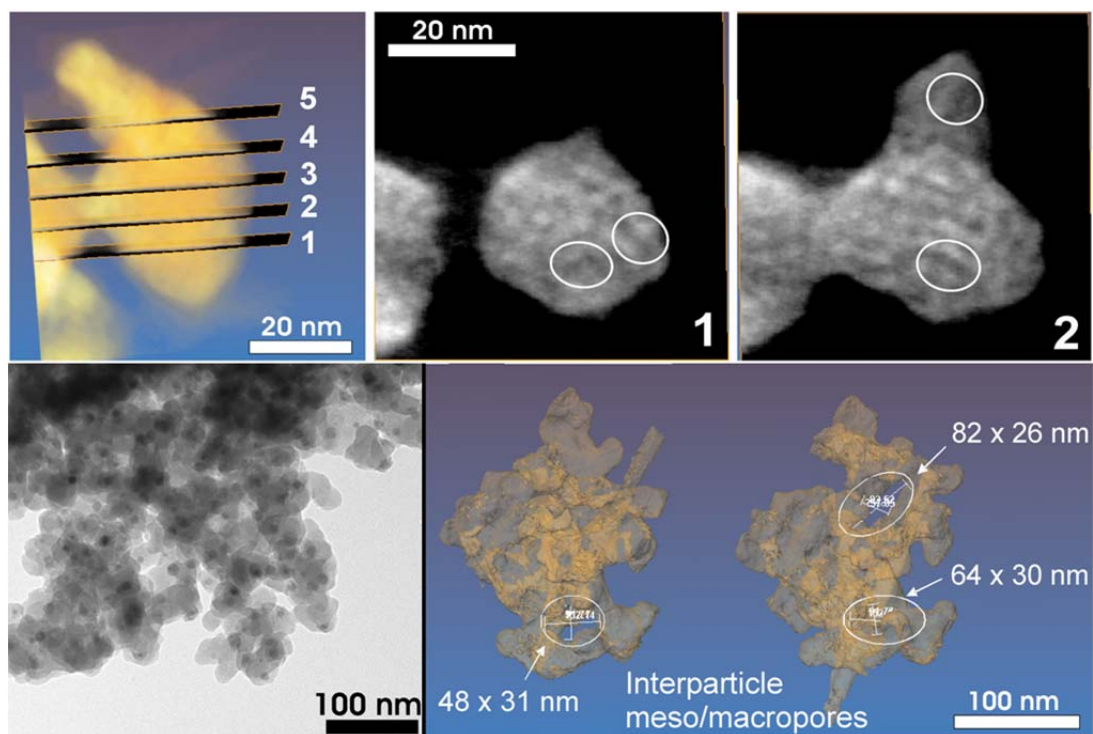
Received 9th February 2012, Accepted 10th July 2012

Published online 25th July 2012

J Nanopart Res (2012) 14:1045
DOI 10.1007/s11051-012-1045-8

Abstract

Nanoparticulated bimodal mesoporous silicas (NBS) have proved to constitute adequate supports in a variety of applications requiring enhanced accessibility to the active sites. Mass-transfer kinetics seems to be highly favored in UVM-7-derived NBS materials. To understand the mass diffusion phenomena throughout UVM-7-like supports requires well-grounded knowledge about their pore architecture. 3-D reconstructions of the UVM-7 mesostructure carried out by electron tomography reveal the existence of a true hierarchic connectivity involving both inter- and intranoparticle pores. This connectivity makes self-supported nanoparticulated mesoporous bimodal carbon replicas of the supports feasible to obtaining by nanocasting. Both the temperature-induced mobility of gold nanodomains and the fast and efficient enzyme adsorption in UVM-7-like silicas are examples of non-constrained diffusion processes happening inside such an open network.



Introduction

The research on porous materials' chemistry experienced a real renaissance after the discovery of the M41S silicas¹. The introduction of supramolecular (micellar) assemblies as structure directing or templating agents permitted a new family of ordered mesoporous compounds to be obtained. As corollary of expanding the available size of micropores in zeotypes, such a novel synthetic technique was profusely explored under the prospects for innovative materials with promising applications in many fields²⁻⁴. With reference to silicas, the hydrolytic and condensation processes leading to polymerization around single micellar templates mimic known liquid-crystal surfactant phases. Such kinetically controlled processes are highly influenced by procedural variables, and the variety of well-characterized materials is enormous⁵.

While there is no doubt about the esthetic and scientific appeal of symmetry, it was also argued that a periodic and ordered unimodal mesoporous structure could not offer specific advantages for certain applications requiring an enhanced accessibility to the active sites. In fact, in some cases, specific uniform pore structures could result in poor accessibility because of pore blocking^{6,7}. To overcome this limitation has been the objective of diverse alternative ways to designing new mesoporous systems. So, some approaches were conceived of for expanding the pore sizes using large surfactants as templates or also by incorporating swelling agents^{8,5,9}. From another point of view, it was considered that the mass-transfer kinetics could be improved by favoring the formation of interconnected pore systems^{5,10,11}. An additional resourceful way to deal with the diffusion constraints problem is based on the search for frameworks including pore systems structured at different length scales (hierarchical porosity)¹².

One of the approaches to tackle the site accessibility problem is conceptually based on the consequences of decreasing (at the nanometric range) the particle size of the mesoporous material. This necessarily implies, at first, the shortening of the pore length. Hence, diffusion constraints must become lowered by reducing the maximum mesopore length from the micro to the nanometric range. So, even though a certain undesired pore blocking might occur, its negative effects would be comparatively

lessened. Moreover, the nanoparticle packing would generate supplementary inter-particle textural porosity¹³⁻¹⁶. Then, regardless of what the ultimate arrangement of the particle aggregates may be, minor diffusion problems should be expected throughout such pore systems.

In practice, the synthesis of nanoparticulated bimodal mesoporous silica (NBS) materials has aroused great interest in recent times. There have been many preparative procedures thought of to achieving this goal the ability of which for yielding NBS materials has been associated to diverse procedural details¹⁷⁻²⁷. In any case, all of them have in common the intention of limiting the growth of the mesoporous silica particles, while regulating their aggregation processes. Our group has been successful in synthesizing a new family of NBS materials (denoted as UVM-7) through a one-pot procedure, starting from molecular atrane complexes of Si as inorganic precursors^{16,14,13,15,28,29}. We finally achieved a rather good independent control of both the intra- and inter-particle pore systems as well as a fine modulation of the particle dimensions²⁸.

Otherwise, the chemistry of the NBS solids, like what happens in the case of the M41-S materials, is compatible with the inclusion in their pore walls of a variety of inorganic and/or organic species. Thus, the synthesis of functionalized NBS materials using nonionic surfactants was initially described by Pauly et al³⁰. (Al-containing HMS silicas). Soon afterward, using a cationic surfactant, our group reported on M-UVM-7 (M = Al, Ti, Zr, V) materials^{16,14,13,15,31}, and also described UVM-7-based materials containing organic functional groups^{16,14,13,15}. In practice, it has also been possible to confirm experimentally the good site accessibility expected for the UVM-7-based materials in different catalytic and sensing processes³²⁻³⁵.

In a general way, we can say that the essential features of the UVM-7 matrices are well characterized²⁸. The materials can be described as bimodal porous silicas constructed by the aggregation of pseudo-spherical mesoporous primary nanoparticles. The intra-nanoparticle pore system consists of regular-sized mesopores disposed in a pseudo-hexagonal disordered array, while the arrangement of the inter-particle meso/macropores exhibits xerogel-like characteristics. However, there is a relevant aspect concerning the ultimate character of the intra-particle mesopore

system that has not been clarified up to date. Thus, we have referred to the lack of long range order characterizing such a mesopore array. In the case of ordered mesophases, TEM images allow to unambiguously determine both the mesopore symmetry and the dimensionality⁵. Nevertheless, dealing with relatively disordered systems, we cannot elucidate from simple techniques how the intra-nanoparticle mesopores interrelate among them (interconnected or independent mesopores).

The aim of this work is to determine in a conclusive way the ultimate nature of the pore architecture in the UVM-7 silicas because of its relevance for a better understanding of the mass-diffusion phenomena throughout them. Once we disregarded the effectiveness of simple TEM images with this purpose, we resorted to alternative procedures and indirect experiments to establish the tridimensional details of the intra-nanoparticle mesopore network in UVM-7. Thus, we have carried out an electron tomography study, and we have also been able to isolate pseudomorphic carbon replicas of the parent material. Additional indirect evidence has been derived from the study of the thermal evolution of Au/UVM-7 composites. All our experimental results indicate that the intra-nanoparticle pore system in the UVM-7 materials is constructed from truly interconnected mesopores, which fits in well with the above-mentioned operational advantages shown by some UVM-7-based materials in catalytic and sensing processes. As we shall see, the good pore connectivity in the UVM-7 skeleton facilitates also the diffusion of relatively large substrates.

Experimental section

Chemicals

All the synthesis reagents are analytically pure and were used as received from Aldrich (tetraethyl orthosilicate (TEOS), triethanolamine [$N(CH_2-CH_2-OH)_3$, hereinafter TEA], cetyltrimethylammonium bromide (CTMABr), trimethylbenzene (TMB), chloroauric acid, ethanol, hydrochloric acid, sulfuric acid).

Preparation of UVM-7 silicas

Nano-sized mesoporous UVM-7 silica samples were synthesized through a one-pot surfactant-assisted procedure working in a homogeneous hydroalcoholic reaction medium (water/TEA). The procedure, a modification of the so-called “atrane route”³⁶, is based on the use of a simple structural directing agent (CTMABr) and a complexing polyalcohol (TEA), which originates silatrane complexes as hydrolytic precursors. To open the intra-nanoparticle mesopores, the surfactant was extracted by chemical exchange using an HCl/ethanol solution (CTMA⁺/H⁺ exchange)²⁸.

Table 1. Selected preparative and physical data for UVM-7 silicas.

Sample	TMB/CTMABr (molar ratio)	Surface ^a (m ² /g)	Volume ^b (cm ³ /g)	Small pore ^b (nm)	Large pore ^b (nm)
UVM-7	-	1105(4)	1.80(7)	2.71(5)	42.5(8)
UVM-7(3)	3	1162(7)	1.23(8)	2.83(7)	18.9(9)
UVM-7(4)	4	1,066(3)	1.26(8)	3.25(6)	11.3(9)

^a Surface area according to the BET model. ^b Pore diameters and volume calculated by means of the BJH model on the adsorption branch of the isotherms

Together with the simple UVM-7 silicas, we synthesized also modified samples having expanded mesopores in order to study enzyme immobilization. We used TMB (1<TMB/CTMABr<4) as organic expander. In these cases, the synthetic protocol was modified in order to favor the stabilization of the expanded micelles, which entails a two-pot procedure. In a typical two-pot synthesis leading to a pore expanded UVM-7 material, a mixture of TEOS (11.16 mL, 0.05 mol) and liquid TEA (13.27 mL, 0.10 mol) was heated at 140 °C for 10 min in order to form silatrane complexes. On the other hand, 4.56 g of CTMABr (0.0125 mol) and 5.22 mL of TMB (0.0375 mol) were solved in a mixture of TEA (9.96 mL, 0.075 mol) and water (80 mL, 4.44 mol). Both solutions were heated at 80 °C, and then were mixed with vigorous stirring at 80 °C. A white suspension quickly appeared. This mixture was allowed to age at room temperature for 12 h. The resulting mesostructured powder was separated by filtration or centrifugation, washed with water and ethanol, and air dried. In order to prepare the

final porous material, the surfactant was removed from the mesostructure by chemical exchange. We prepared different samples by modulating the TMB/CTMABr ratio according to the following molar ratio of the reagents: 2 Si: 7 TEA: 0.5 CTMABr: x TMB: 180 H₂O, where x = 0, 1.5, 2. Summarized in Table 1 are the main synthesis variables and physical data.

Preparation of carbon replicas

A typical UVM-7 carbon replica was prepared by the infiltration method using sucrose as carbon precursor³⁷. Indeed, 1 g of UVM-7 was impregnated with an aqueous solution of sucrose and sulfuric acid (6 mL of H₂O and 0.16 mL of concentrated H₂SO₄). The amount of sucrose was 1.40 g per gram of UVM-7. Once dried at 150 °C, the resulting sucrose/UVM-7 composite was impregnated again with an additional portion of the acidified sucrose solution, which contained half of the sucrose amount used in the initial impregnation step. The resulting solid was dried at 160 °C, and subsequently heated at 900 °C during 3 h (heating ramp 1 °C/min) under Ar atmosphere. Finally, the silica moiety was removed by chemical etching with a NaOH solution (pH>12), leading to final bimodal carbon samples named as C/UVM-7 (with a carbon content of ca 97 %, determined by means of TGA).

Preparation of Au-UVM-7 composites

The incorporation of gold into the UVM-7 matrices was realized by impregnation with HAuCl₄ solutions³⁸. The UVM-7 material was suspended in water while stirring at room temperature and a solution of HAuCl₄.3H₂O was added to provide a nominal final gold content of (2 wt.%). The pH was adjusted to 9 with an aqueous NaOH solution and was then aged for 2 h under stirring. Later, the solid was filtered and extensively washed with water to favor the retention of only Au-complexes interacting with the support. Then, the solid was dried at 120 °C overnight and calcined at 200 °C for 1 h in static air. Finally, the resulting solid was treated (under a gas mixture of 10 % of H₂ in Ar) up to temperatures (800 °C) close to the silica support stability limit.

Enzyme immobilization

Lysozyme immobilization was carried out in heterogeneous reaction conditions. Lysozyme was dissolved (300 mg/mL) in a buffer $\text{NaH}_2\text{PO}_4\text{-Na}_2\text{HPO}_4$ 10 mM solution (pH = 6.0, at 25 °C), and then 100 mg of the silica support were added. Adsorption was monitored by measuring the enzyme concentration in the supernatant for up to 7 h as previously described by Bradford³⁹. Four porous materials (MCM-41, UVM-7, and two different pore-expanded UVM-7 materials) were assayed for lysozyme immobilization under saturating conditions. The MCM-41 samples were prepared as previously described¹³⁻¹⁶.

Experimental techniques

All solids were characterized by X-ray powder diffraction (XRD) at low angles (Seifert 3000TT $\theta\text{-}\theta$) using $\text{CuK}\alpha$ radiation. Patterns were collected in steps of 0.1° over the angular range 1.5–7.0 for 10 s per step. Electron microscopy study (TEM) was carried out with a JEOL JEM-1010 instrument operating at 100 kV and equipped with a CCD camera. HAADF-STEM images were acquired on a FEI Tecnai F20 field emission gun transmission electron microscope operated at 200 kV. A grain of ca 0.30 \times 0.25 μm was selected. For the tomography studies, a single tilt series of HAADF-STEM images was recorded between -72° and +68° every 2° using a Fischione ultrahigh-tilt tomography holder. Image acquisition was undertaken by means of the FEI software package Xplore3D. Alignment of the image stack and tomographic reconstructions were performed with the FEI software package Inspect 3D by means of the iterative routine SIRT⁴⁰. Voxel projections and surface rendering (after a segmentation process when needed) were undertaken by the Amira software. Surface area, pore size, and volume values were calculated from nitrogen adsorption–desorption isotherms (-196 °C) recorded on a Micromeritics ASAP-2020 automated analyzer. Carbon content for the C/UVM-7 sample was characterized by thermogravimetric analysis (TGA) under oxygen atmosphere in a Setaram Setsys 16/18. The Au/UVM-7 composites were analyzed for Si and Au by electron probe microanalysis (EPMA, Philips SEM-515 instrument).

Results and discussion

Typical SEM and TEM images of an UVM-7 silica sample are shown in Figure 1. The basic features of the inter-particle pores can be appreciated from SEM and TEM images. Thus, at micrometric scale, the UVM-7 silica presents rough surfaces (Figure 1a) resulting from the aggregation of pseudospherical clusters/grains defining large true textural macropores among them. In fact, the observed roughness corresponds to these large pores (in the macropore range; size >50 nm) of textural nature. In turn, the clusters/grains under consideration are constructed by aggregation of pseudospherical mesoporous primary nanoparticles the average diameter of which is ca 25–35 nm (Figure 1b).

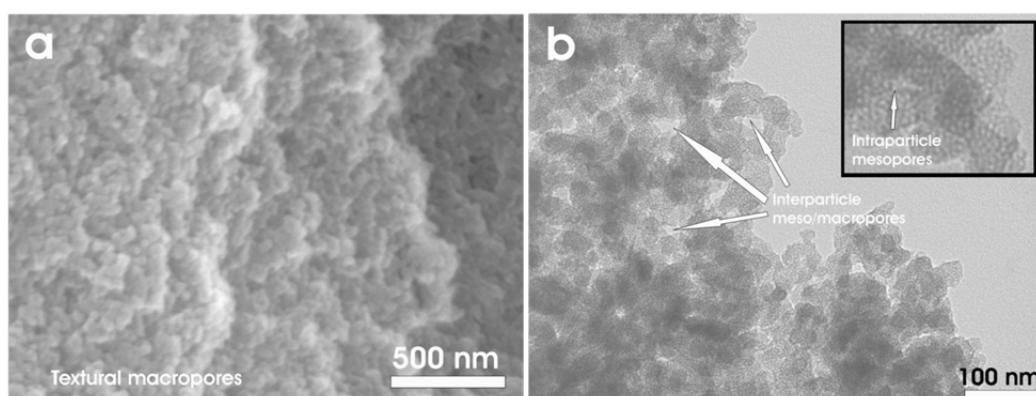


Figure 1. **a** SEM image showing the rough surface of the UVM-7 silicas. **b** TEM micrograph of the UVM-7 silica showing the inter-particle pore system and the intra-particle mesoporous (see inset).

In practice, the formation of a continuous network from the soldered nanoparticles generates a disordered system of large void-pores (with pore sizes in the border between meso and macropores). Indeed, both the large (textural) macropores observed through SEM and the pore arrangement appearing among the primary nanoparticles in TEM images have the same origin, which is consistent with a formation mechanism implying collision and aggregation of primary nanoparticles similar to what happens in the case of xerogels. The non-ordered nature of this large pore system as a whole can be related to the fact that its formation does not involve

the participation of any supramolecular template able to transfer a certain organization. On the contrary, the small intra-particle mesopore system has its origin in the template (and porogen) effect of the surfactant micelles. This pore system consists of regular-sized mesopores disposed in a pseudohexagonal disordered array (Figure 1b). Therefore, the UVM-7 architecture can be thought of as a hierarchic bimodal porous organization.

The bimodal porous character of the UVM-7 silicas is indubitably confirmed by the N_2 adsorption–desorption isotherms (Figure 2). Thus, the corresponding curves show two well-defined adsorption steps. The first, at intermediate P/P_0 values, is characteristic of type IV isotherms and can be related to capillary condensation of N_2 inside the intra-nanoparticle mesopores. The sharpness of this adsorption step supports the existence of mesopores with homogeneous size (BJH pore sizes of ca 2.71 nm; narrow pore size distribution). The second step, at a high relative pressure, corresponds to the filling of the large textural pores among the primary nanoparticles. In this last case, the curves show a characteristic H1 hysteresis loop and a relatively wide pore size distribution. In fact, although application of the BJH model leads to large pore size values falling in the limit between meso and macropores, a pore size distribution ranging from 30 to 100 nm is estimated.

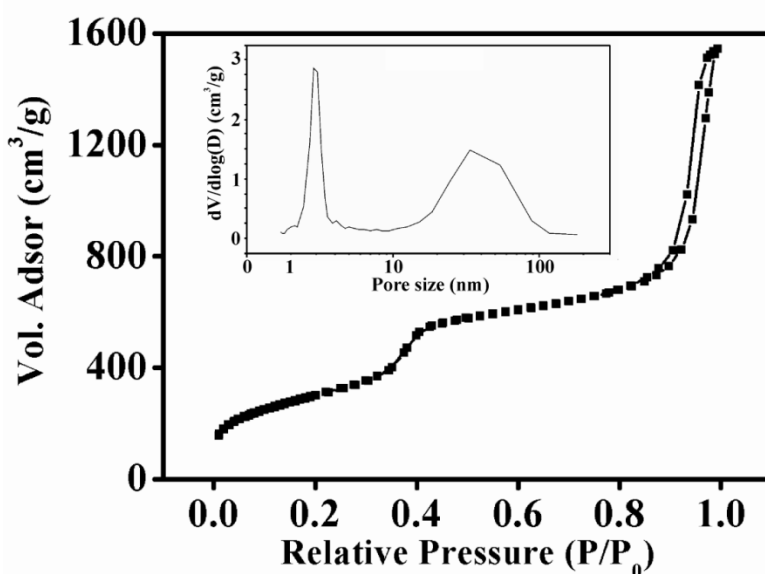


Figure 2. N_2 adsorption–desorption isotherm of UVM-7 silica.

The additional information provided by the corresponding XRD patterns is relatively scarce. In fact, this technique only can inform us about the relative order in the intra-nanoparticle mesopore system. The extremely disordered character of the textural pore system and also the large size of its motives exclude any detection by XRD. Thus, the UVM-7 silicas originate XRD patterns (Figure 3) including one strong and broad diffraction peak and one shoulder (in the low angle region), which is typical of this class of nanoparticulated mesoporous solids. Under the assumption of a basic MCM-41-like hexagonal cell, these signals could be respectively assigned to the (100) and the overlapped (110) and (200) reflections¹. Their observation constitutes a probe of the existence of a certain hexagonal order in the intra-nanoparticle mesopore system.

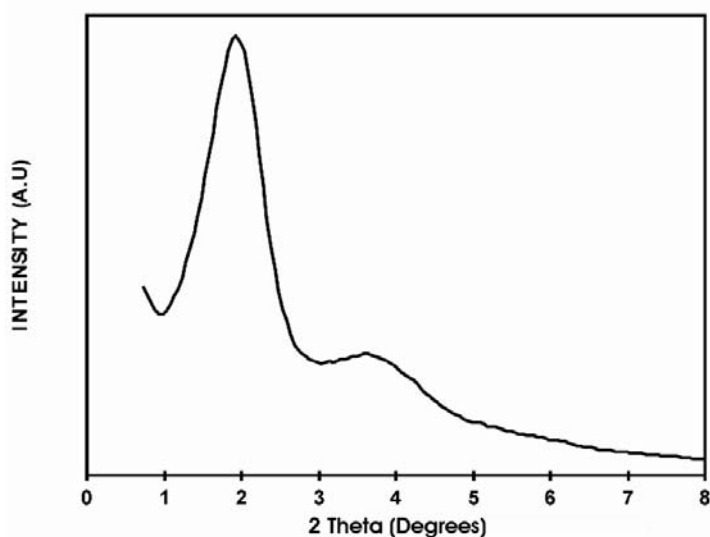


Figure 3. Typical XRD pattern of UVM-7-like materials.

While in the case of ordered MCM-41-like materials (even if they are constructed from nanoparticles), the presence of regular, unimodal, and non-interconnected surfactant-generated mesopores is evident from TEM images, TEM or STEM images are not fully conclusive in the case of partially disordered materials (as the UVM-7 silicas we are dealing with). Thus, although the presence of a bimodal pore structure is evident, the images do not provide us information about the relative

disposal (independent or interconnected) of the intra-nanoparticle mesopores. As mentioned above, the modulation of the accessibility to the active sites located at the pore walls of mesoporous silicas is a critical parameter in a variety of applications in areas such as catalysis, sensing, remediation, or drug delivery³²⁻³⁵. The availability of mesopores with lengths in the nanometric range is a step toward the assumed objective, but it seems clear that there are additional factors related to the internal organization of the mesopore array (independent —tortuous or entangled— or interconnected mesopores), which could play a pivotal role in order to orchestrate the site accessibility. Therefore, to clarify this point requires full knowledge for evaluating new prospects for UVM-7-based materials' applicability.

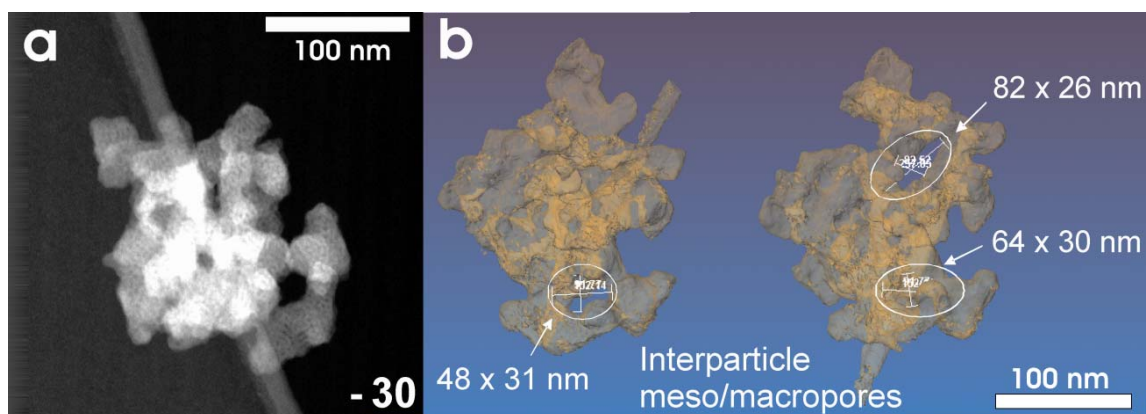


Figure 4. **a** Representative STEM image recorded at -30° . **b** 3D-tomographic reconstruction displayed a view of the iso-surface render of a UVM-7 aggregate showing the nature of the large pore system.

The structural complete elucidation of mesoporous materials can be aided by electron tomography studies⁴¹⁻⁴⁵, especially for complex non-repeating organizations that deviate from ideal regular geometries^{46,47}. The electron tomography allows performing (from STEM images recorded at different angles) 3-D reconstructions of the UVM-7 mesostructure. In contrast to a single STEM image (Figure 4a), which does not furnish added information, the 3-D reconstructions provide a clear enough vision of the material mesostructure (Figures 4b, 5). Indeed, as expected, the existence of the textural inter-particle porosity (with analogous characteristics to that occurring in xerogels) becomes directly and unambiguously confirmed. Also, the tomographic

reconstruction in Figure 4b (displayed a view of the iso-surface render of an UVM-7 aggregate of ca 30 μm) really shows how the textural-like large meso/macropores situate among the nanoparticles the condensation processes leading to cage-like highly interconnected pores displaying a significant dispersion both in shape and size. We can notice in this aggregate pores of rather different sizes (in the 30–80 nm range), and minimal bottlenecks' diameters of ca 15–20 nm can be measured. These values are in good accordance with those estimated from the N_2 adsorption–desorption isotherms. Otherwise, concerning the intra-nanoparticle mesopore system, the voxel projection of the tomographic 3D reconstruction in Figure 5 (corresponding to a primary nanoparticle of ca 40 nm belonging to the mentioned ca 30 μm aggregate) reveals the essentially non-ordered character of the mesopore arrays at the inside of the nanoparticles together with lacking of coherence among consecutive cross sections and a certain level of pore joining (white circles in Figure 5).

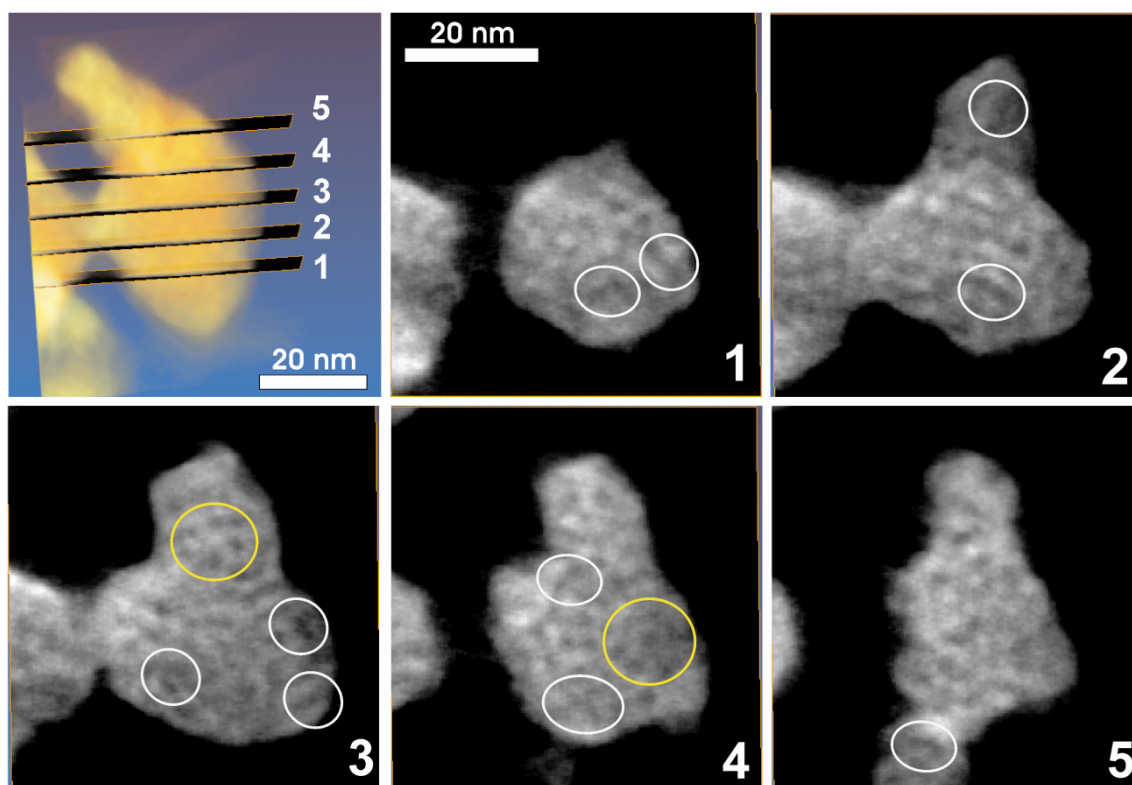


Figure 5. Voxel projection of the reconstructed 3D UVM-7 solid displaying the intra-nanoparticle architecture. Selected pore joining is marked with white circles. In some slices a certain number of disordered hexagonal mesopore arrays can be appreciated (marked yellow circles), but no coherence among consecutive silica is observed.

Although it is true that a certain hexagonal order can be randomly appreciated in some slices (yellow circles in Figure 5), this fact does not seem to be the rule, but the exception. So, it results in not only the tortuous character typical of wormhole-like mesoporous systems, but also the existence of mesopore connections. Finally, it must be stressed that the estimated pore diameter and pore wall values (ca 2.5 and 2.0 nm, respectively) fit in well with the above-mentioned porosimetry results and also with XRD data (2.71 and ca 2.0 nm).

As disclosed above, we have obtained complementary evidence about the pore architecture in the UVM-7 silicas by isolating self-supported carbon replicas of host matrices. The most noticeable point in this concern refers to the conservation of the clustered organization of aggregated porous primary nanoparticles in the replicas. Thus, the TEM micrograph in Figure 6 shows that the C-UVM-7 carbon material consists of nanoparticles which keep the porous inter-particle texture characteristic of the template (UVM-7). Although the replication process induces a certain loss of order in the final material (as compared to the parent UVM-7 silica), both the average size (ca 40–50 nm) and the pseudo-spherical shape characterizing the starting silica nanoparticles are conserved in the carbon replica. Without prejudice from the mesoscopic order lowering, the TEM image in Figure 6 shows that the intra-nanoparticle porosity is preserved. In fact, the corresponding N_2 adsorption–desorption isotherm displays the two typical adsorption steps, which become patent at P/P_0 values similar to those observed for the parent UVM-7 silica. So, the resulting carbon replica maintains a high surface area (1,156 m^2/g), a high pore volume (0.96 cm^3/g), and the hierarchic bimodal porosity. Therefore, the nanocasting formation of the carbon material can be thought of as a pseudomorphic reaction preserving the UVM-7 architecture, a result that only is possible if a highly tortuous (or entangled) and interconnected mesopore system exists. At this point, we must emphasize the claimed impossibility of obtaining MCM-41 carbon replicas precisely because of the absence of connections among the high symmetrically arranged mesopores⁴⁸.

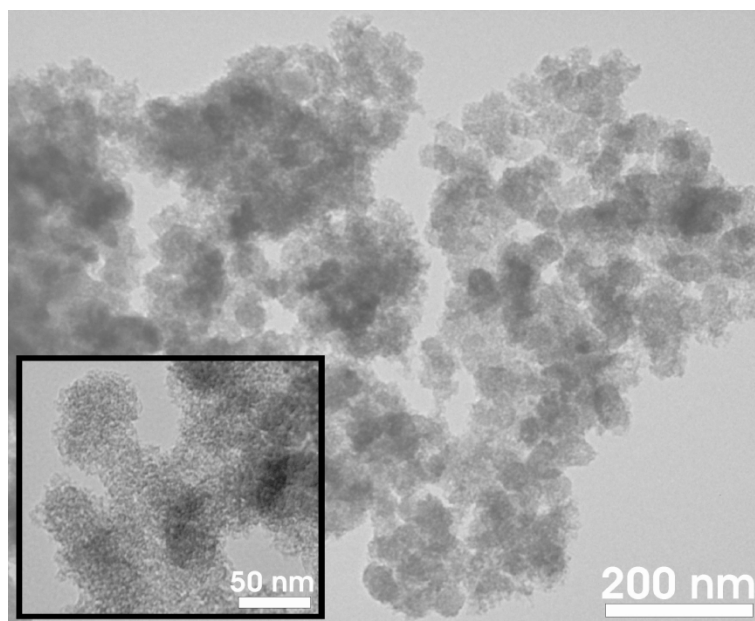


Figure 6. TEM micrograph of a carbon replica of the UVM-7 silica.

On the other hand, our experiments involving Au-UVM-7 composites have provided us qualitative evidence on how the UVM-7 support toward the matter diffusion responds in practice. Thus, starting from Au-impregnated supports, we have studied the Au diffusion throughout the pore network as a consequence of thermal treatments. It is well known that the thermal stability of metal nanoparticles is closely related to their mobility on the support during the thermal treatment. When the Hütting temperature ($T_{\text{Hüttig}} = 319 \text{ }^{\circ}\text{C}$ for bulk gold) is reached, atoms at defects and surfaces will become mobile⁴⁹. The atomic mobility strongly increases when the treating temperature is higher than the Tammann temperature ($T_{\text{Tammann}} = 532 \text{ }^{\circ}\text{C}$ for bulk gold), affecting bulk atoms^{50,51}, with the possible subsequent agglomeration or sintering phenomena⁴⁹. These critical reference temperatures (319 and 532 $^{\circ}\text{C}$) significantly drop down with the particle size, which implies considerably lower temperature effective values when treating with nano-sized gold particles⁵⁰. Well, as the TEM image in Figure 7a shows, the incorporation of gold into the UVM-7 silica by impregnation and later calcination at 200 $^{\circ}\text{C}$ does not modify the texture of the support at mesoscopic level. Even more noticeable is the excellent dispersion of the gold nanoparticles in the Au-UVM-7 composite samples obtained at that temperature. As can be observed, the gold nanoparticles (with an average size around 3 nm) appear

rather homogeneously distributed across the silica support. Changes are observed when the samples are processed at high temperatures. First at all, as expected, gold nanoparticles' aggregation occurs.

Thus, as clearly shown in the TEM image in Figure 7b, after thermal treatment at 800 °C, the size of the gold nanoparticles has risen to attaining sizes in the 7–10 nm range, which requires gold diffusion throughout the support and subsequent sintering. But, as the image reveals, the gold diffusion has resulted in coalescence toward the inside of the UVM-7 nanoparticles. We can see that, in the 800 °C Au-UVM-7 composite, the final dominant primary motif consists of entities involving one (or two) gold nanoparticle per UVM-7 silica nanoparticle. It seems difficult to conceive a gold nanoparticle diffusion and growing path leading to such a final organization (approximately one or two gold nanoparticles inside each UVM-7 primary nanoparticle) which should take place through independent mesopores. Therefore, we can reasonably assume that the present observations constitute an additional indirect probe of the existence of connectivity among the support intra-nanoparticle mesopores, thus favoring the gold species diffusion.

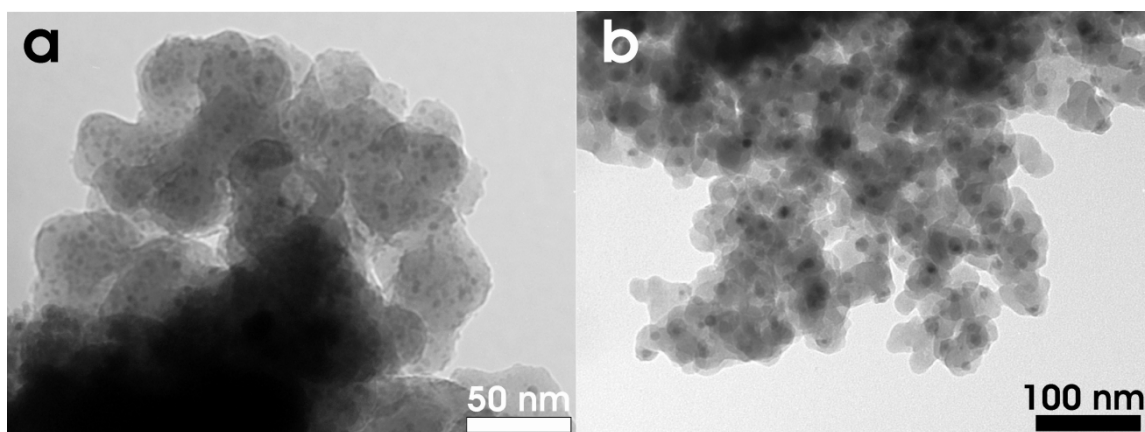


Figure 7. TEM images of Au/UVM-7 nanocomposites after thermal treating at 200 °C **a** and 800 °C **b**. The small dark spots in the a-image correspond to gold nanoparticles included inside the mesopores. The absence of white spots (associated to empty mesopores) suggests that a good dispersion of gold occurs. Aggregation of gold nanoparticles can be clearly appreciated in image **b**.

So far, all our results indicate that mass-transfer processes inside UVM-7-based materials become favored by the availability of hierarchically structured large pore sets the length of which is limited at the nanometric scale. Moreover, the pore networks become interconnected with pore unions affecting even the relatively small intra-nanoparticle mesopores. Very likely, this is interconnected pore organization which can explain the above-mentioned effectiveness of some UVM-7-based materials in catalytic and sensing processes^{32-34,52,35}. Looking for expanding possible applications of UVM-7-like materials in processes requiring enhanced site accessibility, we have tried to expand the intra-nanoparticle pore sizes, while maintaining their interconnectivity (as well as all the remaining essential features of the supports). With this aim, we have introduced in our preparative procedure the use of TMB as an organic micelle-swelling agent⁵³. The preparative procedure was modified with regard to the original one-pot synthesis of the UVM-7 silica in order to make feasible the formation and stabilization of the CTMABr-TMB swelled micelles (templates) prior to starting the hydrolytic and condensation processes of the silatrane precursors. In practice, the final UVM-7 architecture considered as a whole is preserved for materials synthesized by means of TMB/CTMABr molar ratios $\leq 4/1$ (Figure 8). However, both the textural-like and the intra-nanoparticle pore systems experience a certain modification. Indeed, the application of the BJH model (see Table 1) really reveals a progressive growth of the micelle-generated (intra-nanoparticle) mesopore size. In parallel, the size of the textural-like pores significantly drops down. Very likely, this last result is a consequence of the more compact nanoparticle aggregation observed for the pore-expanded UVM-7 materials (see Figure 8), which might be explained on the basis of the concomitant size reduction of the primary nanoparticles. In any case, taking into account the absolute values of the inter-particle pore sizes, it is evident that mass-diffusion inside the modified supports will remain essentially conditioned by the small mesopores.

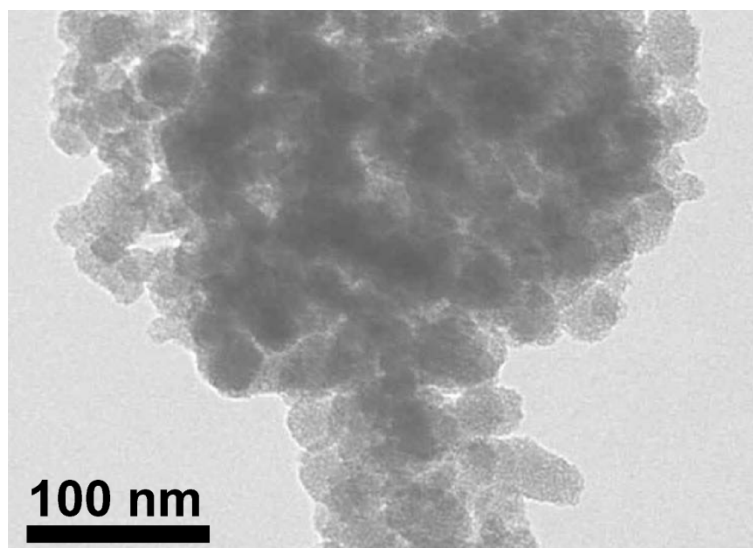


Figure 8. TEM micrograph of the mesopore-expanded UVM-7(3) silica.

In order to evaluate the behavior toward mass transfer of the UVM-7-like architecture, we have studied the adsorption by different matrices (MCM-41, UVM-7, UVM-7(3), and UVM-7(4)) of lysozyme, a relatively small enzyme that has already been used as model for immobilization in other mesoporous materials⁵⁴. Lysozyme was selected due to both its shape and size: a globular enzyme with a hydrodynamic diameter slightly lower than ca 3 nm. According to the above considerations, lysozyme diffusion through the large textural-like pores should not find impediment. Otherwise, due to the similitude between the lysozyme diameter and the mesopore size, this enzyme constitutes a good “local probe” to evaluate the intra-nanoparticle mesopore accessibility. Apart from the enzyme/pore size adequacy, the lysozyme–silica surface interaction strongly depends on the pH conditions. The great difference between the lysozyme and mesoporous silica isoelectric points (11.4 and 3.6, respectively) allows disposing of a wide pH range for the electrostatic immobilization^{55,56}. We have selected pH = 6.0 as a compromise value favoring the protein–silica interaction over the repulsive neighboring lysozyme-lysozyme interactions⁵⁷. Also, for comparative purposes, all the essayed supports have been prepared following the same general procedural principles in order to get silica surfaces with similar distributions of Q⁴ and Q³ sites: $Q^4/Q^3 + Q^2 \approx 1$ ²⁹. The curves in Figure 9 show the evolution of the lysozyme uptake with time (under our experimental conditions) for the different supports. In the

case of the MCM-41 silica (curve d), the maximum lysozyme uptake value (ca 200 mg/g) is similar to those reported in previous publications when working at similar pH values^{58,59}. When compared to a conventional MCM-41 material, the adsorption of lysozyme becomes greatly facilitated in the case of the simple UVM-7 silica (curve c). Both the adsorption rate and the loading level (ca 300 mg/g) appear now noticeably enhanced. The lysozyme uptake evolution is even more striking in the case of the pore-expanded UVM-7 supports (curves b and a). Thus, practically instantaneous ($t < 2$ min) complete immobilization occurs, thus leading to unusually high lysozyme charge levels (around 350 mg/g). The MCM-41 and UVM-7 silicas have similar surfaces, both at chemical level (similar density of silanol groups) and with regard to their surface area absolute values. Moreover, they include also similar-sized (cross-section) mesopores. So, it seems reasonable to conclude that it is the interconnected pore architecture in UVM-7 which facilitates the mass-diffusion (rate and load) throughout the support. When increasing the mesopore size while maintaining the pore architecture, mass-transfer becomes improved.

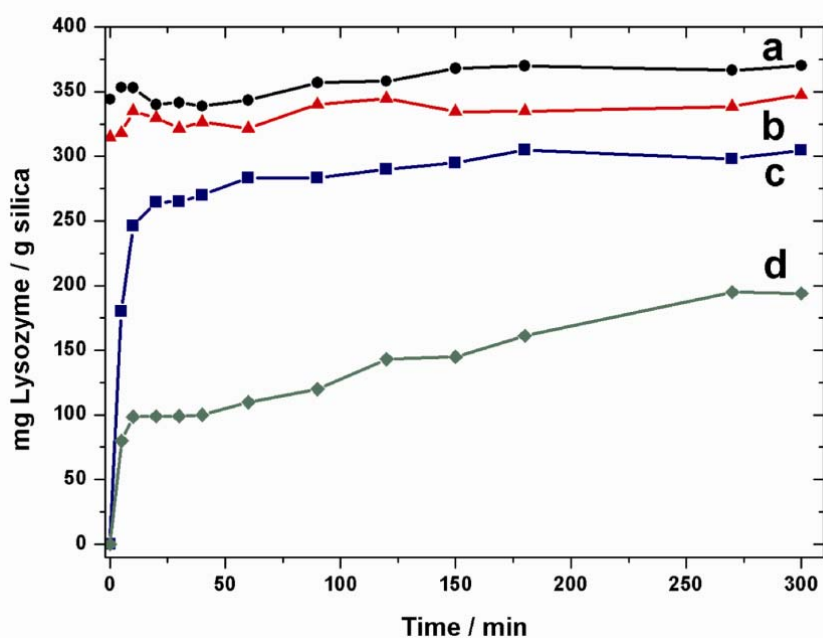


Figure 9. Comparison of the Lysozyme adsorption isotherms on (a) UVM-7(4), (b) UVM-7(3), (c) UVM-7, and (d) MCM-41 supports.

Conclusions

Our main objective with this work was to get a better understanding of the enhanced site accessibility shown by UVM-7-like silicas by clarifying the relation existing between the pore systems in the supports. All our results indicate that there exists a true 3-D hierarchic connectivity in these materials including even the small intra-nanoparticle mesopores. In practice, the case of the UVM-7-like materials constitutes a successful example of how it is possible to combine in a simple preparative strategy various alternatives explored for enhancing site accessibility, namely, pore length reduction (nanoparticulated materials), pore interconnections, and classical pore size expansion.

Acknowledgments

This research was supported by the Ministerio de Educación y Ciencia (MAT2009-14564-C04-04) and the Generalitat Valenciana (PROMETEO/2009/108). J.E.H. thanks the Fundació General de la Universitat de València for financial support. A.M. thanks MEC for a FPI fellowship.

References

1. Kresge, C. T.; Leonowicz, M. E.; Roth, W. J.; Vartuli, J. C.; Beck, J. S. *Nature* **1992**, *359*, 710-712.
2. Soler-illia, G. J. D.; Sanchez, C.; Lebeau, B.; Patarin, J. *Chemical Reviews* **2002**, *102*, 4093-4138.
3. Sanchez, C.; Belleville, P.; Popall, M.; Nicole, L. *Chemical Society Reviews* **2011**, *40*, 696-753.
4. Lee, J. E.; Lee, N.; Kim, T.; Kim, J.; Hyeon, T. *Accounts of Chemical Research* **2011**, *44*, 893-902.
5. Wan, Y.; Zhao, D. *Chemical Reviews* **2007**, *107*, 2821-2860.
6. Rolison, D. R. *Science* **2003**, *299*, 1698-1701.
7. Antonietti, M.; Ozin, G. A. *Chemistry-a European Journal* **2004**, *10*, 29-41.
8. Sayari, A.; Hamoudi, S. *Chemistry of Materials* **2001**, *13*, 3151-3168.
9. Poyraz, A. S.; Dag, O. *Journal of Physical Chemistry C* **2009**, *113*, 18596-18607.
10. Boissiere, C.; Martines, M. A. U.; Tokumoto, M.; Larbot, A.; Prouzet, E. *Chemistry of Materials* **2003**, *15*, 509-515.
11. Zhang, P.; Wu, Z.; Xiao, N.; Ren, L.; Meng, X.; Wang, C.; Li, F.; Li, Z.; Xiao, F.-S. *Langmuir* **2009**, *25*, 13169-13175.
12. Yuan, Z. Y.; Su, B. L. *Journal of Materials Chemistry* **2006**, *16*, 663-677.
13. El Haskouri, J.; de Zarate, D. O.; Guillem, C.; Latorre, J.; Caldes, M.; Beltran, A.; Beltran, D.; Descalzo, A. B.; Rodriguez-Lopez, G.; Martinez-Manez, R.; Marcos, M. D.; Amoros, P. *Chemical Communications* **2002**, 330-331.
14. El Haskouri, J.; de Zarate, D. O.; Perez-Pla, F.; Cervilla, A.; Guillem, C.; Latorre, J.; Marcos, M. D.; Beltran, A.; Beltran, D.; Amoros, P. *New Journal of Chemistry* **2002**, *26*.
15. El Haskouri, J.; Cabrera, S.; Caldes, M.; Guillem, C.; Latorre, J.; Beltran, A.; Beltran, D.; Marcos, M. D.; Amoros, P. *Chemistry of Materials* **2002**, *14*, 2637-2643.
16. El Haskouri, J.; de Zarate, D. O.; Guillem, C.; Beltran-Porter, A.; Caldes, M.; Marcos, M. D.; Beltran-Porter, D.; Latorre, J.; Amoros, P. *Chemistry of Materials* **2002**, *14*, 4502-4504.
17. Zhang, W. Z.; Pauly, T. R.; Pinnavaia, T. J. *Chemistry of Materials* **1997**, *9*, 2491-2498.
18. Sun, J. H.; Shan, Z. P.; Maschmeyer, T.; Coppens, M. O. *Langmuir* **2003**, *19*, 8395-8402.
19. Lin, H. P.; Tsai, C. P. *Chemistry Letters* **2003**, *32*, 1092-1093.
20. Smatt, J. H.; Schunk, S.; Linden, M. *Chemistry of Materials* **2003**, *15*, 2354-2361.
21. Lee, J.; Kim, J.; Hyeon, T. *Chemical Communications* **2003**, 1138-1139.
22. Suzuki, K.; Ikari, K.; Imai, H. *Journal of the American Chemical Society* **2004**, *126*, 462-463.

23. Chao, M. C.; Lin, H. P.; Mou, C. Y. *Chemistry Letters* **2004**, *33*, 672-673.
24. Chao, M. C.; Lin, H. P.; Mou, C. Y.; Cheng, B. W.; Cheng, C. F. *Catalysis Today* **2004**, *97*, 81-87.
25. Wang, X. Z.; Li, W. H.; Zhu, G. S.; Qiu, S. L.; Zhao, D. Y.; Zhong, B. *Microporous and Mesoporous Materials* **2004**, *71*, 87-97.
26. Ikari, K.; Suzuki, K.; Imai, H. *Langmuir* **2006**, *22*, 802-806.
27. Kobler, J.; Moeller, K.; Bein, T. *Acs Nano* **2008**, *2*, 791-799.
28. El Haskouri, J.; Morales, J. M.; de Zarate, D. O.; Fernandez, L.; Latorre, J.; Guillem, C.; Beltran, A.; Beltran, D.; Amoros, P. *Inorganic Chemistry* **2008**, *47*, 8267-8277.
29. Huerta, L.; Guillem, C.; Latorre, J.; Beltran, A.; Martinez-Manez, R.; Marcos, M. D.; Beltran, D.; Amoros, P. *Solid State Sciences* **2006**, *8*, 940-951.
30. Pauly, T. R.; Liu, Y.; Pinnavaia, T. J.; Billinge, S. J. L.; Rieker, T. P. *Journal of the American Chemical Society* **1999**, *121*, 8835-8842.
31. de Zarate, D. O.; Gomez-Moratalla, A.; Guillem, C.; Beltran, A.; Latorre, J.; Beltran, D.; Amoros, P. *European Journal of Inorganic Chemistry* **2006**, 2572-2581.
32. Descalzo, A. B.; Jimenez, D.; Marcos, M. D.; Martinez-Manez, R.; Soto, J.; El Haskouri, J.; Guillem, C.; Beltran, D.; Amoros, P.; Borrachero, M. V. *Advanced Materials* **2002**, *14*.
33. Descalzo, A. B.; Jimenez, D.; El Haskouri, J.; Beltran, D.; Amoros, P.; Marcos, M. D.; Martinez-Manez, R.; Soto, J. *Chemical Communications* **2002**, 562-563.
34. Cimpeanu, V.; Parvulescu, V. I.; Amoros, P.; Beltran, D.; Thompson, J. M.; Hardacre, C. *Chemistry-a European Journal* **2004**, *10*, 4640-4646.
35. Coman, S. M.; Pop, G.; Stere, C.; Parvulescu, V. I.; El Haskouri, J.; Beltran, D.; Amoros, P. *Journal of Catalysis* **2007**, *251*, 388-399.
36. Cabrera, S.; El Haskouri, J.; Guillem, C.; Latorre, J.; Beltran-Porter, A.; Beltran-Porter, D.; Marcos, M. D.; Amoros, P. *Solid State Sciences* **2000**, *2*, 405-420.
37. Lee, J. S.; Joo, S. H.; Ryoo, R. *Journal of the American Chemical Society* **2002**, *124*, 1156-1157.
38. Haruta, M. *Gold Bulletin* **2004**, *37*, 27-36.
39. Bradford, M. M. *Analytical Biochemistry* **1976**, *72*, 248-254.
40. Gilbert, P. *Journal of Theoretical Biology* **1972**, *36*, 105-&.
41. Midgley, P. A.; Weyland, M.; Thomas, J. M.; Johnson, B. F. G. *Chemical Communications* **2001**, 907-908.
42. Midgley, P. A.; Ward, E. P. W.; Hungria, A. B.; Thomas, J. M. *Chemical Society Reviews* **2007**, *36*, 1477-1494.
43. de Jong, K. P.; Koster, A. J. *Chemphyschem* **2002**, *3*, 776-+.
44. Yates, T. J. V.; Thomas, J. M.; Fernandez, J. J.; Terasaki, O.; Ryoo, R.; Midgley, P. A. *Chemical Physics Letters* **2006**, *418*, 540-543.

45. Ersen, O.; Parmentier, J.; Solovyov, L. A.; Drillon, M.; Pham-Huu, C.; Werckmann, J.; Schultz, P. *Journal of the American Chemical Society* **2008**, *130*, 16800-16806.
46. de Jong, K. P.; Janssen, A. H.; van der Voort, P.; Koster, A. J. *Nanotechnology in Mesostructured Materials* **2003**, *146*, 271-274.
47. Friedrich, H.; de Jongh, P. E.; Verkleij, A. J.; de Jong, K. P. *Chemical Reviews* **2009**, *109*, 1613-1629.
48. Liang, C.; Li, Z.; Dai, S. *Angewandte Chemie-International Edition* **2008**, *47*, 3696-3717.
49. Moulijn, J. A.; van Diepen, A. E.; Kapteijn, F. *Applied Catalysis a-General* **2001**, *212*, 3-16.
50. Sun, J.; Bao, X. *Chemistry-a European Journal* **2008**, *14*, 7478-7488.
51. Veith, G. M.; Lupini, A. R.; Rashkeev, S.; Pennycook, S. J.; Mullins, D. R.; Schwartz, V.; Bridges, C. A.; Dudney, N. J. *Journal of Catalysis* **2009**, *262*, 92-101.
52. Candu, N.; Musteata, M.; Coman, S. M.; Parvulescu, V. I.; El Haskouri, J.; Amoros, P.; Beltran, D. *Chemical Engineering Journal* **2010**, *161*, 363-370.
53. Lefevre, B.; Galarneau, A.; Iapichella, J.; Petitto, C.; Di Renzo, F.; Fajula, F.; Bayram-Hahn, Z.; Skudas, R.; Unger, K. *Chemistry of Materials* **2005**, *17*, 601-607.
54. Hudson, S.; Cooney, J.; Magner, E. *Angewandte Chemie-International Edition* **2008**, *47*, 8582-8594.
55. Wilson, K. P.; Malcolm, B. A.; Matthews, B. W. *Journal of Biological Chemistry* **1992**, *267*, 10842-10849.
56. Deere, J.; Magner, E.; Wall, J. G.; Hodnett, B. K. *Journal of Physical Chemistry B* **2002**, *106*, 7340-7347.
57. Su, T. J.; Lu, J. R.; Thomas, R. K.; Cui, Z. F.; Penfold, J. *Langmuir* **1998**, *14*, 438-445.
58. Hartmann, M. *Chemistry of Materials* **2005**, *17*, 4577-4593.
59. Bhattacharyya, M. S.; Hiwale, P.; Piras, M.; Medda, L.; Steri, D.; Piludu, M.; Salis, A.; Monduzzi, M. *Journal of Physical Chemistry C* **2010**, *114*, 19928-19934.

Enlarged pore size in nanoparticulated bimodal porous silicas: improving accessibility

Alaina Moragues^a, Carmen Guillem^a, Adela Mauri-Aucejo^b, Marta Tortajada^c, Aurelio Beltrán^a, Daniel Beltrán^a and Pedro Amorós^a

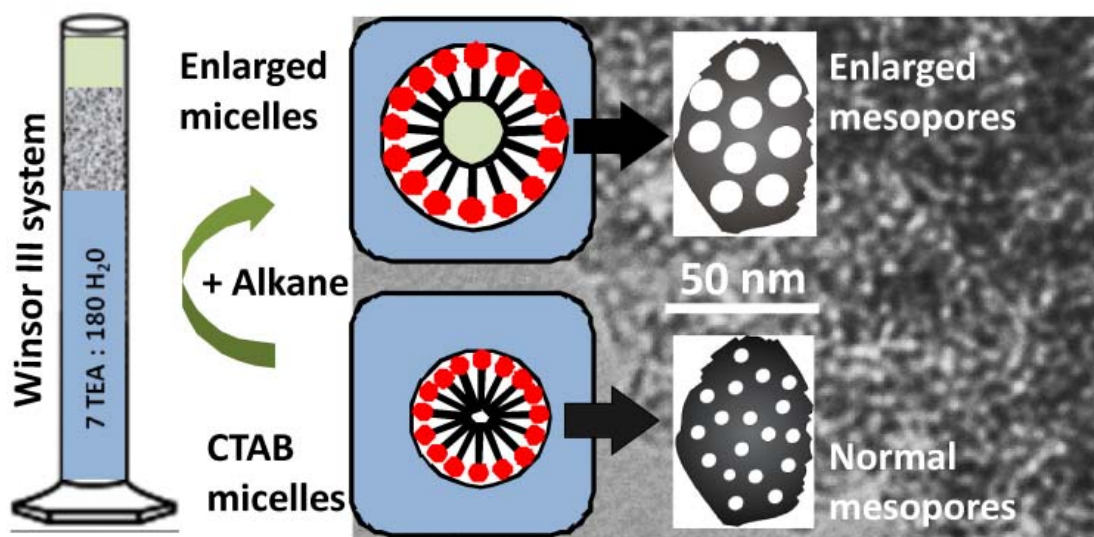
^a Institut de Ciència dels Materials (ICMUV), Universitat de València, P. O. Box 22085, 46071-Valencia, Spain.

^b Departament de Química Analítica. Facultat de Química. Universitat de València, Dr Moliner 50, 46100 Burjassot, València, Spain.

^c Biópolis S. L., C/ Catedrático Agustín Escardino 9, 46980-Paterna, Valencia, Spain.

Abstract

Mass-transfer kinetics seems to be highly favored in siliceous supports consisting of aggregates of mesoporous nanoparticles. Nanoparticle aggregation causes large textural voids. Diffusion constrains through the resulting hierarchically structured pore systems are mainly dependent on the features of the intra-particle mesopores. By using alkanes as swelling agents, we have been able to significantly increase the mesopore size in previously well characterized UVM-7-derived materials. The Winsor-III-like behavior resulting from the presence of alkanes in the hydro-alcoholic reaction media used in surfactant-assisted procedures allows explaining the existence of limits to the pore size expansion. A preliminary study on drug and enzyme charge onto these UVM-7-modified solids offers promising results on their capabilities as supports for processing a variety of biomolecules.



Introduction

One of the most attractive aspects raised by the discovery of the surfactant-templated M41S silicas was the theoretical possibility of tuning their mesopore size over a wide range, an issue that is among the keys to produce suitable materials for desired applications¹. Thus, even in the first full-paper published by Mobil's researchers on the subject, the pore expansion topic was object of interest and analysis². In this seminal work, the authors referred a significant variation of the mesopore size in MCM-41 silicas by using TMB as organic expander under hydrothermal conditions². In the subsequent explosive rise of work on porous materials chemistry, pore-expanding strategies were relegated for a while until prospects for new applications in several fields aroused the need for increasing the pore sizes to process large substrates or biomolecules which cannot be located within small mesopores³⁻⁵. Then, the use of different swelling agents together with the utilization of larger surfactants as templates entailed a breakthrough in the pore size engineering⁶⁻⁸. While conceptually the expansion mechanism looks simple (the swelling agent is solubilized in the presence of surfactant micelles enlarging them, which subsequently results in large pores after template removal), things are not so straightforward. In practice, the process depends on several variables such as, among others, the surfactant nature and its features, the character of the interaction of the surfactant with the silica counterpart (ionic, no ionic) or how the swelling molecules change the preexisting phase diagram of the surfactant⁷. The SBA-15 and FDU-12 solids are archetypal examples of success in expanding the size of pores. For these silicas, isolated by using non-ionic Pluronic surfactants, there have been achieved pore sizes up to 30-40 nm through a judicious selection of the swelling agents under mild temperature conditions⁶⁻¹².

Among the diversity of mesoporous silicas available today, those consisting of particles with sizes smaller than *ca.* 200-300 nm, have attracted the attention of nanomedicine researchers due to their potential as supports to construct new theranostic agents¹³. This prerequisite (particle size < *ca.* 200-300 nm) practically excludes the SBA-15-related materials because, under the acidic conditions necessary for their syntheses, is problematic to avoid the particle growth processes that typically

lead to micrometric solids. In fact, it has only been described one example of a SBA-15 nanometric silica synthesized by using a fluorocarbon surfactant as template¹⁴. Therefore, the search scope of nanoparticulated silicas with expanded pores has been necessarily limited and has focused on MCM-41-related materials synthesized under basic conditions and using alkyltrimethylammonium surfactants as templates¹³ (which is, somehow, return to the original Mobil work)². To the extent that the alkyltrimethylammonium surfactants only allow small increases in the pore sizes^{15,16}, there has made use of a large variety of swelling agents (aromatic hydrocarbons as TMB, alkanes, alkylamines and co-surfactants)^{2,17-25} in order to achieve greater pore sizes in MCM-41-like materials. In general, the maximum expansion attained (preserving cylindrical mesopores with narrow pore size distributions) corresponds to pore size values around 5-6 nm. Furthermore, it has been observed that increasing the amount of swelling agent beyond a certain limit only leads to slight additional expansions and, in all cases, to wide pore size distributions.

Siliceous materials combining particle sizes in the nanometric range and expanded mesopores are much less frequent¹³. As far as we known, there are only four previous papers describing solids with such a combination. Fuertes et al.²⁶ made use of N,N-dimethylhexadecylamine and TMB as swelling agents. Kim and coworkers²⁷ utilized TMB under hydrothermal conditions. Zhang et al.²⁸ used TMB and decane as expanders. In any case, all these mesopore-expanded silicas show highly disordered mesopore systems with worm-hole like organizations and a certain radial growth. Then, it is difficult to relate the resulting pores with the template effect of cylindrical expanded micelles. More recently, Kao et al.²⁹ have introduced alkanes and ethanol as swelling agents, what has resulted in somewhat more symmetric mesopore arrays (similar to those in hexagonal disordered MCM-41 solids).

Our group was successful in synthesizing a new family of nanoparticulated silicas with bimodal porosity (NBS) through a one-pot procedure by using a simple template agent and starting from silicon atrane complexes as inorganic precursors^{15,16,30}. The most outstanding feature concerning these materials, denoted UVM-7 (or M-UVM-7 when inorganically functionalized), is their peculiar (very open) architecture, which is based on a continuous network constructed from covalently bonded pseudospherical mesoporous primary nanoparticles whose aggregation

defines a non-ordered secondary system of large textural pores. Likewise, all our results indicated that mass-transfer processes inside UVM-7-based materials are favored by the good pore connectivity in the siliceous skeleton, which is related to the availability of (hierarchically structured) pore sets whose length is limited at the nanometric scale³¹.

At this point, the aim of this work is dual. First, we intend to expand the mesopore size characteristic of the UVM-7 silicas for further progress in reducing diffusion constraints in these supports. The intra-particle pore system in UVM-7 (originated by the template effect of the surfactant) has similarities with those present in MCM-41-like solids. It is precisely this cylindrical pore system which we want to expand while maintaining all the remaining features of the UVM-7 architecture. That is, we intend to obtain a new series of NBS solids combining, as mentioned above, particle sizes in the nanometric range (as aggregates defining large inter-particle voids) with expanded mesopores (with regard to those in the UVM-7 materials). Secondly, we intend to understand why, according to the up to date reported results, the maximum possible pore size expansion in related materials (see above) is relatively low, even when using great amounts of swelling agents.

Experimental section

Synthesis

The method is an adaptation of the so-called “atrane route”, which is based on the use of (1) a hydroalcoholic reaction medium supporting the formation of “atranes” (i.e., complexes including triethanolamine-related ligand-species) as hydrolytic inorganic precursors and (2) a cationic surfactant as supramolecular template and, consequently, as a porogen agent after template removal. Details of the “atrane route” and its versatility have been reported elsewhere^{15,16,32}. Its application for obtaining conventional UVM-7 materials was widely discussed in the reference 16. In the present case, the use of alkanes as swelling agents requires procedural modifications but enables a certain modulation of the porogen effect of the surfactant.

Chemicals

All the synthesis reagents are analytically pure and were used as received from Aldrich (tetraethyl-orthosilicate (TEOS), triethanolamine [N(CH₂-CH₂-OH)₃, hereinafter TEA], cetyltrimethylammonium bromide (CTMABr), alkanes of different chain length (from n-hexane to hexadecane) and ethanol).

Preparative procedure

All of the silica samples reported in this publication were prepared by the same general method, and using molar ratios of the reagents in the final reaction mixture according to: 2 Si : 7 TEA: x CTMABr : y C_nH_{n+2} : 180 H₂O (0.3 ≤ x ≤ 1.9; 0 ≤ y ≤ 4; n = 6, 8, 10, 12, 14, 16). Insofar as one basic objective was to evaluate the influence of the swelling agents (alkanes) by themselves in the expansion of the pore size, we prepared a series of silicas of reference in which x was fixed at 0.5 (i.e., the x value previously optimized for obtaining the conventional UVM-7 materials through the “atrané” route)¹⁶. In any case, the implication of alkanes in the reaction processes enforced us to modify the original “one-pot” synthetic procedure (UVM-7 silicas) by adopting a “two-pot” strategy. Thus, two reagents, A and B, were independently prepared. A was a dissolution containing silatranes and B a colloidal suspension of expanded micelles. The A dissolution was prepared by mixing 11.2 mL of TEOS and 13.3 mL of TEA. This mixture was heated at 140°C for 5 min to favor the formation of silatrane complexes in TEA medium. The resulting clear solution, which contained practically 0.05 mol of silatranes (mainly in the form of Si(TEA)(TEAH₂)^{15,32}, where TEA is the fully deprotonated ligand), was cooled down to room temperature. B was prepared by dissolving 4.56 g of CTMABr (x = 0.5 series; the corresponding quantity for other x values) in 10 mL of TEA at 120°C. When the temperature dropped to ca. 80°C, 80 mL of water plus the required volume of alkane (according to 0 ≤ y ≤ 4) were added to this solution, what immediately provoked some turbidity (except for y = 0). The resulting colloidal suspension, B, was stirred for 10 minutes and then added to A. After a few seconds, we were already beginning to see a white solid in suspension in the reaction mixture (A+B). This as-prepared mixture was allowed to age at room temperature for 12 hours under stirring at ca. 150 rpm. The resulting mesostructured powder was

separated by filtration, washed with water and ethanol, and air dried (samples denoted as x/yC_n -UVM-7(M)). The preparation of the final porous materials requires removing the surfactant from the as-synthesized powders. This was carried out through two alternative ways: pyrolysis and chemical extraction. Pyrolytic elimination of the surfactant was performed by calcination of the samples at 550°C for 5 hours under static air atmosphere (samples denoted as x/yC_n -UVM-7(C) (Table 1)). On the other hand, although using a soft procedure, we observed that chemical extraction caused significant degradation of the mesostructure (see below). Then, in order to favor a certain increase of the silica condensation in the inorganic framework, the as-prepared (A+ B) reaction mixtures were hydrothermally aged at 70°C during 24 hours (under static conditions). Chemical extraction of the surfactant from the aged mesostructured solids was carried out using an HCl/ethanol solution (*ca.* 1 g of powder, 8.5 mL of HCl 37% and 100 mL of ethanol 99%; $t = 12$ -24 h at 60°C). The final porous materials were separated by filtration, washed with ethanol, and air-dried (samples denoted as x/yC_n -UVM-7(E) (Table 1)).

Chemical analysis

A selected set of as-synthesized mesostructured samples (i.e., solids containing both surfactant and alkane) were analysed by CNH elemental analysis. In all cases, the surfactant content was independently determined spectroscopically. So, 0.025 g of the mesostructured sample were dissolved in 25 mL of 5 M NaOH. Once the silica was dissolved, the organic portion was extracted with chloroform and methyl orange. Then, the specific surfactant content in the samples was easily calculated from the absorbance value at 508 nm³³. In turn, the combination of these results with the CNH analyses allowed us to determine the amounts of the swelling agent (alkane) really included in the as-synthesized samples (x/yC_n -UVM-7(M)) (Table 2).

Drug and enzyme storage

Some selected x/yC_n -UVM-7 powder supports were loaded with ibuprofen through a reproducible one-step procedure previously described in detail³⁴. We used n-hexane as carrier, contact times of *ca.* 4 hours and 25°C as working

temperature. To study the influence of the drug concentration in the uptake process, we used different solutions of ibuprofen in n-hexane (0.47 and 0.58 M). In some cases, successive impregnations with progressively more concentrated solutions (0.47 M + 0.58 M) were applied. As detailed in the reference 34, the strategy was optimized to ensure, as far as possible, that ibuprofen admission occurs at the silica surface. The ibuprofen amount hosted in each support was determined by CNH elemental analysis.

Lysozyme and trypsin immobilization were carried out in heterogeneous reaction conditions. The enzymes were dissolved (300 $\mu\text{g}/\text{mL}$) in a buffer $\text{NaH}_2\text{PO}_4\text{-Na}_2\text{HPO}_4$ 10 mM solution (pH 6, at 25°C), and then 50 mg of the silica support were added. Adsorption was monitored by measuring the enzyme concentration in the supernatant for up to 6h as previously described by Smith et al.³⁵.

Physical measurements

All solids were characterized by X-ray powder diffraction (XRD) at low angles (Seifert 3000TT $\theta\text{-}\theta$) using $\text{CuK}\alpha$ radiation. Patterns were collected in steps of $0.1^\circ(2\theta)$ over the angular range 1-10 for 10 s per step. An electron microscopy study (TEM) was carried out with a Hitachi S-4800 instrument operating at 100 kV. Samples were gently ground in dodecane, and grains were deposited on a holey carbon film supported on a Cu grid. Surface area, pore size and volume values were calculated from nitrogen adsorption-desorption isotherms (-196°C) recorded on a Micromeritics ASAP-2020 automated analyser. Surface areas were estimated according to the BET model, and pore size dimensions and pore volumes were calculated by using the BJH method from the absorption branch of the isotherms³⁶. Particle size measurements were performed using a Malvern Zetasizer ZS instrument. ^{29}Si MAS NMR spectra were recorded on a Varian Unity 300 spectrometer operating at 79.5 MHz, with a magic angle spinning speed of at least 4.0 kHz.

Results and discussion

Synthesis and mesopore-expansion

As mentioned in the experimental section, the procedure for obtaining mesopore-expanded materials implies modifications with regard to the original “one-pot” synthesis of the UVM-7 materials¹⁶. The adoption of a “two-pot” protocol aims to promote the formation and stabilization of CTAMBr-alkane swelled micelles (templates) prior to starting the hydrolytic and condensation processes of the inorganic precursors (silatranes). The total amount of TEA in the final reaction mixture always is significantly greater than that involved in the formation of silatranes. This is because, as previously discussed¹⁵, the polyol additionally acts as a buffer agent (stabilizing the working apparent pH around 9) and produces a hydroalcoholic medium (co-solvent) that favours the nucleation and growth of small primary mesoporous nanoparticles. So, in order to minimize any ulterior co-solvent effect on the concentration of the surfactant in the form of micelles³⁷, we have prepared our reagent B (colloidal suspension of expanded micelles) by adding water and alkane to a solution of CTMABr in TEA (3/7 of the total TEA): the possible swelling effect of the alkane on the CTMABr micelles occurs in the presence of TEA. The remaining TEA (4/7 of the total) is sufficient enough to preserve the 1Si : 2TEA molar ratio required to guarantee the practically total silicon complexation, predominantly as Si(TEA)(TEAH₂) (solution A). Both A and B have to be heated to assist the formation of silatrane complexes (transesterification of TEOS with TEA) and the surfactant dissolution, respectively. In the case of B, the need for a minimum temperature around 80°C becomes a problem in the case of light alkanes, which could be partially eliminated. Thus, as we have verified (see below), n-hexane and octane (boiling points of 68 and 126°C, respectively) are not adequate swelling agents. On the contrary, longer chain alkanes, from decane to hexadecane (boiling points > 174°C) actually yield expanded micelles. After mixing A and B, the subsequent self-assembling processes (that initiate the formation of mesostructured solids) between the (anionic) inorganic moieties (siliceous oligomers resulting from silatrane hydrolysis) and (cationic) surfactant

expanded micelles can be reasonably thought of as analogous to those yielding the conventional UVM-7 materials^{15,16}.

Concerning the series of silicas of reference ($x = 0.5$), most of the $0.5/\gamma C_n$ -UVM-7(C) materials (Samples 1 to 23 in Table 1) originates XRD patterns displaying, at least, one strong and broad diffraction peak in the low angle region (Figure 1), which is a typical feature of UVM-7-like silicas prepared through surfactant-assisted procedures¹⁶. One can see that, for a given alkane (n), this peak gradually widens and tends to shift towards lower 2θ values (higher d_0 in Table 1) as the amount of alkane used in the synthesis (y) increases. These observations suggest that alkane molecules induce some expansion of the mesostructure together with a gradual loss of relative order in the mesopore system. On the other hand, in the case of the solids synthesized in the presence of decane, the widening of the diffraction peak is considerably more marked than that occurring for the remaining swelling agents and, in practice, the diffraction peak almost disappears for high nominal contents ($y \geq 2$) of decane.

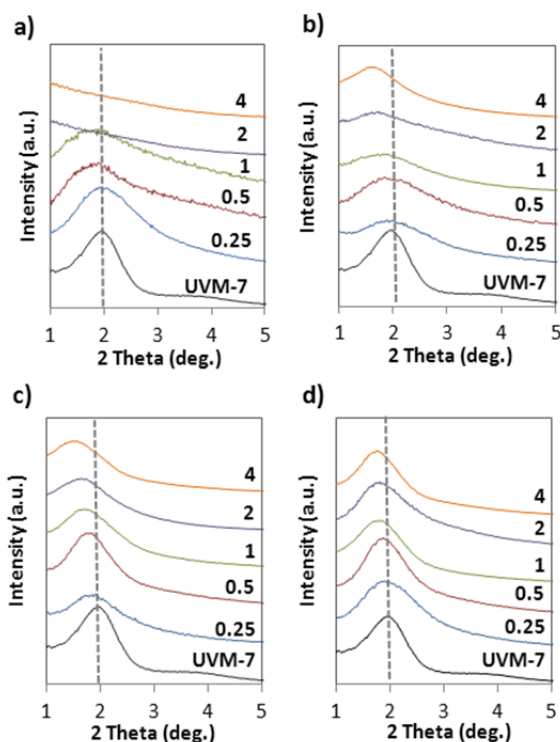


Figure 1. Low-angle XRD pattern of $0.5/\gamma C_n$ -UVM-7(C) materials. **(a)** $n = 10$, Samples 4 to 8, **(b)** $n = 12$, Samples 9 to 13, **(c)** $n = 14$, samples 14 to 18, **(d)** $n = 16$, Samples 19 to 23. The values 0.25, 0.5, 1, 2 and 4 correspond to the nominal alkane content (y). In all series the XRD of the non-expanded UVM-7 silica (Sample 1) is included for comparison.

Table 1. Selected preparative and physical data for the x/yC_n -UVM-7(C) porous silicas.

Sample ^a	n	x	y	d_0^b (Å)	Surface ^c (m ² /g)	Intra-particle mesopore		Inter-particle pore		
						Size ^d (nm)	Volume ^d (cm ³ /g)	Size ^d (nm)	Volume ^d (cm ³ /g)	
1	C	-	0.5	0	42.91	1136.2	2.71	1.02	59.13	1.31
2	C	6	0.5	4	45.75	1108.9	2.86	0.96	24.54	1.22
3	C	8	0.5	4	45.08	987.4	2.78	0.60	12.7	0.50
4	C	10	0.5	0.25	45.99	1130.7	2.77	0.91	15.83	0.67
5	C	10	0.5	0.5	46.40	1114.5	3.17	1.06	17.32	0.46
6	C	10	0.5	1	46.58	1211.5	3.26	1.18	14.33	0.47
7	C	10	0.5	2	-	1048.9	3.58	1.07	23.77	0.53
8	C	10	0.5	4	-	991.8	3.82	1.04	23.03	0.80
9	C	12	0.5	0.25	46.47	1088.1	3.27	1.06	11.76	0.47
10	C	12	0.5	0.5	47.72	1167.2	3.44	1.17	20.79	0.96
11	C	12	0.5	1	49.05	1155.5	3.45	1.19	22.07	1.23
12	C	12	0.5	2	51.51	1002.7	3.46	0.94	21.51	0.90
13	C	12	0.5	4	53.83	1145.7	3.66	1.20	27.62	1.26
14	C	14	0.5	0.25	44.10	1152.4	3.30	1.14	15.85	0.43
15	C	14	0.5	0.5	49.18	1074.7	3.50	1.12	37.64	1.28
16	C	14	0.5	1	51.12	1094.9	3.53	1.14	28.76	0.97
17	C	14	0.5	2	53.97	1104.9	3.55	1.12	22.94	1.36
18	C	14	0.5	4	57.61	1046.6	3.72	1.11	55.72	1.43
19	C	16	0.5	0.25	46.47	1142.7	3.29	1.11	15.49	0.68
20	C	16	0.5	0.5	46.86	1108.6	3.43	1.12	27.87	1.15
21	C	16	0.5	1	48.11	1078.9	3.47	1.11	59.72	1.55
22	C	16	0.5	2	48.90	1104.6	3.53	1.13	28.68	1.53
23	C	16	0.5	4	49.51	1099.9	3.59	1.20	25.14	0.73

Sample ^a	n	x	y	d_o^b (Å)	Surface ^c (m ² /g)	Intra-particle mesopore		Inter-particle pore		
						Size ^d (nm)	Volume ^d (cm ³ /g)	Size ^d (nm)	Volume ^d (cm ³ /g)	
24	C	16	0.3	4	48.64	1032.4	3.23	1.00	35.54	0.73
25	C	16	0.7	4	52.91	1011.6	3.61	1.06	54.96	1.71
26	C	16	1.1	4	55.90	1077.5	4.23	1.26	44.94	1.62
27	C	16	1.5	4	58.05	995.8	3.87	1.09	40.71	1.23
28	C	16	1.9	4	58.10	1106.8	3.88	1.21	49.80	1.25
29	E	12	0.5	4	-	964.2	4.13	0.90	31.19	1.39
30	E	14	0.5	0.5	53.32	1026.1	3.75	1.12	34.80	1.33
31	E	16	1.1	4	53.83	937.8	4.27	0.96	24.93	1.10

^a Surfactant evolution through: C = calcinations, E= chemical extraction after hydrothermal aging. ^b Position of the XRD low-angle peak. ^c Surface area according to the BET model. ^d Pore diameters and volumes calculated by using the BJH model on the adsorption branch of the isotherms.

TEM images in Figure 2 clearly illustrate how the nanoparticulated bimodal mesoporous (NBS) architecture typical of the UVM-7 silicas is preserved regardless the alkane used in the synthesis and its relative concentration (in the explored ranges). So, in all cases we can observe the presence of aggregates of pseudo-spherical mesoporous nanoparticles defining among them textural-type large voids. Also, the magnified images in the insets show the existence of white circular spots arranged under a pseudo-hexagonal disordered organization. Although these circular cross sections themselves cannot tell us anything about the pore tortuosity or their interconnection, they can be associated beyond any reasonable doubt to the presence of enlarged cylindrical-based mesopores.

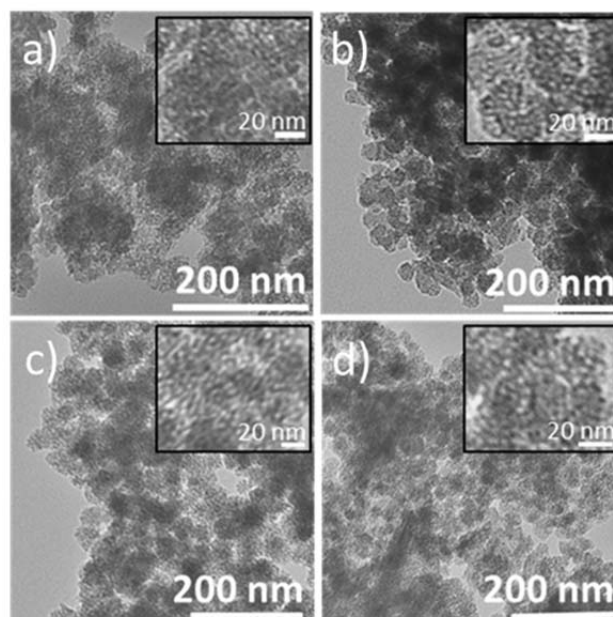


Figure 2. Representative TEM images of 0.5/ γ C_n-UVM-7(C) materials. **(a)** Sample 7 ($n=10$, $\gamma=2$), **(b)** Sample 10 ($n=12$, $\gamma=0.5$), **(c)** Sample 18 ($n=14$, $\gamma=4$) and **(d)** Sample 23 ($n=16$, $\gamma=4$).

Both the bimodal character of the final silicas and the swelling effect of the alkane molecules are further illustrated by the N₂-adsorption-desorption isotherms. All the curves clearly show two adsorption steps (Figure S1), what is consistent with the preservation of the hierarchic bimodal porosity typical of the UVM-7 materials. Thus, the first step, at a comparatively intermediate relative pressure ($P/P_0 < 0.8$) is characteristic of type IV isotherms and can be related to the condensation of N₂ inside the intra-nanoparticle mesopores. The second step, at a high relative pressure ($P/P_0 > 0.8$), corresponds to the filling of the textural large pores among the primary nanoparticles. BET calculations result in high surface area values (*ca.* $> 990 \text{ m}^2/\text{g}$) for all the 0.5/ γ C_n-UVM-7(C) materials (Table 1), and application of the BJH model systematically leads to pore size distributions exhibiting two rather well defined peaks. Shown in Figure 3 is a set of plots corresponding to the intra-nanoparticle mesopores. Regarding these latter, we can note firstly that practically all the solids present very high BJH pore volume values (*ca.* $> 0.90 \text{ cm}^3/\text{g}$, Table 1). In fact, irrespective of the alkane used, the calculated values of the pore volumes associated to the intra-particle mesopores (i.e., the pores generated by the template effect of the expanded micelles) vary in a relatively narrow range (*ca.* $0.90\text{--}1.20 \text{ cm}^3/\text{g}$). This notwithstanding, one can

appreciate certain trends in each series of alkanes. Thus, for a given alkane (n), the relative P/P_0 value for which the first N_2 -adsorption step is observed, shifts to higher values as the alkane nominal content (γ) increases (Figure S1). In turn, this directly results in the concomitant changes in the position of the maxima in the pore size distributions shown in Figure 3.

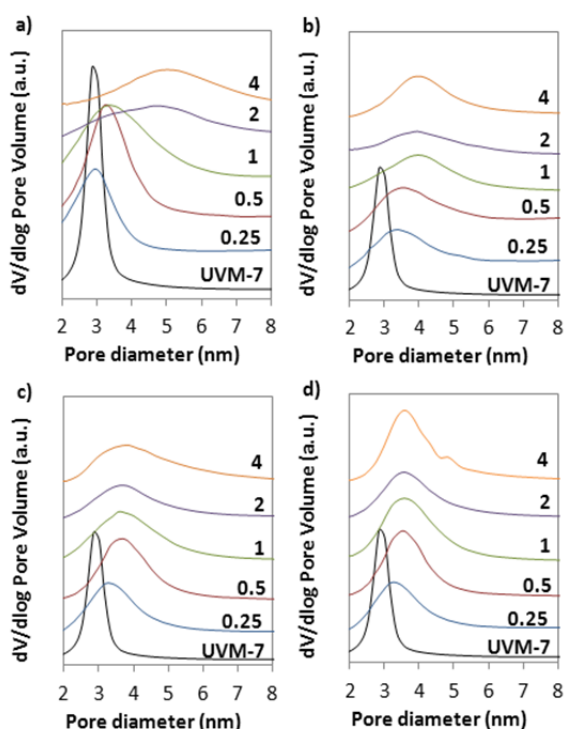


Figure 3. BJH pore size distributions (intra-particle mesoporosity) of 0.5/ γC_n -UVM-7(C) materials. **(a)** $n = 10$, Samples 4 to 8, **(b)** $n = 12$, Samples 9 to 13, **(c)** $n = 14$, samples 14 to 18, **(d)** $n = 16$, Samples 19 to 23. The values 0.25, 0.5, 1, 2 and 4 correspond to the non-expanded UVM-7 silica (Sample 1) is included for comparison.

The final result for each alkane ($n = 10, 12, 14, 16$) is the BJH intra-particle mesopore size evolution (expansion) displayed in Figure 4. For light alkanes ($n = 6, 8$; not included in Figure 4) no appreciable pore size expansion is detected (very likely due to their relatively low boiling points, which would lead to significant losses by evaporation during synthesis). These will be consequently ignored from now on. In contrast, in the case of the weightier alkanes ($n = 12, 14$ and 16), we can see (Figure 4) how the relative mesopore size expansion (as consequence of the swelling of the

micelles) is really significant for low alkane nominal contents ($y \leq 0.5$). Then, as y increases, it takes place in a more smooth way up to reach mesopore size values close to *ca.* 3.6-3.8 nm. On the other hand, the mesopore size evolution with the alkane nominal content (y) seems to occur more evenly in the case of the solids prepared using decane ($n = 10$) as expander. Without prejudice from the above, from a quantitative point of view, it looks that the swelling effect of the alkanes depends more on their nominal contents than on their chain lengths. Thus, regardless the alkane used (from $n = 10$ to 16), a comparable global swelling effect has been achieved through this way: we have reached intra-particle expanded mesopore sizes up to *ca.* 3.6-3.8 nm starting from the *ca.* 2.7 nm in the original ($x = 0.5$) UVM-7 materials.

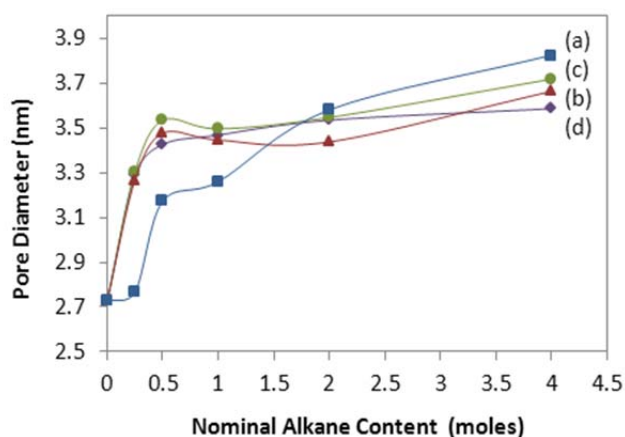


Figure 4. Intra-particle mesopore size evolution with the alkane nominal content. **(a)** $n = 10$, Samples 4 to 8, **(b)** $n = 12$, Samples 9 to 13, **(c)** $n = 14$, samples 14 to 18, **(d)** $n = 16$, Samples 19 to 23.

Considered as a whole, the XRD, TEM and porosimetry data are consistent with the preservation of cylindrical-based mesopores (independently from their tortuosity or interconnections) in the final UVM-7 modified (mesopore-expanded) silicas as a result of the template (CTMABr) swelling induced by the presence of alkanes ($n = 10$ to 16) in the reaction mixture. Although the quantitative expansion of the mesopore size to the border of 4 nm could be considered seemingly small, it really represents an important progress (the relative pore size expansion is around 37%) in terms of enabling the incorporation of certain biomolecules to the silica network (see below).

On the other hand, no definite trend is clearly discernible concerning the textural-type porosity. The values of both the pore-size and pore-volume vary in relatively wide ranges. In any case, in general, we can appreciate that the inter-particle pore size significantly decreases with respect to the conventional UVM-7 materials. Thus, exception made of some samples, the inter-particle pore sizes vary in the range between *ca.* 12 and 29 nm (*ca.* 59 nm in UVM-7). The relative dispersion is even greater in the case of the pore volumes (from *ca.* 0.4 to 1.6 cm³/g), with an average value close to 1 cm³/g. Without ignoring the inherent approximations in the calculation methods used (mainly for large P/P_0 values)³⁶, it is true that the pore volume values calculated for the solids synthesized using decane as swelling agent tend to be minor than in the remaining cases. This relatively lower porosity rate would keep a certain relationship with the XRD and TEM results. Thus, the corresponding TEM images in Figure 2 show comparatively small particles for this series of materials, what should be coherent with a decrease of the inter-particle spaces. At the same time, the number of mesopores per particle decreases as the particle size. It seems reasonable to assume that this lowering of diffraction motifs (i.e. mesopores) per particle, apart from the general loss of symmetry due to the swelling effect, favors the progressive widening of the XRD signal as the decane content increases (until practically disappear for $y = 2$, see Figure 1). However, in all cases, it is evident that the (approximate) size and shape of this secondary (textural) pore system will not be a real problem for diffusion of relatively large substrates (mainly by comparison with the intra-particle mesopore system).

After verifying the swelling effect of the different alkanes ($n = 10$ to 16) via a unified preparative procedure (in which $x = 0.5$), one might wonder whether a fine adjustment of the surfactant to alkane molar ratio could be critical for stabilizing more expanded micelles and, consequently, improving their porogen activity. If so, for each alkane, it should be still possible to optimize such relationship in order to get an even larger expansion of the mesopore size. To explore this possibility, as a proof of concept, we have prepared an additional set of materials in which the alkane (hexadecane) amount was maintained constant ($y = 4$, i.e. that corresponding to the maximum expansion of the mesopore size already observed) while the surfactant amount was varied according to the following molar ratio: 2 Si : 7 TEA: x CTMABr : 4

$C_nH_{n+2} : 180 H_2O$ ($0.3 \leq x \leq 1.9$; $n = 16$). The most significant results from XRD and porosimetry experiments for this series are gathered in Table 1.

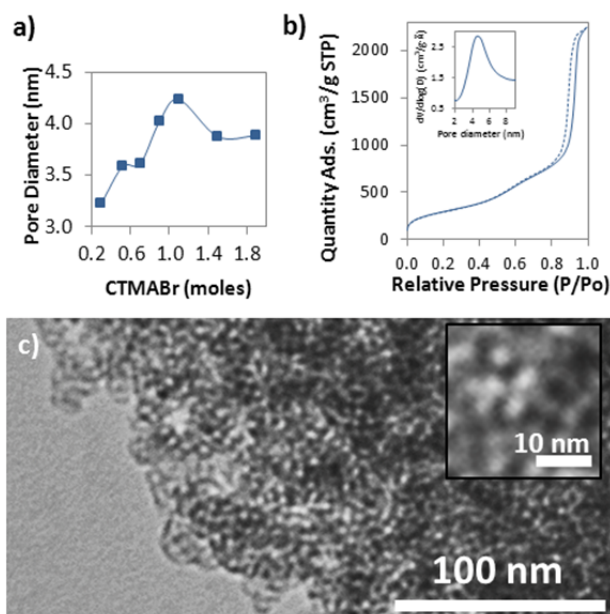


Figure 5. (a) Evolution of the BJH intra-particle mesopore size as the CTMABr nominal content increases for $\gamma=4$ constant value. (b) N₂ adsorption-desorption isotherm (including the BJH pore size distribution) and (c) TEM image of Sample 26 (1.1/4C16-UVM-7(C)).

As clearly shown in Figure 5a, using hexadecane as swelling agent, it becomes possible to expand the intra-particle mesopore size to values greater than 4 nm maintaining the UVM-7 type morphology (Figures 5b and c). Specifically, the BJH mesopore size increases with x up to a maximum (*ca.* 4.2 nm) for x *ca.* 1.1. A further increment of the amount of surfactant not only does not result in additional expansion but even leads to some mesopore size decrease. All suggests that analogous improved results could be achieved by singularizing the preparative procedure for each alkane, an issue that would require supplementary study but is beyond the scope of this report. In any case, it should be noted also that, in the case of hexadecane we are dealing with, the additional mesopore size expansion (*ca.* 17%) after optimizing the surfactant to alkane molar ratio has required more than double the amount of surfactant (for a given amount of Si) participating in the synthesis ($x = 1.1$ vs. $x = 0.5$), a factor that should be taken into account.

The limits of the mesopore expansion

When thinking about the conceptual simplicity of the process of swelling of micelles, and taking into account the large nominal amounts of alkanes involved in the syntheses (not only in our case, but also in others which have been previously described with similar goals)^{24,23,29}, it can be surprising the apparently small (in absolute value) mesopore expansion achieved. In an attempt to shed light on this fact, we have performed (for the first time, as far as we know) chemical analyses (see experimental section) of a representative set of mesostructured derivatives in order to determine the amounts of both surfactant and alkane really trapped in the silica framework. The analytical data corresponding to the solids synthesized using tetradecane and hexadecane as swelling agents are gathered in Table 2. As shown in Figure 6, the real molar proportions alkane/surfactant included in the mesostructure are far below their nominal values in the reaction mixture. Although there has been much conjecture about the location of alkanes in the swelled micelles (either in the core or in the palisade), what the analytical data make clear is that (regardless of the alkane location) micelles expansion is relatively small because the incorporation of alkane is significantly lower than expected (i.e. much less than the nominal one).

Table 2. Analytical data for the 0.5/yC_n-UVM-7(M) (n= 14, 16) as-synthesized materials.

Sample ^a		n	C _n /CTMABr nominal	C _n /CTMABr real ^b	Si/CTMABr real ^b
14	M	14	0.5	0.25	6.20
15	M	14	1	0.34	4.91
16	M	14	2	0.22	4.15
17	M	14	4	0.44	3.95
18	M	14	8	1.23	5.38
20	M	16	1	0.78	4.31
22	M	16	4	0.79	5.29
23	M	16	8	1.86	4.03

^a Mesostructured samples: M = mesostructured. ^b Values determined through chemical analysis.

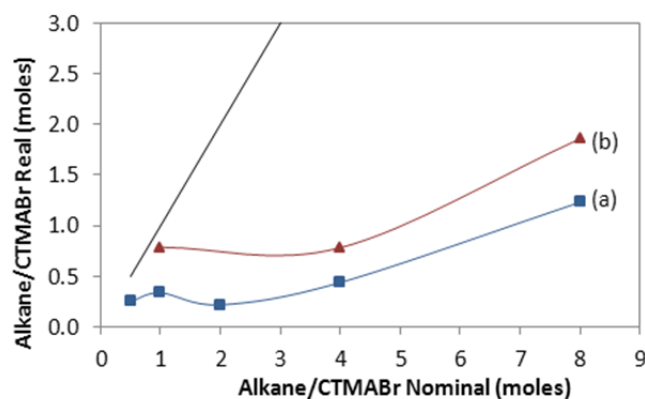


Figure 6. Nominal vs real alkane/CTMABr molar ratio for 0.5/ γ C_n-UVM-7(M) samples. **(a)** n= 14, **(b)** n= 16. The deviation from complete incorporation (straight black line) is very high.

At this point, it seems logical to ask why the amount of alkane inside the micelles is so limited. To improve our understanding of this, we have performed a baseline study on the reaction media in themselves (i.e. in the absence of the silica precursors). Thus, we have prepared four mixtures corresponding to the following molar ratios: 0 Si: 4 TEA: 0.5 CTMABr : γ C_nH_{n+2} : 180 H₂O (γ = 0, 0.5, 2, 4; n = 16). In line with the comments in the experimental section, except for γ = 0, all other mixtures appear like whitish suspensions after stirring. However, when they are left to stand for some hours, gradual phase segregation is observed. This situation is graphically shown in Figure 7c. As we can see, except for the mixture free of alkane (γ = 0), our reaction media (γ = 0.5, 2, 4) have separated in three different phases: two transparent (or almost transparent) phases above and below an intermediate translucent (whitish) phase. The bottom almost transparent phase, which is dominant in volume, must correspond to an essentially aqueous phase (triethanolamine and water are miscible and its molar ratio in the media is 4 TEA: 180 H₂O). The top layer, whose volume increases with the amount of swelling agent, must be an essentially organic (rich in alkane, which is immiscible with TEA) phase. The intermediate translucent layer, whose volume also increases with the alkane amount, can only consist of a bicontinuous microemulsion structure³⁸. To the extent that this phase separation (in the absence of silica) only occurs in the presence of alkane (it is not observed for γ = 0),

this observation must respond to the fact that water-surfactant-oil ternary systems are established.

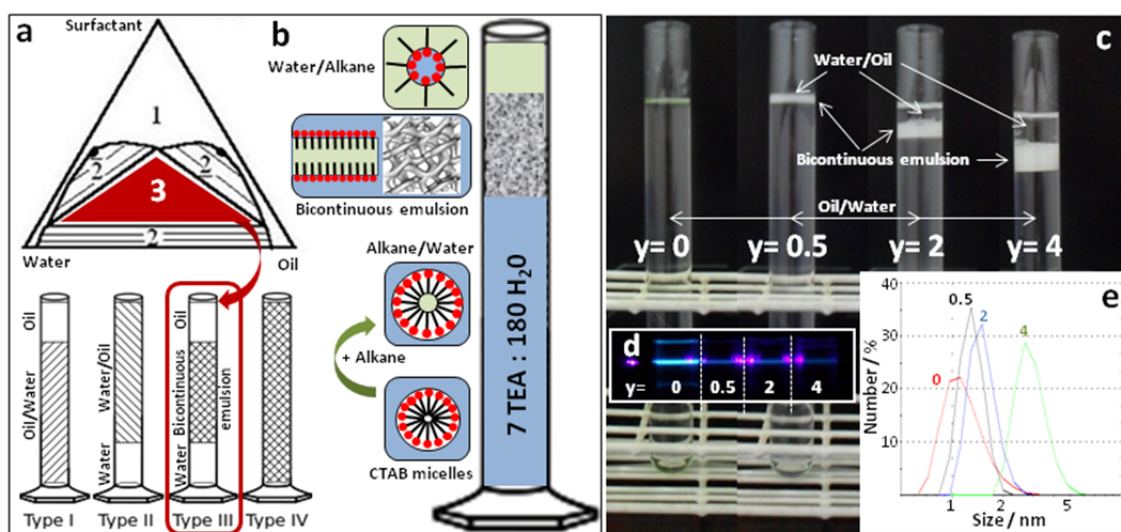


Figure 7. (a) Phase diagram typical of Winsor III ternary systems. (b) Scheme of the different phases in our reaction media. (c) Equilibrium phases of 0.5 CTMABr: y C_nH_{n+2}: 180 H₂O reaction mixtures at different ratios ($y=0, 0.5, 2, 4$) of alkane ($n=16$). (d) Tyndall effect for the lower layer (rich water phase) derived from 0.5 CTMABr: y C_nH_{n+2}: 180 H₂O reaction mixtures ($y=0, 0.5, 2, 4$). (e) DLS curves for the lower water rich phases with different hexadecane content ($y=0, 0.5, 2, 4$).

Several research studies have been published on this classical subject since the early 1900s³⁹⁻⁴¹. In particular, Winsor⁴² developed a systematic study and classification of the different structures of these ternary systems, especially for low surfactant concentrations. He noted four different behaviors, which labeled as Winsor I, II, III and IV (schematically shown in Figure 7a). The three components of a mixture of this kind only can lead to a single-phase (microemulsion) in the case where the surfactant concentration is very high with respect to those of oil and water (Winsor IV). The relatively low surfactant concentration we have used (0.5 CTMABr: y C_nH_{n+2}: 180 H₂O ($y=0, 0.5, 2, 4$)), together with the observation in our case of three-phase systems ($y \neq 0$), allows us to discard the Winsor IV behavior. In a similar way, the Winsor I and II arrangements, which correspond to two-phase systems (oil-in-water microemulsion and an extra oil layer [Winsor I] or water-in-oil and an extra water layer [Winsor II]), also can be discarded. Actually, the behavior observed in our reaction media only can

correspond to a Winsor III-like system. This typically consists of three different phases: 1) a middle layer, formed by a surfactant-rich microemulsion involving similar amounts of water and oil, and 2) two additional phases: one rich in water (bottom layer) and the other rich in oil (upper layer) that also contain the remaining surfactant (Figures 7b, c).

Under these premises, if we consider again our preparative procedure, the fact is that the translucent suspension of expanded micelles (reagent B) is really a complex three-phase system. When this is added over the silicon source dissolution (reagent A; dissolution of silatranes in TEA), it is reasonable to assume that silatranes will mix primarily with the water-rich phase (TEA and water are miscible), in a lower extension with the surfactant-rich bicontinuous phase (aqueous portion), and must remain practically unmixed with the alkane-rich phase. If so, the expanded micelles whose assembling with siliceous oligomers really triggers the formation of the mesostructures must be present in the aqueous phases. In practice, as shown in Figure 7d, we can see that Tyndall effect occurs (water-rich phase) in all the reaction media we have selected ($y = 0, 0.5, 2$ and 4). DLS analyses show that this effect is associated with the existence of supramolecular entities in the size range 1-4 nm (Figure 7e). Also, the size of these entities (compatible with the dimension of CTMA⁺-based micelles) increases with the alkane proportion. Probably, the presence of TEA (acting as an alcoholic co-solvent) favors the formation of expanded micelles (some alkane in water) in contrast to what happens for pure Type III Winsor systems, where the bottom water layer does not contain oil nor surfactant. Moreover, the fact that the nominal ratio of reactants (2Si: 0.5 CTMABr) is roughly maintained in the mesostructured materials (according to the analytical data the average Si/surfactant molar ratio is *ca.* 4.78 (Table 2)), indicates that silica oligomers consume a large proportion of the surfactant species.

Regardless the specific reaction path (displacement of CTMA⁺-based entities from the bicontinuous microemulsion to the water-rich phase as the formation of the mesostructure advances or entering of silica oligomers in the aqueous part of the bicontinuous phase to capture CTMA⁺-based species at the alkane-water interphase), silica precipitation leads to the disappearance of the white bicontinuous intermediate phase due to the nearly complete segregation of surfactant from the Winsor III-like system. Therefore, the supernatant final system is a biphasic mixture of a water-rich phase and the excess of alkane that is not trapped in the micelles.

In short, the very nature of the reaction media allows explain, besides the swelling processes induced by alkanes under mild conditions, how is prevented the trapping of large quantities of alkane in (swelled) micelles. While this approach is consistent with the subsequent isolation of the here described UVM-7-like mesopore-expanded derivatives, it also explains the thermodynamic difficulties for expanding the mesopore sizes beyond a certain limit, as observed in practice. In fact, we think that the Winsor III-like behavior of the reaction media is in the origin of the relatively poor results (concerning mesopore sizes) previously achieved for materials preserving pore systems constructed by packing of cylindrical (straight or worm type) mesopores derived from micellar aggregates^{18,19,23,24,29}.

Chemically extracted materials

As commented above, the preparation of the final porous x/yC_n -UVM-7 materials requires removing the surfactant from the as-synthesized intermediate mesostructured powders (x/yC_n -UVM-7(M)). So far we have been referring to x/yC_n -UVM-7(C) materials for which surfactant removal was carried out by controlled pyrolysis. It is well known that this type of treatment leads to a relatively high condensation of the silica walls, which involves new siloxane links at the cost of reducing the relative proportion of terminal silanol groups⁴³. Nonetheless, there is a diversity of applications for which it is desirable to retain a high density of silanol groups on the surface of the silica, something that normally is favored by mild chemical extraction of the surfactant. In principle, it was a bit surprising that the extraction conditions (60 °C and acidified ethanol) that worked well (no mesostructure deterioration) for the conventional UVM-7 materials^{15,16}, gave rise to significant degradation or collapse of the x/yC_n -UVM-7(M) mesostructures. In fact, as shown in Figure S2, we have recurrently observed loss of the bimodal porosity and a significant decrease in the surface area and pore volume of the final solids after such mild treatment. In our opinion, the characteristics that could most likely be contributing to the comparative weakness (i.e. to the relative inconsistency of the siliceous frameworks because of insufficient Si-O-Si condensation) of the x/yC_n -UVM-7 (M) mesostructures (with regard to those for conventional UVM-7 materials) would be the

small particle size along with the enlarged mesopore sizes. In any case, the experimental observation (mesostructure degradation) clearly suggests a (comparatively) low silica condensation degree in the x/yC_n -UVM-7 (M) mesostructures. To progress in this point, we have performed a ^{29}Si MAS NMR spectroscopic study. Shown in Figure 8 are the ^{29}Si NMR spectra of a representative set of mesostructured samples. All samples show spectra typical of mesostructured/mesoporous silicas exhibiting three partially overlapped signals falling in the *ca.* -90 to -120 ppm range, which are habitually associated to Q^2 (*ca.* -90 ppm), Q^3 (*ca.* -100) and Q^4 (*ca.* -110) Si-sites. The results of the deconvolution of the spectra in Figure 8 are gathered in Table 3.

Table 3. Deconvolution of the ^{29}Si MAS NMR spectra of selected x/yC_n -UVM-7(M) ($n= 16$) as-synthesized materials.

Sample ^a	x	y	Q ² (%)	Q ³ (%)	Q ⁴ (%)	Q ⁴ /(Q ² +Q ³)	
1	M	0.5	0	6.3	42.6	51.1	1.04
21	M	0.5	1	9.8	46.9	43.3	0.76
26	M	1.1	4	7.7	44.8	47.5	0.90
26	H	1.1	4	10.9	33.8	55.3	1.23
26	C	1.1	4	5.1	28.5	66.4	1.97
26	E	1.1	4	9.0	38.1	52.9	1.12

^a M = mesostructured sample, H= hydrothermally aged mesostructured sample, C= calcined sample, and E= chemically extracted sample (after the hydrothermal aging).

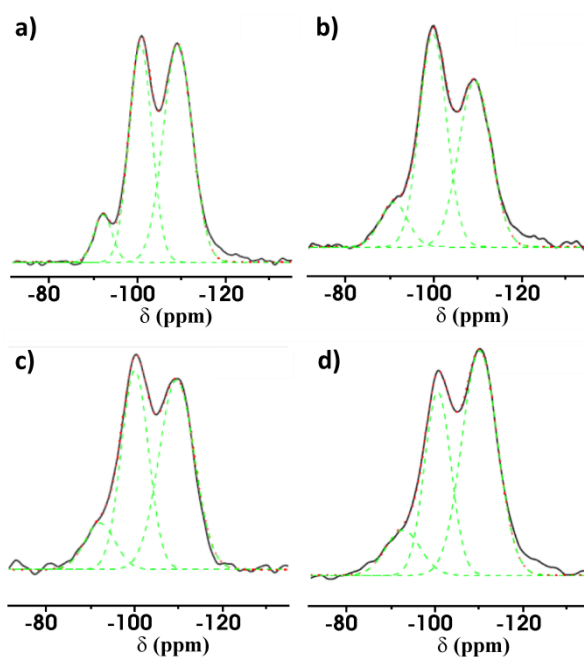


Figure 8. ^{29}Si NMR spectra of selected mesostructured $x/y\text{C}_{16}\text{-UVM-7(M)}$ samples **(a)** $x = 0.5$, $y = 0$ (Sample 1), **(b)** $x = 0.5$, $y = 1$ (Sample 21), **(c)** $x = 1.1$, $y = 4$ (Sample 26) and **(d)** the hydrothermally aged Sample 26 ($1.1/4\text{C}_{16}\text{-UVM-7(H)}$).

As can be noted, the spectra of the as-synthesized mesostructured solids with expanded mesopores (Samples 21(M) and 26(M)) reflect the presence of a relatively low proportion of Q^4 Si sites, with $\text{Q}^4/\text{Q}^2+\text{Q}^3$ ratios lower than *ca.* 0.9. Chemical extraction produces mesostructure degradation in these cases. It seems that the lower limit of the proportion of Q^4 sites ($\text{Q}^4/\text{Q}^2+\text{Q}^3$) in the framework conferring the necessary stability to the mesostructure is close to 1.0, which is what is observed for that corresponding to the conventional UVM-7 material (Sample 1(M)). Likewise, as expected, the hydrothermal aging procedure we have applied (experimental section) allows increasing the silica condensation degree (Sample 26(H): $\text{Q}^4/\text{Q}^2+\text{Q}^3$ *ca.* 1.23). In practice, the stability of the hydrothermally aged samples is sufficient enough to resist the surfactant chemical extraction without mesostructure degradation. Therefore, it becomes possible to synthesize pore expanded UVM-7-like porous silicas with a density of terminal silanol groups higher than those present in the corresponding calcined solids. Let us see. Consider for example the (calcined) Sample 26, which is that having the greatest mesopore size we have synthesized (Table 1). We have indicated

that its as-prepared parent mesostructure (26(M): Q^4/Q^2+Q^3 *ca.* 0.90, Table 3 and Figure 8) does not resist chemical extraction (Figure S2). On the other hand, after pyrolysis, the relative proportion of terminal silanol groups in the resulting porous material becomes significantly reduced because of the induced condensation (26(C): Q^4/Q^2+Q^3 *ca.* 1.97, Table 3 and Figure S3). In contrast, chemical extraction of the surfactant from the hydrothermally aged mesostructure (26(H): Q^4/Q^2+Q^3 *ca.* 1.23, Table 3 and Figure 8) occurs without mesostructure degradation and, as expected, does not involve any remarkable change concerning the silanol groups in the resulting porous silica (26(E): Q^4/Q^2+Q^3 *ca.* 1.12, Table 3 and Figure S3).

The most relevant data of a set of materials prepared by chemical extraction of the surfactant from hydrothermally aged mesostructures have been included in Table 1. Shown in Figures S4 and S5 are the N₂-adsorption-desorption isotherms and TEM images, respectively, corresponding to some selected samples after surfactant evolution. As can be observed, both the bimodal porous nature (including intra-particle mesopore expansion) and the characteristic UVM-7-like architecture are preserved. It does not seem unreasonable to assume that this type of solids would show similar trends to those discussed for the calcined samples.

Drug and enzyme charge

In order to evaluate the possible improvement of the performance towards mass-transfer of the UVM-7-like architecture after mesopore expansion, we have realized a preliminary study of the adsorption by different matrices of a small drug (ibuprofen) and two enzymes (lysozyme and trypsin) of different size, all of which have already been used as models for inclusion in mesoporous materials. In particular, mesoporous silicas have a series of features (such as the presence of regular and adjustable pore systems, high surface areas and pore volumes, among others) that could make them adequate for the storage and release of relatively large substrates of biomedical interest⁴⁴⁻⁴⁶.

Vallet-Regí and col.⁴⁷ published the first complete study on delivery systems based on MCM-41 silicas (sorption and release of ibuprofen, a non-steroidal anti-inflammatory). Later, other unimodal mesoporous materials (like HMS or SBA-15

silicas) also have been utilized for designing ibuprofen delivery systems⁴⁴⁻⁴⁶. As a reference, the highest relative amounts of ibuprofen incorporated into unimodal mesoporous silicas reported to date range approximately from 30% to 59% (by weight, referred to the support), depending on the experimental protocol. In this context, it was suggested that hierarchical porous materials could open new prospects for applications due to their presumably enhanced accessibility across large pores, which should result in higher uptake levels⁴⁸. In fact, we have recently shown how the hierarchic pore architecture typical of the UVM-7 silicas (particularly their nano-scale mesopore length) provides a very open and accessible organization facilitating (in comparison to MCM-41 derivatives) the drug charge (and its posterior delivery) inside the cylindrical mesopores³⁴. What we want to do now is to consider the effect of combining the short length of their mesopores with the size expansion induced by alkanes. To this end, we have used the same protocol previously optimized and described in detail for the conventional UVM-7 silicas³⁴. This protocol was designed to avoid ibuprofen segregation ensuring, as far as possible, that ibuprofen is admitted at the silica surface and confined inside the pores. The supports have been charged by impregnation with ibuprofen solutions (0.47 and 0.58 M) in n-hexane (at 25°C) during relatively short contact times (*ca.* 4 h). We have tried also to increase the ibuprofen uptake by applying successive impregnation cycles with increasingly concentrated solutions (0.47 M + 0.58 M). The silica supports tested have been the conventional UVM-7 (Sample 1) and that having the greatest mesopore size we have synthesized (Sample 26). In both cases, for comparative purposes, we have used calcined mesoporous powders in order to have a similar proportion of silanol groups at the silica surface. This aspect is really important insomuch as the drug-support interaction is mediated by the Si-OH groups³⁴. As the data in Table 4 shown, the ibuprofen uptake by the support, which increases as the drug concentration in the carrier, is appreciably higher for the mesopore-enlarged silica (Sample 26). Besides this, the use of successive impregnation cycles results in an additional increase of the drug charge, which reaches a high relative level (*ca.* 64.5 %). The typical UVM-7-morphology is maintained after charging of the drug (Figure S6).

Table 4. Analytical and physical data for the drug-silica composites.

Sample ^a	Treatment ^b	Ibuprofen ^c (%)	Surface ^d (m ² /g)	Inter-particle pore	
				Size ^e (nm)	Volume ^e (cm ³ /g)
1	0.47	39.7	144.2	29.9	0.72
1	0.58	42.4	120.3	30.1	0.62
26	0.47	48.7	158.3	47.8	1.22
26	0.58	50.3	154.1	44.2	0.93
26	0.47+0.58	64.5	88.2	41.5	0.76

^a Calcined (C) samples. ^b Concentrations of the drug solutions. ^c Drug content. ^d Surface area according to the BET model. ^e Pore diameters and volumes calculated by using the BJH model on the adsorption branch of the isotherms.

Together with the analytical data, the changes in the N₂ adsorption-desorption isotherms (Figure S7, Table 4) suggest that effective incorporation of the drug into the supports occurs. Indeed, the primary mesopore system disappears after ibuprofen uptake in all cases, what means that ibuprofen molecules have already filled (or blocked) all the intra-nanoparticle mesopores. In contrast, the inter-particle pore system remains partially empty. Thus, the samples processed with a single impregnation step (with solutions 0.47 or 0.58 M) still present BET surface area values (120-150 m²/g) typical of UVM-7 materials with closed mesopores. When samples impregnated with a solution of the same concentration are compared (Table 4), it can be noted that the material with expanded pores (Sample 26) incorporates an ibuprofen amount *ca.* 20% higher than the UVM-7 silica (Sample 1). Interestingly, the intra-particle mesopore volume of the pore expanded material (1.26 cm³/g) also is a *ca.* 20% higher than that of the UVM-7 silica (1.02 cm³/g). This trend is clearly consistent with an enhanced accessibility to the expanded mesopores (intra-particle). However, the incorporation of ibuprofen occurs simultaneously in the two pore systems and, in fact, we also observe a progressive decrease in the textural pore volume with the drug content. What is clear is that the *ca.* 10% of additional drug incorporated when using successive impregnation cycles will be necessarily located in

the inter-particle voids, what agrees with the decrease of both the volume and size of these large voids (as well as with the marked lowering of the BET surface area of the composite).

Adsorption onto a silica matrix is one of the most basic methods of enzyme immobilization^{49,50}. It involves surface physical interactions support-enzyme usually driven by combined hydrogen bonding and electrostatic forces. Together with the size and shape of the enzyme, the adsorption processes are highly dependent on the isoelectric point of both the enzyme and the support and, consequently, the enzyme-silica interactions are strongly influenced by the pH^{49,51}. The great difference between the isoelectric point of the silica (3.6) and those of the enzymes we have tested (11.4 and 10.5 for lysozyme and trypsin, respectively) allows disposing of a wide pH range for the electrostatic immobilization. We have selected pH = 6.0 as a compromise value favoring the protein-silica interaction over the repulsive neighboring enzyme-enzyme interactions. Although sometimes obviated, the size matching between pore and enzyme is a mandatory criterion in order to account for the location of the guest inside or at the surface of the support⁵¹. In practice, low load levels are predictable for enzymes whose size (hydrodynamic diameter) is larger than the pore size due that only adsorption on the external surface is feasible. On the contrary, enzymes with sizes smaller than those of the pores also could result included inside the host structure. However, a certain leaching might occur when the enzyme size is considerably smaller than the pore void. Accordingly, we have selected two different enzymes, lysozyme and trypsin, in order to analyze the possible advantages of using matrices with enlarged mesopores for enzyme immobilization. Lysozyme has a shape and size (is a globular enzyme with a hydrodynamic diameter slightly lower than *ca.* 3 nm)⁴⁹ adequate for its inclusion even in the intra-particle mesopores of conventional (non-expanded) UVM-7 silicas³⁴. On the contrary, the size of the weightier globular trypsin (*ca.* 3.7 nm)⁴⁹ only would allow its inclusion inside the intra-particle mesopores of some expanded UVM-7-like derivatives. Therefore, considering both enzymes together, we will have a good “local probe” to evaluate the intra-nanoparticle mesopore accessibility.

Shown in Figure 9 is the evolution of the lysozyme and trypsin uptakes with time for different supports. Figure 9a compares the lysozyme adsorption for three

different supports: MCM-41, conventional (non-expanded) UVM-7 (Sample 1), and the mesopore-enlarged 1.1/4C₁₆-UVM-7 silica (Sample 26). For comparative purposes, all the supports have been prepared by calcination at 550°C in order to get silica surfaces with similar proportions of silanol groups. In all cases, the enzyme/mesopore size adequacy would allow lysozyme incorporation into the intra-particle mesopores. However, the adsorption isotherms show significant differences which, in the present case, must be firstly related with the support morphology. Thus, the MCM-41 material, which consists of comparatively large micrometric particles, is the one with the lowest uptake capacity. For this material, lysozyme adsorption occurs slowly and the maximum loading level (*ca.* 105 mg/g) requires relatively long contact times. Insofar as the mesopore sizes of MCM-41 (*ca.* 2.68 nm) and Sample 1 (*ca.* 2.71 nm) are similar, it seems reasonable to consider that the relatively large length of the mesopores in MCM-41 (due to particle size) is a diffusion obstacle to the guest enzyme, which may be responsible for both the low adsorption capacity and the long contact time required in this solid to reach equilibrium. It should be noted that the charge level we have achieved (under our experimental conditions) is comparable to others reported in previous publications when working at similar pH values and using analogously treated MCM-41 materials (without mesopore expansion) as inorganic supports⁵². The use of UVM-7-like nanoparticulated silicas as supports entails a significant increase of the total lysozyme adsorbed for shortened contact times (in comparison with MCM-41). Moreover, these effects are clearly more pronounced as the size of the intra-particle mesopores increases. Thus, the mesopore size expansion from *ca.* 2.71 nm (Sample 1) to *ca.* 4.23 nm (Sample 26) carries with it an increase of the charge level close to 100% (from *ca.* 200 to 394 mg/g, respectively). Also, as suggested above, the isotherm of the lysozyme adsorption on Sample 26 indicates some leaching for relatively long contact times. Apart from the latter, given that we are now dealing with supports (Samples 1 and 26) constructed from particles of comparable size and having similar textural porosity, it can be assumed that such a large growth in the lysozyme adsorption is really related with the expansion of the intra-particle mesopore system, whose BJH pore volume increases from 1.02 (Sample 1) to 1.26 (Sample 26) cm³/g. In fact, taking into account the molecular weight of the lysozyme and its molecular volume (17.8 nm³)⁴⁹, the mentioned increase in the capability of adsorption of lysozyme by the

Sample 26 (*ca.* 200 mg/g) would correspond to a volume of *ca.* 0.15 cm³/g, which is compatible with (i.e. lower than) the corresponding increase of the intra-particle pore volume (0.24 cm³/g) in the expanded silica (Sample 26). It has to be noted that the lysozyme charge level we have achieved is similar to that described by Kao et al.²⁹ when other M41s nanoparticulated silicas with enlarged pores of 5.6 nm were used as supports. In both cases, the readiness and efficiency towards lysozyme capture are comparable to those reported for Rod-SBA-15 silica supports (with a mesopore size of 6.8 nm)⁵³. All indicates that the performance improvement of the nanoparticulated silicas (NBS) with regard to the micrometric MCM-41 is due to the reduction in length of the mesopores, with a subsequent increase in the number of pore entrances. In practice, a similar influence of the morphology of the support was proposed when comparing Rod-SBA-15 (1-2 mm in length) with Con-SBA-15 (ten mm in length)⁵⁴.

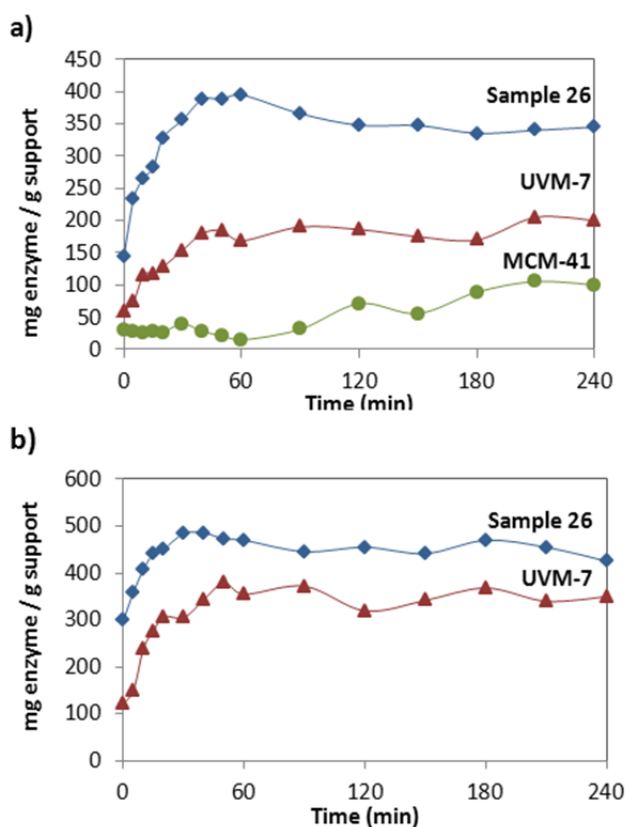


Figure 9. Enzyme adsorption evolution with contact time for (a) lysozyme and (b) trypsin by using as support Sample 26, Sample 1 (UVM-7) and MCM-41 silica (for comparative purposes).

The evolution of the trypsin uptake with time is shown in Figure 9b. In this case, adsorption on the Sample 1 (380 mg/g) takes place necessarily only in the inter-particle pore system. The trypsin molecules would interact through silanol groups at the outer surface of the nanoparticles, what can produce also a significant blockage in the mesopores entries. In fact, the trypsin-UVM-7 composite has a BET surface area of 145.9 m²/g and a BJH pore volume of 0.63 cm³/g. These values, which are in the ranges typical of UVM-7 materials with closed mesopores, should correspond to the outer surface of the nanoparticles and mainly textural voids, though a certain contribution of some unblocked intra-particle mesopores cannot be completely discarded. The adsorption level of trypsin in the mesopore-expanded material (Sample 26) significantly increases, reaching a maximum relative value of *ca.* 485 mg/g. It is readily assumable that much of the additional enzyme incorporated (*ca.* 105 mg/g) will be included into intra-particle mesopores. Thus, an approximate calculation as performed for lysozyme indicates that the volume required to accommodate such additional amount of trypsin (molecular volume 54.76 nm³)⁴⁹ is 0.16 cm³/g, which is lower than (and consequently compatible) the corresponding increase of the intra-particle pore volume in the expanded silica (Sample 26) with regard to the Sample 1. Similar trypsin charge levels have been reported for MCM-41 silicas with expanded mesopores (in the 4-5 nm range)⁵⁵. The trypsin adsorption capacity of Sample 26 only is surpassed by SBA-15-type silicas⁵⁶.

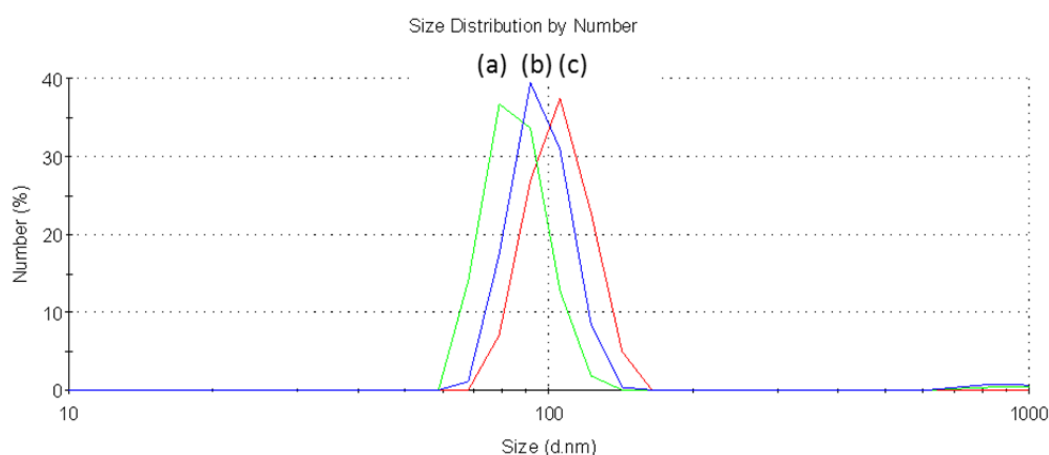


Figure 10. DLS particle size distributions of (a) Sample 23, (b) Sample 26 and (c) Sample 22, after ultrasound treatment.

Once checked the mass-transfer improvement for mesopore-expanded UVM-7-like materials, it is important to confirm that the grain (or particle aggregates) size in these solids is in the range 30-200 nm appropriate for certain biomedical applications⁵⁷. Accordingly, we have prepared relatively high concentrated (500 µg/mL) suspensions of a representative set of our mesoporous samples in water. The solids are easily suspended after treatment during one minute in a standard ultrasound bath. DLS measurements allow us to determine the average size of the suspended grains (Figure 10). In all cases, we observe the stabilization of aggregates with average sizes around 100 nm (78.8, 91.3 and 105.7 nm for Samples 23, 26 and 22, respectively). Now, we can make a rough estimation of the number of individual nanoparticles that would contain grains (suspended) of *ca.* 90 nm (Sample 26). Thus, in this case, an average nanoparticle diameter of *ca.* 30 nm can be considered as representative from the TEM image in Figure 5. The highest possible aggregation would correspond to a close packing of nanoparticles (space filling of 76%). From this, we can estimate that the observed suspended grains of *ca.* 90 nm would be constructed by aggregation of around 20 individual nanoparticles. It can be concluded that the continuous siliceous network involving the two pore systems typical of the UVM-7-like materials are preserved in the grains and, consequently, both intra- and inter-particle pores really are available to host some drugs, biomolecules or other species of interest for nanomedicine applications.

Concluding remarks

Nanoparticulated bimodal mesoporous silicas (NBS) have proved to constitute adequate supports in a variety of applications requiring enhanced accessibility to the active site. When put into play pore systems hierarchically structured, provided that access to the small pores occurs through textural voids, the shortening of the length of the small intra-particle pore at the nano-scale range leads to a reduction of effects due to possible pore blocking. Under this assumption, mass transfer processes throughout the support could be further improved by enlarging the intra-nanoparticle mesopore cross section. We have explored this possibility in the well characterized UVM-7 silicas by using alkanes as swelling agents, what has allowed us to expand their typical

mesopore sizes from *ca.* 2.71 up to *ca.* 4.23 nm (*ca.* 56%). This results in greater capacity to incorporate guest species, including bulky substrates. In any case, this has been possible by judiciously adapting our preparative protocols after a careful rereading of classical concepts of the chemistry of colloids. It is shown that the usually multiphase nature of the reaction media associated to the use of swelling agents in surfactant-assisted procedures, imposes restrictions on the possible expansion of the pores, a point that had not been typically treated in detail.

Acknowledgment

This research was supported by the Ministerio de Economía y Competitividad (MAT2012-38429-C04-03) and the Generalitat Valenciana (PROMETEO/2009/108). A.M. thanks MEC for a FPI fellowship. The authors thank the institutional support from VLC/CAMPUS (MCIs “Sensores y Técnicas Analíticas Rápidas” and “Medicina Regenerativa”).

References

1. Kresge, C. T.; Roth, W. J. *Chemical Society Reviews* **2013**, *42*, 3663-3670.
2. Beck, J. S.; Vartuli, J. C.; Roth, W. J.; Leonowicz, M. E.; Kresge, C. T.; Schmitt, K. D.; Chu, C. T. W.; Olson, D. H.; Sheppard, E. W.; McCullen, S. B.; Higgins, J. B.; Schlenker, J. L. *Journal of the American Chemical Society* **1992**, *114*, 10834-10843.
3. Moeller, K.; Bein, T. *Chemical Society Reviews* **2013**, *42*, 3689-3707.
4. Perego, C.; Millini, R. *Chemical Society Reviews* **2013**, *42*, 3956-3976.
5. Li, Z.; Barnes, J. C.; Bosoy, A.; Stoddart, J. F.; Zink, J. I. *Chemical Society Reviews* **2012**, *41*, 2590-2605.
6. Deng, Y.; Wei, J.; Sun, Z.; Zhao, D. *Chemical Society Reviews* **2013**, *42*, 4054-4070.
7. Kruk, M. *Accounts of Chemical Research* **2012**, *45*, 1678-1687.
8. Soler-illia, G. J. D.; Sanchez, C.; Lebeau, B.; Patarin, J. *Chemical Reviews* **2002**, *102*, 4093-4138.
9. Cao, L.; Man, T.; Kruk, M. *Chemistry of Materials* **2009**, *21*, 1144-1153.
10. Kruk, M.; Cao, L. *Langmuir* **2007**, *23*, 7247-7254.
11. Johansson, E. M.; Ballem, M. A.; Cordoba, J. M.; Oden, M. *Langmuir* **2011**, *27*, 4994-4999.
12. Sun, J. M.; Zhang, H.; Ma, D.; Chen, Y. Y.; Bao, X. H.; Klein-Hoffmann, A.; Pfander, N.; Su, D. S. *Chemical Communications* **2005**, 5343-5345.
13. Wu, S.-H.; Mou, C.-Y.; Lin, H.-P. *Chemical Society Reviews* **2013**, *42*, 3862-3875.
14. Han, Y.; Ying, J. Y. *Angewandte Chemie-International Edition* **2005**, *44*, 288-292.
15. Huerta, L.; Guillem, C.; Latorre, J.; Beltran, A.; Martinez-Manez, R.; Marcos, M. D.; Beltran, D.; Amoros, P. *Solid State Sciences* **2006**, *8*, 940-951.
16. El Haskouri, J.; Morales, J. M.; de Zarate, D. O.; Fernandez, L.; Latorre, J.; Guillem, C.; Beltran, A.; Beltran, D.; Amoros, P. *Inorganic Chemistry* **2008**, *47*, 8267-8277.
17. Wang, S.; Shi, Y.; Ma, X.; Gong, J. *Acs Applied Materials & Interfaces* **2011**, *3*, 2154-2160.
18. Fukuoka, A.; Kikkawa, I.; Sasaki, Y.; Shimojima, A.; Okubo, T. *Langmuir* **2009**, *25*, 10992-10997.
19. Lefevre, B.; Galarneau, A.; Iapichella, J.; Petitto, C.; Di Renzo, F.; Fajula, F.; Bayram-Hahn, Z.; Skudas, R.; Unger, K. *Chemistry of Materials* **2005**, *17*, 601-607.
20. Luechinger, M.; Pirngruber, G. D.; Lindlar, B.; Laggner, P.; Prins, R. *Microporous and Mesoporous Materials* **2005**, *79*, 41-52.
21. Jana, S. K.; Nishida, R.; Shindo, K.; Kugita, T.; Namba, S. *Microporous and Mesoporous Materials* **2004**, *68*.

22. Kleitz, F.; Blanchard, J.; Zibrowius, B.; Schuth, F.; Agren, P.; Linden, M. *Langmuir* **2002**, *18*, 4963-4971.
23. Blin, J. L.; Otjacques, C.; Herrier, G.; Su, B. L. *Langmuir* **2000**, *16*.
24. Blin, J. L.; Su, B. L. *Langmuir* **2002**, *18*, 5303-5308.
25. Kruk, M.; Jaroniec, M.; Sayari, A. *Microporous and Mesoporous Materials* **2000**, *35-6*, 545-553.
26. Fuertes, A. B.; Valle-Vigon, P.; Sevilla, M. *Journal of Colloid and Interface Science* **2010**, *349*, 173-180.
27. Kim, M.-H.; Na, H.-K.; Kim, Y.-K.; Ryoo, S.-R.; Cho, H. S.; Lee, K. E.; Jeon, H.; Ryoo, R.; Min, D.-H. *Acs Nano* **2011**, *5*, 3568-3576.
28. Zhang, J.; Li, X.; Rosenholm, J. M.; Gu, H.-c. *Journal of Colloid and Interface Science* **2011**, *361*.
29. Kao, K.-C.; Mou, C.-Y. *Microporous and Mesoporous Materials* **2013**, *169*, 7-15.
30. El Haskouri, J.; de Zarate, D. O.; Guillem, C.; Latorre, J.; Caldes, M.; Beltran, A.; Beltran, D.; Descalzo, A. B.; Rodriguez-Lopez, G.; Martinez-Manez, R.; Marcos, M. D.; Amoros, P. *Chemical Communications* **2002**, 330-331.
31. Perez-Cabero, M.; Hungria, A. B.; Morales, J. M.; Tortajada, M.; Ramon, D.; Moragues, A.; El Haskouri, J.; Beltran, A.; Beltran, D.; Amoros, P. *Journal of Nanoparticle Research* **2012**, *14*, 12.
32. Cabrera, S.; El Haskouri, J.; Guillem, C.; Latorre, J.; Beltran-Porter, A.; Beltran-Porter, D.; Marcos, M. D.; Amoros, P. *Solid State Sciences* **2000**, *2*, 405-420.
33. Scott, G. V. *Analytical Chemistry* **1968**, *40*, 768-&.
34. Burguete, P.; Beltran, A.; Guillem, C.; Latorre, J.; Perez-Pla, F.; Beltran, D.; Amoros, P. *Chempluschem* **2012**, *77*, 817-831.
35. Smith, P. K.; Krohn, R. I.; Hermanson, G. T.; Mallia, A. K.; Gartner, F. H.; Provenzano, M. D.; Fujimoto, E. K.; Goetze, N. M.; Olson, B. J.; Klenk, D. C. *Analytical Biochemistry* **1985**, *150*, 76-85.
36. Rouquerol, F.; Rouquerol, J.; Sing, K. S. W.; Llewellyn, P.; Maurin, G. *Adsorption by Powders and Porous Solids. Principles, Methodology and Applications.* : Amsterdam, 2014.
37. Laughlin, R. G. *The Aqueous Phase Behavior of Surfactants*: San Diego, 1994.
38. Moon, D.-S.; Lee, J.-K. *Langmuir* **2012**, *28*, 12341-12347.
39. Smith, E. L. *Journal of Physical Chemistry* **1931**, *36*, 1401-1418.
40. Wellman, V. E.; Tartar, H. *Journal of Physical Chemistry* **1929**, *34*, 379-409.
41. Newman, F. R. *Journal of Physical Chemistry* **1913**, *18*, 34-54.
42. Winsor, P. A. *Transactions of the Faraday Society* **1948**, *44*, 376-398.
43. Iller, R. K. *The Chemistry of Silica. Solubility, Polymerization, Colloid and Surface Properties and Biochemistry.*: New York, 1979.
44. Vallet-Regi, M.; Balas, F.; Arcos, D. *Angewandte Chemie-International Edition* **2007**, *46*, 7548-7558.
45. Wang, S. *Microporous and Mesoporous Materials* **2009**, *117*, 1-9.

46. Manzano, M.; Colilla, M.; Vallet-Regi, M. *Expert Opinion on Drug Delivery* **2009**, *6*, 1383-1400.
47. Vallet-Regi, M.; Ramila, A.; del Real, R. P.; Perez-Pariente, J. *Chemistry of Materials* **2001**, *13*, 308-311.
48. Yuan, Z. Y.; Su, B. L. *Journal of Materials Chemistry* **2006**, *16*, 663-677.
49. Hartmann, M. *Chemistry of Materials* **2005**, *17*, 4577-4593.
50. Zhou, Z.; Hartmann, M. *Chemical Society Reviews* **2013**, *42*, 3894-3912.
51. Tran, D. N.; Balkus, K. J., Jr. *Acs Catalysis* **2011**, *1*, 956-968.
52. Kisler, J. M.; Dahler, A.; Stevens, G. W.; O'Connor, A. J. *Microporous and Mesoporous Materials* **2001**, *44*, 769-774.
53. Vinu, A.; Murugesan, V.; Hartmann, M. *Journal of Physical Chemistry B* **2004**, *108*, 7323-7330.
54. Lei, J.; Fan, J.; Yu, C. Z.; Zhang, L. Y.; Jiang, S. Y.; Tu, B.; Zhao, D. Y. *Microporous and Mesoporous Materials* **2004**, *73*, 121-128.
55. Yang, J.; Daehler, A.; Stevens, G. W.; O'Connor, A. J. In *Nanotechnology in Mesoporous Materials*; Park, S. E.; Ryoo, R.; Ahn, W. S.; Lee, C. W.; Chang, J. S. Eds., 2003; pp. 775-778.
56. Karimi, B.; Emadi, S.; Safari, A. A.; Kermanian, M. *Rsc Advances* **2014**, *4*, 4387-4394.
57. Asefa, T.; Tao, Z. *Chemical Research in Toxicology* **2012**, *25*, 2265-2284.

Enlarged pore size in nanoparticulated bimodal porous silicas: improving accessibility

Supplementary Information

Alaina Moragues^a, Carmen Guillem^a, Adela Mauri-Aucejo^b, Marta Tortajada^c, Aurelio Beltrán^a, Daniel Beltrán^a and Pedro Amorós^a

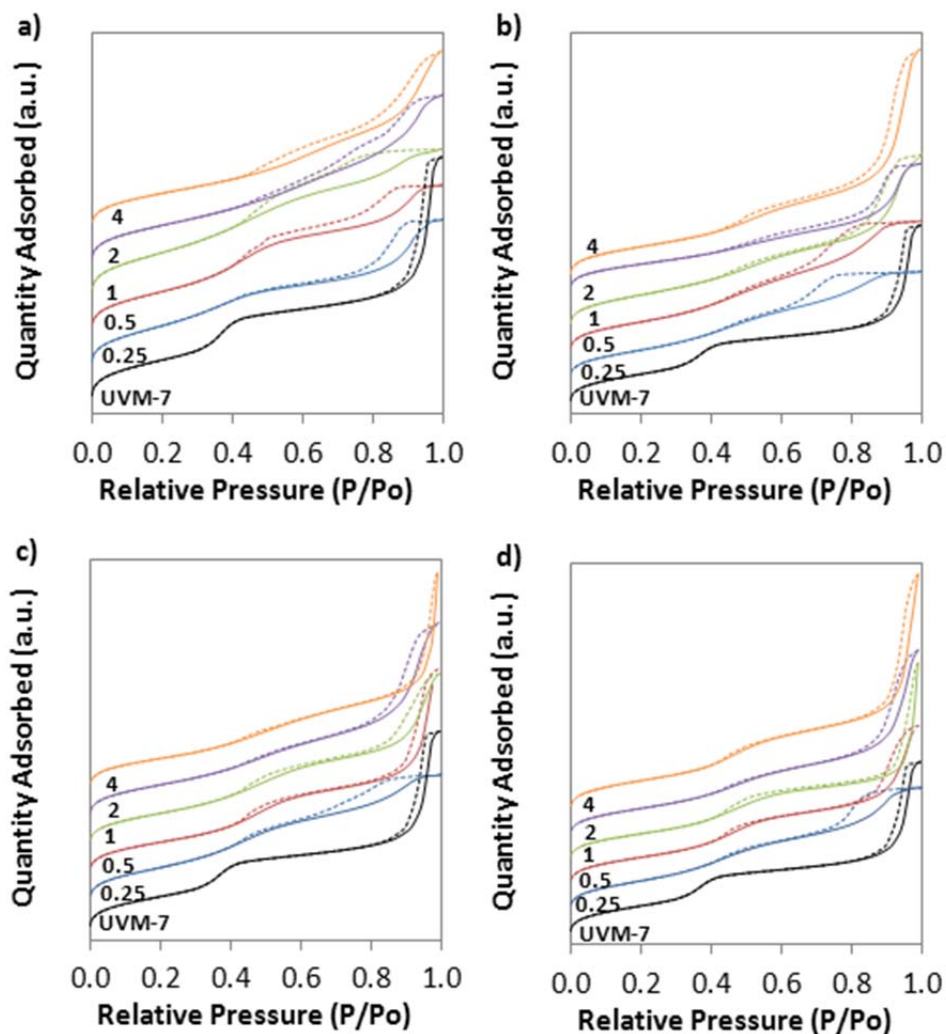


Figure S1. N_2 adsorption-desorption isotherms of $0.5/\gamma C_n$ -UVM-7(C) materials. **(a)** $n=10$, Samples 4 to 8, **(b)** $n=12$, Samples 9 to 13, **(c)** $n=14$, samples 14 to 18, **(d)** $n=16$, Samples 19 to 23. The values 0.25, 0.5, 1, 2 and 4 correspond to the nominal alkane content (γ). In all series the XRD of the non-expanded UVM-7 silica (Sample 1) is included for comparison.

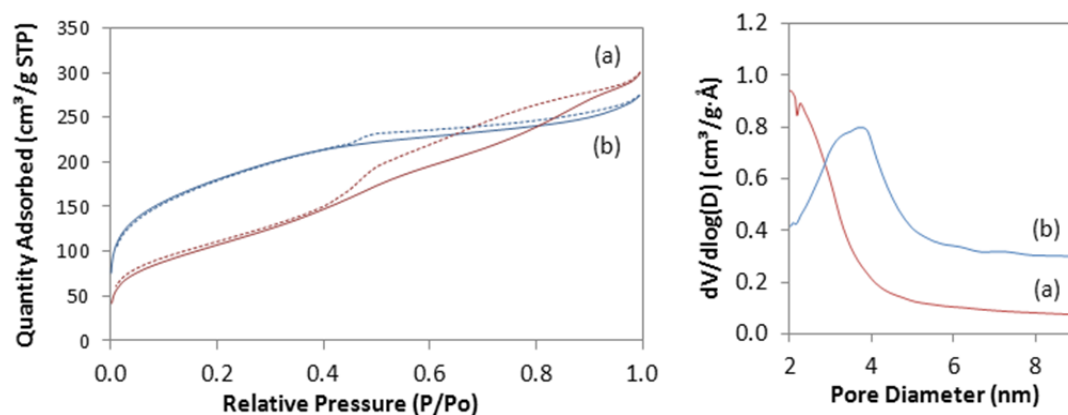


Figure S2. N₂ adsorption-desorption isotherms and BJH pore size distributions of **(a)** 1.1/4C₁₆-UVM-7(M) and **(b)** 0.5/0.5C₁₄-UVM-7(M) after surfactant chemical extraction (without hydrothermal aging). A significant collapse is observed for the 0.5/0.5C₁₄-UVM-7(M) solid (392.7 m²/g, without well-defined mesopores).

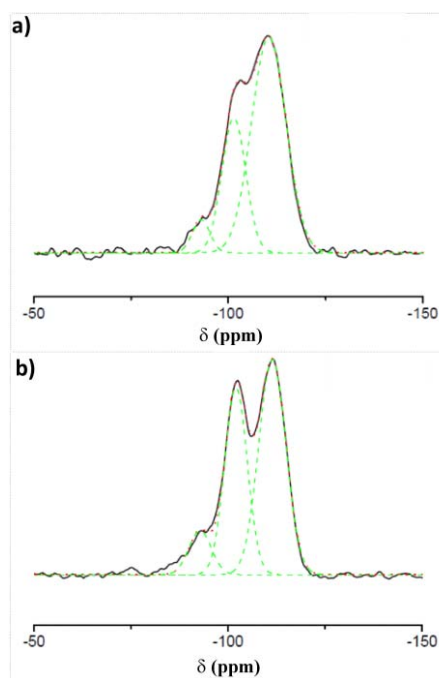


Figure S3. ²⁹Si NMR spectra of calcined and chemically extracted Sample 26: **(a)** 1.1/4C₁₆-UVM-7(C), and **(b)** 1.1/4C₁₆-UVM-7(E).

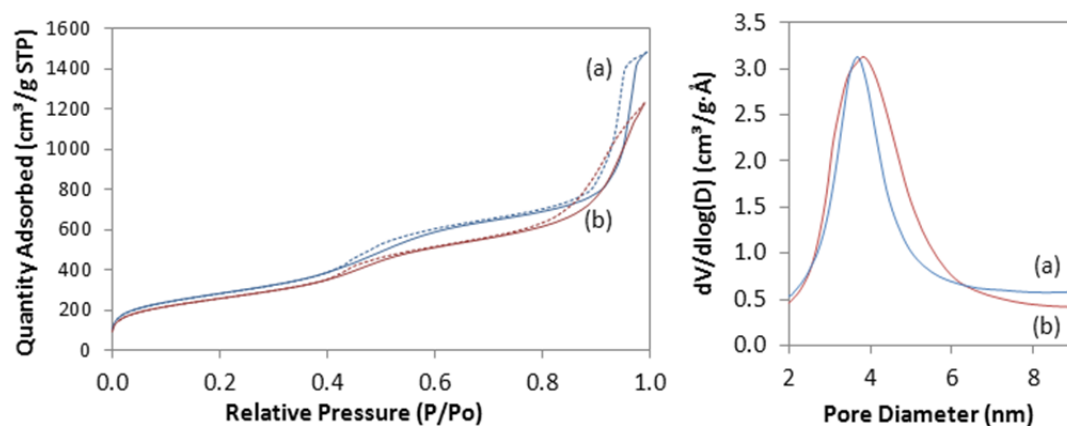


Figure S4. N₂ adsorption-desorption isotherms and BJH pore size distributions of samples **(a)** 0.5/0.5C₁₄-UVM-7(E) (Sample 30) and **(b)** 1.1/4C₁₆-UVM-7(E) (Sample 31).

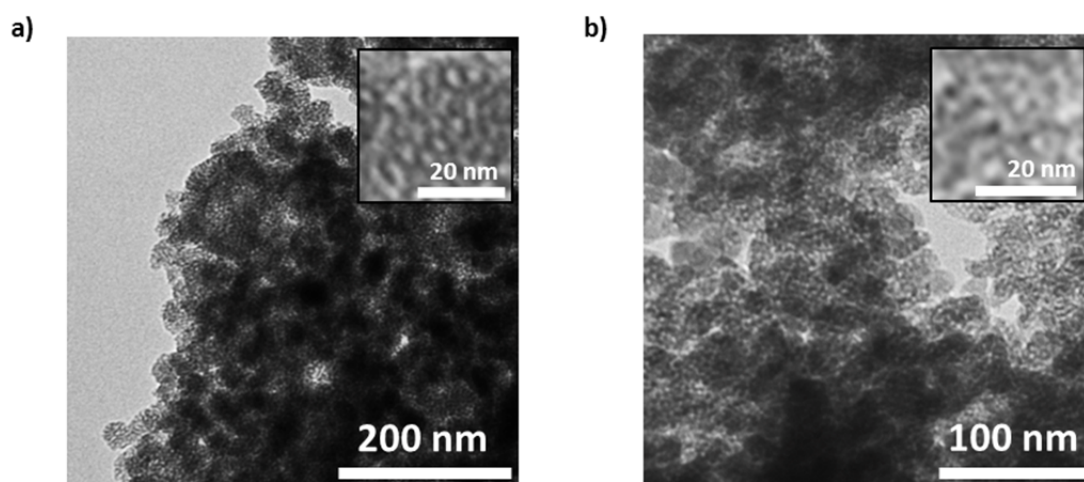


Figure S5. Representative TEM images of samples **(a)** 0.5/0.5C₁₄-UVM-7(E) (Sample 30) and **(b)** 1.1/4C₁₆-UVM-7(E) (Sample 31).

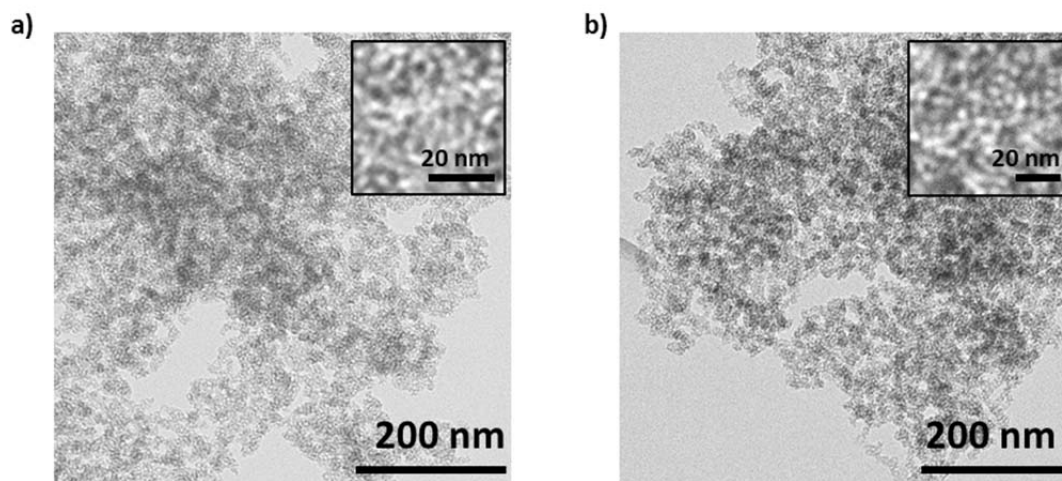


Figure S6. Representative TEM micrographs of the Ibuprofen charged materials. **(a)** Sample 26 (0.58). **(b)** Sample 26 (0.47 + 0.58).

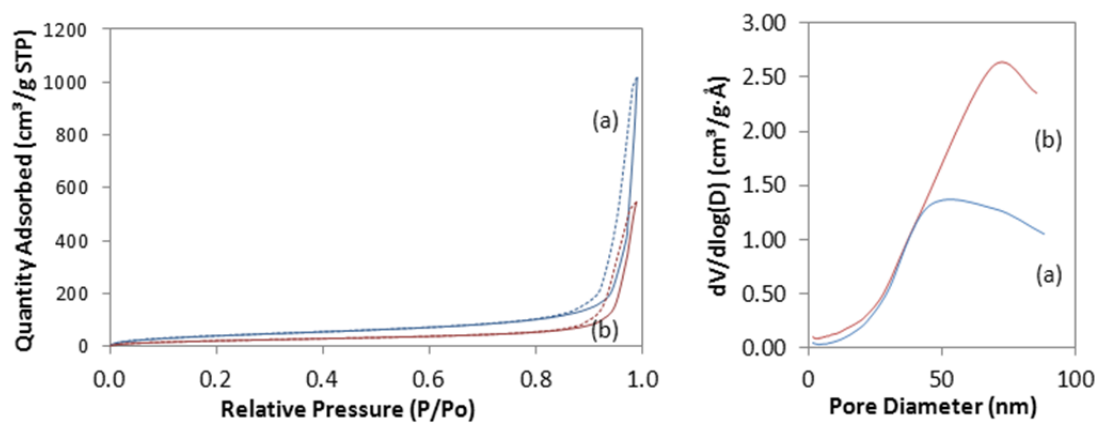


Figure S7. Representative N₂ adsorption-desorption isotherms and BJH pore size distributions of the Ibuprofen charged materials. **(a)** Sample 26 (0.58). **(b)** Sample 26 (0.47 + 0.58).

***3. Gold mesoporous silica nano-
composites used in catalytic
applications***

3.1 - Overview

Gold is the most noble of metals. Since its discovery, it has been used as a source for ornaments and art. It has a high monetary value; in fact, the gold price has been used as an indicative factor of the financial state of the economy.

For a long time, gold was considered an inert material; it has such a high potential ($E^0 = +1.69$ V) that it resists corrosion and oxidation in moist air, and its beauty and lustre remains for millennia. Before the advent of modern chemistry, gold fascinated alchemists. However, its inertia offered few study possibilities. For this reason, gold chemistry was relatively undeveloped for a long time.

In the late 1980s the findings of Hutchings¹ et al. and Haruta² et al. on the exceptional activity of nanometric gold in CO oxidation and ethyne hydrochlorination focused scientific interest on this metal. While large metal particles can be considered as chemically inert, when the particle size is reduced to the nanometric range and it is properly dispersed, usually in/on metal oxides, it can act as a catalyst in reactions such as selective hydrogenation^{3,4}, alkene epoxidation⁵, alcohol oxidation⁶ or direct synthesis of H₂O₂ (in addition to the above mentioned).



Figure 1. Lycurgus cup.

Nowadays, gold is probably the most used element at the nanoscale (apart from silica). But back in history, the use of gold nanoparticles was known for centuries. In the Vedic period (1750-500 B.C.), in India, *blashma* was already being used. It consisted of a gold containing ashes where nanoparticles were used for medical purpose. The most ancient well-documented example is *Lycurgus cup*⁷ (Figure1), from the 4th century A.D., where gold and silver nanoparticles were used for decorative effects.

In 1857, Faraday reported the reduction of a tetrachloroaurate solution with phosphorous disulphide in carbon⁸. He claimed that gold was present in solution “as a finely divided solid state”. In the first half of the XX century there was a growth in knowledge of colloid chemistry, with gold playing an important role. Nevertheless, these developments were marginalized due to the revolutionary advances in physics. In practice, until the nanotechnology apogee in the last decades of the XX century, discoveries in this field did not receive much attention. At this time, many of the old concepts were revised to improve understanding.

The importance of gold in nanotechnology resides in its stability as a pure metal. Generally, when exposed to ambient conditions metals become covered with a rust layer. This fact makes them inappropriate for nanoparticle preparation, where most of the atoms are surface located. Besides, with the exception of silver, no other metal equals gold in terms of controllability and response in optical properties, in particular surface plasmon resonance.

Gold catalysis can be considered as a bridge between model systems produced by materials researchers and real systems used in catalysis⁹. Gold chemistry can be used to understand catalysis, synthesis and the stabilization of materials at the nanoscale.

The use of gold as a catalyst, and the study of gold nanoparticles and their chemistry have generated a great number of publications. Twenty years ago there were just a few papers related to gold chemistry. Nowadays, as shown in Figure 2, more than 1,000 per year are published.

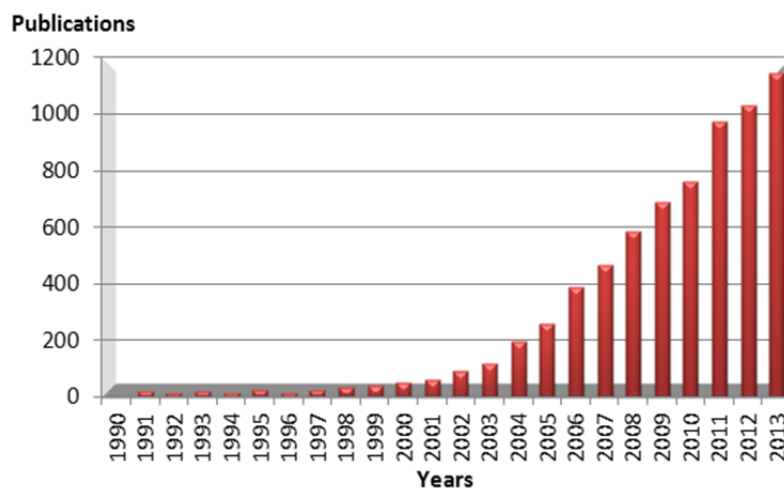


Figure 2. Evolution of papers related to gold catalysis, data from Web of Science.

3.2 - Particle size

An essential characteristic in gold catalysis is the importance of a particle size lower than 5 nm. Some explanations for this phenomena include the high contribution of surface atoms with low coordination (edges, vertices)¹⁰; a change in the metal oxidation state and electronic structure with particle size¹¹⁻¹³; O₂ sensibility to the surface arrangement of gold atoms¹⁴; charge transfer and oxygen spill-over between gold particles and the support^{15,16}; and support-induced strain¹⁷.

Sintering implies the loss of catalytic surface due to crystallite growth; particles can grow into larger ones through different mechanisms. Particles or atoms might move from one particle to another, the movement of atoms being the most important mechanism for the sintering of small particles. This process is highly dependent on temperature: it is known that as the temperature of the material increases so does the mobility of its atoms. The Hüttig and Tamman temperatures of a material indicate the temperature at which such materials sinter (or agglomerate). They are related to the melting temperature.

At the Hüttig temperature, atoms at crystalline defects become mobile¹⁸. Atomic mobility increases when the Tamman temperature is reached; atoms within the bulk material begin showing mobility, causing sintering or agglomeration. Finally,

at the melting temperature the mobility is so high that liquid-phase behaviour is observed. These temperatures are correlated as shown below:

$$T_{\text{Hüttig}} = 0.3 T_{\text{melting}} \quad (1)$$

$$T_{\text{Tamman}} = 0.5 T_{\text{melting}} \quad (2)$$

For gold, the melting, Hüttig and Tamman temperatures are 1336, 668 and 401 K¹⁸, respectively. Several factors such as texture, size and morphology affect these temperatures. A wide variety of materials show a decrease in their melting point as particle size diminishes¹⁹⁻²¹. Melting starts at the surface and for a small particle the surface contribution to the process is greater. Therefore, the smaller the particle the higher the melting point reduction. Shown in Figure 3 is the evolution of the melting temperature for gold particles with their size.

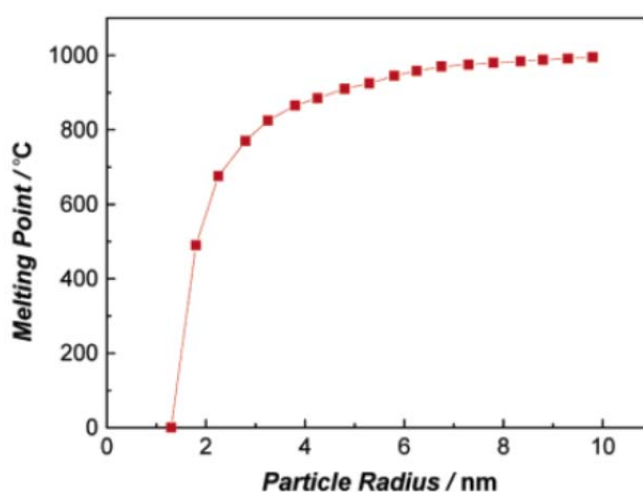


Figure 3. Relationship between the melting point and the size of gold, from reference 22.

Another process that can influence gold particle size is aurophilicity. This is the d^{10} metallic ions propensity to attract each other²³. Aurophilic interactions come from the overlapping of 5d full orbitals with empty 6s and 6p, and can be described as strong van der Waals interactions²⁴. In most cases, gold interaction with metal oxides is weaker than Au-Au bond, leading to easy sintering.

As a consequence of these features, formation and stabilisation of gold nanoparticles is a complicated process that requires specific conditions.

3.3 - Nanoparticle formation

Formation of gold nanoparticles can be accomplished by two different strategies, namely “top down” and “bottom up”. “Top down” processes are based on the breaking of bulk gold to generate nanoparticles of the desired size, controlled by a matrix or a pattern. These methods have limitations related to size control and particle shape, as well as post functionalization. By contrast, with a “bottom up” strategy, nanoparticles are formed from individual molecules. Formation requires a chemical or biological reduction in two steps, nucleation and growth. If both steps take place in the same process the method is known as in situ; otherwise, it is known as seed-growth.

In the following paragraphs in situ strategies and their evolution are described:

- **Turkevich method**

This method, reported by Turkevich in 1951²⁵, consists of the reduction of HAuCl_4 using trisodium citrate dihydrate. By controlling the Au/citrate ratio, the particle size can be modulated²⁶ between 15 and 150 nm. Some research groups have improved the method; in particular, the Kimling group²⁷ indicates that high concentrations of citrate stabilize small particles faster, while with low concentrations large-size nanoparticles are obtained.

Over the years, some changes with respect to the initial conditions have been implemented, such as the use of different reductors (tannic acid/citrate²⁸, NaBH_4 ²⁹) using the citrate only as stabilizing agent. With this method, 5 nm nanoparticles can be formed.

- **Brust-Schiffrin method**

The synthesis of thiolate stabilized gold nanoparticles was described by Mulvaney and Giersing in 1993³⁰. In 1994, with the Brust-Schiffrin method³¹, it was possible to use this reduction in an in situ method. It allows the work to be carried out under atmospheric conditions, obtaining particles with high thermal stability, low size dispersion and easy post-functionalization by ligand substitution. Particles between 2 and 5 nm are stabilized by Au-S bonds.

- **Schimid Au₅₅ cluster**

At the beginning of the 1980s, Schmid³² published a phosphine stabilized gold cluster, [Au₅₅(PPh₃)₁₂Cl₆], with a narrow size dispersion (1,4 nm). He used diborane as the reducing agent of HAuCl₄ and triphenylphosphine as the stabilizing agent. Some modifications of the initial method using different reducing agents^{33,34} or gold precursors³⁵ have been studied.

- **Other ligands**

Nanoparticles can be stabilized using other oxygen and nitrogen-based ligands (amine, carboxyl, carbonyl and phenol groups), polymers³⁶ and dendrimers³⁷.

In comparison with in situ methods, the particle size enlargement in seed-growth methods takes place step by step, allowing the control of particle size and shape. These methods entail two different stages. In the first one, small-size nanoparticles are prepared as seeds. In the second one, these nanoparticles are added to a solution containing HAuCl₄ and reducing and stabilizing agents. New Au⁰ particles grow on the seed surface to form large-sized nanoparticles. Reducing agents used in the second stage are always softer than those from the first. Thus, new reduced gold atoms are only aggregated on the seeds, with no formation of new particles. This step can be repeated until the desired size is obtained.

With traditional synthetic methods, spherical or quasi-spherical particles are obtained. But the shape can be lost if the growth is not controlled. For the synthesis of nanoparticles with a defined morphology, the seed-growth method is preferentially used^{38,39}. Shown in Figure 4 are some examples of gold nanoparticles prepared by the seed-growth method (adapted from reference 40).

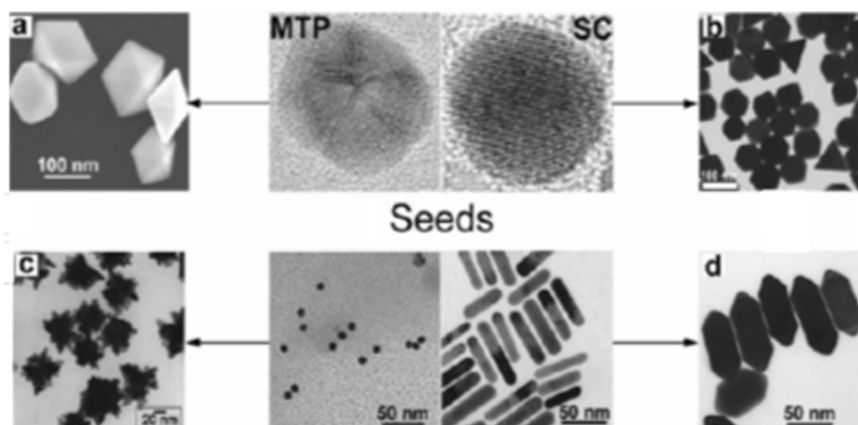


Figure 4. Electron micrographs of Au nanoparticles with different shapes.

“Top down” synthesis starts with a bulk substrate (film or pellet) that undergoes a patterning process to obtain nanoparticles with the desired size and shape. The most common techniques are electron-beam lithography⁴¹ and laser-based ablation⁴².

3.4 - Catalysis

Gold in its nanocrystalline form (colloidal or supported), offers many possibilities as a catalyst. The nature of the active site regarding i.e. metallic or positive gold ($\text{Au}^+/\text{Au}^{3+}$) it is still under debate^{43,44}. There is evidence showing that cationic gold is catalytically active for numerous reactions^{1,45,46}, but there is also evidence linking catalytic activity to small gold clusters⁴⁷. The structural complexity of gold catalysts complicates the interpretation of the results obtained from spectroscopic techniques.

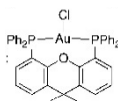
It is known that gold catalytic activity is affected by:

- Size and shape of gold particles
- Synthesis method
- Gold oxidation state
- Support nature
- Gold-support interactions

3.4.1 - Homogeneous catalysis

Some gold complexes act as catalysts in solution⁴⁸⁻⁵¹. Examples of gold catalysed reactions we can find are: alkene hydrogenation⁵², alkyne hydrochlorination⁵³, alkyne⁵⁴, allene⁵⁵ and alkene⁵⁶ hydroamination.

Table 1. Some reaction catalyzed by gold(I) and gold(III) complexes in solution, from reference 43.

Reaction	Gold precursor	Ref.
Ethylene hydrogenation	HAuCl ₄	58
Enantioselective hydrogenation of imines	Gold(I)–Me-duphos ^a	49
Hydrochlorination of alkynes	HAuCl ₄	53
Hydroamination of alkynes	NaAuCl ₄	54
Hydrothiolation of allenes	AuCl	50
Hydroarylation of alkenes	AuCl ₃	59
Asymmetric aldol reaction	Ferrocenylphosphine gold(I) complexes	60
Hydroarylation of alkynes	AuCl ₃	61
Intramolecular addition of phenols and carboxylic acids to alkenes	Ph ₃ PAuCl	62
Carbonylation of olefins	Au(CO)	63
Dehydrogenative silylation of alcohols		51
Cycloisomerisation of α-aminoallenes to 3-pyrrolines	AuCl ₃	64
Phenol synthesis	AuCl ₃	65

^a Me-duphos = 1,2-bis((2R,5R)-2,5-dimethylphospholano)benzene

Catalytic activity of gold complexes is comparable with that of palladium^{48,54,57}. For example, carbon-carbon coupling reactions, usually catalysed with palladium, can also be catalysed with gold. Table 1 shows some reactions catalysed by gold complexes in solution.

Although many reactions have been catalysed using homogeneous gold catalysts, this type of catalysis has a few drawbacks. Separation and recovery of homogeneous catalysts from the reaction medium often requires several steps that might even deactivate the catalyst. For this reason, homogeneous catalysts are rarely recycled. Besides, higher amounts of gold are usually required for homogeneous catalysts. Both factors make homogeneous catalysts more expensive than the heterogeneous ones.

3.4.2 - Supported (heterogeneous catalysis)

A good way to stabilize gold nanoparticles is to support them, obtaining a well-dispersed, catalytically active and stable material. Hutchings group¹ supported gold on active carbon at the end of the 1980s and used it as a catalyst in acetylene hydrochlorination. Haruta's group² used gold supported on group VIII metal oxides (Fe_2O_3 , Co_3O_4 , NiO) in CO oxidation at low temperature.

Table 2. Ongoing and potential applications of Au catalysts, from reference 47.

Fields of applications	Reactants or Reactions	Support materials
Indoor air quality control	odour (commercialized), CO	Fe_2O_3
	sick house gases	TiO_2
Pollutant abatement	dioxin oxidation-decomposition	Fe_2O_3
	NO reduction	Al_2O_3
	N_2O decomposition	Co_3O_4
H₂ energy carrier	water-gas shift	ZrO_2 , CeO_2
	CO removal	Al_2O_3 , Mn_2O_3 , Fe_2O_3
	fuel cell anode	carbon black
	hydrochlorination	AuCl_3 / activated carbon
Chemical process	hydrogenation	ZnO
	[C=C, C=O \nrightarrow C=C, C-OH]	
	liquid-phase selective oxidation	activated carbon
	propylene epoxidation	TiO_2 (anatase) and Ti-SiO ₂

Since then, supported gold has been studied as a catalyst in many reactions such as propylene epoxidation⁶⁶, hydrogen peroxide synthesis⁶⁷, alcohol selective oxidation⁶⁸ and carbon-carbon bond coupling⁶⁹ among others. As can be seen in Table 2, a wide variety of materials have been used as supports.

3.4.2.1 - Anchoring

The main role of the support is to avoid sintering of gold nanoparticles. For this reason, interaction between gold and the support (metal-support interaction, MSI⁷⁰) plays an important role in catalysis^{71,72}. Supports can be classified by their nature into two groups: reducible metal oxides (i.e. oxides with different valences that are easily reducible) such as Fe₂O₃, CeO₂ or TiO₂ and, irreducible metal oxides; hardly reducible materials.

Reducible metal oxides participate directly or indirectly in the catalytic reaction. For example, in CO oxidation the support has two main roles: to provide oxygen or assist its activation, and to eliminate CO₂ by reaction with the hydroxyl groups on the surface⁷³. In contrast, irreducible supports do not participate in the reaction. When supported on irreducible supports, gold particles need to be smaller than in the case of reducible oxides in order to be active; in this way low coordination gold atoms are accessible^{74,75}.

Due to the high metal-support interaction, when gold is supported on reducible oxides it tends to have a hemispheric structure. The wetting of gold over the surface generates larger interfaces. Besides, the support can induce strains on gold particles, especially at the interface between the gold and the support^{76,17}. When supported at irreducible supports (such as carbon or silica), nanoparticles have a spherical shape because of the weak interaction between the gold and the support. For this reason, particles with the same size have different catalytic activity on diverse supports. Another factor to take into account is the electronic effect; CeO₂ can stabilize gold nanoparticles by attracting gold electrons⁷⁷, while MoO_x does this by donating electrons⁷⁸.

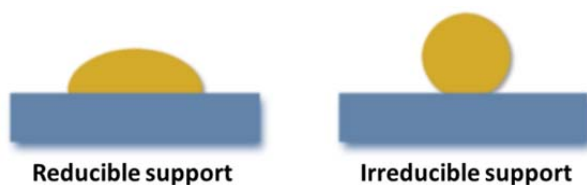


Figure 5. Scheme on gold interaction with different support.

The size and shape of the support can influence the catalyst efficiency, the number of active centres being proportionally lower when the size of the support is much greater than the nanoparticles^{79,80}. It has been suggested that a decrease in the support particle size generates a better metal-support contact, as well as more oxygen vacancies, making its activation and migration easier⁸¹.

Supported gold catalysts are usually prepared using pristine supports, which in most cases are metal oxides, but in others they can be a metal salt⁸²⁻⁸⁶.

3.4.2.2 - Anchoring methods

Impregnation of gold nanoparticles on metal oxides is complicated since gold has a lower melting point and a lower affinity for oxides than Pd and Pt. Moreover, HAuCl_4 crystals dispersed on the support aggregate during the calcination step, with chloride ions favouring coagulation. However, there are other methods that permit deposition of gold nanoparticles with sizes lower than 10 nm.

Many studies show that gold dispersion on the support is determined by the preparation process. It is important to choose a suitable method depending on the support used. These methods can be classified as shown in Table 3.

The first group is characterized by the preparation of well-mixed precursors, hydroxides, oxides or gold metal mixtures with the support metal by coprecipitation⁸⁷, amorphous-alloying⁸⁸ or co-sputtering⁸⁹. Coprecipitation is the most used and simplest. In this method, an aqueous solution containing HAuCl_4 and metal salts, such as nitrates, is mixed for a few minutes and aged. The obtained precipitate needs to be calcined to obtain the catalyst. The application of this method is limited to metal hydroxide or carbonates that can be coprecipitated with $\text{Au}(\text{OH})_3$.

Table 3. Preparation techniques for nanoparticulate gold catalysts, from reference 47.

Categories	Preparation techniques	Support materials	Ref.
Preparation of mixed precursors of Au and the metal component of supports	coprecipitation (hydroxides or carbonates)	Be(OH) ₂ , TiO ₂ *, Mn ₂ O ₃ , Fe ₂ O ₃ , Co ₃ O ₄ , NiO, ZnO, In ₂ O ₃ , SnO ₂	90-92
	amorphous alloy (metals)	ZrO ₂	88
	co-sputtering (oxides) in the presence of O ₂	Co ₃ O ₄	89
Strong interaction of Au precursors with support materials	deposition-precipitation (HAuCl ₄ in aqueous solution)	Mg(OH) ₂ *, Al ₂ O ₃ , TiO ₂ , Fe ₂ O ₃ , Co ₃ O ₄ , NiO, ZnO, ZrO ₂ , CeO ₂ , Ti-SiO ₂	93,94
	liquid phase grafting (organo-gold complex in organic solvents)	TiO ₂ , MnO _x , Fe ₂ O ₃	95,96
	gas phase grafting (organo-gold complex)	all kinds, including SiO ₂ , Al ₂ O ₃ -SiO ₂ , and activated carbon	97,98
Mixing colloidal Au with support materials	colloid mixing	TiO ₂ , activated carbon	99
Model catalysts using single crystal supports	vacuum deposition (at low temperature)	Defects are the sites for deposition, MgO, SiO ₂ , TiO ₂	100-102

* The addition of Mg citrate during or after coprecipitation or deposition-precipitation is important for depositing Au as nanoparticles

The second group is based on the deposition or adsorption of gold compounds such as gold hydroxide by deposition-precipitation⁹³ or an organic complex by liquid phase grafting^{95,96} and gas phase grafting⁹⁷. The deposition-precipitation method was first used by Haruta¹⁰³ and since then it has become the most used. It consists of HAuCl₄ hydrolysis at a high pH to obtain [Au(OH)_nCl_{4-n}]⁻ species, with as few chloride groups as possible, and its subsequent precipitation on the support. The support nature is very important; this method is appropriate for supports with an isoelectric point (IEP) higher than 5. The ideal solid must have a high density of hydroxyl groups and a high surface area. But nanoparticle formation is more complex than was suggested by Geus and Haruta¹⁰⁴. After gold adsorption on the surface, particles are formed by growth and nucleation processes. Final size depends on many factors such as gold charge, the nature of the support, chloride presence, thermic treatments, etc. Working at a high pH reduces the chloride amount, obtaining smaller particles with less mobility. The last step of this process is gold reduction with a thermal treatment to form metal clusters.

Liquid phase grafting in an organic solvent is not appropriate for an IEP lower than 5. Besides, it needs freshly prepared metal hydroxides⁹⁵ to ensure a high hydroxyl concentration on the surface that allows the interaction with organic gold complexes. By contrast, gas phase grafting can be used with any support⁹⁸.

In the third group, gold monodisperse colloids are used, stabilized with organic ligands or polymers⁹⁹. This method is used for the deposition of gold on carbon, which is not possible with the preceding methods because of its low hydroxyl density.

The last group is chemical vapour deposition, an efficient method to synthesize small gold nanoparticles on almost all kinds of supports. The major drawbacks of this method are the high price of the organic precursors needed and the complicated procedure.

3.4.2.3 - Mesoporous silica

One of the most used irreducible supports is mesoporous silica, owing to its high surface area, corrosion resistance, low cost and modifiable morphology. In many gold catalysts, gold nanoparticles are located on the external surface of the material. There is great interest in its incorporation on mesoporous materials^{105,106} because the incorporation of the nanoparticles in the pore system prevents their leaching and sintering.

Nevertheless, nanoparticle anchoring on these materials is not easy. Materials prepared by HAuCl_4 or AuCl_2 impregnation have relatively large particles, since chloride ions favour particle sintering¹⁰⁷. Moreover, preparation by deposition-precipitation is complicated. Due to the low isoelectric point of silica, the interaction between gold and the support is very weak and low gold loading materials are obtained⁸².

Gold nanoparticles have been currently confined in mesoporous silica, but sintering is observed at high temperatures¹⁰⁸. The use of chemical vapour deposition, although complicated, could be an alternative, but organic gold precursors are very expensive.

To enhance gold-support interaction, pores have been functionalized using organic (mercaptopropyl¹⁰⁹, propylamine¹¹⁰, polydentate amines¹¹¹) and inorganic groups. In the latter, gold-reducible oxide structures have been deposited on the silica surface¹¹², the silica surface has been modified with reducible oxides¹¹³⁻¹¹⁵ or non-silica mesoporous have been used (Figure 6). Another method could be the confinement of the gold nanoparticles into hollow spheres¹¹⁶, which allows good control of the size with no possibility of sintering. Silica¹¹⁷ or an organic polymer¹¹⁸ can be used as the coating .

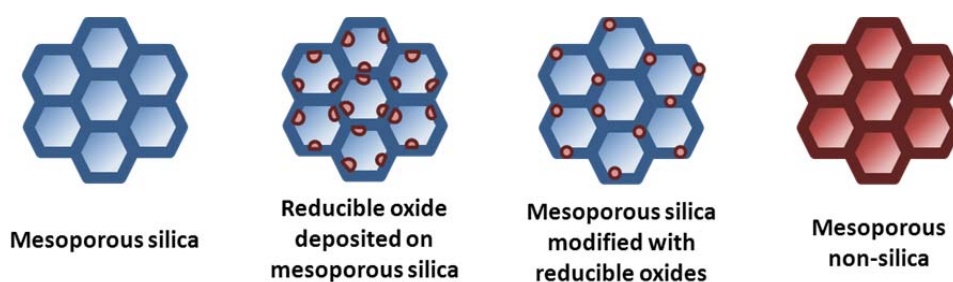


Figure 6. Modification of mesoporous silica with reducible oxides.

Although functionalization with organic groups enhances interaction with gold and facilitates the anchoring by deposition-precipitation, the thermal stability of these materials is low, restricting their applications to those where soft conditions are used.

In contrast, modification with inorganic groups offers great possibilities. It improves interaction with gold and permits its use at high temperatures. Besides, the possible formation of reducible oxide crystalline domains makes this interaction stronger.

Depending on the method used for metal oxide incorporation, amorphous or crystalline domains can be obtained. With a one-pot synthesis a great dispersion of the oxide inside the silica matrix is obtained, but in the form of amorphous domains integrated in the network. On the other hand, the use of a two-pot method permits the formation of crystalline domains.

In some cases an epitaxial growth¹¹⁹ of gold on the crystalline domain (Figure 7) has been observed, indicating a strong interaction of gold nanoparticles with the metal

oxide surface. As a result of this interaction, gold particles are less prone to sintering and the thermal stability of the material is enhanced.

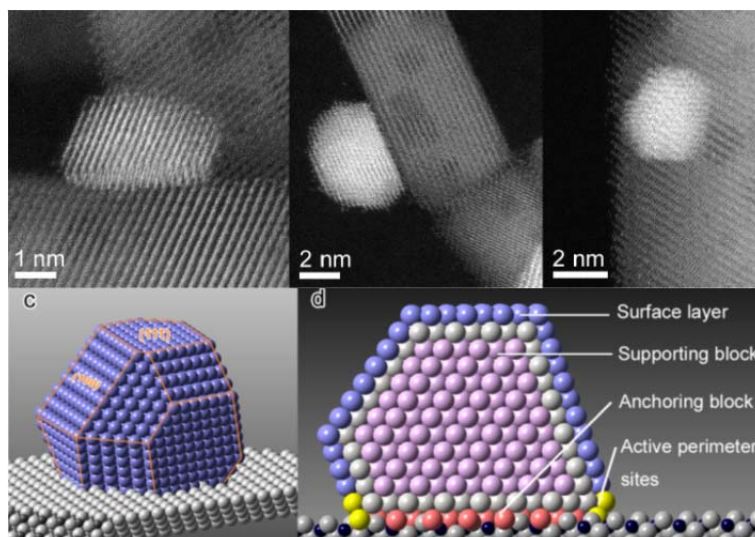


Figure 7. Epitaxial growth of gold nanoparticles supported on ceria; (down) atomic scheme of a gold nanoparticle anchoring onto a CeO_2 nanorod, illustrating the functions of different domains. Adapted from reference 119.

The characteristic features of supported gold catalysts are the remarkable structure sensitivity of their catalytic performance, the low apparent activation energies (active at low temperatures), and moisture activation.

3.5 - Objectives

The objective of this chapter is the preparation and evaluation of heterogeneous gold catalysts. As previously explained, silica itself does not have a strong interaction with gold, resulting in nanoparticle aggregation. For this reason, different methods have been followed to include reducible oxide domains in UVM-7 silica.

Both soft and strong anchoring of gold over metal oxides have been studied. In the first case, a mesoporous silica containing Ni and Ce (or Sn) nanodomains is

obtained through a one pot method, using the atrane route¹²⁰. With this method, small oxide domains are included in the silica matrix. In the second case, one pot and post-treatment methods are compared for the incorporation of titanium oxide in UVM-7 silica. In both cases, gold is added by a deposition-precipitation method, obtaining nanoparticles of less than 5 nm diameter.

The materials obtained are used as catalysts in the selective oxidative condensation of benzylamine to N-benzylidenebenzylamine and in the oxidation of CO to CO₂, respectively.

References

1. Hutchings, G. J. *Journal of Catalysis* **1985**, *96*, 292-295.
2. Haruta, M.; Kobayashi, T.; Sano, H.; Yamada, N. *Chemistry Letters* **1987**, 405-408.
3. Corma, A.; Serna, P. *Science* **2006**, *313*, 332-334.
4. Mukherjee, P.; Patra, C. R.; Kumar, R.; Sastry, M. *Physchemcomm* **2001**, art. no.-5.
5. Yu, N.; Ding, Y.; Lo, A.-Y.; Huang, S.-J.; Wu, P.-H.; Liu, C.; Yin, D.; Fu, Z.; Yin, D.; Hung, C.-T.; Lei, Z.; Liu, S.-B. *Microporous and Mesoporous Materials* **2011**, *143*, 426-434.
6. Sun, H.; Tang, Q.; Du, Y.; Liu, X.; Chen, Y.; Yang, Y. *Journal of Colloid and Interface Science* **2009**, *333*, 317-323.
7. Mulvaney, P. *Mrs Bulletin* **2001**, *26*, 1009-1014.
8. Faraday, M. *Philos. Trans. R. Soc. London* **1857**, 147.
9. Corma, A.; Garcia, H. *Chemical Society Reviews* **2008**, *37*, 2096-2126.
10. Janssens, T. V. W.; Clausen, B. S.; Hvolbaek, B.; Falsig, H.; Christensen, C. H.; Bligaard, T.; Norskov, J. K. *Topics in Catalysis* **2007**, *44*, 15-26.
11. Valden, M.; Lai, X.; Goodman, D. W. *Science* **1998**, *281*, 1647-1650.
12. Chen, M. S.; Goodman, D. W. *Catalysis Today* **2006**, *111*, 22-33.
13. Wang, J. G.; Hammer, B. *Topics in Catalysis* **2007**, *44*, 49-56.
14. Boronat, M.; Corma, A. *Dalton Transactions* **2010**, *39*, 8538-8546.
15. Bond, G. C.; Thompson, D. T. *Catalysis Reviews-Science and Engineering* **1999**, *41*, 319-388.
16. Sanchez, A.; Abbet, S.; Heiz, U.; Schneider, W. D.; Hakkinen, H.; Barnett, R. N.; Landman, U. *Journal of Physical Chemistry A* **1999**, *103*, 9573-9578.
17. Mavrikakis, M.; Stoltze, P.; Norskov, J. K. *Catalysis Letters* **2000**, *64*, 101-106.
18. Moulijn, J. A.; van Diepen, A. E.; Kapteijn, F. *Applied Catalysis a-General* **2001**, *212*, 3-16.
19. Coombes, C. J. *Journal of Physics F-Metal Physics* **1972**, *2*, 441-&.
20. Buffat, P.; Borel, J. P. *Physical Review A* **1976**, *13*, 2287-2298.
21. Beck, R. D.; Stjohn, P.; Homer, M. L.; Whetten, R. L. *Science* **1991**, *253*, 879-883.

22. Burda, C.; Chen, X. B.; Narayanan, R.; El-Sayed, M. A. *Chemical Reviews* **2005**, *105*, 1025-1102.
23. Bardaji, M.; Laguna, A. *Journal of Chemical Education* **1999**, *76*, 201-203.
24. Pyykko, P. *Angewandte Chemie-International Edition* **2004**, *43*, 4412-4456.
25. Turkevich, J.; Stevenson, P. C.; Hillier, J. *Discussions of the Faraday Society* **1951**, 55-&.
26. Frens, G. *Nature-Physical Science* **1973**, *241*, 20-22.
27. Kimling, J.; Maier, M.; Okenve, B.; Kotaidis, V.; Ballot, H.; Plech, A. *Journal of Physical Chemistry B* **2006**, *110*, 15700-15707.
28. Slot, J. W.; Geuze, H. J. *European Journal of Cell Biology* **1985**, *38*, 87-93.
29. Brown, K. R.; Fox, A. P.; Natan, M. J. *Journal of the American Chemical Society* **1996**, *118*, 1154-1157.
30. Giersig, M.; Mulvaney, P. *Langmuir* **1993**, *9*, 3408-3413.
31. Brust, M.; Walker, M.; Bethell, D.; Schiffrin, D. J.; Whyman, R. *Journal of the Chemical Society-Chemical Communications* **1994**, 801-802.
32. Schmid, G.; Pfeil, R.; Boese, R.; Bandermann, F.; Meyer, S.; Calis, G. H. M.; Vandervelden, W. A. *Chemische Berichte-Recueil* **1981**, *114*, 3634-3642.
33. Weare, W. W.; Reed, S. M.; Warner, M. G.; Hutchison, J. E. *Journal of the American Chemical Society* **2000**, *122*, 12890-12891.
34. Shem, P. M.; Sardar, R.; Shumaker-Parry, J. S. *Langmuir* **2009**, *25*, 13279-13283.
35. Moores, A.; Goettmann, F.; Sanchez, C.; Le Floch, P. *Chemical Communications* **2004**, 2842-2843.
36. Shan, J.; Tenhu, H. *Chemical Communications* **2007**, 4580-4598.
37. Balogh, L.; Valluzzi, R.; Laverdure, K. S.; Gido, S. P.; Hagnauer, G. L.; Tomalia, D. A. *Journal of Nanoparticle Research* **1999**, *1*, 353-368.
38. Perez-Juste, J.; Liz-Marzan, L. M.; Carnie, S.; Chan, D. Y. C.; Mulvaney, P. *Advanced Functional Materials* **2004**, *14*, 571-579.
39. Bastus, N. G.; Comenge, J.; Puentes, V. *Langmuir* **2011**, *27*, 11098-11105.
40. Grzelczak, M.; Perez-Juste, J.; Mulvaney, P.; Liz-Marzan, L. M. *Chemical Society Reviews* **2008**, *37*, 1783-1791.
41. Hu, M.; Ou, F. S.; Wu, W.; Naumov, I.; Li, X.; Bratkovsky, A. M.; Williams, R. S.; Li, Z. *Journal of the American Chemical Society* **2010**, *132*, 12820-12822.
42. Huang, W.; Qian, W.; El-Sayed, M. A. *Journal of the American Chemical Society* **2006**, *128*, 13330-13331.

43. Fierro-Gonzalez, J. C.; Gates, B. C. *Chemical Society Reviews* **2008**, *37*, 2127-2134.
44. Chen, M.; Goodman, D. W. *Chemical Society Reviews* **2008**, *37*, 1860-1870.
45. Hashmi, A. S. K.; Rudolph, M. *Chemical Society Reviews* **2008**, *37*, 1766-1775.
46. Marion, N.; Nolan, S. P. *Chemical Society Reviews* **2008**, *37*, 1776-1782.
47. Haruta, M. *Gold Bulletin* **2004**, *37*, 27-36.
48. Hashmi, A. S. K. *Chemical Reviews* **2007**, *107*, 3180-3211.
49. Gonzalez-Arellano, C.; Corma, A.; Iglesias, M.; Sanchez, F. *Chemical Communications* **2005**, 3451-3453.
50. Morita, N.; Krause, N. *Angewandte Chemie-International Edition* **2006**, *45*, 1897-1899.
51. Ito, H.; Takagi, K.; Miyahara, T.; Sawamura, M. *Organic Letters* **2005**, *7*, 3001-3004.
52. Erkelens, J.; Kemball, C.; Galwey, A. K. *Transactions of the Faraday Society* **1963**, *59*, 1181-&.
53. Norman, R. O. C.; Parr, W. J. E.; Thomas, C. B. *Journal of the Chemical Society-Perkin Transactions 1* **1976**, 1983-1987.
54. Fukuda, Y.; Utimoto, K.; Nozaki, H. *Heterocycles* **1987**, *25*, 297-300.
55. Morita, N.; Krause, N. *European Journal of Organic Chemistry* **2006**, 4634-4641.
56. Kobayashi, S.; Kakumoto, K.; Sugiura, M. *Organic Letters* **2002**, *4*, 1319-1322.
57. Hashmi, A. S. K.; Hutchings, G. J. *Angewandte Chemie-International Edition* **2006**, *45*, 7896-7936.
58. Muller, M. C. *Gold Bulletin* **1974**, *7*, 2.
59. Hashmi, A. S. K.; Schwarz, L.; Choi, J. H.; Frost, T. M. *Angewandte Chemie-International Edition* **2000**, *39*, 2285-2288.
60. Ito, Y.; Sawamura, M.; Hayashi, T. *Journal of the American Chemical Society* **1986**, *108*, 6405-6406.
61. Shi, Z. J.; He, C. *Journal of Organic Chemistry* **2004**, *69*, 3669-3671.
62. Yang, C. G.; He, C. *Journal of the American Chemical Society* **2005**, *127*, 6966-6967.
63. Xu, Q.; Imamura, Y.; Fujiwara, M.; Souma, Y. *Journal of Organic Chemistry* **1997**, *62*, 1594-1598.
64. Morita, N.; Krause, N. *Organic Letters* **2004**, *6*, 4121-4123.

65. Hashmi, A. S. K.; Frost, T. M.; Bats, J. W. *Organic Letters* **2001**, *3*, 3769-3771.
66. Stangland, E. E.; Stavens, K. B.; Andres, R. P.; Delgass, W. N. *Journal of Catalysis* **2000**, *191*, 332-347.
67. Landon, P.; Collier, P. J.; Papworth, A. J.; Kiely, C. J.; Hutchings, G. J. *Chemical Communications* **2002**, 2058-2059.
68. Abad, A.; Concepcion, P.; Corma, A.; Garcia, H. *Angewandte Chemie-International Edition* **2005**, *44*, 4066-4069.
69. Carrettin, S.; Guzman, J.; Corma, A. *Angewandte Chemie-International Edition* **2005**, *44*, 2242-2245.
70. Liu, J. *Chemcatchem* **2011**, *3*, 934-948.
71. Ma, Z.; Dai, S. *Nano Research* **2011**, *4*, 3-32.
72. Schubert, M. M.; Hackenberg, S.; van Veen, A. C.; Muhler, M.; Plzak, V.; Behm, R. J. *Journal of Catalysis* **2001**, *197*, 113-122.
73. Haruta, A. *Chemical Record* **2003**, *3*, 75-87.
74. Chen, M. S.; Goodman, D. W. *Science* **2004**, *306*, 252-255.
75. Molina, L. M.; Hammer, B. *Applied Catalysis a-General* **2005**, *291*, 21-31.
76. Lopez, N.; Norskov, J. K.; Janssens, T. V. W.; Carlsson, A.; Puig-Molina, A.; Clausen, B. S.; Grunwaldt, J. D. *Journal of Catalysis* **2004**, *225*, 86-94.
77. Concepcion, P.; Carrettin, S.; Corma, A. *Applied Catalysis a-General* **2006**, *307*, 42-45.
78. Wang, F.; Ueda, W.; Xu, J. *Angewandte Chemie-International Edition* **2012**, *51*, 3883-3887.
79. Rolison, D. R. *Science* **2003**, *299*, 1698-1701.
80. Pietron, J. J.; Stroud, R. M.; Rolison, D. R. *Nano Letters* **2002**, *2*, 545-549.
81. Zhang, X.; Wang, H.; Xu, B. Q. *Journal of Physical Chemistry B* **2005**, *109*, 9678-9683.
82. Yan, W. F.; Brown, S.; Pan, Z. W.; Mahurin, S. M.; Overbury, S. H.; Dai, S. *Angewandte Chemie-International Edition* **2006**, *45*, 3614-3618.
83. Venugopal, A.; Scurrrell, M. S. *Applied Catalysis a-General* **2003**, *245*, 137-147.
84. Liu, J.; Chen, W.; Liu, X.; Zhou, K.; Li, Y. *Nano Research* **2008**, *1*, 46-55.
85. Dominguez, M. I.; Romero-Sarria, F.; Centeno, M. A.; Odriozola, J. A. *Applied Catalysis B-Environmental* **2009**, *87*, 245-251.
86. Liu, Y.; Tsunoyama, H.; Akita, T.; Tsukuda, T. *Chemical Communications* **2010**, *46*, 550-552.

87. Haruta, M.; Kageyama, H.; Kamijo, N.; Kobayashi, T.; Delannay, F. *Studies in Surface Science and Catalysis* **1989**, *44*, 33-42.
88. Shibata, M.; Kawata, N.; Masumoto, T.; Kimura, H. *Chemistry Letters* **1985**, 1605-1608.
89. Kobayashi, T.; Haruta, M.; Tsubota, S.; Sano, H.; Delmon, B. *Sensors and Actuators B-Chemical* **1990**, *1*, 222-225.
90. Haruta, M.; Yamada, N.; Kobayashi, T.; Iijima, S. *Journal of Catalysis* **1989**, *115*, 301-309.
91. Kageyama, H.; Kamijo, N.; Kobayashi, T.; Haruta, M. *Physica B* **1989**, *158*, 183-184.
92. Sanchez, R. M. T.; Ueda, A.; Tanaka, K.; Haruta, M. *Journal of Catalysis* **1997**, *168*, 125-127.
93. Tsubota, S.; Haruta, M.; Kobayashi, T.; Ueda, A.; Nakahara, Y. *Preparation of Catalysts V: Scientific Bases for Preparation of Heterogeneous Catalysts* **1991**, *63*, 695-704.
94. Vogel, W.; Cunningham, D. A. H.; Tanaka, K.; Haruta, M. *Catalysis Letters* **1996**, *40*, 175-181.
95. Yuan, Y. Z.; Kozlova, A. P.; Asakura, K.; Wan, H. L.; Tsai, K.; Iwasawa, Y. *Journal of Catalysis* **1997**, *170*, 191-199.
96. Okumura, M.; Haruta, M. *Chemistry Letters* **2000**, 396-397.
97. Okumura, M.; Tanaka, K.; Ueda, A.; Haruta, M. *Solid State Ionics* **1997**, *95*, 143-149.
98. Okumura, M.; Tsubota, S.; Iwamoto, M.; Haruta, M. *Chemistry Letters* **1998**, 315-316.
99. Grunwaldt, J. D.; Kiener, C.; Wogerbauer, C.; Baiker, A. *Journal of Catalysis* **1999**, *181*, 223-232.
100. Wallace, W. T.; Whetten, R. L. *Journal of Physical Chemistry B* **2000**, *104*, 10964-10968.
101. Kishi, K.; Date, M.; Haruta, M. *Surface Science* **2001**, *486*, L475-L479.
102. Valden, M.; Pak, S.; Lai, X.; Goodman, D. W. *Catalysis Letters* **1998**, *56*, 7-10.
103. Haruta, M.; Tsubota, S.; Kobayashi, T.; Kageyama, H.; Genet, M. J.; Delmon, B. *Journal of Catalysis* **1993**, *144*, 175-192.
104. Geus, J. W.; van Veen, J. A. R. *Catalysis: an Integrated Approach, Second Ed.* **1999**, *123*, 459-485.

105. Kresge, C. T.; Leonowicz, M. E.; Roth, W. J.; Vartuli, J. C.; Beck, J. S. *Nature* **1992**, *359*, 710-712.
106. Beck, J. S.; Vartuli, J. C.; Roth, W. J.; Leonowicz, M. E.; Kresge, C. T.; Schmitt, K. D.; Chu, C. T. W.; Olson, D. H.; Sheppard, E. W.; McCullen, S. B.; Higgins, J. B.; Schlenker, J. L. *Journal of the American Chemical Society* **1992**, *114*, 10834-10843.
107. Lin, S. D.; Bollinger, M.; Vannice, M. A. *Catalysis Letters* **1993**, *17*, 245-262.
108. Liu, J. H.; Chi, Y. S.; Lin, H. P.; Mou, C. Y.; Wan, B. Z. *Catalysis Today* **2004**, *93-5*, 141-147.
109. Yang, C.; Wustefeld, H.; Kalwei, M.; Schuth, F., 2004; pp. 2574-2580.
110. Patra, C. R.; Ghosh, A.; Mukherjee, P.; Sastry, M.; Kumar, R. *Nanoporous Materials Iii* **2002**, *141*, 641-646.
111. Hagaman, E. W.; Zhu, H. G.; Overbury, S. H.; Dai, S. *Langmuir* **2004**, *20*, 9577-9584.
112. Yin, H.; Wang, C.; Zhu, H.; Overbury, S. H.; Sun, S.; Dai, S. *Chemical Communications* **2008**, 4357-4359.
113. Perez-Cabero, M.; El Haskouri, J.; Solsona, B.; Vazquez, I.; Dejoz, A.; Garcia, T.; Alvarez-Rodriguez, J.; Beltran, A.; Beltran, D.; Amoros, P. *Journal of Materials Chemistry* **2010**, *20*, 6780-6788.
114. Ma, G.; Binder, A.; Chi, M.; Liu, C.; Jin, R.; Jiang, D.-e.; Fan, J.; Dai, S. *Chemical Communications* **2012**, *48*, 11413-11415.
115. Solsona, B.; Perez-Cabero, M.; Vazquez, I.; Dejoz, A.; Garcia, T.; Alvarez-Rodriguez, J.; El-Haskouri, J.; Beltran, D.; Amoros, P. *Chemical Engineering Journal* **2012**, *187*, 391-400.
116. Wu, S.-H.; Tseng, C.-T.; Lin, Y.-S.; Lin, C.-H.; Hung, Y.; Mou, C.-Y. *Journal of Materials Chemistry* **2011**, *21*, 789-794.
117. Mulvaney, P.; Liz-Marzan, L. M.; Giersig, M.; Ung, T. *Journal of Materials Chemistry* **2000**, *10*, 1259-1270.
118. Otsuka, H.; Nagasaki, Y.; Kataoka, K. *Advanced Drug Delivery Reviews* **2003**, *55*, 403-419.
119. Ta, N.; Liu, J.; Chenna, S.; Crozier, P. A.; Li, Y.; Chen, A.; Shen, W. *Journal of the American Chemical Society* **2012**, *134*, 20585-20588.
120. Cabrera, S.; El Haskouri, J.; Guillem, C.; Latorre, J.; Beltran-Porter, A.; Beltran-Porter, D.; Marcos, M. D.; Amoros, P. *Solid State Sciences* **2000**, *2*, 405-420.

New multicomponent catalysts for the selective aerobic oxidative condensation of benzylamine to N-benzylidenebenzylamine

Cristina Madalina Opris^a, Octavian Dumitru Pavel^a, Alaina Moragues^b,
Jamal El Haskouri^{b,c}, Daniel Beltrán^b, Pedro Amorós^b, Maria Dolores
Marcos^d, Laura Elena Stoflea^e and Vasile I. Parvulescu^a

^a Department of Organic Chemistry and Catalysis, University of Bucharest, 030016 Bucharest, Romania

^b Institut de Ciència dels Materials, Universitat de València, 46071 Valencia, Spain

^c Fundació General, Universitat de Valencia, 46071 Valencia, Spain

^d Centro de Reconocimiento Molecular y Desarrollo Tecnológico (IDM), Departamento de Química, Universidad Politécnica de Valencia, 46022 Valencia, Spain

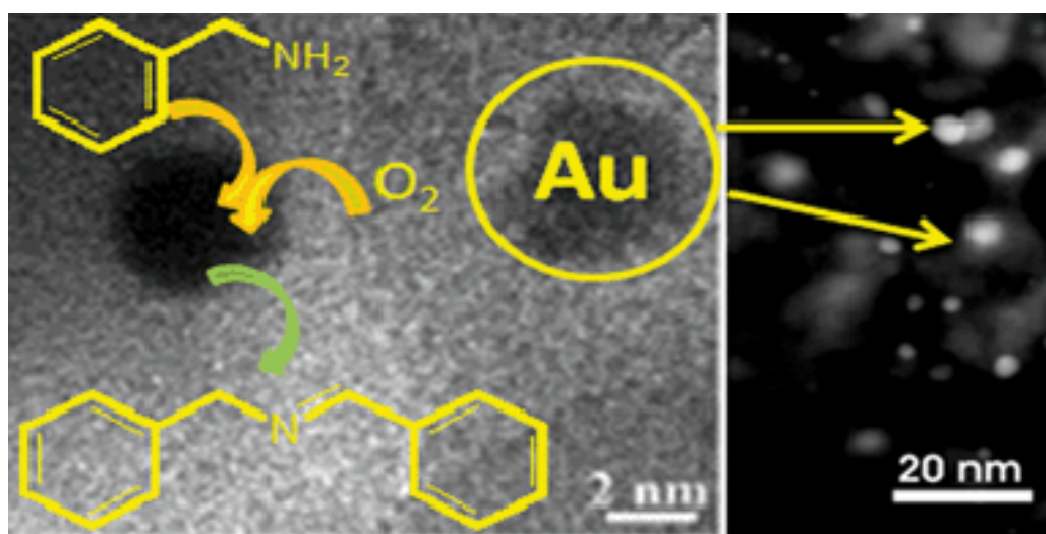
^e National Institute of Materials Physics, 077125 Bucharest-Magurele, Romania

Received 18th June 2014, Accepted 22nd July 2014

Published online 23rd July 2014

Abstract

Aerobic oxidative condensation of benzylamine to N-benzylidenebenzylamine was carried out on new gold-based catalysts using as supports bimodal UVM-7-like mesoporous silica containing Ni and Ce (or Sn) as oxide nanodomains partially embedded inside the mesoporous UVM-7 silica walls. These nanodomains acted as effective and stable inorganic anchors favoring the nucleation, growth and stability of supported gold particles. Following the atrane method (a “one-pot” strategy able to harmonize the hydrolytic reactivity of different heteroelements through the use of complexes containing triethanolamine-derived ligands (atranes) as precursors) the stability of the oxide nanodomains during oxidation and thermal treatments was ensured. The catalysts were prepared in a two-step synthesis in which gold was incorporated through impregnation of previously synthesized bimodal porous silicas containing different heteroelements trapped by the silica mesostructure. The versatility of the preparative approach allowed the high surface and accessibility of the mesoporous silica and also an easy and homogeneous inclusion of heteroelements in one pot. Aerobic oxidative condensation of benzylamine on these catalysts occurred selectively only with the formation of N-benzylidenebenzylamine.



While selectivity was total, the productivities ($\text{mol}_{\text{product}} \text{g}_{\text{cat}}^{-1} \text{h}^{-1}$) varied in a wide range as a function of the catalysts composition (chemical composition and atomic ratios of the constitutive support elements). The catalytic behavior was merely controlled by the size of gold particles, but the support also exerts an influence. The best results were obtained on the mesoporous Au/Ce₆₀-Ni₁₀-UVM-7 catalyst having a 0.97 (wt.%) gold content (in the form of nanoparticles of *ca.* 4 nm) and preserving a relatively high surface area (566 m²/g) and pore volume (0.91 cm³/g). The comparison with the individual or bicomponent catalysts led to the conclusion of a cooperative interaction between the catalyst components. However, gold itself exhibits a higher activity than the promoters or co-catalysts (*i.e.* phases containing Ni and/or Ce).

Introduction

Catalytic selective oxidation of benzylamine to correspondent imine is an important reaction in organic chemistry since the product of reaction is a valuable intermediate in organic synthesis¹. Imines, due to their reactivity, have multiple applications^{2,3} as building blocks for the manufacture of fine chemicals, pharmaceuticals⁴, agrochemicals, dyes, polymers⁵, lipoxygenase inhibitors, anti-inflammatory and anti-cancer agents⁶. They can undergo a large variety of transformations including hydrogenations, cycloaddition and nucleophilic addition⁷.

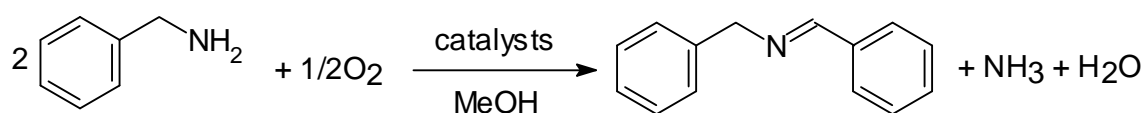
Traditionally, aerobic oxidative condensation of benzylamines to imines is performed using stoichiometric amounts of oxidants^{8,9} or by condensation of carbonyl compound with amines in the presence of a Lewis acid catalyst: TiCl₄, Al₂O₃, MgSO₄, K-10⁶. Due to the recent consideration of environmental issues, the use of stoichiometric reactive is undesirable⁹. In addition, some disadvantages such as complex procedures, long reaction time, high temperatures and use of aromatic solvents¹⁰ led to the development of catalytic systems which use organic and inorganic peroxides as oxidants¹¹. A green alternative is the use of oxygen as final oxidant. Unfortunately, the reactivity of molecular oxygen is difficult to be controlled, and as a consequence, the selectivity of the reaction is rather low⁴. Aerobic oxidative condensation of benzylamine leads to a Schiff base through the oxidative dehydrogenation of primary

amine and, consequently, to condensation with a second molecule of the unreacted amine¹². This reaction takes place in the presence of various catalysts, such as: Au/CeO₂¹³, Au/TiO₂, Au/C, Au/Al₂O₃¹⁴, Pd/TiO₂, Pt/TiO₂^{7,15}, CuCl, CuCl₂¹⁶, gold powder¹⁷, rhodium complexes⁶, Au, Au-Pd and Pd supported on porous steel fiber matrices⁸, and doped polyaniline emeraldine salt¹⁸. Results for this reaction conducted under ultrasound irradiation in the presence of solid supported catalysts (clay, silica or resin)¹⁹ or under photochemical irradiation with the use of molecular oxygen in the presence of acridinium salts²⁰, mesoporous graphite carbon nitride²¹, or TiO₂ as photocatalysts were reported as well. In addition, working under microwave irradiation allows the solvent-free synthesis of imines, but this method is limited to a few compounds. Moreover, it uses magnesium perchlorate as the catalyst, which is known for its potentially explosive character¹⁰. Recent advances on the aerobic oxidation of amines have been discussed in several review papers including the results achieved by using gold-based catalysts^{22,23}. The relevance of these nano-gold catalysts in fine chemical synthesis has been also reviewed²⁴.

Supported gold nanoparticles were reported to exhibit high activity in the selective aerobic oxidative condensation of benzylamines to N-benzylidenebenzylamine. Obviously, using gold as the catalyst, in addition to the particle size (typically less than 5 nm, the gold catalyst efficiency increased exponentially as the average gold particle decreased)^{7,14,15,17,25-28} the nature of the support is very important^{7,23,29-31}. Indeed, a series of supports such as reducible Co₃O₄, ZnO, TiO₂, Fe₂O₃, and nanocrystalline Ce₂O₃ reducible oxides but also carbons have been indicated as being adequate for preparing highly active gold-supported catalysts, while others such as non-reducible oxides SiO₂ and Al₂O₃ were reported to be less efficient²⁶. In a recent paper Wachs and Routray indicated that NiO exhibited surface active sites and reactivity in oxidation reactions close to ceria³². In another recent report, the peculiar influence of a NiO support was studied by preparing supported gold catalysts where Au nanoparticles showed high activity for the selective oxidation of glycerol and ethane-1,2-diol. A detailed characterization of the resulting Au catalysts revealed a preferential deposition of the metal nanoparticles on the NiO phase³³. On the other hand, Au/Ni₂O₃ was indicated as an efficient catalyst for low-temperature

gas-phase oxidation of alcohols³⁴. Au supported on tin oxides also showed interesting oxidation properties. Gold-supported tin dioxide nanocatalysts are active for low-temperature CO oxidation³⁵, while gold nanoparticle doped hollow super-symmetric SnO₂ nanostructures demonstrated improved photocatalytic properties³⁶.

Taking into account the state of the art (*i.e.* the role of the size of gold nanoparticles in this reaction and of reducible nano-oxide supports and of NiO in selective oxidation), herein we propose new materials for aerobic oxidative condensation of benzylamine to N-benzylidenebenzylamine (Scheme 1) that can achieve high conversions and selectivities in a very short range of time. The new gold-based catalysts are considered a more complex support. In this study we prepared Ni and Ce (or Sn) oxide nanodomains partially embedded inside mesoporous UVM-7 silica walls as effective and stable inorganic anchors favoring the nucleation, growth and stability of supported gold particles. Following the atrane method (a “one-pot” strategy able to harmonize the hydrolytic reactivity of different inorganic precursors)³⁷ the stability of the oxide nanodomains during oxidation and thermal treatments was ensured. After the deposition of gold using the deposition-precipitation procedure, gold nanoparticles in direct interaction with the Ni and Ce (or Sn) oxide nanodomains were generated. The versatility of the preparative approach used allows us to exploit both the high surface area and the accessibility of mesoporous silica and also an easy and homogeneous inclusion of heteroelements in one pot.



Scheme 1. Aerobic oxidative condensation of benzylamine to N-benzylidenebenzylamine.

Experimental details

Catalysts preparation

All the synthesis reagents were analytically pure and were used as received from Aldrich: tetraethyl orthosilicate (TEOS), nickel nitrate, cerium and tin chlorides, triethanolamine (hereinafter TEA), cetyltrimethylammonium bromide (CTMABr) and $\text{HAuCl}_4 \cdot 3\text{H}_2\text{O}$.

All of the catalysts were prepared in a two-step synthesis in which gold was incorporated through impregnation of the previously synthesized bimodal porous silicas containing different heteroelements. In order to analyze the effect of the different species included inside the pore walls, we have prepared materials containing (in addition to Si) only Ni (Ni_x -UVM-7 materials), Ni and Ce (Ce_y - Ni_x -UVM-7) and Ni and Sn (Sn_y - Ni_x -UVM-7). Heteroelement incorporation inside the silica walls was carried out using the atrane method³⁷. This one-pot method is based on the use of complexes (detected through mass-spectral analysis) that include TEA-related ligand species (*i.e.* “atranes” of Si, Ni, Ce and Sn in the present case) as hydrolytic inorganic precursors and surfactant micelles as templating agents able to generate mesopores after their evolution. In all cases the use of TEA plays a double role: as a ligand to form the atranes and as a buffer agent to stabilize the pH around 9-10, favoring the isolation of a bimodal nanoparticle rich silica support^{38,39}. A typical synthesis of support Ce_{10} - Ni_{10} -UVM-7 (see Table 1) can be described as follows: (1) a mixture of TEOS (11 mL, 0.045 mol), CeCl_3 (1.84 gr, $4.94 \cdot 10^{-3}$ mol) and $\text{Ni}(\text{NO}_3)_2 \cdot 6\text{H}_2\text{O}$ (1.43 gr, $4.94 \cdot 10^{-3}$ mol) was slowly added to a solution of TEA (23 mL, 0.17 mol) and heated at 150 °C for 10 min to give a mixture of atrane complexes. After cooling of the previous solution to 90 °C, CTMABr (4.77 g, 0.014 mol) was added and dissolved. This last solution containing the atrane complexes and the template was cooled to 60 °C and mixed with water (80 mL, 4.44 mol). After a few seconds, a white powder appeared and it was allowed to age at room temperature for 4 h. The final mesostructured powder was filtered off, washed with water and ethanol, and air-dried. Finally, surfactant removal was accomplished through calcination at 550 °C (ramp heating: 1 degree/min) for 7 h. In all cases, the molar ratio of the reagents in the mother liquor was adjusted to 2 Si: *a* Ni: *b* Ce or Sn: 7

TEA: 0.52 CTMABr: 180 H₂O (where $a = 0.033, 0.066$ and 0.2 , and $b = 0$ for samples Ni_x-UVM-7; $a = 0.2$, and $b = 0.033, 0.066$ and 0.2 for samples denoted as Ce(Sn)_yNi₁₀-UVM-7). Some samples are denoted as Ce(Sn)_y-Ni_x-UVM-7, where x and y are the Si/Ni and Si/Ce(Sn) nominal atomic ratios, respectively. Regardless of the nature and composition of the support, gold incorporation was carried out by the same procedure.

Table 1. Analytical and textural data for the Ce(Sn)_y-Ni_x-UVM-7 mesoporous supports.

Sample	Si/Ni ^a	Si/M ^a	Si/Ni ^b	Si/M ^b	S _{BET} (m ² /g)	Mesopore		Large pore	
						Size ^c (nm)	Vol. ^c (cm ³ /g)	Size ^d (nm)	Vol. ^d (cm ³ /g)
Ni ₆₀ -UVM-7	60	-	78	-	1195	2.95	0.99	56.2	1.51
Ni ₃₀ -UVM-7-	30	-	55	-	1061	2.92	0.99	53.3	0.88
Ni ₁₀ UVM-7	10	-	42	-	1011	2.90	0.98	41.3	0.63
Ce ₆₀ -Ni ₁₀ -UVM-7	10	60	43	62	990	3.00	0.88	48.1	0.30
Ce ₃₀ -Ni ₁₀ -UVM-7	10	30	44	38	983	2.97	0.83	43.9	0.29
Ce ₁₀ -Ni ₁₀ -UVM-7	10	10	42	16	850	3.01	0.71	41.5	0.21
Sn ₆₀ -Ni ₁₀ -UVM-7	10	60	46	64	972	3.00	0.92	42.0	0.38
Sn ₃₀ -Ni ₁₀ -UVM-7	10	30	43	24	932	2.98	0.82	39.1	0.35
Sn ₁₀ -Ni ₁₀ -UVM-7	10	10	42	8	755	2.68	0.65	32.2	0.33

^a Si/Ni, Si/Ce and Si/Sn molar ratio in the mother liquor. M= Ce or Sn. ^b Si/Ni, Si/Ce and Si/Sn molar ratio values in the solids from EPMA and ICP-OES. M= Ce or Sn. ^c Mesopore volume values and mesopore diameters calculated by using the BJH model on the adsorption branch of the isotherms for $P/P_0 < 0.75$. ^d Large textural-type pore volume values and diameters calculated by using the BJH model on the adsorption branch of the isotherms for $P/P_0 > 0.75$.

Gold was incorporated through deposition-precipitation in aqueous HAuCl₄·3H₂O solutions⁴⁰. The porous supports (1 g) were suspended in an aqueous solution (10 mL) of HAuCl₄·3H₂O (2%). The pH was adjusted to 8-9 with an aqueous NaOH solution and the solution was then aged for 1 h under stirring at 75°C. In fact, at the working pH, Au(OH)₄⁻ species are dominant^{41,42}. The low isoelectric point of the silica surface (*ca.* 2–3) hinders the interaction with anionic species. Au(OH)₄⁻ complexes require a positively charged surface provided by NiO_x and CeO₂ anchoring

nanodomains having zpc values in the range 9.9–11.3 and 6.7–8.6, respectively. As occurs for the silica surface, no anchoring effects are expected for the SnO₂ domains taking into account its relatively low zpc value (4.5–5). Then, Au complexes will interact in a preferred way on the NiO_x nanodomains embedded inside the mesopore walls instead of on the silica surface and to a lesser extent on the CeO₂ particles. The resulting homogeneity and dispersion of gold particles will reflect those achieved for NiO_x anchors.

The solids were filtered and exhaustively washed with water to favor the evolution of the adsorbed Cl⁻ species, which usually leads to catalysts poisoning. Finally, the solid was dried at 80°C overnight and calcined at two different temperatures, 200 or 500°C, for 1h in static air to favor the reduction of the Au complexes and the formation of gold nanoparticles.

In this way, three families of gold catalysts were obtained: Au/Ni₁₀-UVM-7(*T*), Au/Ce_x-Ni₁₀-UVM-7(*T*) and Au/Sn_x-Ni₁₀-UVM-7(*T*) (*T*= 200, 500°C). Table 1 summarizes the main synthesis variables and physical data. XPS analysis indicated no residual chlorine in the prepared catalysts.

For comparison, we synthesized two additional gold-containing catalysts by impregnation of silica UVM-7 and commercial CeO₂ with a HAuCl₄·3H₂O solution following the strategy described in the literature^{43,44}. The loading of gold in these catalysts was of the same order as that in the multicomponent catalysts, *i.e.* 1.25 wt % and 1.19 wt.%, respectively.

Catalysts characterization

Chemical analysis of the samples was carried out using electron probe microanalysis (EPMA, Philips SEM 515 instrument) and ICP-OES analysis (Agilent 710 Series ICP-OES). Powder X-ray diffraction patterns were recorded with a Seifert 3000TT θ - θ diffractometer using CuK α radiation. Patterns were collected in steps of 0.02° (2 θ) over the angular ranges 1°–10° (2 θ) or 10°–80° (2 θ) for 25 s per step. TEM and HRTEM microstructural characterizations was carried out using a JEOL JEM-1010 instrument operating at 100 kV and equipped with a CCD camera and a Tecnai G2F20 (FEI) instrument, respectively. STEM-HAADF images were acquired on a JEOL-2100F

microscope, and particle size distributions were determined from a total number of gold particles counted in the 300-400 range. The N₂ adsorption–desorption isotherms were recorded at –196 °C using a Micromeritics ASAP2020 automated instrument. Calcined samples were degassed for 15 h at 130 °C and 10^{–6} torr before analysis. Surface areas were estimated according to the BET model, and pore size dimensions were calculated using the BJH method. XPS spectra for both fresh and tested catalysts were recorded at room temperature using a SSX-100 spectrometer (Model 206, Surface Science Instruments). The pressure in the analysis chamber during the analysis was 1.33 mPa. Monochromatized Al-K α radiation ($h\nu = 1486.6$ eV) generated by bombarding the Al anode with an electron gun operated with a beam current of 12 mA and acceleration voltage of 10 kV has been used. The spectrometer energy scale was calibrated using the Au 4f_{7/2} peak centered at 83.98 eV. Charge correction was made referenced to the C1s signal of adventitious carbon (C – C or C – H bonds) located at 284.8 eV. Atomic surface compositions were calculated using the sensitivity factors provided with the apparatus software and applied to the surface below the corresponding fitted XPS signals. An estimated error of ± 0.1 eV can be assumed for all measurements. The zeta potential of selected samples was measured at 25 °C using dynamic light scattering (Malvern Zetasizer Nano ZS instrument).

Catalytic tests

Catalytic activity tests were performed under batch conditions in the temperature range of 75°C - 115°C. Experiments were performed in a 100 mL stainless steel autoclave provided with a magnetic stirrer, using an amount of 18.2 mmoles benzylamine (Sigma-Aldrich), and 0.12 mol methanol (Sigma-Aldrich) as solvent and a pressure of 5 bar O₂ (Linde). *Note that in the presence of an ignition source, such as a spark or flame, there is a risk of explosion! Extreme precaution is necessary to avoid danger.* The amount of the catalyst introduced in the reaction corresponded to 2x10^{–5} mol of heteroelement (Ni, Ce, Sn). Diffusion constraints were checked using catalysts with particles size between 170 and 400 μ m and modifying the stirring rate in the range 0-1400 rpm. Particles size of 200 μ m and a stirring rate of 1200 rpm eliminated

any diffusional effects as has been proved from the variation in the conversion. After 0.5-5 h reaction time the autoclave was cooled and the catalyst separated by filtration. The liquid sample was analyzed by GC-MS using a Trace GC 2000 coupled with DSQ MS from Thermo Electron Corporation equipped with FID detector, a capillary column with DB5 stationary phase (30m length and 0.324 mm diameter), and highly pure N₂ (99.999%) as carrier gas. Ammonia resulting as by-product was analyzed using a Dionex ICS3000 ion-chromatograph (Thermo) equipped with a medium hydrophobic Dionex Ionpac CS18 analytical column using a 4 mM isocratic methanesulfonic acid eluent at a flow rate of 0.25 mL/min. The reproducibility of the results was carefully checked using the above analytic tools.

The performance of the catalysts was compared based on the conversion of benzylamine and the selectivity to *N*-benzylidenebenzylamine. Since the reaction occurs at different rates on all the individual components the calculation of TOF for the multicomponent catalysts will change its meaning because the calculated value will correspond to a mean average value of all these components. Thus, to avoid any misinterpretations of the activity we calculated the productivity of catalysts as $\text{mol}_{\text{product}} \text{g}_{\text{cat}}^{-1} \text{h}^{-1}$ and the results were interpreted using this parameter consider as g_{cat} is the entire mass of the components exhibiting catalytic activity (Ni, Ce, Sn and Au) (see Table 2 and 3). However, for comparison, TOF values were calculated for the gold-containing catalysts, considering only the contribution of Au.

Blank experiments were performed using the same experimental set-up and the same range of temperatures (75°C - 115°C) using 18.2 mmol of benzylamine, 0.12 mol of methanol as solvent and a pressure of 5 bar O₂. In order to support the reaction mechanism additional experiments were carried out in the range of O₂ pressure of 1-5 bars, and experiments in which benzaldehyde was added to the reaction mixtures in the different stages of the reaction. In this respect benzylamine-to-benzaldehyde molar ratios between 5 and 1 were considered. Water has been also introduced in separate experiments in volumes of 1-20 μL using a chromatographic syringe.

Table 2. Analytical and textural data for the Au/Cey-Nix-UVM-7 mesoporous catalysts.

Sample	Si/ Ni ^a	Si/ Ce ^a	Au ^b (wt.%)	Gold ^c (nm)	S _{BET} (m ² /g)	Mesopore		Large pore	
						Size ^d (nm)	Vol. ^d (cm ³ /g)	Size ^e (nm)	Vol. ^e (cm ³ /g)
Au/Ni ₁₀ -UVM-7(200)	42	-	0.96	4.0±1.3	653	2.5	0.62	47.6	0.36
Au/Ce ₆₀ -Ni ₁₀ -UVM-7(200)	47	67	0.97	3.9±1.2	566	2.5	0.56	49.3	0.35
Au/Ce ₃₀ -Ni ₁₀ -UVM-7(200)	44	38	1.05	4.2±1.4	518	2.6	0.52	48.6	0.18
Au/Ce ₁₀ -Ni ₁₀ -UVM-7(200)	42	16	1.20	4.3±1.2	455	2.6	0.45	40.4	0.26
Au/Ni ₁₀ -UVM-7(500)	42	-	0.96	4.4±1.2	603	2.4	0.47	36.1	0.33
Au/Ce ₆₀ -Ni ₁₀ -UVM-7(500)	47	67	0.97	4.3±1.5	473	2.4	0.45	43.2	0.26
Au/Ce ₃₀ -Ni ₁₀ -UVM-7(500)	44	38	1.05	5.1±1.7	484	2.4	0.40	40.5	0.23
Au/Ce ₁₀ -Ni ₁₀ -UVM-7(500)	42	16	1.20	4.9±1.6	470	2.4	0.40	38.0	0.17

^a Si/Ni and Si/Ce molar ratio values in the solids from EPMA and ICP-OES. ^b Percentage weight of gold determined by atomic absorption. ^c Gold particle size determined through HAADF. ^d Mesopore volume values and mesopore diameters calculated by using the BJH model on the adsorption branch of the isotherms for $P/P_0 < 0.75$. ^e Large textural-type pore volume values and diameters calculated by using the BJH model on the adsorption branch of the isotherms for $P/P_0 > 0.75$.

Table 3. Analytical and textural data for the Au/Sny-Nix-UVM-7 mesoporous catalysts.

Sample	Si/ Ni ^a	Si/ Ce ^a	Au ^b (wt.%)	Gold ^c (nm)	S _{BET} (m ² /g)	Mesopore		Large pore	
						Size ^d (nm)	Vol. ^d (cm ³ /g)	Size ^e (nm)	Vol. ^e (cm ³ /g)
Au/Sn ₆₀ -Ni ₁₀ -UVM-7(200)	47	64	1.22	4.5±1.5	712	2.6	0.67	48.4	0.39
Au/Sn ₃₀ -Ni ₁₀ -UVM-7(200)	43	24	1.15	4.8±1.5	675	2.7	0.63	46.6	0.48
Au/Sn ₁₀ -Ni ₁₀ -UVM-7(200)	42	8	1.10	4.9±1.4	628	2.6	0.54	42.0	0.41
Au/Sn ₆₀ -Ni ₁₀ -UVM-7(500)	46	64	0.98	5.5±1.6	592	2.4	0.58	43.9	0.33
Au/Sn ₃₀ -Ni ₁₀ -UVM-7(500)	43	24	1.15	5.3±1.5	654	2.5	0.54	42.3	0.38
Au/Sn ₃₀ -Ni ₁₀ -UVM-7(500)	42	8	1.10	5.3±1.5	561	2.5	0.52	41.8	0.39

^a Si/Ni and Si/Sn molar ratio values in the solids from EPMA and ICP-OES. ^b Percentage weight of gold determined by atomic absorption. ^c Gold particle size determined through HAADF. ^d Mesopore volume values and mesopore diameters calculated by using the BJH model on the adsorption branch of the isotherms for $P/P_0 < 0.75$. ^e Large textural-type pore volume values and diameters calculated by using the BJH model on the adsorption branch of the isotherms for $P/P_0 > 0.75$.

To check the effect of water experiments with dried methanol (Sigma-Aldrich, puriss.pa.), benzylamine (dried with 3 Å molecular sieves), and O₂ (passed on a 3 Å molecular sieves column) were also carried out.

Results and discussion

Characterization

Tables 1-3 compile the analytical and textural characterization of the investigated samples. Regarding the gold-free Ce(Sn)_y-Ni_x-UVM-7 mesoporous supports, summarized in Table 1 are the corresponding Si/Ni, Si/Ce and Si/Sn molar ratio values (averaged from data of about 50 different particles) of the resulting solids from EPMA and ICP-OES. All samples are chemically homogeneous at micrometric level with a regular dispersion of Ni, Ce and Sn species (and silicon) throughout the inorganic walls at the spot size (*ca.* 1µm). EPMA shows that the reported Ce(Sn)_y-Ni_x-UVM-7 materials contain Si/Ce or Si/Sn molar ratios similar to those present in the mother solutions. This indicates that, in general, there is no preferential incorporation of Ce (or Sn) or Si into the final porous walls. This behavior is related to the low solubility of Ce or Sn species under the working pH conditions⁴², and the consequently quick and easy formation of the respective oxides. On the contrary, the Ni content in the final solids is significantly lower than that present in the starting solutions. This fact could be tentatively attributed to the well-known affinity of nickel for nitrogen donors. It must be pointed out that, in aqueous solution, TEA essentially behaves as a tertiary amine, and a certain amount of nickel could be stabilized in solution in the form of Ni-TEA complexes. A similar tendency was observed in the case of Co-MCM-41 derivatives⁴⁵.

All supports display low-angle XRD patterns with one strong peak and one broad signal of relatively low intensity (Figure S1), which can be associated to the (100) and the overlapped (110) and (200) reflections of a MCM-41-like hexagonal cell, respectively. These patterns are characteristic of hexagonal disordered UVM-7 mesoporous silicas. The observed regular and smooth shift of the (100) intense peak

towards low $2\theta(^{\circ})$ values as the heteroelement content increases suggests a certain growing process of the mesoporous wall sizes due to the incorporation (completely embedded or partially trapped) of the NiO_x , CeO_2 and SnO_2 nanodomains (as can be seen below, the BJH pore size results are practically unchanged). High-angle XRD patterns (Figure S2 and S3) show appreciable differences dealing with the incorporation of the three heteroelements. Regardless of the Ni, Ce or Sn content, no signals assigned to NiO_x oxides appear in the diffractograms. This is due to the good dispersion of Ni along the porous walls in the form of extremely low size nanodomains (<2 nm) as occurs for the incorporation of Co and Zn under similar conditions^{46,45}. On the contrary, even for the samples with lower Ce amount, we unambiguously observe several diffraction peaks due to the presence of crystalline CeO_2 particles. The intensity of these peaks increases while the *fwhm* decreases with the Ce content, as expected. This behavior is consistent with the high insolubility of ceria. Then, before blocking by the silica-surfactant mesostructure, the growth achieved by CeO_2 domains seems to be higher than those achieved for the NiO_x ones. An intermediate situation is observed for tin incorporation. In this case, only for the Sn-rich supports SnO_2 diffraction peaks are appreciated. The low intensity and large *fwhm* of the SnO_2 peaks are indicative of very small crystallite sizes.

TEM images allow discarding segregation of non-porous oxides (NiO_x , CeO_2 or SnO_2) in the form of large particles (Figure 1). Images of medium magnification confirm the absence of non-porous particles that could be ascribed to Ni, Sn or Ce oxide. In fact, TEM images of the $\text{Ce}(\text{Sn})_y\text{-Ni}_x\text{-UVM-7}$ supports (Figure S4 and 1) are very similar to those of pure UVM-7 silica and confirm that two pore systems are present: intra-particle mesopores (white spots in the TEM images; insets of Figure S4 and 1) and large inter-particle pores of textural-type. Changes in Ni content do not affect the UVM-7 morphology. Then, in the case of $\text{Ni}_x\text{-UVM-7}$ supports (Ce or Sn-free samples) the TEM images are practically indistinguishable from those of UVM-7 silica. As the Ce or Sn content increased, although the UVM-7 morphology is preserved, we observe two effects that principally affect the textural porosity: (a) a wider size distribution in the primary silica-based particles, and (b) a higher inter-particle condensation (this favoring aggregation), when compared to pure UVM-7 or $\text{Ni}_x\text{-UVM-7}$ supports.

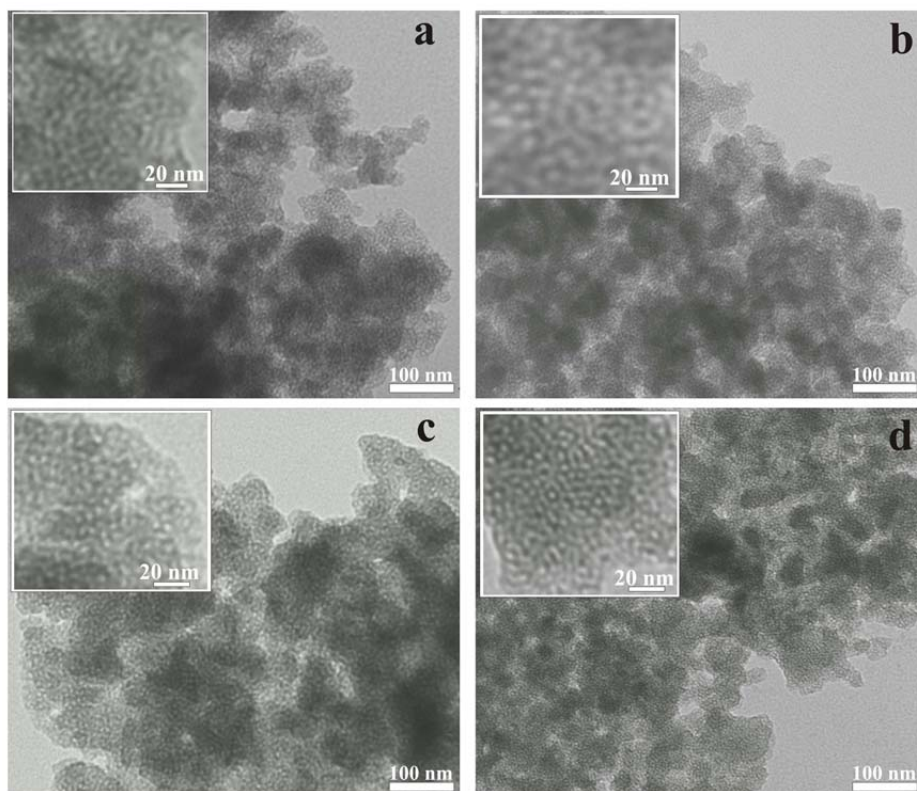


Figure 1. TEM images of (a) Ce₁₀-Ni₁₀-UVM-7, (b) Ce₆₀-Ni₁₀-UVM-7, (c) Sn₁₀-Ni₁₀-UVM-7 and (d) Sn₆₀-Ni₁₀-UVM-7.

On the other hand, the above-mentioned absence of large-scale NiO_x, SnO₂ or CeO₂ segregation suggests that these particles must be basically present in the form of small nanodomains partially embedded inside the silica-based pore walls. TEM images display numerous small black spots with spherical or pseudo-spherical shapes with dimensions in the 2-7 nm range. Then, although a small segregation in the form of micrometric particles cannot be completely discarded (overcoat in the case of CeO₂), TEM micrographs are consistent with a homogeneous nanodispersion of Ni, Sn and Ce oxidic domains forming together with the amorphous silica mesopore walls.

The preservation of a certain bimodal porosity of our supports is further illustrated by N₂ adsorption-desorption isotherms (Figure S5). All curves show, a well-defined adsorption step at intermediate relative pressure ($0.2 < P/P_0 < 0.4$ range;

corresponding to the filling of the intra-particle mesopores), and a second adsorption step, at a high relative pressure, due to the filling of the inter-particle large textural pores. The progressive reduction of this second adsorption step with the Ce and Sn content is related to the previously mentioned enhanced inter-particle condensation (with the subsequent decrease in the inter-particle voids). As the heteroelement content increases, BET surface area and pore volume slightly decrease in a progressive way (see Table 1). On the other hand, the progressive incorporation of heteroelements practically does not affect the mesopore size of the final materials. Then, in the light of the results, all samples can really be considered as high surface area materials without significant pore blocking associated to the incorporation of oxidic nanoparticles.

Gold was incorporated through deposition-precipitation in aqueous $\text{HAuCl}_4 \cdot 3\text{H}_2\text{O}$ solutions (2 %) using strictly the same protocol for all supports. In all cases, a similar proportion of inorganic anchors in the form of NiO_x domains exists (Si/Ni molar ratios in the 42-47 range) (Tables 2 and 3). The amount of gold incorporated increases in a gradual way from 0.96 to 1.20 (wt.%) with the Ce content. On the contrary, no clear evolution is observed with regard to the Sn-containing materials. This behavior is probably due to the different *zpc* of CeO_2 (6.7-8.6) and SnO_2 (4.5-5). At the working pH (*ca.* 8-9), while a negative charge is expected for the SnO_2 surface, some residual positive charge will remain for the CeO_2 surface. Then, as mentioned above, CeO_2 domains cooperate with NiO_x (*zpc* in the 10.3-11.1 range depending on the hydroxylation surface degree) both acting as effective anchors to interact with $\text{Au}(\text{OH})_4^-$ anionic species. We have measured *zpc* values of 2.4, 2.7 and 2.9 for UVM-7, Ni_{10} -UVM-7 and Ce_{60} - Ni_{10} -UVM-7 supports, respectively. We observe an increase of the *zpc* value due to the presence of Ni and Ce as heteroelements. However, as the silica is the principal component in our composites, the presence of a relatively low proportion of NiO_2 and/or CeO_2 domains does not modify significantly the experimental *zpc* values. In any case, a certain local effect related to the *zpc* values of the different included oxides seems to be operative, which favors the adsorption of anionic gold complexes. On the other hand, EDX analysis performed on gold-containing catalysts allowed us to discard the presence of Cl^- species which is consistent with the exhaustive washing mentioned above.

The treatment for gold incorporation does not alter in a qualitative way the UVM-7-like architecture at the mesoscopic level. In fact, with the exception of the richest Sn material treated at 500°C, all Au/Ce(Sn)_y-Ni_x-UVM-7 catalysts display low-angle XRD patterns (Figure 2) with a signal or a shoulder associated with the (100) reflection. As observed in related systems, the intensity decrease of the (100) peak after gold inclusion must be attributed to a high phase-cancellation phenomenon associated with the introduction of scattering material (Au species) into the pore voids. The high-angle XRD patterns maintain the CeO₂ and SnO₂ peaks of the parent supports, but surprisingly, no signals attributed to metallic gold are observed (Figure S1 and S2) regardless of the calcination temperatures used (200 or 500°C). This fact is indicative of an extremely low particle size (< 5 nm) on the NiO_x or CeO₂ domains. The absence of XRD peaks associated with gold particles has also been reported for Au/CeO₂ catalysts having very small Au crystalline domains and/or low gold concentration (< 1wt. %) ⁴⁷.

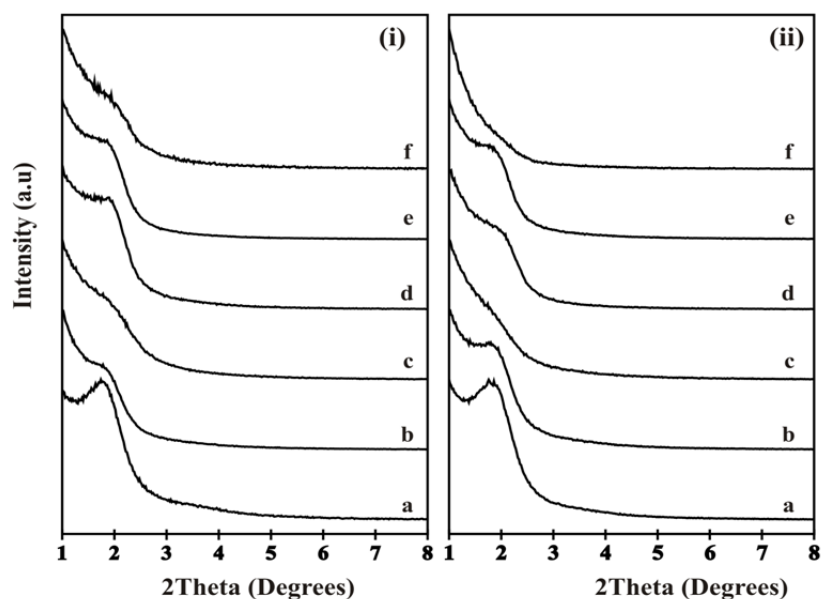


Figure 2. Low-angle XRD patterns of the gold-containing catalysts processed at (i) 200°C and (ii) 500°C. (a) Au/Ce₆₀-Ni₁₀-UVM-7, (b) Au/Ce₃₀-Ni₁₀-UVM-7, (c) Au/Ce₁₀-Ni₁₀-UVM-7, (d) Au/Sn₆₀-Ni₁₀-UVM-7, (e) Au/Sn₃₀-Ni₁₀-UVM-7 and (f) Au/Sn₁₀-Ni₁₀-UVM-7.

According to the XRD analysis, Au/Ce_y-Ni_x-UVM-7 catalysts show similar TEM images similar to those of the parent gold-free Ce(Sn)_y-Ni_x-UVM-7 supports (Figure 4 and 5). Apparently, there is no clear evidence on the gold incorporation from TEM images. At this point, only a small amount of white spots, probably ascribed to the largest gold particles, are detected by TEM. However, together with the chemical analysis, XEDS mapping supports not only the gold presence, but also the quality of the gold, nickel and ceria spatial distribution achieved in our catalysts treated at 200°C (Figure 3 and 4). A certain aggregation of Au and Ce(or Sn) is suggested by XEDS mapping carried out on samples calcined at 500°C, as expected.

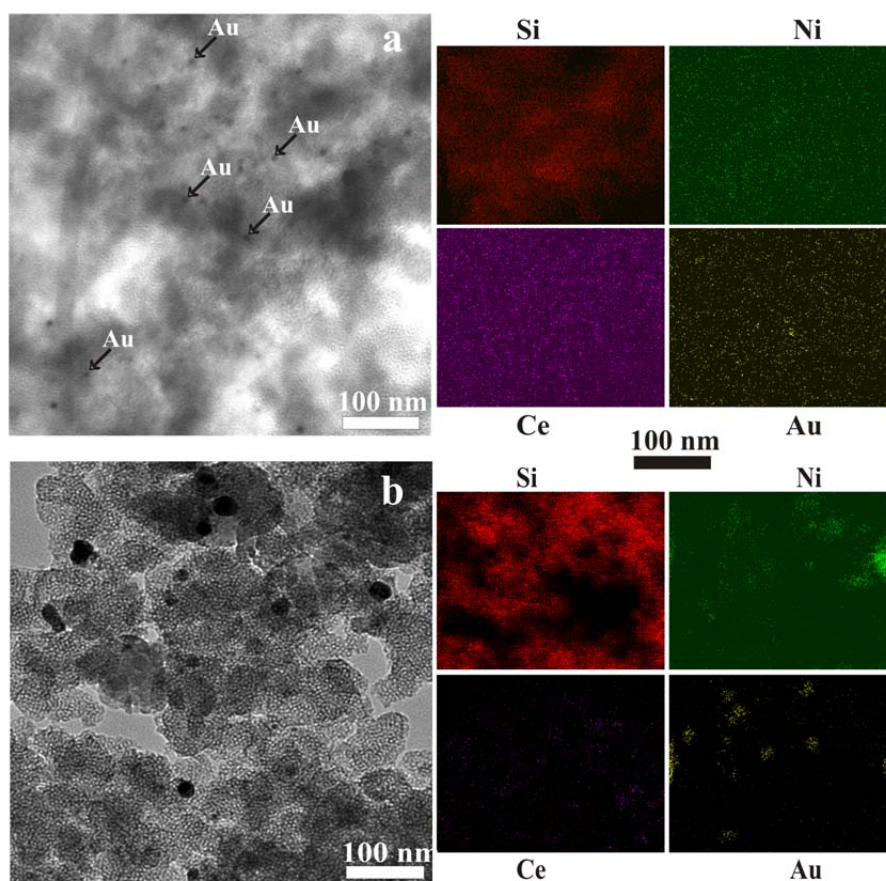


Figure 3. TEM and XEDS mapping of Au/Ce₁₀-Ni₁₀-UVM-7 catalyst treated at (a) 200°C and (b) 500°C.

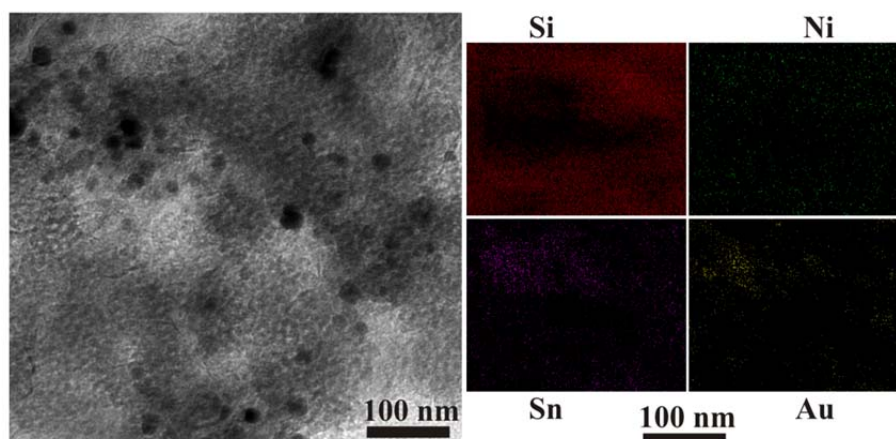


Figure 4. TEM and XEDS mapping of Au/Sn₁₀-Ni₁₀-UVM-7 catalyst treated at 500°C.

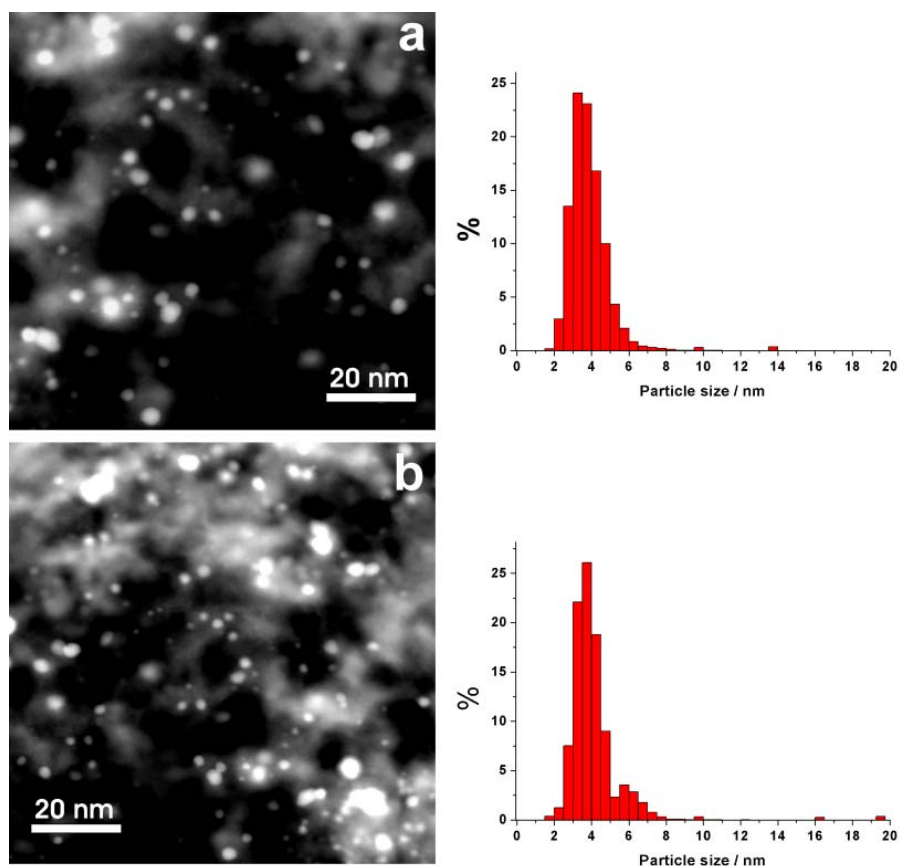


Figure 5. STEM-HAADF images and gold particle size distribution histograms of Au/Ce₆₀-Ni₁₀-UVM-7 catalyst (a) treated at 200°C, and (b) treated at 500°C.

At this point, we record STEM-HAADF images of the gold-containing catalysts in order to achieve higher contrast between the gold nanoparticles and the silica-based support. Gold particles (white dots) are fairly uniformly distributed over the support (gray regions) (Figure 5). Similar gold particle sizes (see Tables 2 and 3) and distributions have been obtained for Au/Ce_y-Ni_x-UVM-7 and Au/Sn_y-Ni_x-UVM-7 catalysts. The majority of gold particles show an average size in the 3-5 nm range according to the particle size distribution histograms (Figure 5). Moreover, a certain proportion of particles in the 5-7 nm range and even larger (*ca.* 20 nm) minority of gold domains (according to TEM images in Figures 3 and 4) can be observed in the samples heated at 500°C. This last behavior with temperature calcination is observed for all analyzed materials.

Then, slightly larger mean particle sizes have been measured for samples treated at 500°C when compared to catalysts processed at 200°C. On the other hand, HRTEM allows us to detect individual gold crystalline nanoparticles in the solids processed at 500°C (Figure 6). These particles show a *d* spacing of 0.23 nm, typical of fcc Au⁴⁸, measured on the image and confirmed through the FFT process. An average gold nanoparticle size in the 3-7 nm range has been determined through HRTEM. TEM analysis of Au-CeO₂ and Au-UVM-7 catalysts indicated larger gold particles, *i.e.* 5-11 nm. This small size of gold domains is consistent with the absence of XRD signals as discussed above.

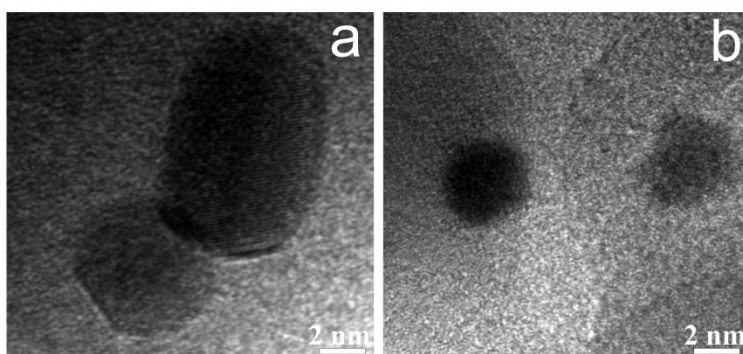


Figure 6. HRTEM images of (a) Au/Ce₁₀-Ni₁₀-UVM-7 and (b) Au/Sn₁₀-Ni₁₀-UVM-7 catalysts treated at 500°C and showing isolated gold nanoparticles.

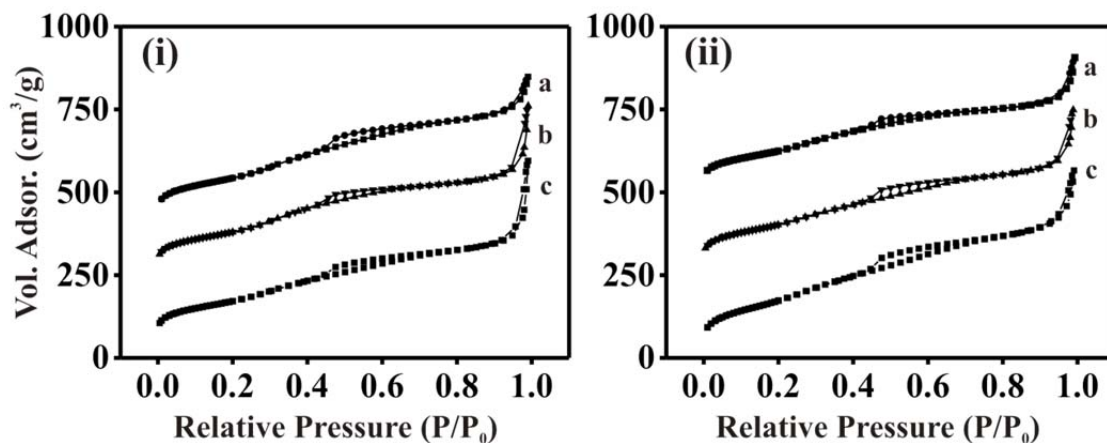


Figure 7. N₂ adsorption-desorption isotherms of catalysts (a) Au/Ce₁₀-Ni₁₀-UVM-7, (b) Au/Ce₃₀-Ni₁₀-UVM-7 and (c) Au/Ce₆₀-Ni₁₀-UVM-7, processed at (i) 200°C and (ii) 500°C.

The mesophase and porosity preservation after gold incorporation is further supported by N₂-adsorption-desorption isotherms (Figure 7 and 9). Regardless of the calcination temperature, all solids maintain the two adsorption steps reminiscent of the UVM-7 silica (although somewhat lower). BJH pore size distributions show a first peak at mesopore sizes in the 2-3 nm range and a second signal without a definite maximum (large textural pores) (Figure S5-8).

These features indicate that the simultaneous incorporation of Ni and Ce (or Sn) together with the pH conditions used for the gold incorporation favor inter-particle condensation through the formation of Si-O-Si, Si-O-M and M-O-M bonds (M= Ni, Ce or Sn). Moreover, we observe a decrease in adsorption capacity at high pressure for samples treated at 500°C. This suggests that additional inter-particle condensation is favored at higher temperature, as expected. In any case, all catalysts present high surface areas and pore volumes (Tables 2 and 3). In each series, the BET surface area and pore volume values slightly decrease with the Ce or Sn content (the nickel content can be considered as constant: $42 < \text{Si/Ni} < 47$). This effect is more pronounced in the case of the Ce-containing catalysts and could be tentatively attributed to the relatively greater size of the CeO₂ domains when compared to that of SnO₂ (according to XRD). Obviously, gold incorporation leads to a significant BET surface area and pore volume decrease when compared to those parameters of the respective parent gold-free

supports. Finally, dealing with the mesopore size, no significant changes are observed for each family. This is an expected behavior as no appreciable mesopore size changes were previously observed for the gold-free supports with the Ni, Ce and Sn content. However, two general tendencies can be mentioned: (a) BJH mesopore sizes decrease from *ca.* 3 to 2.5 nm after gold incorporation (due the inclusion of Au species inside the mesopores), and (b) an additional pore size decrease from *ca.* 2.5 to 2.3-2.4 nm occurs when samples were processed at 500°C (this effect seems to be related with silica condensation processes).

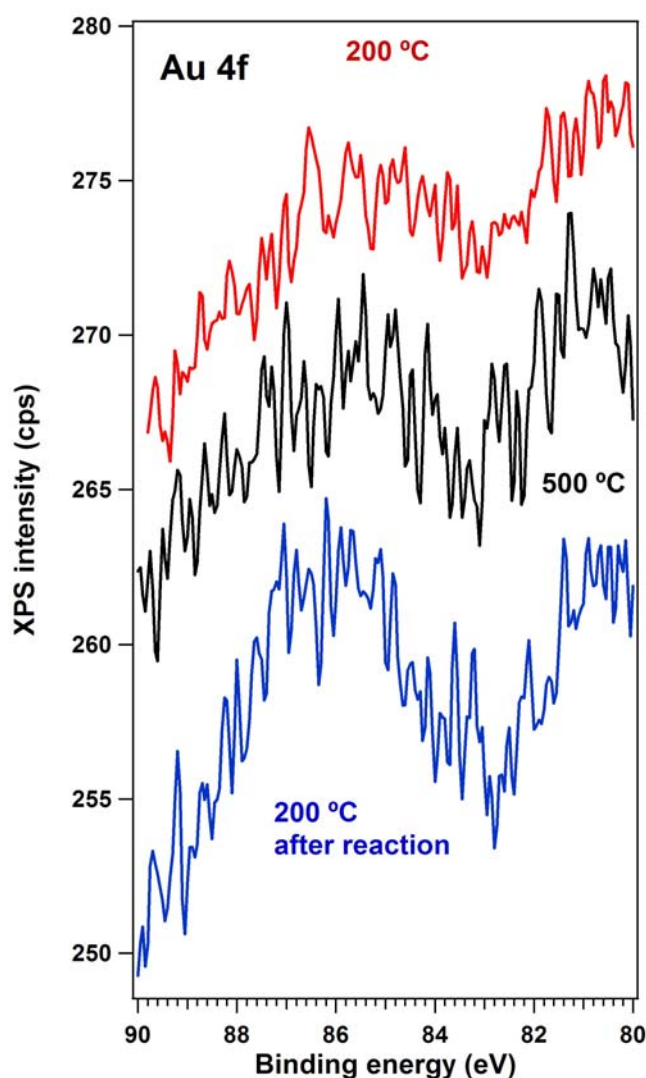


Figure 8. XPS spectra of Au/Ce₁₀-Ni₁₀-UVM-7(200) and Au/Ce₁₀-Ni₁₀-UVM-7(500) samples in the region of Au 4f level.

XPS spectra corresponding to fresh and tested Au/Ce₆₀-Ni₁₀-UVM-7(200) and Au/Ce₆₀-Ni₁₀-UVM-7(500) catalysts are presented in Figures 8-10. In addition, Table 4 compiles the binding energies of Au4f, Ce3d, Ni2p_{3/2}, O1s and N1s levels for the series of Ni-, Au-Ni-, Ce-Ni- and Au-Ce-Ni- catalysts. Typically, the main components of Au 4f_{7/2} peaks corresponding to the presence of gold in metallic state are centred at binding energies around 84.2 eV⁴¹, while higher than 84.5 eV indicates the presence of the electropositively charged Au states. Although the signal-to-noise ratio is very low due to the very small content and high dispersion of gold, the binding energies measured in Figure 10 denote for the investigated catalysts, according to the literature data, only the presence of oxidized Au species (Table 4)⁴⁹. For the spent samples no evident change occurred in the oxidation state of gold. However, the very low signal-to-noise ratio does not allow a comparison of atomic XPS and analytical Au/Si ratios as a function of catalyst composition or of calcination temperature.

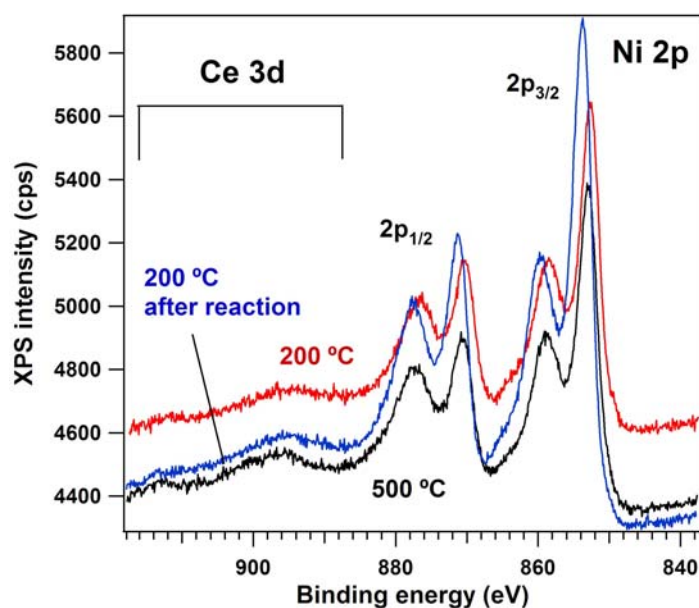


Figure 9. XPS spectra of Au/Ce₁₀-Ni₁₀-UVM-7(200) and Au/Ce₁₀-Ni₁₀-UVM-7(500) samples in the region of Ce 3d and Ni 2p levels.

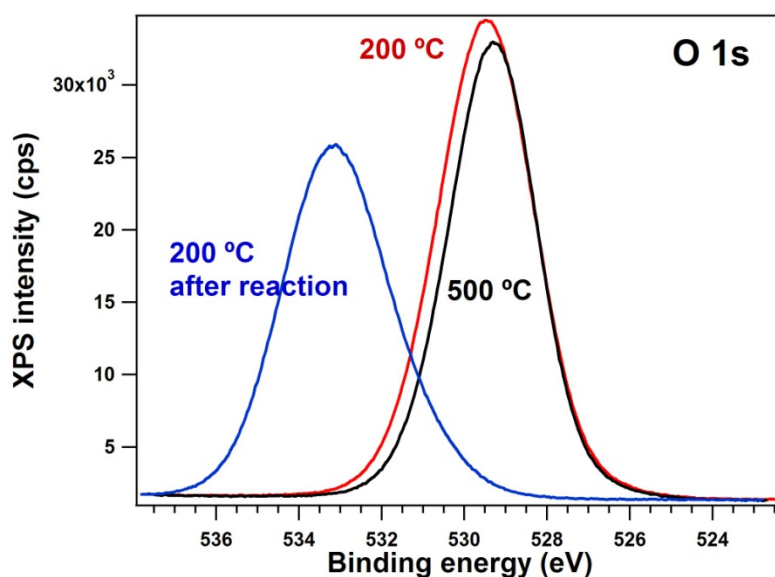


Figure 10. XPS spectra of Au/Ce₆₀-Ni₁₀-UVM-7(200) and Au/Ce₆₀-Ni₁₀-UVM-7(500) samples in the region of O 1s level.

The calcination at 500 °C and the exposure to reaction also caused an oxidation of nickel as evidenced by the values of the Ni2p_{3/2} and 2p_{1/2} energy levels for the investigated catalysts (Figure 9, Table 4)⁵⁰. These values demonstrate that for nickel both the thermal treatment and especially the exposure to the reaction led to an oxidation of the metal (for Au/Ce₆₀-Ni₁₀-UVM-7(200): BE of 852.5 and 858.4 eV, for Au/Ce₆₀-Ni₁₀-UVM-7(500): BE of 853.9 and 859.8 eV, and for the spent Au/Ce₆₀-Ni₁₀-UVM-7(200): BE of 853.7 and 859.7 eV). A certain aggregation is also suggested by Figure 9 for Ni. Also, an important shift of the binding energy was determined for the O1s level after the reaction (for Au/Ce₆₀-Ni₁₀-UVM-7(200): BE of 529.5 eV, for Au/Ce₆₀-Ni₁₀-UVM-7(500): BE of 529.3 eV, and for the spent Au/Ce₆₀-Ni₁₀-UVM-7(200): BE of 533.1 eV) (Figure 10).

This indicates that an evolution occurs in the surface oxygen species during the catalytic process from lattice to electrophilic oxygen (O⁻, O₂⁻) probably related to the formation of metal-OH bonds and the generation of anionic defects in the oxygen lattices^{51,52}. This evolution is consistent with the catalyst nature (amorphous and easily hydroxylated silica-based walls, and cerium oxide domains able to cycle easily between Ce³⁺ and Ce⁴⁺ with the subsequent oxygen transport) and the catalytic process (benzylamine oxidation). In addition, for the spent catalyst no band assigned to N1s was detected. No change in the position and the intensity of the bands assigned to

Ce3d (Figure 9, Table 4) or Si2p (for Au/Ce₆₀-Ni₁₀-UVM-7(200): BE of 103.4 eV, for Au/Ce₆₀-Ni₁₀-UVM-7(500): BE of 103.6eV, and for the spent Au/Ce₆₀-Ni₁₀-UVM-7(200): BE of 103.5 eV) was detected in these measurements. Obviously, the presence of the peak in the region of 913 eV or at higher energies is proof of the presence of Ce⁴⁺ species⁴⁵. Replacing cerium by tin or compositional changes does not alter the tendencies observed for the XPS spectra of Au/Ce₆₀-Ni₁₀-UVM-7 catalysts.

Table 4. XPS binding energies of Au4f, Ce3d, Ni2p_{3/2}, O1s and N1s levels and composition for Ni_x-, Ni_x-Cey-, and Au-Ni_x-Cey-UVM-7 catalysts.

Catalyst	XPS level Binding energy, eV					Atomic Au/Si ratio x 10 ³	
	Au4f _{7/2}	Ce3d _{5/2} / Ce3d _{5/2} shake up	Ni2p _{3/2}	O1s	N1s	XPS	Analytic
Ni ₆₀ -*	-	-	852.5	529.3	-	-	-
Ni ₃₀ -*	-	-	852.4	529.2	-	-	-
Ni ₁₀ -*	-	-	852.3	529.4	-	-	-
Ce ₆₀ -Ni ₁₀ -*	-	882.4/916.1	852.4	529.5	-	-	-
Ce ₃₀ -Ni ₁₀ -*	-	881.9/915.6	852.3	529.4	-	-	-
Ce ₁₀ -Ni ₁₀ -*	-	882.1/915.8	852.4	529.3	-	-	-
Au/Ni ₁₀ -*	86.0	-	852.5	529.4	-	3.41	3.10
Au/Ce ₆₀ -Ni ₁₀ -*	86.1	882.3/916.0	852.5	529.5	-	3.52	3.23
Au/Ce ₆₀ -Ni ₁₀ -***	86.2	882.5/916.2	853.7	533.1	-	3.46	3.23
Au/Ce ₃₀ -Ni ₁₀ -*	86.1	882.2/915.9	852.6	529.3	-	3.78	3.61
Au/Ce ₁₀ -Ni ₁₀ -*	86.2	882.3/916.0	852.6	529.2	-	4.29	4.52
Au/Ni ₁₀ -**	86.1	-	853.8	533.2	-	3.92	3.10
Au/Ce ₆₀ -Ni ₁₀ -**	86.2	882.3/916.0	853.9	533.3	-	4.01	3.23
Au/Ce ₃₀ -Ni ₁₀ -**	86.1	882.4/916.1	853.8	533.2	-	4.31	3.61
Au/Ce ₁₀ -Ni ₁₀ -**	86.1	882.2/915.9	853.8	533.2	-	5.02	4.52

*-calcined at 200 °C; **-calcined at 500 °C; ***-calcined at 200 °C after reaction.

Catalytic tests

Previous work of Corma and Garcia²⁸ using gold supported on various supports demonstrated that while the selectivity was almost not influenced by metal loading that implicitly meant particle size, the conversion of benzylamine to the desired imine was strongly influenced. In the series these authors have been investigated the nature of the support was less important.

Although in a small extent, blank experiments showed that this reaction proceeds, indeed with the formation of a secondary product (benzaldehyde), even in the absence of the catalyst (Table 4, entry 1). Metal-free oxidation of benzyl amines to imines was also recently reported working with oxygen⁵³ or with hydrogen peroxide⁵⁴. Like in our case the selectivity to imine was partial. A very similar result was obtained using pure siliceous UVM-7 support. CeO₂ led to a very low conversion and productivity, but again the reaction occurred selectively to imine (Table 5).

Previous studies on gold indicated that for this reaction the support nature has a relatively low influence, more important being the size of the metal particles⁷. Here we have firstly compared the activity of a Au-UVM-7 catalyst (Table 5, entry 14) with that of a supported Au/CeO₂ (Table 5, entry 15), the first one prepared by embedding Au colloids, and the second by impregnation of a cerium oxide support. Both catalysts exhibited comparable gold particle sizes (4 nm). Data presented in Table 5 (entries 14 and 15) show that the two catalysts had comparable productivities. Hence, the relatively small influence of the support nature was indeed reconfirmed for single oxide supports such as CeO₂ and SiO₂.

The experiments carried out in the presence of new multicomponent catalysts also led selectively to N-benzylidenebenzylamine. However, important differences in the activity expressed as productivity were determined as a function of composition (Table 5).

Table 5. Performances of the multicomponent catalysts in aerobic oxidative condensation of benzylamine to N-benzylidenebenzylamine.

Entry	Catalyst	Conversion, %		Selectivity, %	Productivity $\text{mol}_{\text{product}} \text{g}_{\text{cat}}^{-1} \text{h}^{-1}$		TOF 4h
		75°C	115°C		75°C	115°C	115°C
1	Blank experiment*	4.8	6.1	87**			
2	Ni ₁₀ -UVM-7	7.4	9.2	100	2.12	2.64	
3	Ni ₃₀ -UVM-7	6.9	8.6	100	1.40	1.75	
4	Ni ₆₀ -UVM-7	6.2	7.4	100	0.96	1.15	
5	CeO ₂	5.6	-	100	0.03	-	
6	Ce ₆₀ -Ni ₁₀ -UVM-7	43.6	47.5	100	2.81	3.05	
7	Ce ₃₀ -Ni ₁₀ -UVM-7	41.6	46.9	100	1.61	1.82	
8	Ce ₁₀ -Ni ₁₀ -UVM-7	39.8	43.9	100	1.04	1.15	
9	Sn ₆₀ -Ni ₁₀ -UVM-7	16.2	22.7	100	1.17	1.64	
10	Sn ₃₀ -Ni ₁₀ -UVM-7	15.8	20.9	100	0.60	0.80	
11	Sn ₁₀ -Ni ₁₀ -UVM-7	14.8	20.0	100	0.26	0.35	
12	Au/Ni ₁₀ -UVM-7(200)	30.1	41.8	100	3.52	4.89	
13	Au/Ni ₁₀ -UVM-7(500)	28.8	39.4	100	3.37	4.61	
14	Au-UVM-7	4.9	6.5	100	2.10	2.78	456
15	Au-CeO ₂	18.5	23.7	100	2.08	2.67	458
16	Au/Ce ₆₀ -Ni ₁₀ -UVM-7(200)	71.5	99.4	100	4.04	5.62	919
17	Au/Ce ₃₀ -Ni ₁₀ -UVM-7(200)	65.4	94.2	100	2.33	3.36	805
18	Au/Ce ₁₀ -Ni ₁₀ -UVM-7(200)	62.0	88.7	100	1.51	2.16	662
19	Au/Ce ₆₀ -Ni ₁₀ -UVM-7(500)	58.7	81.6	100	3.31	4.61	754
20	Au/Ce ₃₀ -Ni ₁₀ -UVM-7(500)	55.6	76.2	100	1.98	2.72	651
21	Au/Ce ₁₀ -Ni ₁₀ -UVM-7(500)	51.1	71.5	100	1.24	1.74	534
22	Au/Sn ₆₀ -Ni ₁₀ -UVM-7(200)	47.2	59.2	100	2.86	3.59	435
23	Au/Sn ₃₀ -Ni ₁₀ -UVM-7(200)	44.7	54.7	100	1.55	1.90	426
24	Au/Sn ₁₀ -Ni ₁₀ -UVM-7(200)	41.7	53.5	100	0.70	0.90	435
25	Au/Sn ₆₀ -Ni ₁₀ -UVM-7(500)	44.1	58.4	100	2.67	3.54	429
26	Au/Sn ₃₀ -Ni ₁₀ -UVM-7(500)	41.2	53.4	100	1.43	1.85	416
27	Au/Sn ₁₀ -Ni ₁₀ -UVM-7(500)	39.8	50.5	100	0.67	0.85	411

Reaction time: 4h; *-24h; **-secondary product: benzaldehyde.

In order to verify the role played by the different included/deposited heteroelements, we have studied the catalytic behavior in a sequential way from mono- to multicomponent (Ce, Sn, Ni) containing materials to catalysts in which these materials served as supports for gold. As mentioned the results were presented in terms of productivity. Data compiled in the Table 5 were collected after 4h reaction and the reason was to compare at the same reaction time catalysts with different activities. It is important to mention that i) all the presented data were collected before the conversion reached a plateau, ii) the reaction was not affected by mass transfer limitations in these experiments as confirmed by Koros-Novak criterion (slope of $\ln r/\ln f_m$ close to 1)⁵⁵, and iii) productivities calculated at very short reaction times (less than 10 min) had the same values as those presented in Table 5.

Nickel oxide entrapped in the UVM-7 structure presented productivities in the range 0.96 – 2.12 mol_{product} g_{cat}⁻¹ h⁻¹ at 75 °C and 1.15 – 2.64 at 115 °C, showing a linear dependence on the nickel content. The addition of the second heteroelement led to a different behavior. Thus, the addition of tin oxide caused a decrease in the productivities (Table 5, entries 9-11), while cerium oxide induced an increase of the productivities to 40% (Table 5, entries 6-8).

Compared to Ni₁₀-UVM-7, Ce_x-Ni₁₀-UVM-7 or Sn_x-Ni₁₀-UVM-7 the addition of gold led to an increase in the productivity irrespective of the nature of the support (Table 5, entries 12-14 and 16-27), which is in a good agreement with previously reported data on the role of gold in this reaction^{4,17,27,56}. However, the increase was more evident when the supports contain Ni or a combination of the Ce and Ni as heteroelements (Table 5, entries 12-13 and 16-21). Thus, in the case of the Au/Ce₆₀-Ni₁₀-UVM-7(200) catalyst the productivity was of 4.04 and 5.62 mol_{product} g_{cat}⁻¹ h⁻¹ at 75 and 115 °C, respectively. Such a catalyst corresponds to a Si/Ce ratio of 60 and Si/Ni ratio of 10. These results may account for a more advanced interaction of gold with nickel. More evident arguments that the direct interactions of Au/Ni are beneficial are provided by the Au/Ni₁₀-UVM-7(200) catalyst. It was almost as active as the Au/Ce₆₀-Ni₁₀-UVM-7(200) catalyst (Table 5). Changes in the activity with the atomic ratios of the constitutive elements may also support this affirmation. Thus, higher loadings of

Ce or Sn led to a decrease in the productivity, showing a less effective interaction with gold.

Since the deposition of gold onto UVM-7 including different heteroelements took place in an alkaline solution followed by a calcination step at 200 or 500 °C, these materials were separately treated following the same procedure in order to determine if such a treatment may exhibit an influence on the catalytic behavior. However, the experiments indicated no real differences between pre-calcined and non-calcined materials. But the calcination of the Au-containing catalysts at 500°C corresponded to a decrease in the productivity irrespective of the catalyst composition as compared to samples calcined at 200°C that has been correlated to the increase in the metal particle size, typically occurring for temperatures higher than 500 °C (Tables 2 and 3)⁵¹. According to Guirrane et al.^{28,7}, a significant increase in the number of unsaturated gold atoms (probably the active sites) must occur when decreasing the gold crystal size.

In conclusion, the data presented in Table 5 indicate that for more complex supports like multi-heterocomponent Ce(Sn)_y-Ni_x-UVM-7 oxides (as demonstrated by XPS) the support is not a simple spectator. A very high surface area (typical of M41s materials) in addition to an improved accessibility (as occurs for UVM-7-like silicas) can be correlated in the case of the entrapped metal catalysts with a better dispersion of the active species. Such a behavior has a direct influence on the productivity of these catalysts. These data also demonstrate that in addition to the support architecture (on the mesoscale) the local organization and nanodispersion of anchors, promoters and catalytic sites is very important. The inclusion of inorganic anchors and promoters must be considered as efficient assembly tools to improve the “cooperative properties” of our catalysts. The final effect associated with the support design and selection of heteroelements results in a better dispersion of gold nanoparticles. Thus, the Ce content does not significantly affect the size of the gold nanoparticles. We have observed similar dispersions of Ni, Ce and Au for samples with varying amount of Ce (see TEM, Figure 3-5, and comments on that). CeO₂ appears to act as an inorganic anchor. The Au content increased somewhat with the increase in Ce content. Even changing the metal, *i.e.* cerium with tin, does not affect the size of the gold

nanoparticles under our working conditions. However, the data presented in Table 5 show that the gold particle size is not the only parameter of influence on catalytic efficiency. Hence, we observe different values of the productivity (entries 12-13 and 16-27) when the chemical composition of the support changes (maintaining the average size for the gold domains).

The performance of the new multicomponent Au catalysts (Table 5) is very close to those reported in the literature for gold-supported catalysts on titania⁷ but higher than those reported for gold deposited on ceria¹⁵. This is also valuable for the reference Au-CeO₂ catalyst (Table 5, entry 15) and Au-UVM-7 (Table 5, entry 14). Taking into account that the proposed active catalytic sites for the benzylamine oxidation are unsaturated gold atoms located at the particle corners and/or the interphases^{22,7}, a decrease in the gold nanoparticle size should be considered as a beneficial aspect. The average gold particle size in our catalysts is around 4 nm for Au deposited on Ce_y-Ni_x-UVM-7, and 4.5-5 nm for Au deposited on Sn_y-Ni_x-UVM-7, leading to high conversions for Au/Ce_y-Ni_x-UVM-7 mesoporous materials. These values are in good agreement with previous data in the literature on Au-TiO₂ solids (gold particle size and TOF values of 3.5 nm and 70 h⁻¹, respectively). Then, the activities of Au-UVM-7 (TOF 456 h⁻¹) and Au-CeO₂ (TOF 458 h⁻¹) catalysts (entries 14 and 15 in Table 5) must be also associated with the gold particle size (around 4 nm). Since the XPS data do not show important differences in the oxidation state of gold on the different supports, it shows that, indeed, the particle size is the main factor controlling the activity of Au in this reaction.

Figure 11 shows the variation of the conversion with time on Ni-, Au-Ce, and Au-Ce,Ni-UVM-7 catalysts. A continuous conversion increase in time until around 3h was observed for all of the catalysts.

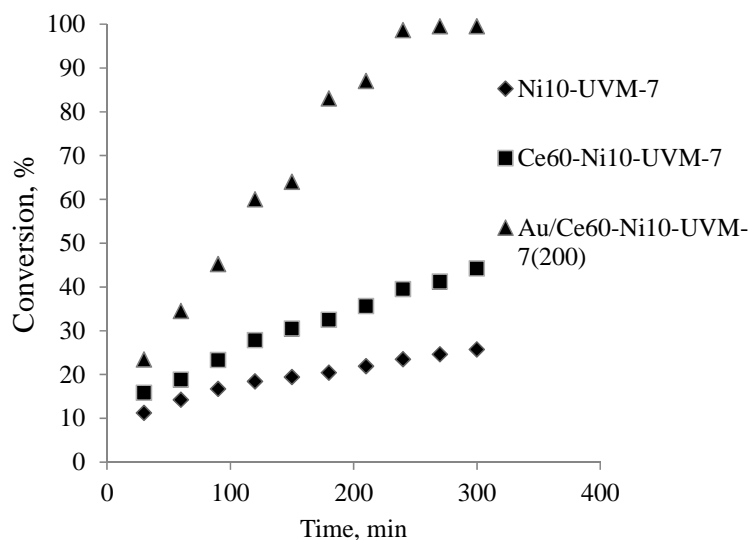


Figure 11. The variation of the conversion in time on Ni-, Au-Ce, and Au-Ce,Ni-UVM-7 catalysts.

Kinetic studies carried on gold powder-catalyzed reaction by Lazar and Angelici showed that the rate of this reaction is independent of the O_2 concentration/pressure^{14,56}. Experiments carried out at different oxygen pressures with Au/Ce₆₀-Ni₁₀-UVM-7(200) and Au/Ce₃₀-Ni₁₀-UVM-7(200) catalysts showed an increase in the conversion until the pressure reaches 5 atm. (Figure 12). Further increase of the oxygen pressure above 5 atm. accounted for the results of Lazar and Angelici^{14,57}. No changes in the selectivity or reaction products have been observed under these conditions.

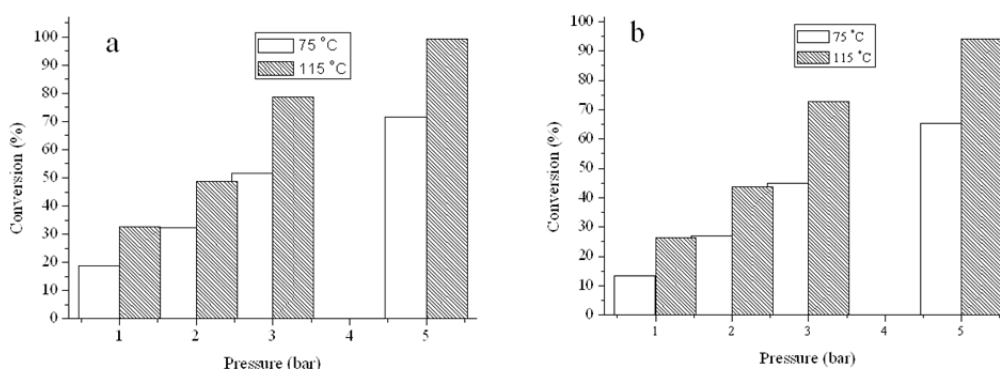


Figure 12. Conversion of benzylamine on Au/Ce₆₀-Ni₁₀-UVM-7(200) (a) and Au/Ce₃₀-Ni₁₀-UVM-7(200) (b) under different pressures of oxygen after 4h.

Activation of molecular oxygen on gold was reported to depend on both size and environments. Corma and coworkers indicated that gold nanoparticles act as a bifunctional catalyst able to dissociate molecular oxygen on unsaturated atoms to generate oxygen reactive species and also to activate the organic substrate at the same time⁵⁸⁻⁶⁰. The presence of an additional element in the close proximity of gold may also affect the activation of oxygen. Thus, periodic density functional theory calculations investigating the effect of doping a gold model surface with Ni showed that this transitional element may stabilize the adsorbate–surface interactions with a concomitant decrease of the activation energy barriers for the oxygen dissociation to values that are smaller than the adsorption energies of molecular oxygen on gold⁶¹. These findings are in line with our results showing an improvement of the activity when gold nanoparticles were supported on Ni and Ce oxide nanodomains partially embedded inside the mesoporous UVM-7 silica walls. These catalysts were superior to those supported on Sn or large loadings of Ce oxide nanodomains inside the same mesoporous UVM-7 silica walls.

Thus, it appears that the new catalysts we proposed in this study bring together advantages that recommend them as effective for selective oxidation of benzylamine to N-benzylidenebenzylamine, *i.e.* stabilized Ni and Ce oxide nanodomains by partially embedding inside the mesoporous UVM-7 silica walls that activate gold nanoparticles. These particularities are in line with recent suggestions of Stowers *et al.*⁶² indicating that stabilization methods of active gold particles may include partially coating the surface of the material and the use of metal oxides in interaction with the catalyst.

On bulk gold, reports indicated that molecular oxygen can be activated *via* a hydroperoxyl (OOH) intermediate produced by abstracting a hydrogen atom from substrate or water, and the fact that extra water molecules significantly promote the hydrogen-transfer reactions, lowering the activation barrier of OOH formation⁶¹. On the other hand, on these surfaces molecular oxygen is suggested to dissociate to form the active oxygen species that generates a reaction site, which selectively activates the substrate leading to OH groups. Hydroxyls formed on the surface rapidly disproportionate to form water⁶³.

Table 6. The effect of water on performances of the multicomponent catalysts in aerobic oxidative condensation of benzylamine to N-benzylidenebenzylamine.

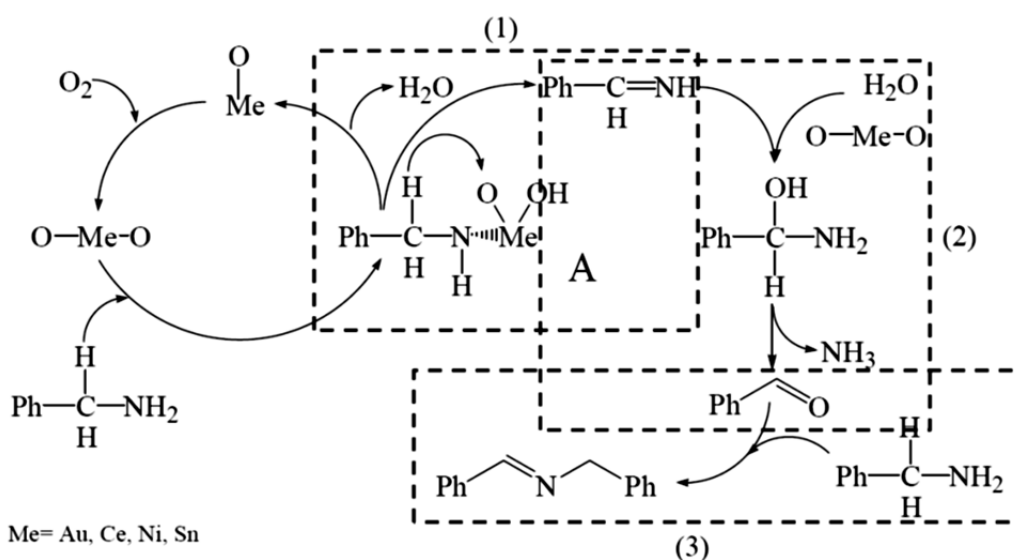
Entry	Catalyst	Additional water, μL	Conversion %	Selectivity %	Productivity $\text{mol}_{\text{product}} \text{g}_{\text{cat}}^{-1} \text{h}^{-1}$
1	Au/Ce ₆₀ -Ni ₁₀ -UVM-7(200)	dried reactants*	62.4	100	1.76
2	Au/Ce ₆₀ -Ni ₁₀ -UVM-7(200)	1.0	73.5	100	4.15
3	Au/Ce ₆₀ -Ni ₁₀ -UVM-7(200)	2.0	78.4	100	4.43
4	Au/Ce ₆₀ -Ni ₁₀ -UVM-7(200)	5.0	81.2	100	4.58
5	Au/Ce ₆₀ -Ni ₁₀ -UVM-7(200)	10.0	81.7	100	4.62
6	Au/Ce ₆₀ -Ni ₁₀ -UVM-7(200)	20.0	80.6	100	4.55
7	Au/Ce ₃₀ -Ni ₁₀ -UVM-7(200)	dried reactants*	53.2	100	0.94
8	Au/Ce ₃₀ -Ni ₁₀ -UVM-7(200)	1.0	68.4	100	2.33
9	Au/Ce ₃₀ -Ni ₁₀ -UVM-7(200)	2.0	72.7	100	2.60
10	Au/Ce ₃₀ -Ni ₁₀ -UVM-7(200)	5.0	75.0	100	2.68
11	Au/Ce ₃₀ -Ni ₁₀ -UVM-7(200)	10.0	75.1	100	2.68
12	Au/Ce ₃₀ -Ni ₁₀ -UVM-7(200)	20.0	72.8	100	2.60

Temperature 75 °C; Reaction time: 4h; *-required an induction period of 4h; **-results collected after 8h.

These achievements may confirm our results indicating that the role of water is important in systems containing Au particles. In addition, in our system water is also a substrate participating in the hydration of aldimine. The addition of water (1-20 μL) to the catalysts described in entries 12-13 and 16-27, was found to influence the activity but without any effect on selectivity. To check in more detail the effect of water, experiments with dried benzylamine, methanol and oxygen have been carried out as well. Compared to the case where non-dried reactants have been used the reaction in which dried reactants were tested required an induction period (Table 6, entries 1 and 7). Thus, it varied from around 30 min for Au/Ce₆₀-Ni₁₀-UVM-7(200) and Au/Ce₃₀-Ni₁₀-UVM-7(200) till 50 min for Au/Sn₃₀-Ni₁₀-UVM-7(500) and Au/Sn₁₀-Ni₁₀-UVM-7(500). The supplementary addition of 10 μL water to the reaction system caused an increase of productivity from 4.04 (Table 5, entry 16) to 4.62 $\text{mol}_{\text{product}} \text{g}_{\text{cat}}^{-1} \text{h}^{-1}$ (Table 6, entry 5)

for the Au/Ce₆₀-Ni₁₀-UVM-7(200) catalyst. A similar behavior was determined for Au/Ce₃₀-Ni₁₀-UVM-7(200) (Table 5, entry 17, and Table 6, entries 8-12).

Then, benzaldehyde was considered in many examples as a key intermediate^{23,64}. The produced benzaldehyde was suggested to react with the excess benzylamine to form benzylidene benzylamines resulting in the final product for the benzylamine self-coupling reactions. To confirm this behavior we have carried out experiments on the same Au/Ce₆₀-Ni₁₀-UVM-7(200) and Au/Ce₃₀-Ni₁₀-UVM-7(200) catalysts by introducing benzaldehyde in the reaction mixture. Compared to the results presented in the Table 5, on these catalysts the conversion was total even at 75 °C after 2h (productivities of 5.65 and 3.57 mol_{product} g_{cat}⁻¹ h⁻¹, respectively). This fact confirms that, indeed, the addition of benzaldehyde modifies the dynamics of the product formation. In fact, in the range of investigated benzylamine/benzaldehyde molecular ratios (from 5:1 to 1:1), benzaldehyde was detected in the reaction product only for the 1:1 benzylamine/benzaldehyde ratio, in 9% and 12% for samples Au/Ce₆₀-Ni₁₀-UVM-7(200) and Au/Ce₃₀-Ni₁₀-UVM-7(200), respectively.



Scheme 2. Mechanism of the aerobic oxidative condensation of benzylamine to N-benzylidenebenzylamine.

Based on the experimental evidences we collected in this study, the following reaction mechanism has been reconfirmed (Scheme 2)¹⁷. Although not detected, the oxidative dehydrogenation of benzylamine giving an aldimine is assumed as a first step of reaction (Scheme 2 (1)). It may also occur as a single-electron oxidation catalyzed by gold nanoparticles²⁸ deposited on Ni and Ce (or Sn) oxide nanodomains partially embedded inside the mesoporous UVM-7 silica walls. It occurs *via* the intermediate (A) that generates an aldimine and water. Then, hydrolysis of the aldimine occurs as a second step (Scheme 2 (2)), where ammonia is released and benzaldehyde is generated. Finally, benzaldehyde condenses with benzylamine leading to N-benzylidenebenzylamine (Scheme 2 (3)). It is worth noting that in the presence of oxygen smaller benzylamine/benzaldehyde ratios than 1:1 do not inhibit the steps 1 and 2 but only increase the amount of non-reacted benzaldehyde.

Among the elements included in the new multicomponent catalysts gold is more favored in this reaction as active site because, as opposed to nickel, tin or even cerium oxides it can easily release oxygen. XPS showed that nickel is, however, irreversible oxidized. As shown from the productivity values silica-embedded nickel nanoxide is also a valuable catalyst. In addition, silica-embedded nickel nanoxides in connection with silica-embedded cerium nanoxides also provide excellent nano-supports for gold. Supporting this conclusion, XPS analysis revealed that for gold, although the thermal treatment and exposure to the reaction determined a slight agglomeration, it preserved its oxidation state along ten catalytic cycles.

Figure S9 shows the evolution of the conversion for the ten cycles for two Au/multicomponent supports catalysts. No change in the conversion was determined under these conditions. However, the results included in this figure were collected from experiments performed at high conversions which may not prove good recyclability. Therefore, we completed these tests with results collected at lower conversions (Figure S10). Indeed, they confirmed the recyclability of the catalysts. This has also been confirmed by ICP-OES analysis of the reaction products checking for Au and by the characterization of the catalysts using the techniques described above. As shown in Scheme 2, on the basis of the analytic measurements, ammonia is a by-product of this reaction. It is important to note that none of the investigated catalysts

has been deactivated by ammonia, and their reuse led to similar conversions. In addition, XPS spectra of the spent catalysts did not show the presence of nitrogen, an additional confirmation of the stability of these catalysts.

General assessments

The success of a supported catalyst depends on a variety of key parameters affecting both the support nature and the design of the individual catalytic site. But this is not enough, and in most cases a regular and homogeneous distribution of the catalytic centers is required. This last aspect, dealing with the spatial distribution on the nanoscale, must be viewed as a collective property of the catalytic sites considered as a whole, as has been nicely discussed in a recent paper⁶⁵. In dealing with catalysts based on metal nanoparticles inside mesoporous materials, in addition to a good selection of the support, nanoparticle assembly tools are usually required in order to tune and control the “cooperative properties” of the nanoparticles.

While there is no doubt about the esthetic appeal of symmetry, it was also argued that a periodic and ordered unimodal mesoporous support could not offer specific advantages for catalytic applications requiring an enhanced accessibility to the active sites and easy diffusion of reagents and products⁶⁶. Then, we have selected as support the disordered UVM-7 porous silica, with a topology constructed by aggregation of mesoporous primary nanoparticles defining large inter-particle pores^{67,38,39}. This architecture leads to 3D interconnected and tortuous mesopores having nanometric lengths. These features favor accessibility to the active sites and prevent the undesirable migration and growth of metal nanoparticles^{68,67}.

Although mesoporous silicas could be considered as useful supports for noble metal nanoparticles due to the expected nanosize confinement effect, the poor affinity between silica and noble metal precursors hinders the optimization of the previously mentioned “collective properties” (nanoparticle size and dispersion) and drastically restricts the catalyst working temperature⁶⁹. In fact, thermal stability constitutes a major drawback to any noble metal-based nanomaterials. Hence, when Hüttig and

Tamman temperatures are reached, atoms at defects and surfaces and at bulk level will become mobile⁶⁹. Moreover, these temperatures drastically drop down with the particle size⁶⁹. The usual approach to minimize this problem is to modify the host surface with anchoring species able to interact with gold complexes or nanoparticles. For this purpose both organic and inorganic functional groups can be used. As expected, an improved thermal stability is achieved with inorganic anchors like metal oxide nanodomains. In fact noble metal-MO_x materials are good catalysts for a variety of processes^{24,70,41}. In this work we used NiO_x nanodomains partially embedded inside the silica walls as effective and stable inorganic anchors favoring the nucleation, growth and stability of supported gold particles (see below). In addition to Ni, we included in our supports Ce (or Sn) as oxide domains. Their incorporation inside the silica walls is supported by different techniques: a) the absence of segregation according to XRD, b) the preservation of porosity (without significant pore blocking), and c) the observation of small black spots (inside the silica-based walls) in the TEM images of Figure 2 that could be attributed to NiO_x, SnO₂ or CeO₂ nanodomains.

Multiple roles seem to be played by the CeO₂ embedded particles. In a similar way as NiO_x, the CeO₂ particles could also act as inorganic anchors depending on the specific pH conditions during the impregnation with gold complexes (see below). In fact, ceria is also a typical support for gold nanoparticles⁷¹. Cerium oxide has the ability to transport oxygen in combination with the ability to cycle easily between reduced (Ce³⁺) and oxidized (Ce⁴⁺) states⁷². This behavior benefits redox reactions such as the benzylamine oxidation. Then, CeO₂ could be considered as co-catalyst or promoter. Moreover, the presence of CeO₂ in the medium could favor the formation of NiO particles with smaller dimensions avoiding undesirable mesopore blocking phenomena⁷². In contrast, no similar benefits are expected in the case of SnO₂ included domains. Despite these effects, the presence of nano-oxide domains did not generate a strong enough interfacial interaction with gold nanoparticles to hinder the particle increase with the temperature.

Conclusions

The aerobic oxidative condensation of benzylamine to N-benzylidenebenzylamine was carried out on new gold-based catalysts using as supports bimodal UVM-7-like mesoporous silica containing Ni and Ce (or Sn) as oxide nanodomains partially embedded inside the mesoporous UVM-7 silica walls. These nanodomains acted as effective and stable inorganic anchors favoring the nucleation, growth and stability of supported gold particles. The versatility of the used preparative approach allowed exploiting both the high surface area and accessibility of the mesoporous silica and also an easy and homogeneous inclusion of heteroelements in one pot.

Aerobic oxidative condensation of benzylamine on these catalysts occurred selectively only with the formation of N-benzylidenebenzylamine. While the selectivity was total, the conversion varied in a large range as a function of the catalysts composition (chemical composition and atomic ratios of the constitutive support elements). The catalytic behavior was mostly controlled by the size of the gold particles. However, other heteroelements also have an effect as shown in Table 5. Changes in the values of the productivities led also to the conclusion that the support is not a simple spectator for this reaction.

The best results were obtained on gold deposited on mesoporous Ni₁₀-UVM-7(200) as support, *i.e.* Au/Ni₁₀-UVM-7(200) and Au/Ce₆₀-Ni₁₀-UVM-7 catalysts. The comparison of the productivities of the individual and bicomponent catalysts led to the conclusion of a cooperative effect between the components. However, the main active specie of these catalysts was gold and the method used for the preparation of these catalysts allowed a high enough dispersion of it to provide the determined activity. The most active catalysts corresponded to a lower Ce content and higher Ni content. TEM and XEDS mapping measurements indicated that the dispersion of these elements ensures the best configurations to activate the deposited Au nanoparticles. Smaller Au particle sizes corresponded to the most active catalysts.

None of these catalysts were deactivated by ammonia (which is a by-product of this reaction) and the catalysts were reused ten times without any evident loss in the activity.

Acknowledgements

Vasile I. Parvulescu thanks PN II ID PCE 2011/3-0060 for the financial support. This research was partially supported by the Ministerio de Economía y Competitividad (MAT2009-14564-C04-04 and MAT2012-38429-C04-03) and the Generalitat Valenciana (PROMETEO/2009/108). J.E.H. thanks the Fundació General de la Universitat de València for financial support. A.M. thanks MEC for a FPI fellowship, and C.M.O. thanks the POS-DRU for a fellowship.

References

1. Wang, J.-R.; Fu, Y.; Zhang, B.-B.; Cui, X.; Liu, L.; Guo, Q.-X. *Tetrahedron Letters* **2006**, *47*, 8293-8297.
2. Zanardi, A.; Mata, J. A.; Peris, E. *Chemistry-a European Journal* **2010**, *16*, 10502-10506.
3. Samec, J. S. M.; Ell, A. H.; Backvall, J. E. *Chemistry-a European Journal* **2005**, *11*, 2327-2334.
4. Lang, X.; Ji, H.; Chen, C.; Ma, W.; Zhao, J. *Angewandte Chemie-International Edition* **2011**, *50*, 3934-3937.
5. Saidi, O.; Blacker, A. J.; Farah, M. M.; Marsden, S. P.; Williams, J. M. J. *Angewandte Chemie-International Edition* **2009**, *48*, 7375-7378.
6. Yuan, Q.-L.; Zhou, X.-T.; Ji, H.-B. *Catalysis Communications* **2010**, *12*, 202-206.
7. Gorrane, A.; Corma, A.; Garcia, H. *Journal of Catalysis* **2009**, *264*, 138-144.
8. Guo, H.; Kemell, M.; Al-Hunaiti, A.; Rautiainen, S.; Leskela, M.; Repo, T. *Catalysis Communications* **2011**, *12*, 1260-1264.
9. Yamaguchi, K.; Mizuno, N. *Angewandte Chemie-International Edition* **2003**, *42*, 1480-1483.
10. Hosseini-Sarvari, M. *Chinese Chemical Letters* **2011**, *22*, 547-550.
11. Landge, S. M.; Atanassova, V.; Thimmaiah, M.; Torok, B. *Tetrahedron Letters* **2007**, *48*, 5161-5164.
12. Kamiguchi, S.; Nakamura, A.; Suzuki, A.; Kodomari, M.; Nomura, M.; Iwasawa, Y.; Chihara, T. *Journal of Catalysis* **2005**, *230*, 204-213.
13. Perez, Y.; Aprile, C.; Corma, A.; Garcia, H. *Catalysis Letters* **2010**, *134*, 204-209.
14. Angelici, R. J. *Catalysis Science & Technology* **2013**, *3*, 279-296.
15. Aschwanden, L.; Mallat, T.; Grunwaldt, J.-D.; Krumeich, F.; Baiker, A. *Journal of Molecular Catalysis a-Chemical* **2009**, *300*, 111-115.
16. Rakotzyay, K.; Kaszonyi, A.; Vajcsek, S. *Applied Catalysis a-General* **2010**, *378*, 33-41.
17. Zhu, B.; Lazar, M.; Trewyn, B. G.; Angelici, R. J. *Journal of Catalysis* **2008**, *260*, 1-6.
18. Chi, K.-W.; Hwang, H. Y.; Park, J. Y.; Lee, C. W. *Synthetic Metals* **2009**, *159*, 26-28.
19. Guzen, K. P.; Guarezemini, A. S.; Orfao, A. T. G.; Cella, R.; Pereira, C. M. P.; Stefani, H. A. *Tetrahedron Letters* **2007**, *48*, 1845-1848.
20. Nicolas, C.; Herse, C.; Lacour, J. *Tetrahedron Letters* **2005**, *46*, 4605-4608.
21. Su, F.; Mathew, S. C.; Moehlmann, L.; Antonietti, M.; Wang, X.; Blechert, S. *Angewandte Chemie-International Edition* **2011**, *50*, 657-660.
22. Schuemperli, M. T.; Hammond, C.; Hermans, I. *Acs Catalysis* **2012**, *2*, 1108-1117.
23. Largeton, M. *European Journal of Organic Chemistry* **2013**, *2013*, 5225-5235.

24. Zhang, Y.; Cui, X.; Shi, F.; Deng, Y. *Chemical Reviews* **2012**, *112*, 2467-2505.
25. Haruta, M.; Tsubota, S.; Kobayashi, T.; Kageyama, H.; Genet, M. J.; Delmon, B. *Journal of Catalysis* **1993**, *144*, 175-192.
26. Budroni, G.; Corma, A. *Angewandte Chemie-International Edition* **2006**, *45*, 3328-3331.
27. Angelici, R. J. *Journal of Organometallic Chemistry* **2008**, *693*, 847-856.
28. Gorrane, A.; Corma, A.; Garcia, H. *Science* **2008**, *322*, 1661-1664.
29. So, M.-H.; Liu, Y.; Ho, C.-M.; Che, C.-M. *Chemistry-an Asian Journal* **2009**, *4*, 1551-1561.
30. Aschwanden, L.; Mallat, T.; Maciejewski, M.; Krumeich, F.; Baiker, A. *Chemcatchem* **2010**, *2*, 666-673.
31. Al-Hmoud, L.; Jones, C. W. *Journal of Catalysis* **2013**, *301*, 116-124.
32. Wachs, I. E.; Routray, K. *Acs Catalysis* **2012**, *2*, 1235-1246.
33. Villa, A.; Veith, G. M.; Ferri, D.; Weidenkaff, A.; Perry, K. A.; Campisi, S.; Prati, L. *Catalysis Science & Technology* **2013**, *3*, 394-399.
34. Zhao, G.; Hu, H.; Chen, W.; Jiang, Z.; Zhang, S.; Huang, J.; Lu, Y. *Catalysis Science & Technology* **2013**, *3*, 404-408.
35. Huang, J.; Xue, C.; Wang, B.; Guo, X.; Wang, S. *Reaction Kinetics Mechanisms and Catalysis* **2013**, *108*, 403-416.
36. You, H.; Liu, R.; Liang, C.; Yang, S.; Wang, F.; Lu, X.; Ding, B. *Journal of Materials Chemistry A* **2013**, *1*, 4097-4104.
37. Cabrera, S.; El Haskouri, J.; Guillem, C.; Latorre, J.; Beltran-Porter, A.; Beltran-Porter, D.; Marcos, M. D.; Amoros, P. *Solid State Sciences* **2000**, *2*, 405-420.
38. El Haskouri, J.; de Zarate, D. O.; Guillem, C.; Latorre, J.; Caldes, M.; Beltran, A.; Beltran, D.; Descalzo, A. B.; Rodriguez-Lopez, G.; Martinez-Manez, R.; Marcos, M. D.; Amoros, P. *Chemical Communications* **2002**, 330-331.
39. El Haskouri, J.; Manuel Morales, J.; Ortiz de Zarate, D.; Fernandez, L.; Latorre, J.; Guillem, C.; Beltran, A.; Beltran, D.; Amoros, P. *Inorganic Chemistry* **2008**, *47*, 8267-8277.
40. Haruta, M. *Gold Bulletin* **2004**, *37*, 27-36.
41. Corma, A.; Garcia, H. *Chemical Society Reviews* **2008**, *37*, 2096-2126.
42. Baes, C. F.; Mesmer, R. E. *In the Hydrolysis of Cations*: New York, 1976.
43. Magureanu, M.; Mandache, N. B.; Hu, J.; Richards, R.; Florea, M.; Parvulescu, V. I. *Applied Catalysis B-Environmental* **2007**, *76*, 275-281.
44. Neatu, F.; Li, Z.; Richards, R.; Toullec, P. Y.; Genet, J.-P.; Dumbuya, K.; Gottfried, J. M.; Steinrueck, H.-P.; Parvulescu, V. I.; Michelet, V. *Chemistry-a European Journal* **2008**, *14*, 9412-9418.
45. Parvulescu, V. I.; Grange, P.; Delmon, B. *Applied Catalysis B-Environmental* **2001**, *33*, 223-237.

46. Fernandez, L.; Garro, N.; El Haskouri, J.; Perez-Cabero, M.; Alvarez-Rodriguez, J.; Latorre, J.; Guillem, C.; Beltran, A.; Beltran, D.; Amoros, P. *Nanotechnology* **2008**, *19*.
47. Sakwarathorn, T.; Luengnaruemitchai, A.; Pongstabodee, S. *Journal of Industrial and Engineering Chemistry* **2011**, *17*, 747-754.
48. Zhang, P.; Zhou, X. T.; Tang, Y. H.; Sham, T. K. *Langmuir* **2005**, *21*, 8502-8508.
49. Pireaux, J. J.; Liehr, M.; Thiry, P. A.; Delrue, J. P.; Caudano, R. *Surface Science* **1984**, *141*, 221-232.
50. Lenglet, M.; Hochu, F.; Durr, J.; Tuilier, M. H. *Solid State Communications* **1997**, *104*, 793-798.
51. Prieto, P.; Nistor, V.; Nouneh, K.; Oyama, M.; Abd-Lefdil, M.; Diaz, R. *Applied Surface Science* **2012**, *258*, 8807-8813.
52. Chen, M.; Zheng, X. M. *Journal of Molecular Catalysis a-Chemical* **2003**, *201*, 161-166.
53. Liu, L.; Zhang, S.; Fu, X.; Yan, C.-H. *Chemical Communications* **2011**, *47*, 10148-10150.
54. Wu, X.-F.; Petrosyan, A.; Ghochikyan, T. V.; Saghyan, A. S.; Langer, P. *Tetrahedron Letters* **2013**, *54*, 3158-3159.
55. Parvulescu, V.; Coman, S.; Frunza, L.; Macovei, D.; Sandulescu, I.; Parvulescu, V. I. *Spillover and Migration of Surface Species on Catalysts* **1997**, *112*, 161-170.
56. Tiseanu, C.; Parvulescu, V. I.; Boutonnet, M.; Cojocaru, B.; Primus, P. A.; Teodorescu, C. M.; Solans, C.; Sanchez Dominguez, M. *Physical Chemistry Chemical Physics* **2011**, *13*, 17135-17145.
57. Lazar, M.; Angelici, R. J. *Journal of the American Chemical Society* **2006**, *128*, 10613-10620.
58. Boronat, M.; Corma, A. *Journal of Catalysis* **2011**, *284*, 138-147.
59. Alves, L.; Ballesteros, B.; Boronat, M.; Ramon Cabrero-Antonino, J.; Concepcion, P.; Corma, A.; Angel Correa-Duarte, M.; Mendoza, E. *Journal of the American Chemical Society* **2011**, *133*, 10251-10261.
60. Leyva-Perez, A.; Oliver-Meseguer, J.; Cabrero-Antonino, J. R.; Rubio-Marques, P.; Serna, P.; Al-Resayes, S. I.; Corma, A. *Acs Catalysis* **2013**, *3*, 1865-1873.
61. Chang, C.-R.; Yang, X.-F.; Long, B.; Li, J. *Acs Catalysis* **2013**, *3*, 1693-1699.
62. Stowers, K. J.; Madix, R. J.; Friend, C. M. *Journal of Catalysis* **2013**, *308*, 131-141.
63. Fajin, J. L. C.; Cordeiro, M. N. D. S.; Gomes, J. R. B. *Applied Catalysis a-General* **2013**, *458*, 90-102.
64. Atanassova, V.; Ganno, K.; Kulkarni, A.; Landge, S. M.; Curtis, S.; Foster, M.; Toeroek, B. *Applied Clay Science* **2011**, *53*, 220-226.
65. Prieto, G.; Zecevic, J.; Friedrich, H.; de Jong, K. P.; de Jongh, P. E. *Nature Materials* **2013**, *12*, 34-39.
66. Rolison, D. R. *Science* **2003**, *299*, 1698-1701.

67. Perez-Cabero, M.; Hungria, A. B.; Morales, J. M.; Tortajada, M.; Ramon, D.; Moragues, A.; El Haskouri, J.; Beltran, A.; Beltran, D.; Amoros, P. *Journal of Nanoparticle Research* **2012**, *14*, 12.
68. Perez-Cabero, M.; El Haskouri, J.; Solsona, B.; Vazquez, I.; Dejoz, A.; Garcia, T.; Alvarez-Rodriguez, J.; Beltran, A.; Beltran, D.; Amoros, P. *Journal of Materials Chemistry* **2010**, *20*, 6780-6788.
69. Sun, J.; Bao, X. *Chemistry-a European Journal* **2008**, *14*, 7478-7488.
70. Hutchings, G. J. *Journal of Materials Chemistry* **2009**, *19*, 1222-1235.
71. Carrettin, S.; Concepcion, P.; Corma, A.; Nieto, J. M. L.; Puentes, V. F. *Angewandte Chemie-International Edition* **2004**, *43*, 2538-2540.
72. Solsona, B.; Concepcion, P.; Hernandez, S.; Demicol, B.; Lopez Nieto, J. M. *Catalysis Today* **2012**, *180*, 51-58.

**New multicomponent catalysts for the selective
aerobic oxidative condensation of benzylamine
to N-benzylidenebenzylamine**

Supplementary Information

Cristina Madalina Opris, Octavian Dumitru Pavel, Alaina Moragues, Jamal
El Haskouri, Daniel Beltrán, Pedro Amorós, Maria Dolores Marcos,
Laura Elena Stoflea, Vasile I. Parvulescu

Catalysts characterization

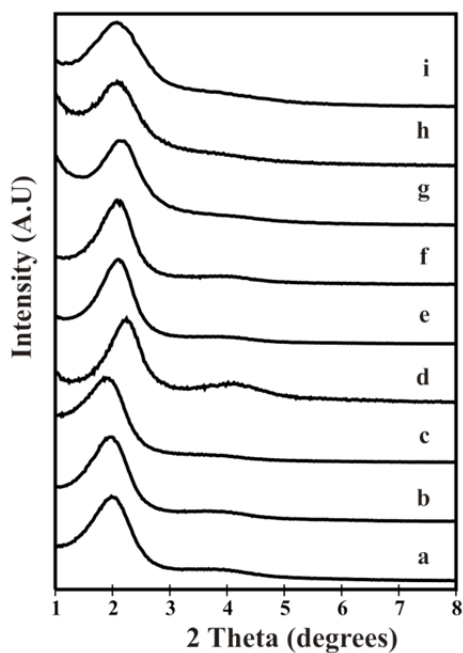


Figure S1. Low-angle XRD patterns of the gold-free supports. (a) Ni60-UVM-7, (b) Ni30-UVM-7, (c) Ni10-UVM-7, (d) Ce60-Ni10-UVM-7, (e) Ce30-Ni10-UVM-7, (f) Ce10-Ni10-UVM-7, (g) Sn60-Ni10-UVM-7, (h) Sn30-Ni10-UVM-7 and (i) Sn10-Ni10-UVM-7.

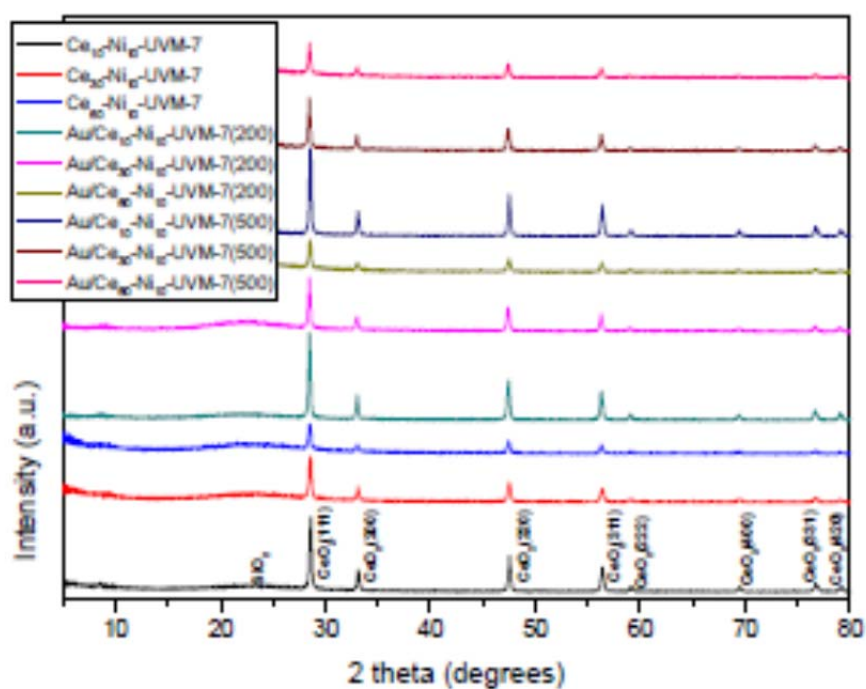


Figure S2. High-angle XRD patterns of the supports and final catalysts containing Ce.

Figures S2 and S3 show the high-angle XRD patterns of all synthesized UVM-7-based materials, after and before the gold incorporation and thermally processed at 200 and 500°C.

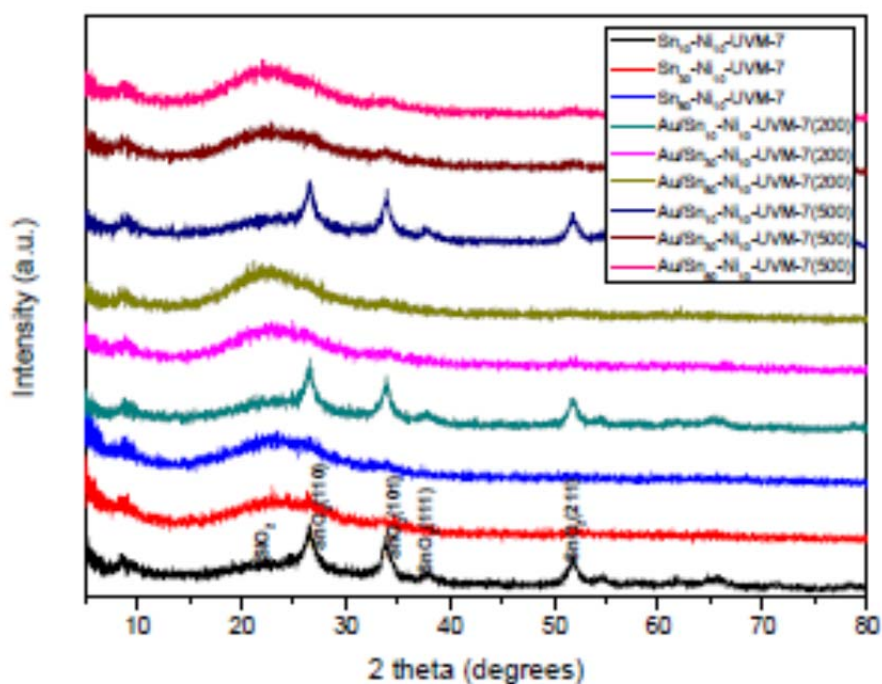


Figure. S3. High-angle XRD patterns of the supports and final catalysts containing Sn.

Figures S4 and S5 correspond to TEM images and N₂ adsorption-desorption isotherms of the gold-free support/catalysts. The nickel inclusion does not affect the mesostructure when compared with a TEM image of UVM-7 pure silica. The two pore systems (intra-particle surfactant generated mesopore system and the inter-particle disordered large pores) result clearly appreciated. The Ce and Sn inclusion although does not affect in a qualitative way the original mesostructure, the incorporation of these heteroelements favors a certain inter-particle condensation with the subsequent relatively loss of textural-type porosity.

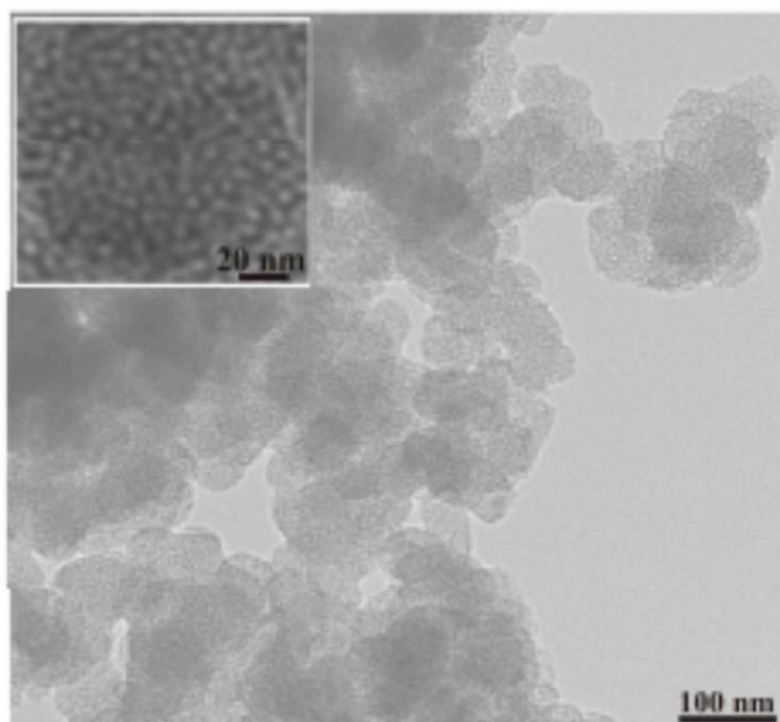


Figure S4. Representative TEM image of Nix-UVM-7 samples ($x=10$).

Figures S5 and S6 present N₂ adsorption desorption isotherms of catalysts: S5 (a) Au/Sn₁₀-Ni₁₀-UVM-7, (b) Au/Sn₃₀-Ni₁₀-UVM-7 and (c) Au/Sn₆₀-Ni₁₀-UVM-7, processed at (i) 200°C and (ii) 500°C. S6 (a) Au/Ce₁₀-Ni₁₀-UVM-7, (b) Au/Ce₃₀-Ni₁₀-UVM-7 and (c) Au/Ce₆₀-Ni₁₀-UVM-7, processed at (i) 200°C and (ii) 500°C

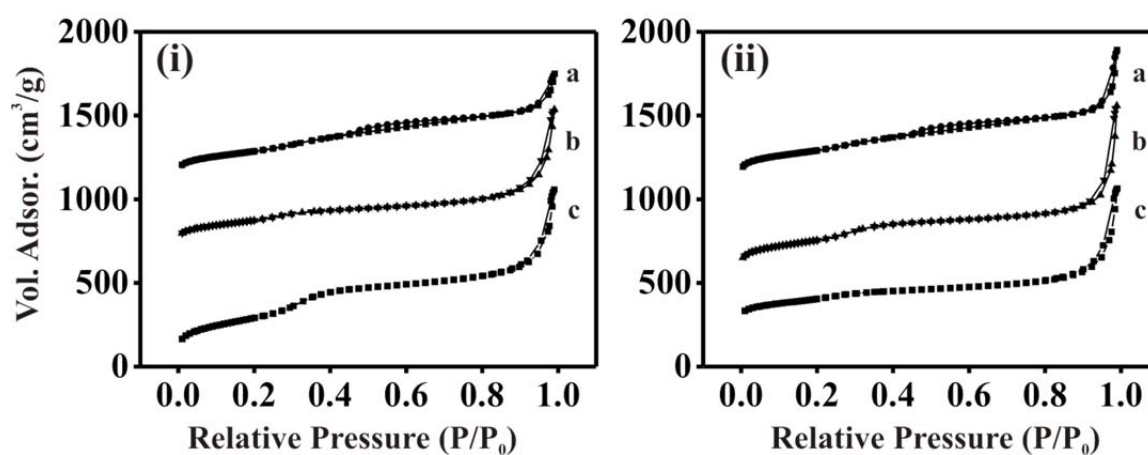


Figure S5. N₂ adsorption desorption isotherms of catalysts (a) Au/Sn₁₀-Ni₁₀-UVM-7, (b) Au/Sn₃₀-Ni₁₀-UVM-7 and (c) Au/Sn₆₀-Ni₁₀-UVM-7, processed at (i) 200°C and (ii) 500°C.

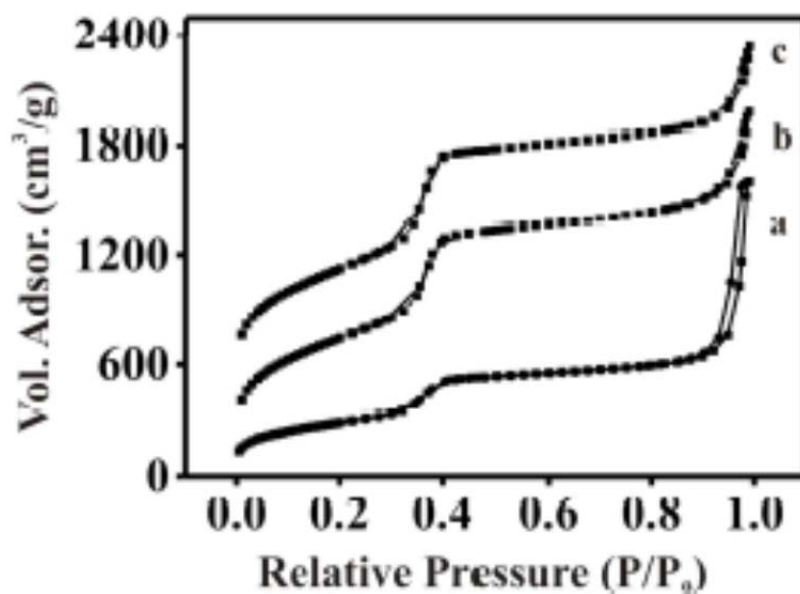


Figure S6. Representative N₂ adsorption-desorption isotherms of the gold-free supports. (a) Ni₆₀-UVM-7, (b) Ce₆₀-Ni₁₀-UVM-7 and (c) Sn₆₀-Ni₁₀-UVM-7.

Figures S7 and S8 present the BJH pore size distributions from the adsorption branches of the N₂ adsorption-desorption isotherms of catalysts S5 (a) Au/Ce₁₀-Ni₁₀-UVM-7, (b) Au/Ce₃₀-Ni₁₀-UVM-7 and (c) Au/Ce₆₀-Ni₁₀-UVM-7, processed at (i) 200°C and (ii) 500°C S6 (a) Au/Sn₁₀-Ni₁₀-UVM-7, (b) Au/Sn₃₀-Ni₁₀-UVM-7 and (c) Au/Sn₆₀-Ni₁₀-UVM-7, processed at (i) 200°C and (ii) 500°C.

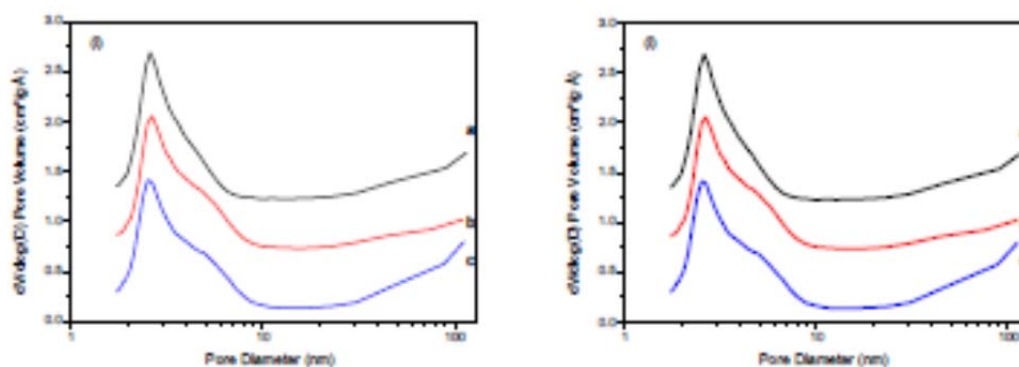


Figure S7. BJH pore size distributions from the adsorption branches of the N₂ adsorption-desorption isotherms of catalysts (a) Au/Ce₁₀-Ni₁₀-UVM-7, (b) Au/Ce₃₀-Ni₁₀-UVM-7 and (c) Au/Ce₆₀-Ni₁₀-UVM-7, processed at (i) 200°C and (ii) 500°C.

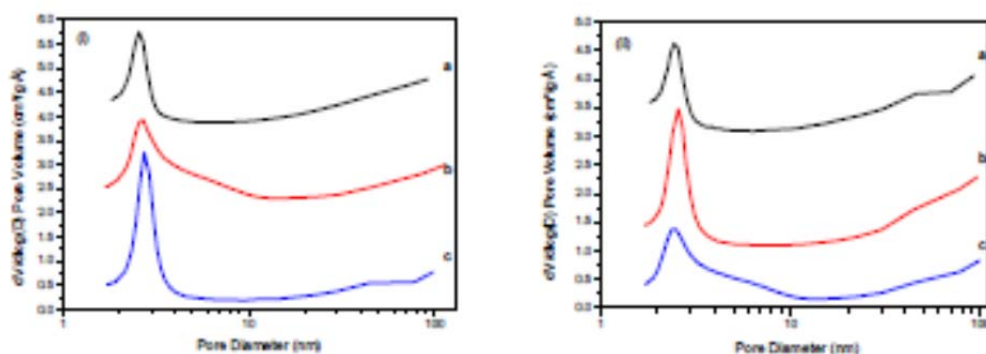


Figure S8. BJH pore size distributions from the adsorption branches of the N₂ adsorption desorption isotherms of catalysts (a) Au/Sn₁₀-Ni₁₀-UVM-7, (b) Au/Sn₃₀-Ni₁₀-UVM-7 and (c) Au/Sn₆₀-Ni₁₀-UVM-7, processed at (i) 200°C and (ii) 500°C.

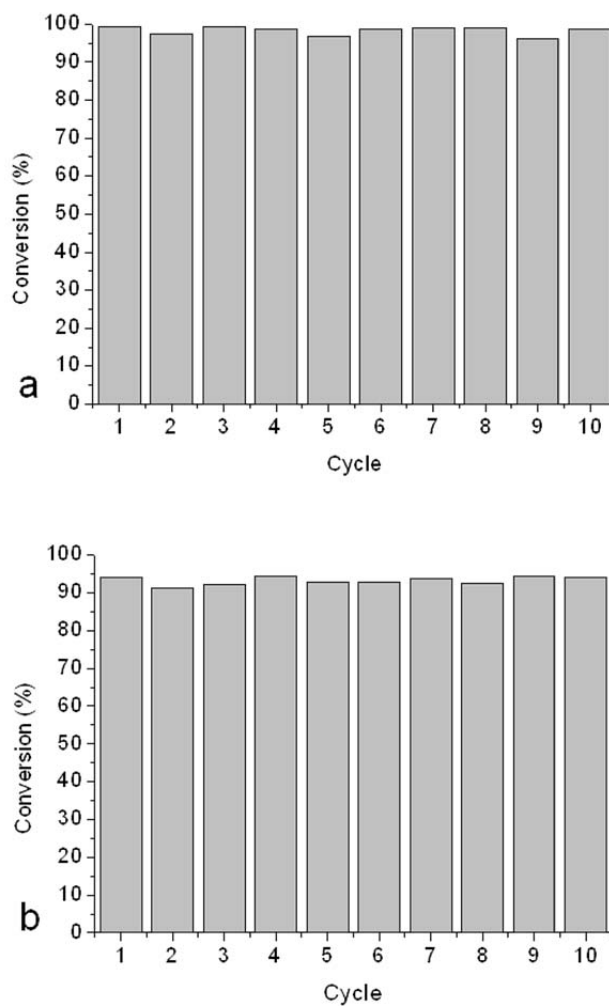


Figure S9. Conversion of benzylamine on Au/Ce₆₀-Ni₁₀-UVM-7(200) (a) and Au/Ce₃₀-Ni₁₀-UVM-7(200) (b) catalysts over 10 successive cycles at 5 bar O₂ (115 °C, 4h, selectivity 100%).

Figures S9 and S10 present conversion results in recycling experiments.

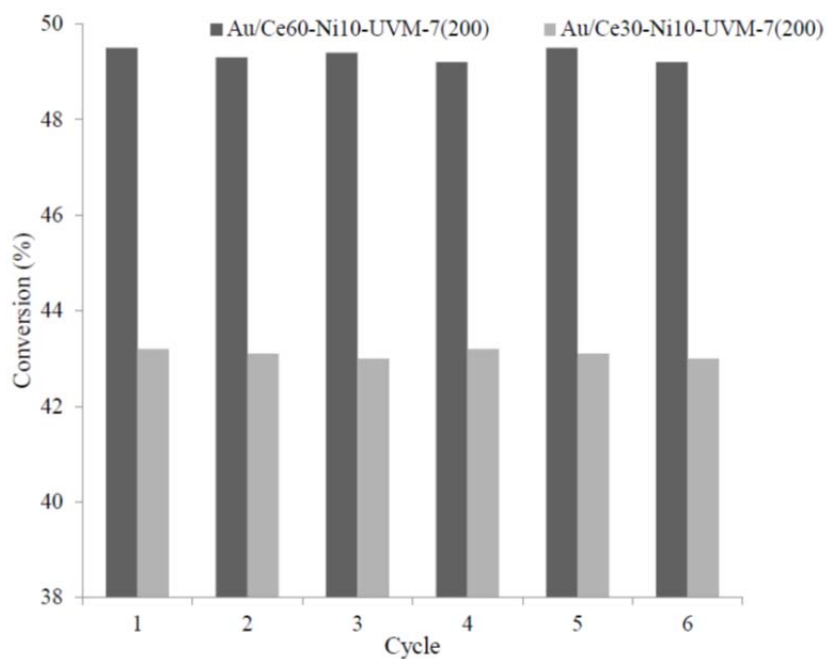


Fig. S10. Conversion of benzylamine on Au/Ce₆₀-Ni₁₀-UVM-7(200) and Au/Ce₃₀-Ni₁₀-UVM-7(200) catalysts over 6 successive cycles at 2 bar O₂ (115 oC, 4h, selectivity 100).

High Temperature Stable Gold Nanoparticle Catalysts for Application under Severe Conditions: The Role of TiO₂ Nanodomains on Structure and Activity

Begoña Puértolas^a, Álvaro Mayoral^b, Raul Arenal^{b,c}, Benjamín Solsona^d,
Alaina Moragues^e, Sonia Murcia-Mascaros^e, Pedro Amorós^e, Ana B.
Hungria^f, Stuart H. Taylor^g and Tomás García^a

^a Instituto de Carboquímica (ICB-CSIC), 50018 Zaragoza, Spain

^b Laboratorio de Microscopias Avanzadas (LMA), Instituto de Nanociencia de Aragón (INA) Universidad de Zaragoza, 50018 Zaragoza, Spain

^c Fundación Agencia Aragonesa para Investigación y Desarrollo (ARAID), 50018 Zaragoza, Spain

^d Departamento de Ingeniería Química, Universitat de València, 46071 Valencia, Spain

^e Institut de Ciència dels Materials, Universitat de València, 46071 Valencia, Spain

^f Departamento de Ciencia de Materiales, Ingeniería Metalúrgica y Química Inorgánica, Universidad de Cádiz, 11510 Puerto Real, Spain

^g Cardiff Catalysis Institute, School of Chemistry, Cardiff University, CF10 3AT Cardiff, United Kingdom

Received 5th November 2014, Accepted 26th December 2014

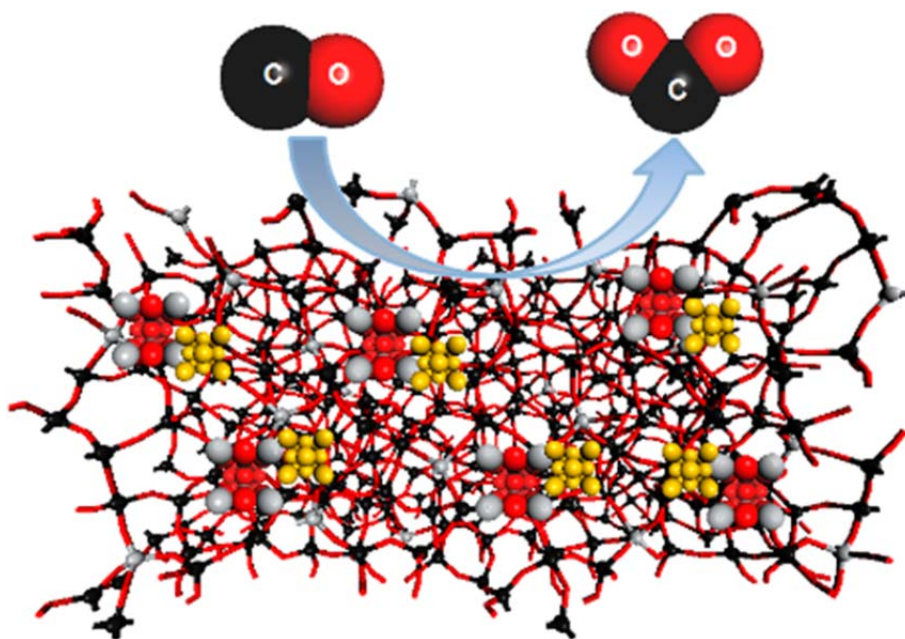
Published online 6th January 2015

ACS Catalysis 5 (2015) 1078-1086

DOI: 10.1021/cs501741u

Abstract

Metal nanoparticles with precisely controlled size are highly attractive for heterogeneous catalysis. However, their poor thermal stability remains a major concern in their application at realistic operating conditions. Here, we demonstrate the possibility of synthesizing gold nanoparticles with exceptional thermal stability. This has been achieved by using a simple conventional deposition-precipitation technique. The material employed as a catalyst consists of gold supported on a TiO₂ impregnated SiO₂ bimodal mesoporous support. The resulting material shows gold nanoparticles with a narrow size distribution around 3.0 nm, homogeneously dispersed over the TiO₂/SiO₂ material. Most interestingly, the gold nanoparticles show exceptional thermal stability, calcination temperatures as high as 800 °C have been employed and negligible changes in the gold particle size distribution are apparent. Additionally, the presence of an amorphous titanium silicate phase is partially preserved, and these factors lead to remarkable activity to catalyze a range of oxidation reactions.



Introduction

The nature and properties of catalysts based on gold nanoparticles dispersed on oxide supports have received much recent attention^{1,2}, due to their high activity in many industrially and environmentally important reactions. Especially significant is the capacity of sub-nanometer gold to oxidize CO to CO₂ at very low temperatures^{3,4}. To date, the most active gold catalysts for CO oxidation are generally supported on reducible metal oxides, such as TiO₂ or Fe₂O₃ which are either uncalcined or calcined at temperatures lower than 500 °C⁵⁻⁷. The discovery of gold-based catalysts showing exceptional low temperature CO oxidation activity resulted in an explosion of interest into these types of catalysts, and they have now been successfully applied to catalyze a wide range of reactions. However, an inherent problem for nanoparticulated catalysts is their well-documented lack of thermal stability under highly demanding operating conditions⁸⁻¹⁰. Supported and unsupported metal nanoparticles show rapid particle aggregation, especially at elevated reaction temperatures^{8,9}. For many industrially important catalytic applications, reaction temperatures typically exceed 600 °C, and hydrothermal stability of the catalysts becomes a crucial issue^{11,12}. Indeed, the development of heat-stable Au-based catalysts represents a true challenge and will offer new opportunities for Au nanoparticle catalysis if innovative routes to Au nanoparticle stabilization at high temperatures are proposed. Strategies such as post modification of Au/TiO₂ by amorphous SiO₂ decoration¹³, the production of core-shell nanostructures¹⁴⁻¹⁶ FeO_x modified hydroxyapatite supported gold catalysts¹⁷, or the synthesis of thin porous alumina sheets¹⁸ have been adopted to address this problem. These strategies certainly reduce the tendency to sinter at high temperatures. However, they have limitations, as they can use expensive precursors or highly complex synthesis procedures.

One of the main areas of opportunity concerns the automotive industry where low-temperature start-up performance of catalysts remains an area in which improvement is sought. The most widespread technologies of hybrid vehicles or micro hybrid cars (start-stop systems) require the development of efficient catalytic systems for the control of vehicle exhaust emissions during this period. Moreover, in addition

to the promising technical performance afforded by gold-based catalysts, the relative stable lower price and greater availability of gold compared with the platinum group metals remain excellent economic reasons for pursuing the development of pollution control technologies based on this metal¹⁹. In this respect, there is a desire to be able to prepare gold nanoparticulated catalysts which have increased stability at high temperatures, as this will significantly extend the application of these catalysts for new processes.

Herein, we demonstrate the possibility of synthesizing gold nanoparticles with exceptional thermal stability. The material employed as a catalyst consists of gold nanoparticles supported on a UVM-7 nanoparticulated bimodal mesoporous material²⁰⁻²², which has first been modified by impregnation to form TiO₂ domains. The resulting material shows gold nanoparticles with a narrow size distribution around 3.0 nm, homogeneously dispersed over the TiO₂/SiO₂ material, the nanoparticles sizes do not increase after calcination at temperatures as high as 800 °C. To the best of our knowledge, such a result has not been reported previously.

Experimental section

Materials

The synthesis of UVM-7 was based on the “atran route” with a molar composition of 2TEOS-7TEA-0.52CTMABr-180H₂O²⁰. In a typical synthesis, the corresponding amounts of TEOS (Fluka 98%) and TEA (Sigma Aldrich ≥ 99%) were mixed under continuous stirring at 140 °C until a homogeneous dispersion was achieved. Then, the temperature was decreased to 120 °C and the CTMABr (Sigma Aldrich 98%) was added. The resulting gel was cooled to 80 °C when distilled water was added. This mixture was allowed to age at room temperature overnight under continuous stirring. The resulting mesostructured powder was separated by filtration, washed extensively with deionized water and ethanol and dried at 60 °C overnight. In order to prepare the final porous material, the template was removed by calcination at 550 °C for 6 hours (heating ramp = 5 °C/min) under static air atmosphere.

Different metal oxides were incorporated into the UVM-7 support: TiO_2 , ZrO_2 and $\text{CeO}_2\text{-ZrO}_2$. Although we used a similar impregnation strategy regardless the different metal oxides included inside the UVM-7 mesopores, some experimental details have been optimized depending on the chemical nature of the reagent used.

$\text{TiO}_2/\text{UVM-7}$ was synthesized by a post synthetic wet impregnation procedure previously described by Narkhede et al.²³ Four different titania loadings were tested: from $\text{Ti}/(\text{Ti}+\text{Si})$ of 3 to 40 wt.%. To achieve these loadings, the corresponding weight of $\text{TiO}(\text{acac})_2$ (Sigma Aldrich 90%) was taken in 100 cm^3 of pure ethanol (Scharlau, HPLC grade). Then, deionized water was slowly added while continuous vigorous stirring. Subsequently, the impregnation of the calcined UVM-7 silica support (0.6 g) was carried out by stirring the sample for 2 hours with the Ti solution. The mixture was filtered and washed thoroughly. The cake was allowed to dry overnight at room temperature and the $\text{TiO}_2/\text{UVM-7}$ was calcined in air at $300\text{ }^\circ\text{C}$ for 5 hours with a heating rate of $1\text{ }^\circ\text{C}/\text{min}$.

$\text{ZrO}_2/\text{UVM-7}$ was synthesized by a conventional wet impregnation procedure. 1.83 g of $\text{ZrO}(\text{NO}_3)_2\cdot x\text{H}_2\text{O}$ (Sigma Aldrich, technical grade) were dissolved in 30 cm^3 of deionized water under vigorous stirring. Impregnation of the calcined UVM-7 silica support (0.6 g) was carried out by stirring the sample for 13 hours with the Zr solution. The mixture was allowed to dry overnight at $110\text{ }^\circ\text{C}$ and the resulting $\text{ZrO}_2/\text{UVM-7}$ was calcined in air at $550\text{ }^\circ\text{C}$ for 4 hours with a heating rate of $1\text{ }^\circ\text{C}/\text{min}$. The Zr loading was 54.6 wt.%.

$\text{CeO}_2\text{-ZrO}_2/\text{UVM-7}$ was also synthesized by a conventional wet impregnation procedure. 0.91 g of $\text{ZrO}(\text{NO}_3)_2\cdot x\text{H}_2\text{O}$ and 1.42 g of $\text{Ce}(\text{NO}_3)_3\cdot 6\text{H}_2\text{O}$ (Sigma Aldrich 99%) were dissolved in 30 cm^3 of deionized water under vigorous stirring. Impregnation of the calcined UVM-7 silica support (0.6 g) was carried out by stirring the sample for 13 hours with the Ce-Zr solution. The mixture was allowed to dry overnight at $110\text{ }^\circ\text{C}$ and the $\text{CeO}_2\text{-ZrO}_2/\text{UVM-7}$ was calcined in air at $550\text{ }^\circ\text{C}$ for 4 hours with a heating rate of $1\text{ }^\circ\text{C}/\text{min}$. The cerium and zirconium loadings were 37.6 and 43.3 wt.%, respectively. Compared to TiO_2 , in which relatively soft thermal conditions were used to favor first the melting of the $\text{TiO}(\text{acac})_2$ and later its thermal evolution to oxide, in the case of Zr

and Ce derivatives different calcination conditions were employed to promote the evolution of nitrates and oxide formation.

The gold incorporation onto the TiO₂/UVM-7, ZrO₂/UVM-7 and CeO₂-ZrO₂/UVM-7 matrixes was carried out by the conventional deposition-precipitation technique. 43.4 cm³ of an aqueous solution (5.078·10⁻³ M) of KAuCl₄ (Sigma Aldrich 98%) were heated in a water bath wrapped by an aluminum foil to exclude light at 70 °C. The initial pH was around 2.5. It was carefully adjusted to neutral pH by drop wise addition of a 0.1 M aqueous solution of NaOH (Sigma Aldrich ≥ 98%). The pH was maintained around 7 for 30 minutes. 0.5 g of the required UVM-7 support was then added and pH excursions into the acidic region were controlled by adding NaOH. After the pH was constant for 15 minutes, the suspension was stirred for another hour at the same temperature. Finally, the suspension was cooled, filtered and washed with deionized water. The resulting cake was heated at 90 °C for 13 hours. After the preparation, the samples were stored in the dark in a vacuum desiccator at room temperature. Each sample was divided into three portions: the first portion was kept uncalcined; the second portion was calcined at 400 °C in static air for 4 hours with a heating rate of 1 °C/min and the third portion was calcined at 800 °C in static air under the same conditions. In all cases, the final catalysts were stored in a vacuum desiccator at room temperature.

Characterization

For electron microscopy analyses, the samples were dispersed in ethanol and placed onto a carbon coated copper microgrid and left to dry before observation. Spherical aberration (Cs) corrected scanning transmission electron microscopy high-angle annular field (STEM-HAADF) imaging analyses were performed in a XFEG FEI Titan microscope operated at 300 kV. The microscope was equipped with a CEOS aberration corrector for the electron probe, achieving a point resolution of 0.8 Å, an EDAX EDS detector and Gatan Energy Filter Tridiem HR865 for electron energy loss spectroscopy (EELS). These spectroscopic data were obtained using the spectrum-image acquisition mode^{24,25}.

X-Ray Photoelectron Spectroscopy (XPS) measurements were made on an Omicron ESCA+ photoelectron spectrometer using a non-monochromatized MgK α X-Ray source ($h\nu = 1253.6$ eV). Analyzer pass energy of 50 eV was used for survey scans and 20 eV for detailed scans. Binding energies were referenced to the C1s peak from adventitious carbonaceous contamination, assumed to have a binding energy of 284.5 eV.

Powder X-ray diffraction (XRD) was carried out using a Bruker D8 Advance diffractometer with monochromatic Cu K α source operated at 40 kV and 40 mA.

The textural characterization of the samples was carried out by N₂ adsorption at -196 °C, using a Micromeritics ASAP 2020 apparatus. Prior to the adsorption measurements, the samples were outgassed in situ in vacuum at 250 °C for 4 hours to remove adsorbed gases. Surface areas were calculated from nitrogen adsorption isotherms in the relative pressure range from 0.1 to 0.25 using the BET equation (SBET). Both BJH pore size distributions and volumes were obtained from the adsorption branch of the N₂ adsorption isotherms. In addition, specific surface area, and total intra-particle pore volume (micro and mesopore) were also estimated using the Non Localized Density Functional Theory (NLDFT) method. The model used for the NLDFT evaluation was N₂ adsorbed on silica with cylindrical pores, considering the adsorption branch of the isotherm.

Raman spectra were obtained using a HORIBA Jobin Yvon iHR320 spectrometer with Peltier-cooled CCD and a 532 nm and 785 nm doubled YAG laser as excitation.

²⁹Si MAS NMR spectra were recorded on a Varian Unity 300 spectrometer operating at 79.5 MHz, and using a magic angle spinning speed of at least 4.0 kHz.

The gold loading was determined by energy dispersive X-ray spectroscopy EDX analysis using a Scanning Electron Microscope (Philips - SEM-XL 30).

Catalytic testing

CO catalytic oxidation was performed at atmospheric pressure and at a temperature of 20 °C, using a fixed bed reactor with an inner diameter of 5.8 mm. A mixture of 0.4 % v/v CO, 20 % v/v O₂ and argon balance was passed over 10 mg of catalyst with a flow rate of 100 cm³/min which corresponded to a space velocity of 600,000 cm³/(g_{cat}·h). Analyses were performed by an on-line gas chromatograph (Varian CP-3800) with thermal conductivity, and the conversion of CO and the formation of CO₂ were both quantify which led us to measure a carbon balance with and accuracy of ± 2%. After being used in the reactor, the catalysts were stored at room-temperature in a vacuum desiccator before spectroscopic analysis.

The Au/Ti8/UVM-7 800 catalyst performance was tested under simulated cold-start conditions by means of cold-start tests (CST). CST experiments were carried out in a fixed-bed reactor (diameter = 0.457 cm) under conditions that closely resembled the automotive “cold-start”. In the course of the simulated CSTs, the reactor temperature was increased from 30 °C to 600 °C at 50 °C/min, and held at this temperature for a further 30 min. The temperature was measured by a thermocouple located at the top of the catalyst bed. The inlet gas composition used for CST experiments was 1.6 % v/v CO, 0.01 % v/v propene, 0.0087 % v/v toluene, 1 % v/v oxygen, 10 % v/v water in argon leading to a total flow of 100 cm³ STP/min and a gas hourly space velocity (GHSV) of 200,000 h⁻¹. Aliquots of the outlet stream were analyzed on line using a quadrupole spectrometer (Omnistar, Pfeiffer Vacuum). The following masses were monitored: m/z = 40 for argon, 28 for CO, 42 for propene, 91 for toluene, 32 for oxygen and 18 for water; m/z = 44 related to CO₂ formation was also followed during the experiment. Finally, ten consecutive CSTs were performed once the reactor was cooled down to assess the reusability and stability of the catalyst. Carbon balances were closed in all the experiments (100 ± 3%).

Moreover, in order to evaluate the hydrothermal stability of the Au/Ti8/UVM-7 800 catalyst and its performance as a three-way catalyst, three consecutive cycles were performed under a gas flow that simulated the real exhaust gases of a diesel engine. The inlet gas composition used in the experiments was 1 % v/v CO, 0.1 % v/v

propane, 0.03 % v/v NO, 8 % v/v O₂, 6 % v/v CO₂, 8 % v/v H₂O and nitrogen balance under a total flow of 200 cm³/min. Flow rates of all gases were controlled by mass flow controllers. The experiments were run in a fixed-bed reactor (GHSV = 40,000 h⁻¹) externally heated and coupled to an Infrared Spectrometer (Gaset DX4000). Carbon balances were closed in all the experiments with an accuracy of ± 3%.

The Au/Ti8/UVM-7 800 catalyst performance was also tested for methane combustion. The activity test for catalytic methane oxidation was conducted in a fixed-bed reactor under isothermal conditions. 1 % v/v CH₄ in air were flowed by mass flow controllers at a space velocity of 60,000 h⁻¹. Analyses were performed by an on-line gas chromatograph (Varian CP-3800) with thermal conductivity and flame ionization detectors, and the conversion of CH₄ and the formation of CO₂ were both quantified, giving a carbon balance with an accuracy of ± 2%.

Results and discussion

The mesoporous silica UVM-7 is loaded with four different concentrations of TiO₂ to achieve a Ti/(Ti+Si) ratio of 3, 8, 15 and 40 wt.%. The preparation method is based on a simple wet impregnation of UVM-7 with titanium (IV) oxyacetylacetonate (TiO(acac)₂) calcining the samples at 300 °C with a very slow heating ramp and the conventional deposition-precipitation technique is employed for the addition of gold onto the mesoporous TiO₂/UVM-7 matrix. The use of a slow heating ramp is crucial to obtain beneficial dispersion of the titanium species. The TiO(acac)₂ melts at *ca.* 200 °C, which is below the temperature of complex degradation, and leads to a homogeneous dispersion of Ti-species over the internal surface of the UVM-7 silica. After gold deposition, several catalysts were prepared by heating the samples in air at temperatures of 400 and 800 °C, and comparison is made with a sample which is dried, but not calcined at high temperature. The samples are coded Au/TiX/UVM-7 CT, where X and CT represent the titania loading (3, 8, 15 and 40 wt.%) and the calcination temperature (400 or 800 °C), respectively. Gold loadings of representative uncalcined and calcined catalysts are compiled in Table S1, and range from 2 to 5 wt.% depending on titania loading. Additionally, a slightly higher gold loading is observed in the

uncalcined samples. Experimental error in the determination of the gold content (± 0.2 wt.%) can have an influence on these differences. However, it cannot be completely discarded that the marginal evaporation of large gold particles into the gas phase followed by the treatment at high temperatures²⁶ could be taking place. The simplicity of the preparation method as well as ease of scale-up are major advantages from the perspective of application.

Table 1. Comparison of CO oxidation activity of the UVM-7 based catalysts with other catalysts reported in the literature.

Support	Gold content (wt.%) ^a	Catalytic performance	T _{cal} (°C)	D _{Au} (nm) ^b	space velocity (cm ³ /(g _{cat} ·h))	mol CO/(g _{cat} ·h)·(10 ³) at 20 °C	Ref
TiO ₂ /SiO ₂	2.2	T ₅₀ = 64 °C	700	6.5	44,000	9.0 ^{at 64 °C}	13
ZrO ₂	-	T ₅₀ = 200 °C	800	15	80,000	2.3	14
TiO ₂ /Si-Al ₂ O ₃	1	T ₅₀ = 50 °C	600	3.0	36,000	6.0 ^{at 30 °C}	15
FeO _x	3.2	T ₅₀ = 22 °C	600	4.5	20,000	3.6	17
AlO _x	3.0	T ₅₀ = -3 °C	700	2.2	80,000	30.0	18
AlO _x	3.0	T ₅₀ = -3 °C	900	2.2	80,000	2.6	18
TiO ₂ /UVM-7	2.1	X _{CO} = 15%	800	3.5 ± 1.6	600,000	17.5	This study
ZrO ₂ /UVM-7	5.7	X _{CO} = 45%	800	8.7 ± 3.9	25,000	2.6	This study
CeO ₂ -ZrO ₂ /UVM-7	3.2	X _{CO} = 72%	800	6.4 ± 2.6	35,000	6.1	This study

^a The gold loading (wt.%) in our catalysts is determined by EDX. ^b The gold mean particle size in our catalysts is determined by TEM. T_{cal}: calcination temperature (°C). X_{CO}: CO conversion for the CO oxidation reaction. Conditions: 0.4 % v/v CO, 20 % v/v O₂ and argon balance, reaction temperature = 20 °C.

Ambient temperature CO oxidation was used as an initial model reaction to probe the catalysts performance (Figure S1 and S2). The optimal titanium loading is 8 wt.% (Figure S1 and Table S2). Increasing the calcination temperature of the catalysts leads to a decrease of the CO conversion but the catalyst stability increases (Figure S2). Following calcination at 400 and 800 °C there is no deactivation over the test period,

whilst for the uncalcined catalyst conversion is not stable as the catalytic activity slightly decreases with time-on-line. It is noteworthy, that in addition to the excellent stability, the catalyst calcined at 800 °C still presents very high activity, as test conditions employ a very short contact time. Table 1 shows comparative CO oxidation results from the literature for gold-based catalysts heat treated at 600 °C and above. Our Au/Ti8/UVM-7 800 catalyst oxidizes CO at 20 °C using a high space velocity of 600,000 cm³/(g_{cat}·h), with a CO conversion rate of 0.0175 mol CO/(g_{cat}·h), which is, to the best of our knowledge, the highest activity currently reported in the literature for gold catalysts calcined at high temperature.

A wide variety of different silica supports are available, but we specifically select UVM-7 due to its open framework and enhanced accessibility, as a consequence of hierarchic porosity with large inter-particle voids and 3D interconnected short-length (*ca.* 25-30 nm) nanometric mesopores of *ca.* 3 nm (when CTMABr is used as template). These characteristics, which are not present in other silicas such as MCM-41, MCM-48 or SBA-15 (usually obtained as large micrometric particles with unimodal long-length mesopores), favor mass diffusion throughout the hierarchic pore structure²². This aspect could be beneficial, both at the preparative level, as a very homogeneous dispersion of both titanium and gold nanoparticles can be achieved, favoring the impregnation with the TiO(acac)₂ and KAuCl₄ solutions, and also for accessibility to active sites of the catalyst during operation. Accordingly, this catalytic system both uncalcined and calcined at conventional temperature (400 °C) also shows higher catalytic activity than a commercial gold/TiO₂ based catalysts supplied by the World Gold Council (Table S2). Therefore, an outstanding activity and stability is obtained for this material, which is even more noteworthy considering it is calcined at the high temperature of 800 °C. In contrast to that observed for Au/TiO₂/UVM-7 800 catalyst, the heat-treatment of the Au/TiO₂ catalyst supplied by the World Gold Council at 800 °C led to a severe deactivation of the catalyst, which exhibited a productivity *ca.* 600 times lower than that observed for Au/Ti8/UVM-7 800. An accused sintering of the gold particles takes place and most of the gold crystallites are in the 12 to 20 nm range.

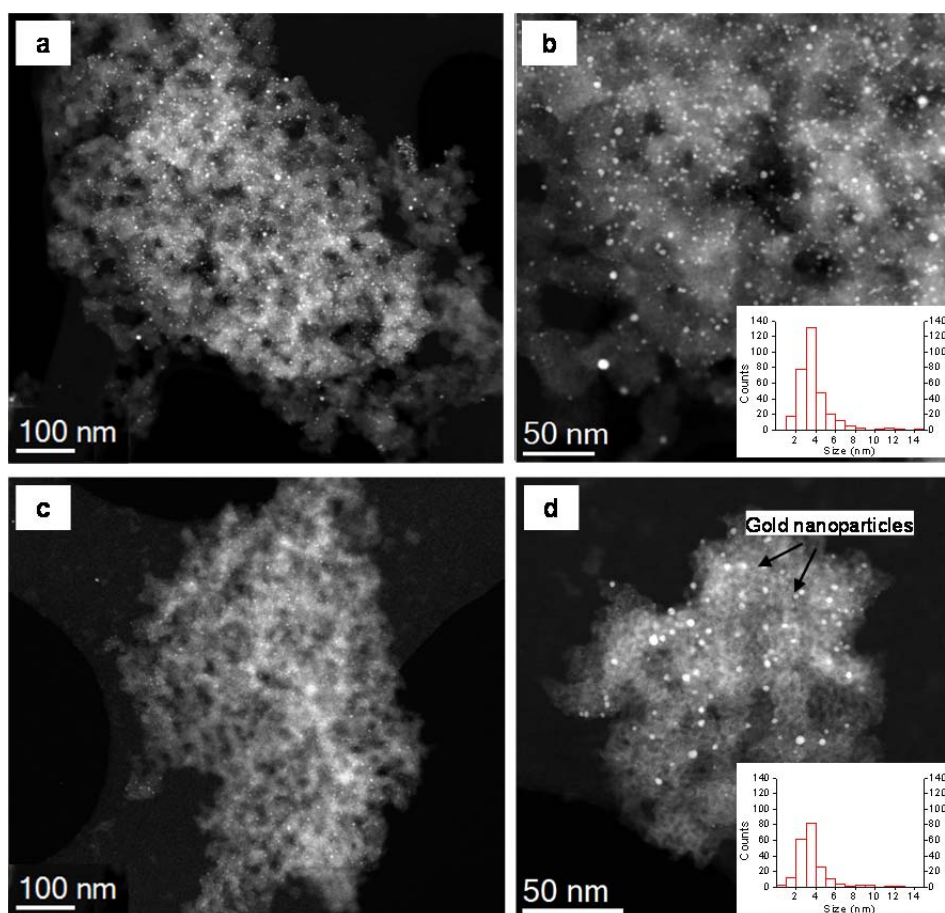


Figure 1. Cs-corrected STEM-HAADF images and gold particle size distribution of the (a, b) uncalcined and (c, d) calcined at 800 °C Au/Ti8/UVM-7 catalysts. Particle size distributions are shown as insets for (b) uncalcined and (d) calcined samples.

The remarkable performance of this catalytic system can be related firstly to the presence of small gold nanoparticles, which are resistant to sintering. Figure 1a and b shows Spherical aberration (Cs) corrected scanning transmission electron microscopy high-angle annular field (STEM-HAADF) images of the uncalcined Au/Ti8/UVM-7 catalyst. Similar images of the sample after calcination at 800 °C for 4 hours (Figure 1c and d) confirm that the gold nanoparticles are thermally stable, as the high temperature treatment does not result in sintering, preserving their original size and maintaining an homogeneous distribution over the mesoporous support. The uncalcined sample shows some small 1 nm gold nanoparticles, and has a unimodal

particle size distribution, with most particles in the 1-6 nm range. The predominant particle size of the uncalcined sample is 3.73 ± 1.60 nm, which surprisingly does not dramatically increase after calcination at 800 °C (3.50 ± 1.57 nm). Powder X-Ray Diffraction (XRD) is also used to probe the dispersion and stability of the gold nanoparticles (Figure S3). Unchanged diffraction peaks (of very low intensity) from gold species are observed before and after calcination at 800 °C (even for the samples after the catalytic reaction), consistent with the TEM, indicating that gold species remain well dispersed on the support even after high temperature treatment (Figure 1d).

The exceptional catalytic performance of these materials also can be related to the way in which titanium is present on the UVM-7 support. For the uncalcined sample, different spectroscopic techniques support the formation of species including Ti-O-Si bonds between Ti-oligomers (produced after degradation of the $\text{TiO}(\text{acac})_2$ precursor at 300 °C) and the silica surface, where a certain proportion of Ti^{4+} occupies a tetrahedral coordination site similar to Si in SiO_2 (Figure S4). In fact, a slight increase of the binding energy of both Ti $2p_{3/2}$ and the second component of O 1s compared to pure TiO_2 are observed, consistent with diffusion of Ti species into the silica wall^{27,28} (Table S3). This shift is also accompanied by an increase of the oxidation potential of the Ti(IV) cations, which may enhance the oxygen mobility at the gold/Ti-O-Si interface, thus enhancing the CO oxidation activity at low temperature²⁹ (Table 1). Accordingly, the existence of a regular and homogeneous dispersion of titanium for the uncalcined sample is also confirmed by STEM images in Figure 2. This extremely regular dispersion of Ti species on the silica surface also favors the subsequent homogeneous distribution of AuCl_4^- complexes and finally of gold nanoparticles achieved during the deposition-precipitation step.

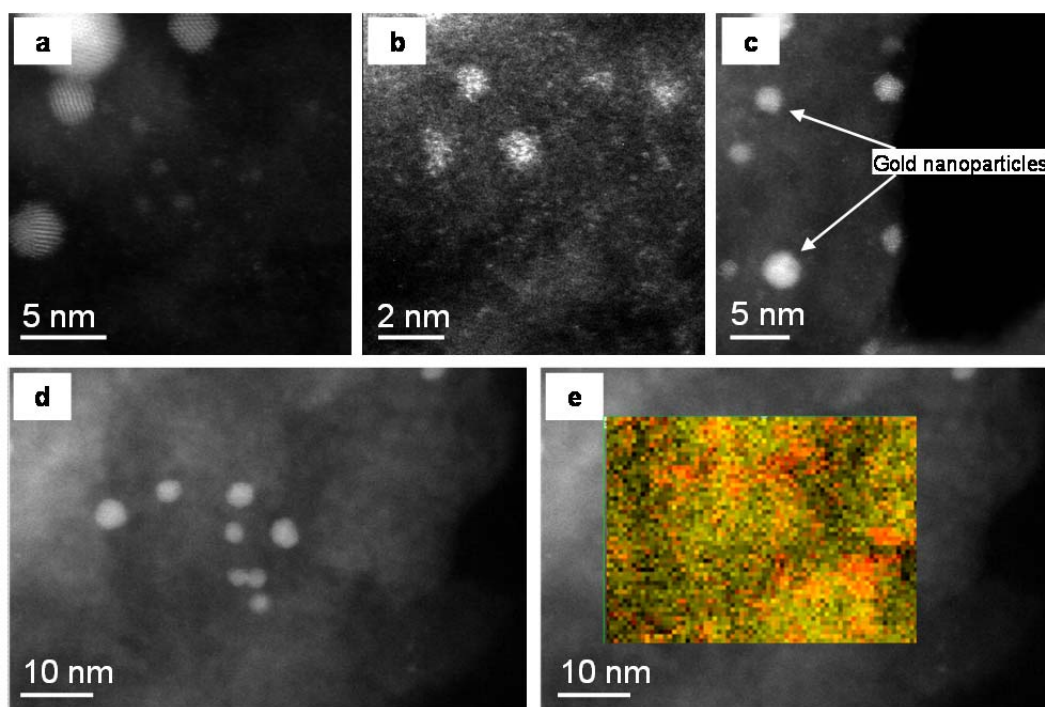


Figure 2. Cs-corrected STEM-HAADF images of Au/Ti8/UVM-7. (a), (b), (c) High-magnification images where gold nanoparticles are identified. (d) Cs-corrected STEM-HAADF image where an EELS spectrum-image is recorded. (e) Ti-L_{3,2} (red) and O-K (yellow) maps superimposed on the experimental STEM image.

Upon calcination at 800 °C, the catalyst still presents very high activity, although a certain loss of activity is clearly observed when compared to uncalcined materials. This loss of activity can be linked to different factors. With respect to gold, although the nanoparticle size is preserved, it cannot be discounted that there could be a decrease of activity due to a change of the gold surface oxidation state^{30,31}. Accordingly, the oxidation state of gold on the surface of the nanoparticles is investigated using X-ray Photoelectron Spectroscopy (XPS). The uncalcined catalyst has some cationic gold, ($\text{Au}^{3+}/\text{Au}^0 = 0.24$), while only metallic gold is present after heat treatment at 800 °C (Figure S5 and Table S4). More importantly, the calcination probably induces changes to the Ti species, although these are more complex, and may not directly relate with the catalytic activity. Firstly, it is observed that Ti species only remains partly as Ti-O-Si species, supported by XPS results (Figure S4 and Table S3), and corroborated by ²⁹Si NMR (Figure S6). The ²⁹Si NMR spectrum of the Ti8/UVM-7 support shows a 5% increase of the signals at *ca.* -100 and -93 ppm (corresponding to

Si environments with 1 and 2 atoms of Ti as neighbors, respectively: Si (3Si, 1Ti) and Si (2Si, 2Ti))³² and a decrease in the Q⁴ signal (at *ca.* -110 ppm) when compared with the spectrum of the UVM-7 silica pure support and calcined at the same temperature, in which some Si-OH groups are still preserved (signal at *ca.* -110 ppm, Figure S6 and Table S5). These data allow us to determine that an additional 38% of titanium atoms are incorporated into the UVM-7 silica wall (by diffusion at 800 °C) and the remaining Ti (62%) must initiate a process of nucleation and growth of TiO₂ domains.

Table 2. Textural characterizations of UVM-7 materials loaded with titania and gold/titania.

Catalysts	Surface area (m ² /g)	Intrap. pore size (nm)	Intrap. pore volume (cm ³ /g)	Interp. pore size (nm)	Interp. pore volume (cm ³ /g)
UVM-7	1136	2.87	1.01	29.0	1.20
Ti8/UVM-7	931	2.81	0.79	25.5	0.88
Au/Ti8/UVM-7	845	2.82	0.72	36.8	1.30
Au/Ti8/UVM-7 800	245	1.30 / 2.75 ^a	0.14	27.2	0.68

^a Intra-particle pore size determined by the application of the DFT model.

It is worth mentioning that the modification of the architecture/mesostructure of the siliceous support could be a key parameter upon calcination, leading to ultrastable gold nanoparticles. Thus, although calcination results in an expected reduction of both surface area and pore volume, when compared with the uncalcined material, the highly active Au/Ti8/UVM-7 800 catalyst still preserves a relatively high specific BET surface area of 245 m²/g and a total pore volume of 0.82 cm³/g, which includes 0.14 cm³/g associated with the internal porosity (Table 2, Figure S7 and Table S6). Applying a density functional theory (DFT) model also allows us to detect the existence of some microporosity in the calcined sample. This microporosity along with a partial preservation of the original mesoporosity seems to be improved by the presence of TiO₂ and Au (Figure S8), since the UVM-7 support completely collapses after calcination at 800 °C. Thus, values of 151 m²/g and 0.14 cm³/g can be estimated for the intra-particle porosity (excluding the textural component) in the case of sample

Au/Ti8/UVM-7 800. The generation/preservation of this micro-mesoporosity, that must be understood as the result of a partial collapse of the original mesostructure, is most likely the key to explain both the high catalytic activity (directly related to resistance to sintering of the particles of Au), and the loss of activity compared to the uncalcined catalyst due to a certain loss of accessible active sites that become trapped.

Therefore, it can be assumed that the TiO₂ crystallites covering the internal porous surface of the support could have an important role in enhancing the thermal stability of the UVM-7 mesostructure, acting as a scaffold of the support, as suggested by the surface area increase with the Ti content of the Au/Ti15/UVM-7 800 (Table S6) and the total collapse of the Au/UVM-7 800 structure (Figure S9). Accordingly, it was observed that the high BET surface area and bimodal porosity of the materials was preserved for titania loadings up to *ca.* 15 wt.% (Ti15/UVM-7 sample) (Table S7). For higher titania loading (40 wt.%), a dramatic decrease of these textural parameters occurred, which indicates a significant mesopore blocking (affecting both the gold deposition and the CO accessibility), with the subsequent loss of catalytic activity. Upon calcination, TiO₂ partially agglomerates in the form of small TiO₂ nanodomains with sizes just slightly larger than that of the gold nanoparticles (Figure 3, Figure S4 and Table S3). The absence of titania diffraction in the XRD is a further evidence for the small size of the TiO₂ domains (Figure S3). Accordingly, microscopy data shows (Figure 3a) the high-resolution images of the gold and the TiO₂ nanoparticles. The titania FFT diffractograms can be indexed assuming I41/amd symmetry corresponding to anatase and lattice parameters $a = 3.78 \text{ \AA}$ and $b = 9.51 \text{ \AA}$. (Figure 3b). Laser Raman spectroscopy (Figure S10) also confirms the presence of titania with anatase as the predominant crystalline phase for the Au/Ti8/UVM-7 800 sample³³. UVM-7 support seemed to stabilize the anatase phase, although a retarding effect over the phase transition from anatase to rutile due to the presence of gold nanoparticles could not be ruled out. Although this agglomeration of the Ti species seems to be detrimental for the catalyst performance²⁹, as also suggested by the loss of activity with the increasing Ti content, the nanocrystalline nature of the anatase domains also seemed to induce a strong interfacial anchoring effect between TiO₂ and the gold nanoparticles negating their sintering after high temperature calcination³⁴. Indeed, for gold supported directly

on the mesoporous UVM-7 support the gold nanoparticles readily agglomerate and, for the calcined sample, large gold nanoparticles together with small nanoparticles are formed (Figure S9) and a total structure collapse is evident. The presence of both small and large nanoparticles is in accordance to Qian et al. who reported the co-existence of both small and large size of gold nanoparticles for Au/SiO₂ catalysts calcined at high temperatures²⁶, proposing that small gold nanoparticles formed by an evaporation-deposition mechanism. Accordingly, gold nanoparticles are only observed close to the titania nanodomains on the UVM-7 surface (Figure 3), which is corroborated by the combination of STEM-HAADF images and chemical mapping based on electron energy loss spectroscopy (EELS) measurements (Figures 3b and c). The TiO₂ domains have dual roles, as a scaffold³⁵, preventing the complete mesostructure collapse, and as an anchoring island to avoid gold sintering. Hence, the exceptional thermal stability of gold nanoparticles in Au/Ti8/UVM-7 could be viewed as the combined result of a strong anchoring of gold on titania nanoparticles homogeneously dispersed on the preserved UVM-7 internal surface, and the confinement effect that is provided by the silica mesostructure and the anatase nanocrystals.

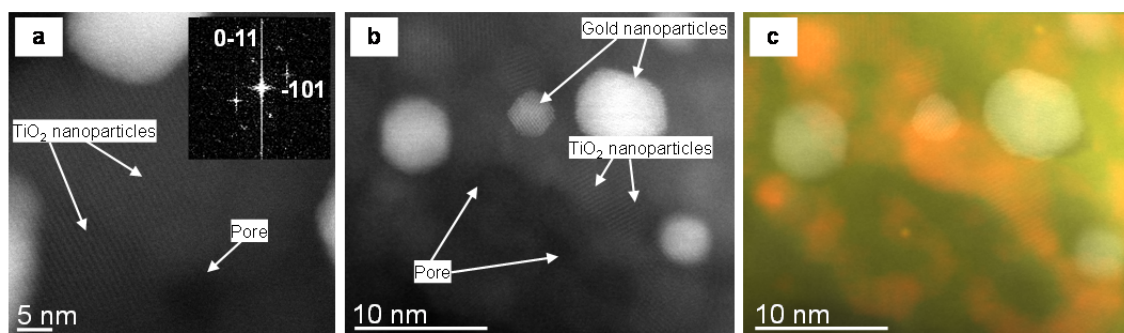


Figure 3. Cs-corrected STEM-HAADF images of Au/Ti8/UVM-7 800. (a) High-magnification image where the TiO₂ nanoparticles are identified together with the Au nanoparticles. The FFT of the TiO₂ phase is shown as an inset. (b) Cs-corrected STEM-HAADF image where an inset. (b) Cs-corrected STEM-HAADF image where an EELS spectrum-image is recorded. (c) Ti-L_{3,2} (red) and O-K (yellow) maps superimposed on the HRSTEM-HAADF image.

We have studied UVM-7 supported gold catalysts modified by other metal oxides by using this simple preparation method, to see if the highly active and stable gold nanoparticles are specific to titania modification. After an optimization procedure to select the proper metal oxide loadings, gold nanoparticles are deposited onto $\text{ZrO}_2/\text{UVM-7}$ and $\text{CeO}_2\text{-ZrO}_2/\text{UVM-7}$ supports. It should be commented that regardless of the metal oxide nanodomains included inside the mesopores, a preferred interaction of the gold nanoparticles with these metal oxides is observed. This is again a key factor favoring the presence of highly dispersed small gold nanoparticles. Additionally, as observed for $\text{TiO}_2/\text{UVM-7}$ supports, these metal oxide nanodomains also act as scaffolds for the UVM-7 support, preventing silica from the complete collapse and preserving a certain porosity to favor the diffusion of CO to the active sites, and as anchoring islands for gold nanoparticles, providing stability against sintering after calcination at 800 °C, resulting in highly thermally stable gold nanoparticles (Figure 4 and Figure S11).

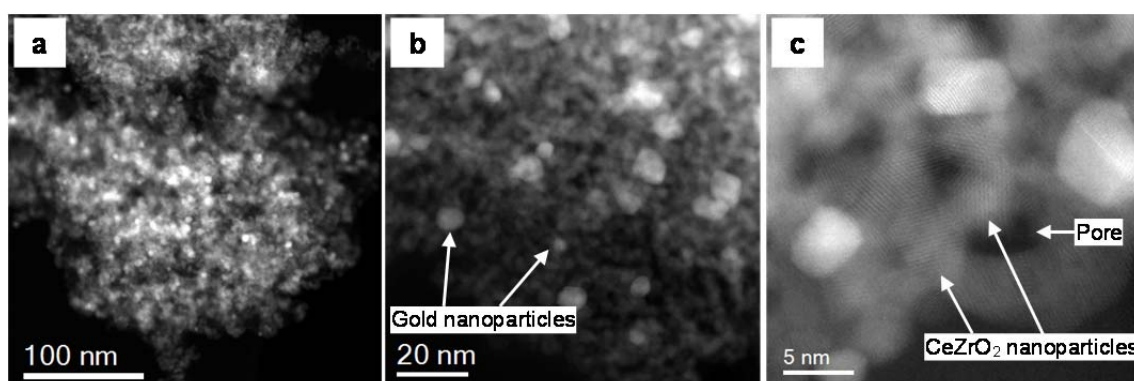


Figure 4. Cs-corrected STEM-HAADF images of $\text{Au/CeO}_2\text{-ZrO}_2/\text{UVM-7}$ 800 at (a) low-magnification observing a homogeneous distribution of gold, (b) medium-magnification image and (c) high-magnification observing *fcc* Au nanoparticles and some crystalline CeZrO_2 domains.

As shown in Table 1 these gold catalysts calcined at 800 °C are also very active for the model CO oxidation reaction at 20 °C. The catalytic activity is lower for both zirconia and cerium modified zirconia than for titania, but $\text{Au/ZrO}_2/\text{UVM-7}$ 800 still has a productivity of 0.0026 mol $\text{CO}/(\text{g}_{\text{cat}}\cdot\text{h})$ and $\text{Au/CeO}_2\text{-ZrO}_2/\text{UVM-7}$ 800 is more active

achieving a productivity of $0.0061 \text{ mol CO}/(\text{g}_{\text{cat}}\cdot\text{h})$ (Table S8). The addition of zirconia is known to increase the thermal stability of CeO_2 ³⁶, and this is consistent with our observations. Importantly, although some differences might be expected in the final oxides depending on the type of precursor used, our preliminary results with Zr and Ce oxides indicate that there are no differences in the role played by the oxidic domains (TiO_2 , ZrO_2 , $\text{CeO}_2\text{-ZrO}_2$) from the structural/morphological point of view: they act as inorganic anchors for the gold particles and as scaffolds to prevent a massive mesostructure collapse. However, we note that the gold nanoparticles anchored on ZrO_2 and $\text{CeO}_2\text{-ZrO}_2$ have slightly higher sizes than those observed on anatase domains (Table 1). These differences together with the intrinsic characteristics of each catalytic system could be responsible for the different catalytic activity observed. Thus, it appears that the beneficial stabilization effect is not restricted to titania with the UVM-7 support, as similar beneficial effects are also observed with zirconia and ceria-zirconia, which highlights the versatility of these nanostructured materials to be implemented into new high-temperature processes.

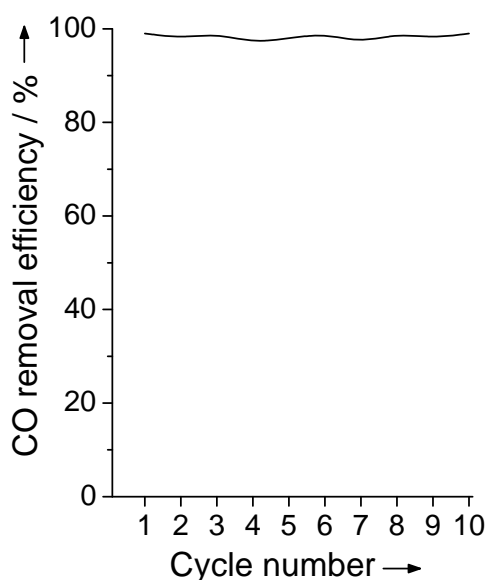


Figure 5. CO removal efficiency under simulated cold-start conditions of Au/Ti8/UVM-7 800 catalyst. Conditions: 1.6 % v/v CO, 0.01 % v/v propene, 0.0087 % v/v toluene, 1 % v/v oxygen, 10 % v/v water and Ar balance, GHSV = 200,000 h⁻¹. Temperature is increased from 30 to 600 °C at 50 °C/min.

We are able to illustrate the exceptional thermal stability of gold nanoparticles on metal oxide modified UVM-7 by employing the catalyst for several high-temperature applications. We have exemplified this using CO emission control during the cold-start process of an engine. The evolution of CO concentration of a stream of 1.6 % v/v CO, 0.01 % v/v propene, 0.0087 % v/v toluene and 1 % v/v O₂ by increasing the reactor temperature from 30 to 600 °C at 50 °C/min over the Au/Ti8/UVM-7 800 shows 100 % CO removal in the presence of 10 % v/v H₂O after ten consecutive cycles at a space velocity of 200,000 h⁻¹ (Figure 5). There is no appreciable gold nanoparticle sintering after use (2.3 ± 0.6 nm, Figure 6). Figure 6a and 6b confirms the homogeneous nanoparticle dispersion after reaction preserving a diameter below 5 nm and, as already described, the chemical analysis corroborates the affinity between the position of the TiO₂ domains and the Au nanoparticles, preventing gold sintering under severe conditions.

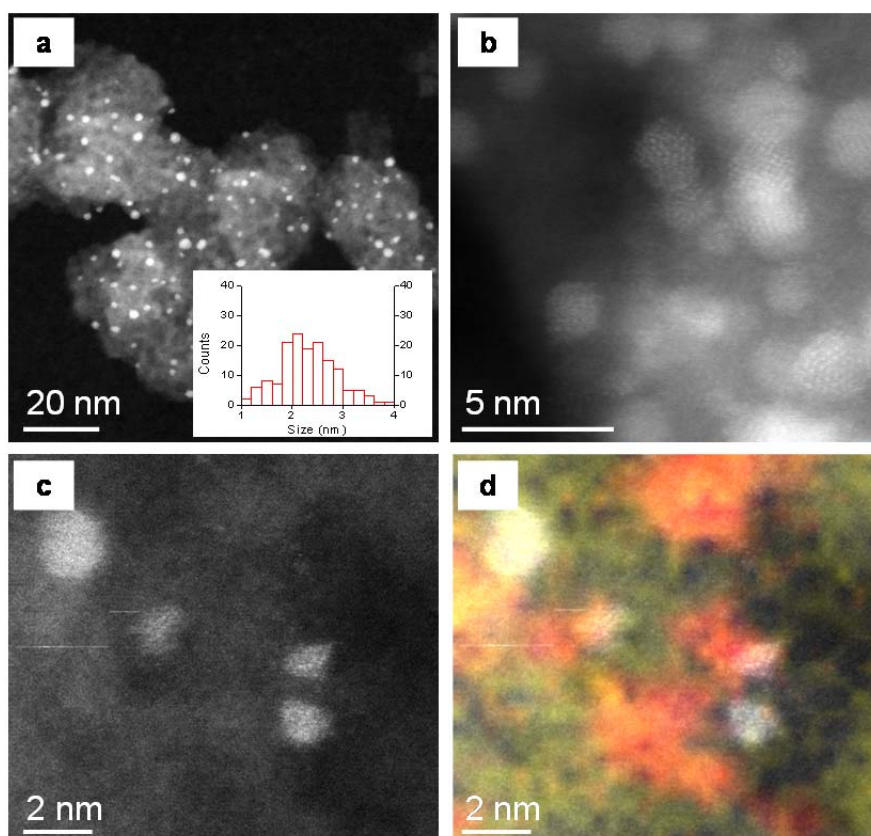


Figure 6. Cs-corrected STEM-HAADF images of the Au/Ti8/UVM-7 800 catalyst after ten consecutive cold-start tests. (a) Low-magnification image showing the nanoparticle distribution as inset. (b) High-magnification image. (c) Cs-corrected STEM-HAADF image where an EELS spectrum-image is recorded (d) Ti-L_{3,2} (red) and O-K (yellow) maps superimposed on the HRSTEM-HAADF image.

This catalyst is also tested as a three-way catalyst under a reaction mixture of 1 % v/v CO, 0.1 % v/v propane, 0.03 % v/v NO, 8 % v/v O₂, 6 % v/v CO₂ and 8 % v/v H₂O, space velocity of 40,000 h⁻¹ and at a reaction temperature of 500 °C showing remarkable hydrothermal stability after three consecutive cycles (Figure S12). The stability and activity was also validated using methane catalytic oxidation of 1 % v/v CH₄ in air by increasing the reactor temperature from 300 to 800 °C at a space velocity of 60,000 h⁻¹. Stable catalyst performance is maintained for at least five consecutive cycles (Figure 7).

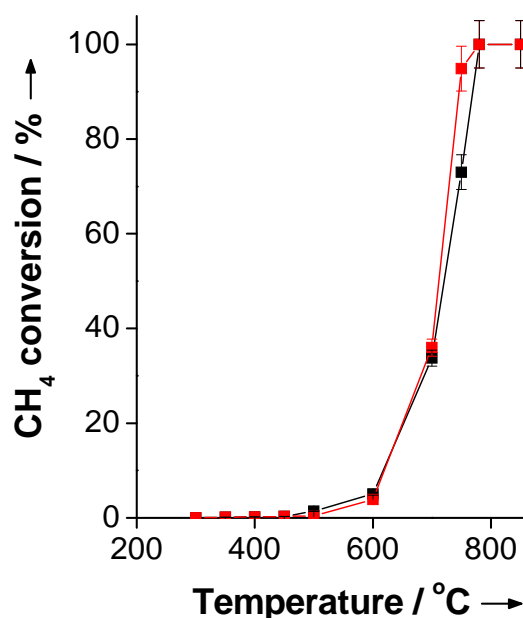


Figure 7. Methane conversion vs reactor temperature of Au/Ti8/UVM-7 800 catalyst in methane catalytic oxidation. Black line and red line correspond to the first and the fifth cycle, respectively. Conditions: 1 % v/v CH₄ in air, GHSV = 60,000 h⁻¹.

Conclusions

Gold nanoparticles with exceptional thermal stability have been synthesized in an easy and reproducible method, following a wet impregnation procedure of UVM-7 porous silica with titanium(IV) oxyacetylacetonate followed by a conventional deposition-precipitation approach. As a model reaction, CO oxidation was initially selected to evaluate the performance of Au/TiO₂/UVM-7 catalysts. An extraordinary

stability and excellent catalytic activity after high temperature treatment was achieved, which is in agreement with the small size and high dispersion of gold nanoparticles. The open architecture of the UVM-7 silica combined with the presence of anatase nanocrystals inside the pore system leads to establish strong interfacial interactions with Au nanoparticles, which are responsible for stabilizing Au nanoparticles at temperatures as high as 800 °C. The optimum performance of the Au/Ti8/UVM-7 sample was linked to an optimal interplay between the presence of Ti as amorphous titanium silicate, the presence of small gold nanoparticles with high sintering resistivity (both beneficial for the catalytic activity), and TiO₂ nanocrystallites (beneficial for the stabilization of both the UVM-7 porosity and the gold nanoparticles). Moreover, the anti-sintering ability of gold nanoparticles was demonstrated by several high-temperature catalytic applications. Finally, the extension of titania modification to other metal oxides make these catalysts broadly applicable for a variety of catalytic applications, such as catalytic combustion, steam reforming or automobile exhaust control, especially for its application in novel hybrid and micro hybrid cars.

Acknowledgements

This research was supported by the Spanish Ministerio de Economía y Competitividad and European Feder Funds (MAT2012-38429-C04-03, CTQ2012-37984-C02-01, CTQ2012-37925-C03-2). The TEM measurements were performed in the Laboratorio de Microscopías Avanzadas (LMA) at the Instituto de Nanociencia de Aragon (INA) - Universidad de Zaragoza (Spain) and received funding from the European Union Seventh Framework Program under Grant Agreement 312483 - ESTEEM2 (Integrated Infrastructure Initiative - I3). B. Puértolas thanks the Ministry of Education for FPU grant (FPU grant AP2009-3544). A. Moragues thanks the Ministry of Economía y Competitividad for FPI grant (FPI grant BES2009-040029).

References

1. Bond, G. C.; Thompson, D. T. *Catalysis Reviews-Science and Engineering* **1999**, *41*, 319-388.
2. Rodriguez, J. A.; Vines, F.; Illas, F.; Liu, P.; Takahashi, Y.; Nakamura, K. *Journal of Chemical Physics* **2007**, *127*.
3. Haruta, M. *Gold Bulletin* **2004**, *37*, 27-36.
4. Guzman, J.; Carrettin, S.; Corma, A. *Journal of the American Chemical Society* **2005**, *127*, 3286-3287.
5. Haruta, M.; Tsubota, S.; Kobayashi, T.; Kageyama, H.; Genet, M. J.; Delmon, B. *Journal of Catalysis* **1993**, *144*, 175-192.
6. Haruta, M.; Date, M. *Applied Catalysis a-General* **2001**, *222*, 427-437.
7. Lee, I.; Joo, J. B.; Yin, Y.; Zaera, F. *Angewandte Chemie-International Edition* **2011**, *50*, 10208-10211.
8. Campbell, C. T.; Parker, S. C.; Starr, D. E. *Science* **2002**, *298*, 811-814.
9. Joo, S. H.; Park, J. Y.; Tsung, C.-K.; Yamada, Y.; Yang, P.; Somorjai, G. A. *Nature Materials* **2009**, *8*, 126-131.
10. Narayanan, R.; El-Sayed, M. A. *Journal of the American Chemical Society* **2003**, *125*, 8340-8347.
11. Zarur, A. J.; Ying, J. Y. *Nature* **2000**, *403*, 65-67.
12. Gandhi, H. S.; Graham, G. W.; McCabe, R. W. *Journal of Catalysis* **2003**, *216*, 433-442.
13. Zhu, H.; Ma, Z.; Overbury, S. H.; Dai, S. *Catalysis Letters* **2007**, *116*, 128-135.
14. Arnal, P. M.; Comotti, M.; Schueth, F. *Angewandte Chemie-International Edition* **2006**, *45*, 8224-8227.
15. Chen, C.; Shi, M.; Cargnello, M.; Fornasiero, P.; Murray, C. B.; Gorte, R. J. *Catalysis Letters* **2014**, *144*, 1939-1945.
16. Zhang, T.; Zhao, H.; He, S.; Liu, K.; Liu, H.; Yin, Y.; Gao, C. *Acs Nano* **2014**, *8*, 7297-7304.
17. Zhao, K.; Qiao, B.; Wang, J.; Zhang, Y.; Zhang, T. *Chemical Communications* **2011**, *47*, 1779-1781.
18. Wang, J.; Lu, A.-H.; Li, M.; Zhang, W.; Chen, Y.-S.; Tian, D.-X.; Li, W.-C. *Acs Nano* **2013**, *7*, 4902-4910.
19. Corti, C. W.; Holliday, R. J.; Thompson, D. T. *Gold Bulletin* **2002**, *35*, 111-136.
20. El Haskouri, J.; de Zarate, D. O.; Guillem, C.; Latorre, J.; Caldes, M.; Beltran, A.; Beltran, D.; Descalzo, A. B.; Rodriguez-Lopez, G.; Martinez-Manez, R.; Marcos, M. D.; Amoros, P. *Chemical Communications* **2002**, 330-331.
21. El Haskouri, J.; Morales, J. M.; de Zarate, D. O.; Fernandez, L.; Latorre, J.; Guillem, C.; Beltran, A.; Beltran, D.; Amoros, P. *Inorganic Chemistry* **2008**, *47*, 8267-8277.

22. Perez-Cabero, M.; Hungria, A. B.; Morales, J. M.; Tortajada, M.; Ramon, D.; Moragues, A.; El Haskouri, J.; Beltran, A.; Beltran, D.; Amoros, P. *Journal of Nanoparticle Research* **2012**, *14*, 12.
23. Narkhede, V. S.; De Toni, A.; Narkhede, V. V.; Guraya, M.; Niemantsverdriet, J. W.; van den Berg, M. W. E.; Gruenert, W.; Gies, H. *Microporous and Mesoporous Materials* **2009**, *118*.
24. Jeanguillaume, C.; Colliex, C. *Ultramicroscopy* **1989**, *28*, 252-257.
25. Arenal, R.; de la Pena, F.; Stephan, O.; Walls, M.; Tence, M.; Loiseau, A.; Colliex, C. *Ultramicroscopy* **2008**, *109*, 32-38.
26. Qian, K.; Jiang, Z.; Huang, W. *Journal of Molecular Catalysis a-Chemical* **2007**, *264*, 26-32.
27. Castillo, R.; Koch, B.; Ruiz, P.; Delmon, B. *Journal of Catalysis* **1996**, *161*, 524-529.
28. Santacesaria, E.; Cozzolino, M.; Di Serio, M.; Venezia, A. M.; Tesser, R. *Applied Catalysis a-General* **2004**, *270*, 177-192.
29. Venezia, A. M.; Liotta, F. L.; Pantaleo, G.; Beck, A.; Horvath, A.; Geszti, O.; Kocsonya, A.; Gucci, L. *Applied Catalysis a-General* **2006**, *310*, 114-121.
30. Hutchings, G. J.; Hall, M. S.; Carley, A. F.; Landon, P.; Solsona, B. E.; Kiely, C. J.; Herzing, A.; Makkee, M.; Moulijn, J. A.; Overweg, A.; Fierro-Gonzalez, J. C.; Guzman, J.; Gates, B. C. *Journal of Catalysis* **2006**, *242*, 71-81.
31. Guzman, J.; Gates, B. C. *Journal of the American Chemical Society* **2004**, *126*, 2672-2673.
32. Labouriau, A.; Higley, T. J.; Earl, W. L. *Journal of Physical Chemistry B* **1998**, *102*, 2897-2904.
33. Kirchhoff, M.; Specht, U.; Vesper, G. *Nanotechnology* **2005**, *16*, S401-S408.
34. Debeila, M. A.; Raphulu, M. C.; Mokoena, E.; Avalos, M.; Petranovskii, V.; Coville, N. J.; Scurrill, M. S. *Materials Science and Engineering a-Structural Materials Properties Microstructure and Processing* **2005**, *396*, 61-69.
35. Knowles, J. A.; Hudson, M. J. *Journal of the Chemical Society-Chemical Communications* **1995**, 2083-2084.
36. Murrell, L. L.; Tauster, S. J. *Catalysis and Automotive Pollution Control II* **1991**, *71*, 547-555.

High Temperature Stable Gold Nanoparticle Catalysts for Application under Severe Conditions: The Role of TiO₂ Nanodomains on Structure and Activity

Supplementary Information

Begoña Puértolas, Álvaro Mayoral, Raul Arenal, Benjamín Solsona, Alaina Moragues, Sonia Murcia-Mascaros, Pedro Amorós, Ana B. Hungría,
Stuart H. Taylor and Tomás García

Catalysts characterization

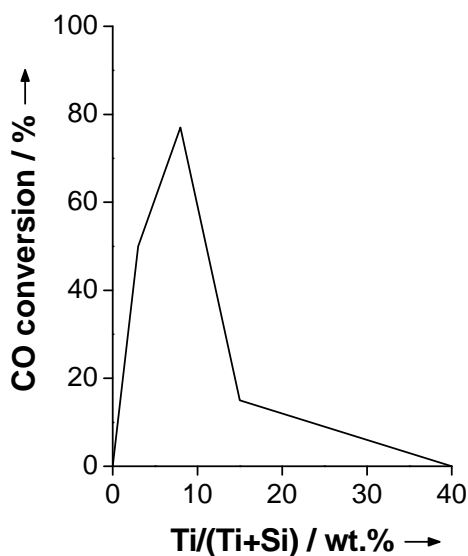


Figure S1. CO conversion values vs. Ti/(Si+Ti) (wt.%) for uncalcined catalysts after 2 days *time-on-line*. Conditions: 0.4 % v/v CO, 20 % v/v O₂ and argon balance, space velocity = 600,000 cm³/(g_{cat}·h), reaction temperature = 20 °C.

The optimal titanium loading is 8 wt.%.

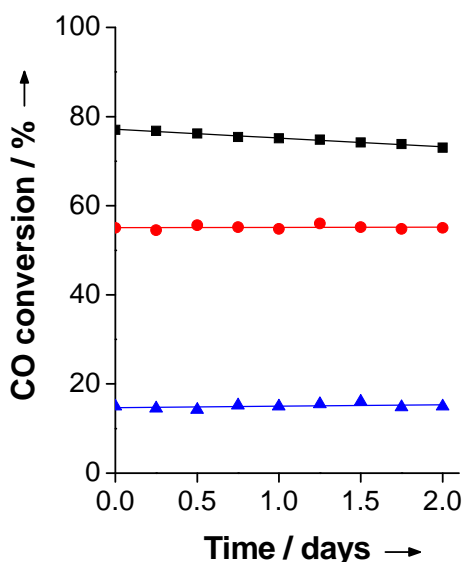


Figure S2 CO conversion vs. time for catalysts containing 8 wt.% titanium. Black squares, red circles and blue triangles correspond to Au/Ti8/UVM-7, Au/Ti8/UVM-7 400 and Au/Ti8/UVM-7 800 catalysts, respectively. Conditions: 0.4 % v/v CO, 20 % v/v O₂ and argon balance, space velocity = 600,000 cm³/(g_{cat}·h), reaction temperature = 20 °C.

The uncalcined catalyst deactivates with *time-on-line*. Following calcination at 400 and 800 °C there is no deactivation over the test period.

Table S1. Gold loading (wt.%) of the final Au/TiO₂/UVM-7 catalysts calcined at 800 °C. Values in parenthesis correspond to uncalcined catalysts.

Ti/(Ti+Si) (wt.%)	Gold loading (wt. %)*
3	2.4 (2.6)
8	2.1 (2.4)
15	4.8 (5.0)

* Determined by EDX.

Table S2. Activity results of the different catalysts tested in moles CO converted/(g_{cat}·h)·(10³) at a space velocity of 600,000 cm³/(g_{cat}·h). Values in parenthesis corresponds to a space velocity of 60,000 cm³/(g_{cat}·h). Conditions: 0.4 % v/v CO, 20 % v/v O₂ and argon balance, reaction temperature = 20 °C. The activity results of the AuTiO₂ WGC (World Gold Council) reference catalyst have been included for comparison.

Ti/(Ti+Si) = 3 wt.%		
Calcination temperature (°C)	t = 0	t = 2 days
-	70.2	58.5
400	35.1	17.5
800	(0.0)	(0.0)
Ti/(Ti+Si) = 8 wt.%		
-	90.1	87.7
400	64.3	64.3
800	17.5	17.5
Ti/(Ti+Si) = 15 wt.%		
-	46.8	21.1
400	(5.7)	(5.5)
800	(0.6)	(0.6)
AuTiO ₂ WGC	35.1	

XRD results support the dispersion and stability of the gold nanoparticles. Unchanged diffraction peaks (of very low intensity) from gold species are observed before and after calcination at 800 °C (even for the samples after the catalytic reaction), indicating that gold species remain well dispersed on the support even after high temperature treatment.

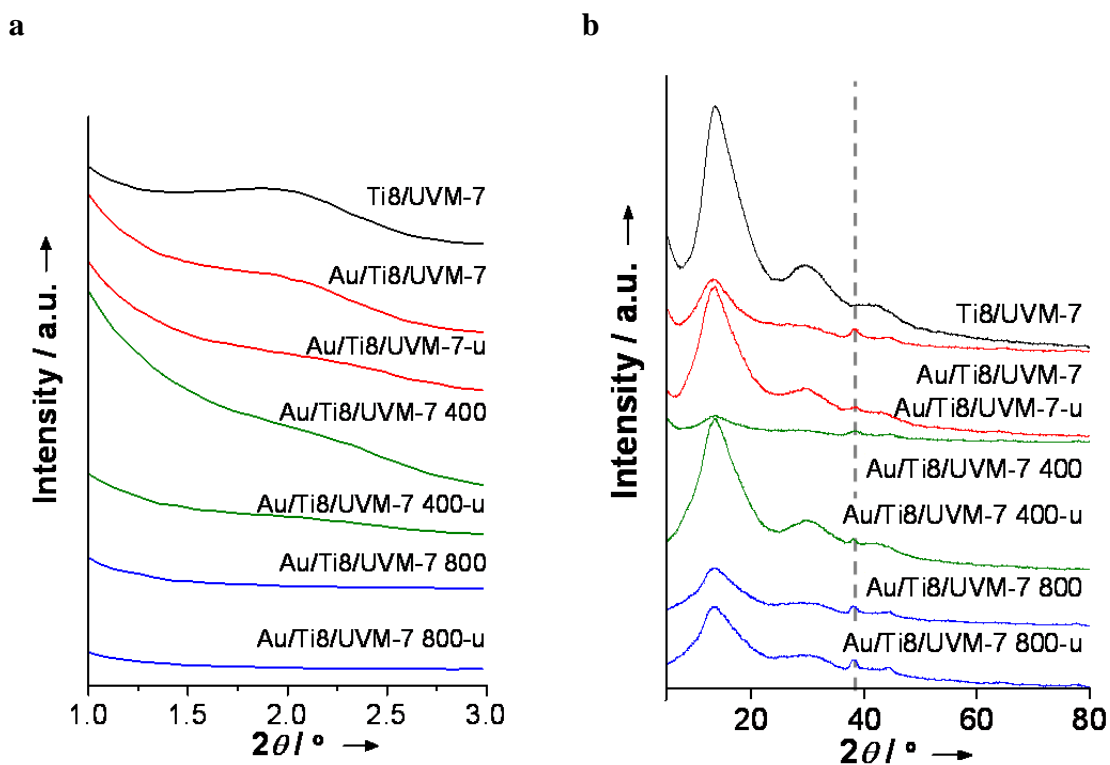


Figure S3. (a) Low-angle and (b) high-angle XRD patterns for gold catalysts with 8 wt.% titania loading. “u” denotes used samples. Marked reflections at $2\theta = 38^\circ$ corresponds to Au^0 cubic structure (ICSD PDF-number 01-089-3697).

From the XPS results, a slight increase of the binding energy of both Ti $2p_{3/2}$ and the second component of O 1s compared to pure TiO_2 (in parenthesis) are observed, consistent with diffusion of Ti species into the silica wall and the formation of Ti-O-Si species. These species are partly preserved after calcination at 800 °C.

Table S3. Ti $2p_{3/2}$ and O 1s binding energies of Au/Ti8/UVM-7 and Au/Ti8/UVM-7 800 catalysts. Values in parenthesis correspond to the binding energy of Ti $2p_{3/2}$ and O 1s in pure TiO_2 .

Catalyst	Ti $2p_{3/2}$ (eV)	O 1s (eV)
Au/Ti8/UVM-7	458.7 (458.4)	532.8, 530.4 (529.6)
Au/Ti8/UVM-7 800	458.5 (458.4)	532.5, 529.8 (529.6)

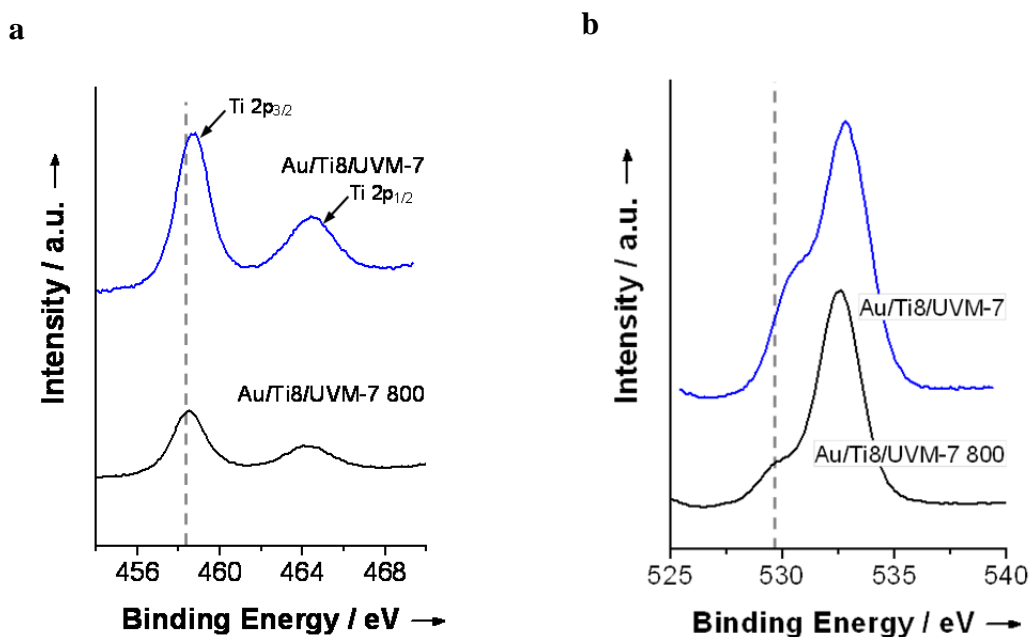


Figure S4. (a) Ti 2p and (b) O 1s XPS spectra of Au/Ti8/UVM-7 and Au/Ti8/UVM-7 800. The straight lines indicate the position of Ti $2p_{3/2}$ and O 1s in pure TiO_2 .

For the uncalcined sample, a shift from the position of Ti $2p_{3/2}$ and O 1s in pure TiO_2 supports the formation of species including Ti-O-Si bonds between Ti-oligomers (produced after degradation of the $\text{TiO}(\text{acac})_2$ precursor at 300 °C) and the silica surface, where a certain proportion of Ti^{4+} occupies a tetrahedral coordination site similar to Si in SiO_2 . After calcination, it is observed that Ti species only remains partly

as Ti-O-Si species. The remaining Ti species tend to agglomerate forming TiO₂ crystallites.

Table S4. XPS results of Au/Ti8/UVM-7 catalyst, fresh catalyst calcined at 800 °C and catalyst calcined at 800 °C used in the CST.

Catalyst	Atomic ratios		Surface atomic concentrations (wt. %)			
	Au ³⁺ /Au ⁰	O _{sup} /O _{lattice}	Au	Ti	Si	O
Au/Ti8/UVM-7	0.24	2.91	3.91	10.1	29.1	57.0
Au/Ti8/UVM-7 800 (fresh)	0.00	2.74	2.99	9.37	31.7	56.0
Au/Ti8/UVM-7 800 (used)	0.00	4.09	1.87	7.04	37.2	53.9

The uncalcined catalyst has some cationic gold, (Au^{δ+}/Au⁰ = 0.24), while only metallic gold is present after heat treatment at 800 °C.

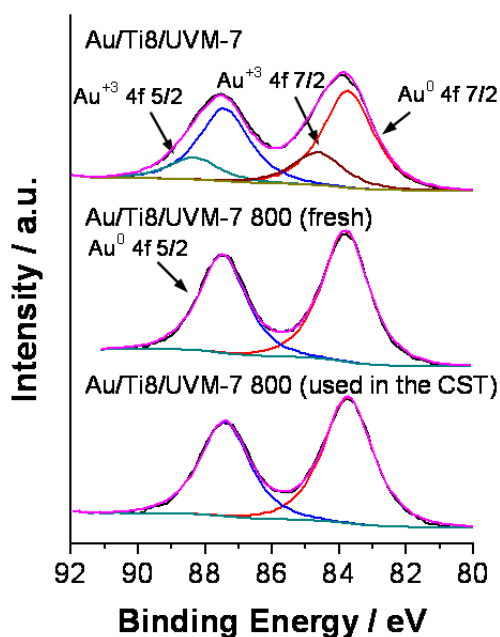


Figure S5. XPS of Au/Ti8/UVM-7 catalyst, fresh catalyst calcined at 800 °C and catalyst calcined at 800 °C used in the CST.

Table S5. Data from the deconvolution of the ^{29}Si NMR spectra.

Catalyst	Q^4		Q^3 and Si (3Si, 1Ti)		Q^2 and Si (2Si, 2Ti)	
	δ (ppm)	%	δ (ppm)	%	δ (ppm)	%
UVM-7 calcined at 800 °C	-114.0	76	-104.6	23	-95.0	1
Ti8/UVM-7 calcined at 800 °C	-110.9	71	-102.0	26	-93.5	3

The ^{29}Si NMR spectrum of the Ti8/UVM-7 support shows a 5% increase of the signals at *ca.* -100 and -93 ppm (corresponding to Si environments with 1 and 2 atoms of Ti as neighbors, respectively: Si (3Si, 1Ti) and Si (2Si, 2Ti)) and a decrease in the Q^4 signal (at *ca.* -110 ppm) when compared with the spectrum of the UVM-7 silica pure support and calcined at the same temperature, in which some Si-OH groups are still preserved (signal at *ca.* -110 ppm).

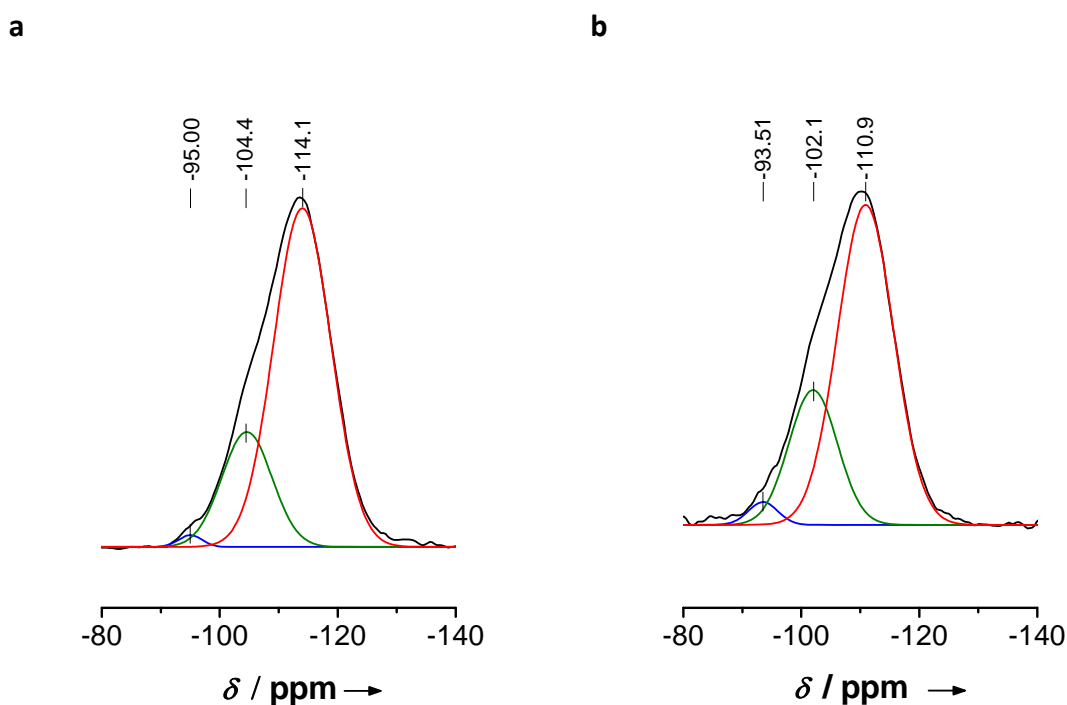
**Figure S6.** ^{29}Si NMR MAS spectra of (a) Ti-free UVM-7 silica calcined at 800 °C and (b) Ti8/UVM-7 support calcined at 800 °C.

Table S6. BET surface areas (m²/g) of the catalysts.

UVM-7 support	
	1232
Ti/(Ti+Si) = 3 wt. %	
Calcination temperature (°C)	
-	928
400	1021
800	265
Ti/(Ti+Si) = 8 wt. %	
-	846
400	623
800	245
Ti/(Ti+Si) = 15 wt. %	
-	779
400	566
800	345

Table S7. Textural characterization of UVM-7 materials with different titania loadings.

Catalyst	Surface area (m²/g)	Total pore volume (cm³/g)	Intrap. pore size (nm)^a	Intrap. pore volume (cm³/g)	Inter. pore size (nm)	Interp. pore volume (cm³/g)
Ti3/UVM-7	1030	1.74	2.83	0.88	24.4	1.01
Ti8/UVM-7	931	1.56	2.81	0.79	25.5	0.88
Ti15/UVM-7	912	1.50	2.84	0.78	25.6	0.84
Ti40/UVM-7	1.4	0.003	-	-	-	-

^a Intra-particle pore size determined by the application of the DFT model

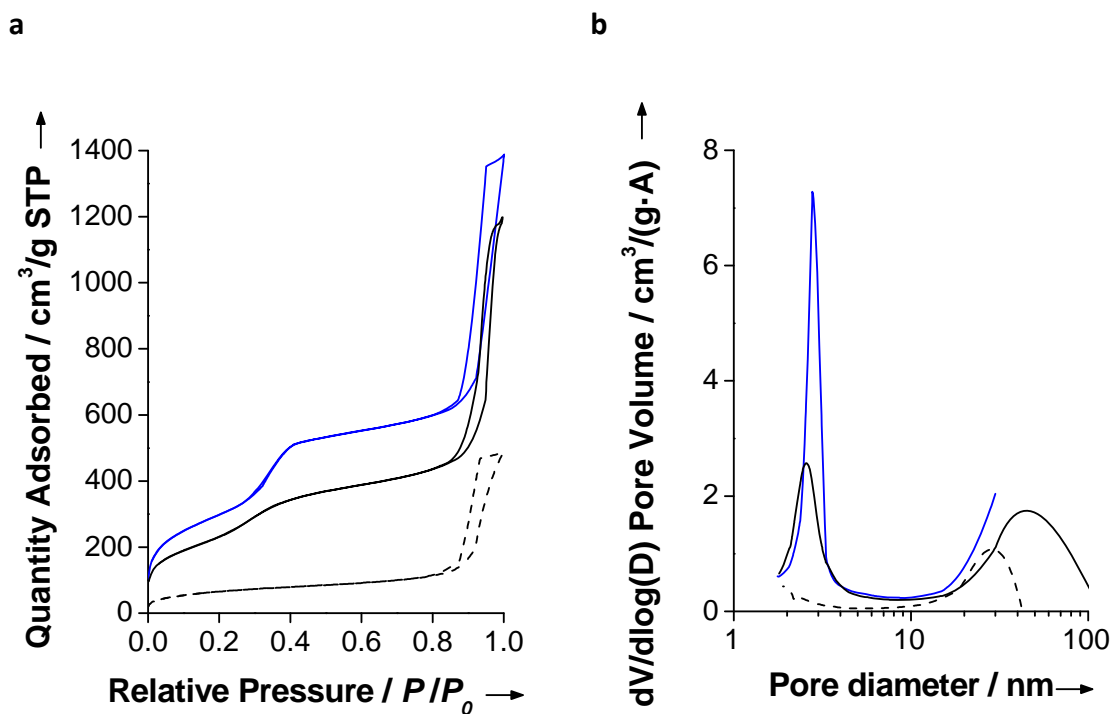


Figure S7. (a) N₂ isotherm and (b) BJH pore size distribution of UVM-7 and Au/Ti8/UVM-7 catalysts uncalcined and calcined at 800 °C. Blue line corresponds to UVM-7, black solid line and dotted line correspond to Au/Ti8/UVM-7 and Au/Ti8/UVM-7 800, respectively.

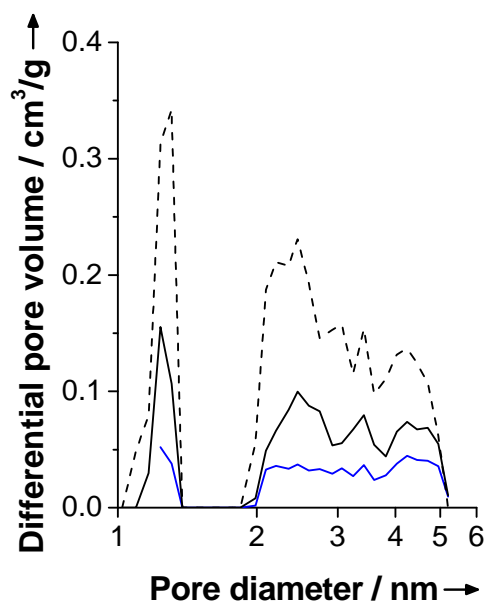


Figure S8. NLDFT pore size distribution of UVM-7, Ti8/UVM-7 and Au/Ti8/UVM-7 catalysts calcined at 800 °C. Blue line corresponds to UVM-7, black solid line and dotted line correspond to Ti8/UVM-7 and Au/Ti8/UVM-7 800, respectively.

For gold supported directly on the mesoporous UVM-7 support, the gold nanoparticles readily agglomerate and large gold nanoparticles are formed after calcination at 800 °C. Moreover, a total structure collapse is evident.

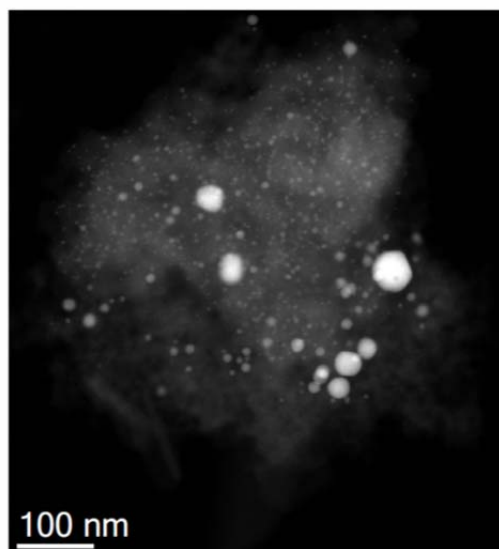


Figure S9. STEM-HAADF images of the Ti-free Au/UVM-7 800 catalyst. Calcination temperature = 800 °C.

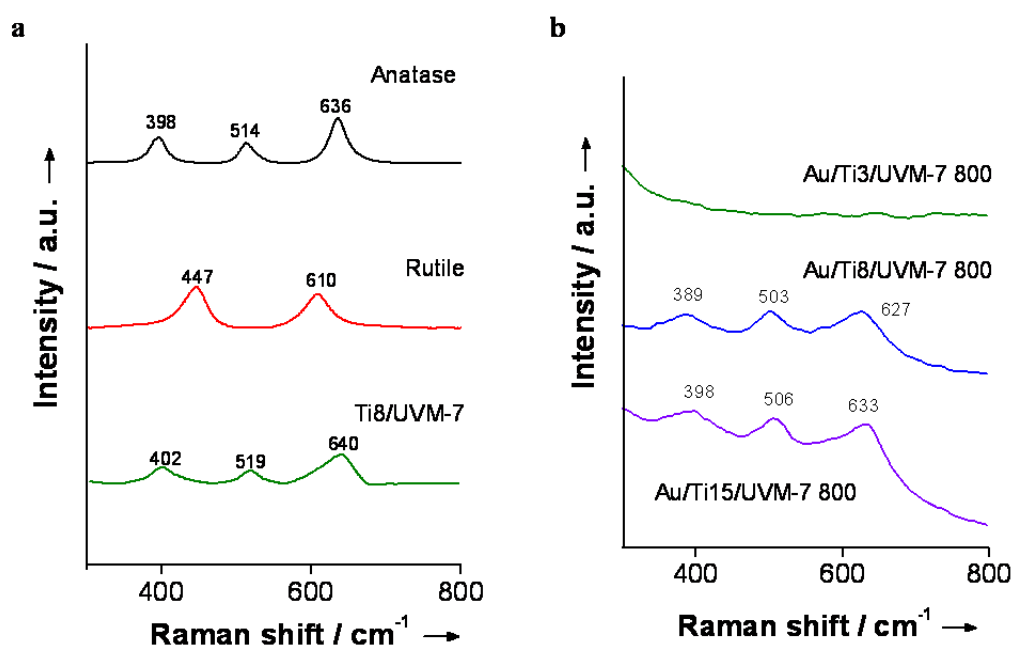


Figure S10. Laser Raman spectra of (a) the Ti8/UVM-7 support and (b) Au/TiO₂/UVM-7 800 catalysts with different Ti/(Ti+Si) loadings (3, 8 and 15 wt.%). Laser Raman spectra of pure rutile and anatase have been including for comparison.

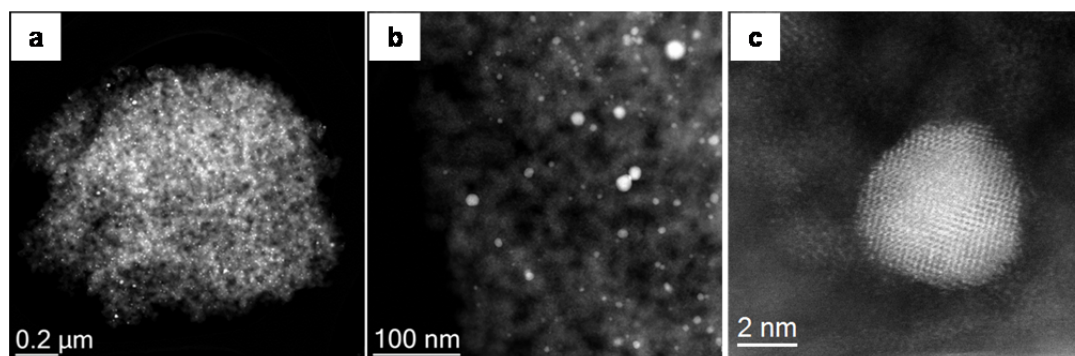


Figure S11. Cs-corrected STEM-HAADF images of Au/ZrO₂/UVM-7 800 at (a) low-magnification observing a homogeneous distribution of gold, (b) medium-magnification image and (c) high-magnification observing a twinned Au nanoparticle and some crystalline ZrO₂ domains.

TEM images clearly show that ZrO₂ nanodomains act as scaffolds for the UVM-7 support, and as anchoring islands for gold nanoparticles, providing stability against sintering after calcination at 800 °C.

Table S8. Activity results of Au/ZrO₂/UVM-7 and Au/ CeO₂-ZrO₂/UVM-7 catalysts in moles CO converted/(g_{cat}·h)·(10³). Conditions: 0.4 % v/v CO, 20 % v/v O₂ and argon balance, reaction temperature = 20 °C.

Calcination temperature (°C)	GHSV (h ⁻¹)	Zr-based catalyst	CeZr-based catalyst
-	100,000	7.6	29.2
400	18,000	5.3	8.6
800	25,000	2.6	6.1

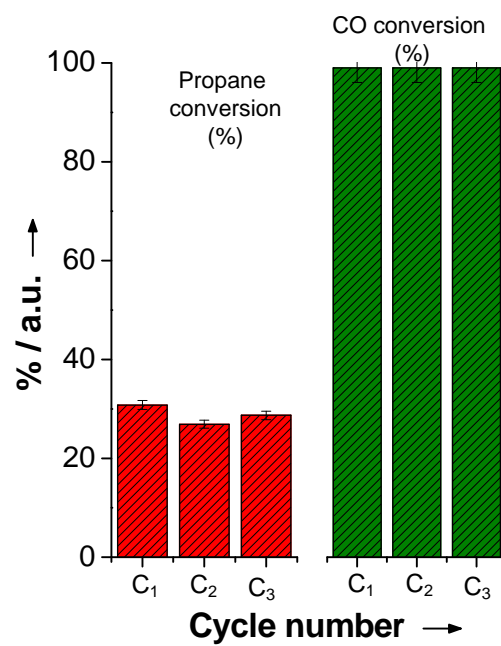


Figure S12. Propane and CO conversion of Au/Ti8/UVM-7 800 catalyst after three consecutive cycles. Conditions: 1 % v/v CO, 0.1 % v/v propane, 0.03 % v/v NO, 8 % v/v O₂, 6 % v/v CO₂, 8 % v/v H₂O and nitrogen balance, GHSV = 40,000 h⁻¹, reaction temperature = 500 °C. C₁, C₂ and C₃ represent the first, second and third cycle, respectively.

***4. Non-silica mesoporous materials:
new iron phosphates and hybrid
phosphonates***

4.1 - Overview

Since the discovery of mesoporous silica there has been huge interest in extending these structures to non-silica compositions. The exceptional properties of mesoporous materials make them highly suitable for different applications. The high surface area is beneficial in processes such as adsorption, catalysis or electrochemical applications where interaction happens on the surface¹⁻³; the mesoporous structure supposes an advance on zeolite size restrictions easing catalysis, adsorption, separation and DNA and drug delivery, among others⁴⁻⁶; and the nanometric structure also provides quantic and surface effects that endow the materials with good performance in sensors, Li-ion batteries and nanodevices⁷⁻¹⁰.

A major difference in the chemistry of these materials with respect to silica ones resides in the reactivity of the precursors: metal alkoxides are more susceptible to hydrolysis and condensation than silica alkoxides. This leads to fast polymerization that needs to be partially blocked in order to avoid organic and inorganic phase separation and to form the mesostructure. This blocking can be achieved by adjusting the pH¹¹, using condensation inhibitors¹², working in non-aqueous solvents¹⁴, using the EISA process^{13,14}, etc.

Moreover, transition metals can present different oxidation states, which may result in instability against surfactant removal due to possible redox reactions or phase transitions¹⁵. Referring to coordination, tetra-connected covalent bonds in silicates and aluminosilicates make them chemically stable. For non-siliceous materials, charge, size and valence frequently impose polyhedra of higher coordination numbers as well as not only corner-sharing, but also connections through faces or edges. This leads to polyhedral skeletons which are more rigid and less versatile with regard to shape and curvature.

In general, syntheses of non-silica mesoporous materials are more difficult than those of silica. It is hard to control alkoxide reactivity, so mesostructured materials are not easily obtained. Besides, even when a good condensation rate is achieved,

surfactant removal is a crucial step that often is not overcome. For these reasons, it is necessary to individually adapt the synthesis method for each metal.

As for silica, different kind of surfactant (cationic, anionic or nonionic) can be used depending on the preparative conditions. Shown in Table 1 are some examples of non-silica mesostructured materials.

Table 1. Mesostructured non-silica oxide materials, adapted from reference 16.

Mineral precursor	Template	Conditions	Template removal	Ref.
$[M^{2+}(\text{NO}_3)_2]$, $[M^{3+}(\text{NO}_3)_3]$ M = Co, Ni, Zn, Mn, Mg, Fe, Al, Ga	$\text{C}_{12}\text{H}_{25}\text{OPO}_3\text{H}_2$, n = 12-18	pH 3-4.5 100 °C/5-13 days	550 °C	17
$[M^{2+}(\text{NO}_3)_2]$, M = Fe, Co, Ni, Mn	$\text{C}_n\text{H}_{2n+1}\text{OSO}_3\text{Na}$	pH <3 RT/18 h	550 °C	17
$\text{Al}(\text{NO}_3)_3 \cdot 9\text{H}_2\text{O}$ or $\text{Al}_2(\text{SO}_4)_3 \cdot 16\text{H}_2\text{O}$	$\text{C}_{12}\text{H}_{25}\text{OSO}_3\text{Na}$ (SDS)	Urea (homog. alkalinization) pH 3.6-7/7.5	600 °C	18
$\text{Ln}(\text{NO}_3)_3$ or LnCl_3 Ln = La, Pr, Nd, Sm, Gd, Dy, Er, Yb, Lu, Eu	SDS	Urea (homog. alkalinization) 80 °C, >20 h	Exch. CH_3COO	19
SnCl_4 , $[\text{Sn}(\text{OH})_6]^{2-}$	$\text{C}_{18}\text{H}_{37}(\text{CH}_3)_3\text{NBr}$ (C_{18}TABr)	pH 10 75 °C/1 day 90 °C/1 day	500 °C	20
Y and Zr glycolates	C_{18}TABr	NaOH 80 °C/5 days OH:Fe = 1.5	600 °C	21
$\text{FeCl}_3 \cdot 6\text{H}_2\text{O}$	$\text{C}_{16}\text{H}_{33}\text{SO}_3\text{Na}$ (SHS)	$\text{H}_2\text{O}/\text{PrOH}$ 80 °C	300 °C	22
$\text{Fe}(\text{NO}_3)_3$	SHS	$\text{Na}_2\text{HPO}_4/\text{HF}$	Exch. CH_3COO	23
$\text{V}_2\text{O}_5/\text{VO}$	C_{16}TACl or C_{16}TAOH	H_3PO_4 pH 2.6-4.5	400 °C	24
$\text{V}_2\text{O}_5\text{H}_2\text{WO}_4$ Na_2MoO_4 or H_2MoO_4	C_{12}TABr	pH 6-8 pH 2.6-6.6 HT: 3-5 h		25
HfCl_4 , $(\text{NH}_4)_2\text{SO}_4$	C_{18}TABr	pH 2.1 100 °C, 1 day	500 °C	26
$\text{Zr}(\text{SO}_4)_2 \cdot 4\text{H}_2\text{O}$	C_nTABr , n = 16, 18, 20	$\text{H}_3\text{PO}_4/2$ h		27
$\text{ZrOCl}_2 \cdot 8\text{H}_2\text{O}$	(C_nTABr) $\text{C}_n\text{H}_{2n+1}(\text{CH}_3)_3\text{NOH}$	pH 11.48 pH 11.60	450 °C	28
$\text{Al}(\text{OBU}^5)_3$	$\text{C}_n\text{H}_{2n+1}\text{COOH}$, n = 11, 17	alcohols RT/1 day 110 °C/2 days	430 °C	18

Mineral precursor	Template	Conditions	Template removal	Ref.
$\text{Al}(\text{OBU}^5)_3$	Triton, Igepal, Tergitol, Pluronic [(POE) ₁₃ (POP) ₃₀ (POE) ₁₃]	RT/16 h 100 °C/6 h	500 °C	31,32
$\text{Pb}(\text{NO}_3)_2$	$\text{C}_{16}\text{H}_{33}\text{SO}_3\text{H}$	pH 7-8 90 °C/3 days	550 °C	17,29
$\text{VO}(\text{OPr}^i)_3$	$\text{C}_{12}\text{H}_{25}\text{NH}_2$	RT 1 day 100 °C/1 day		30
$\text{Ti}(\text{OPr}^i)_4$, acetylacetone	$\text{C}_{12}\text{H}_{25}\text{OPO}_3\text{H}_2$	pH 4-6 80 °C/5 days	350 °C acid wash washing EtOH	33,34
$\text{Sn}(\text{OPr}^i)_4$	$\text{C}_{14}\text{H}_{29}\text{NH}_2$ (TDA)	RT/2 days	+ 300 °C + 350 °C + 400 °C	35
$\text{Ti}(\text{OEt})_4$, H_2O_2	C_{16}TACl	aq soln pH 11.5 100 °C/15 days	300 °C	36
$\text{Zr}(\text{OPr}^n)_4$, acetylacetone	$\text{C}_{16}\text{H}_{33}\text{NH}_2$	RT/5 days H_2SO_4	extr 110 °C 550 °C	37
$\text{Nb}(\text{OEt})_5$	$\text{C}_n\text{H}_{2n+1}\text{NH}_2$, n = 12, 18	RT/1-3 days 100 °C/1 day 180 °C/7 days	washing PrOH/ HNO_3	38
$\text{Ta}(\text{OEt})_5$	$\text{C}_n\text{H}_{2n+1}\text{NH}_2$, n = 12, 18	RT/1-3 days 80 °C/1 day 100 °C/1 day 180 °C/7 day		33
MCl_n in EtOH M = Zr, Ti, Sn, Nb, Ta, W, Hf, Ge, V, Zn, Cd, In, Sb, Mo, Re, Ru, Ni, Fe, Cr, Mn, Cu, ... and mixed ZrTi, Al_2Ti , ...	(PEO) _m (PPO) ₇₀ (PEO) _m Pluronic P123 (m = 20) Pluronic F127 (m = 106)	40-60 °C 1-7 days EISA, open recipients	400 °C	14,39
$\text{Al}(\text{OBU}^5)_3$, TEA H_3PO_4	C_{12}TABr	pH 10-11 pH 8-9 after H_3PO_4 P/Al = 0.12-0.74	300 °C 400 °C 500 °C	40

The first non-silica mesostructured materials were reported by Huo⁴¹ et al. in 1994. They prepared transition and other metal oxide mesophases using cationic or anionic surfactants under variable conditions of pH. Lamellar and hexagonal tungsten (VI) oxide were prepared using cationic surfactants, as well as cubic and hexagonal antimony (V) oxide mesostructures. By contrast, hexagonal phases of iron and lead oxides were obtained using an anionic surfactant ($\text{C}_{16}\text{H}_{33}\text{SO}_3\text{H}$), and lamellar phases of Mg, Al, Mn, Fe, Co, Ni and Zn oxides were prepared with $\text{C}_{12}\text{H}_{25}\text{PO}_4\text{H}_2$. However, it was impossible to obtain the related mesoporous solids, since surfactant removal produced a structure collapse. In 1995, Ying's group⁴² obtained the first mesoporous non-silica

material: it was a thermally stable titanium oxide prepared by a sol-gel process involving titanium isopropoxide bis-acetylacetonate and alkylphosphate surfactants.

As mentioned above, the synthesis method used to obtain silica mesostructures is not always appropriate for other materials, often yielding lamellar organic-inorganic composites, or collapsed materials after surfactant removal. Synthesis conditions, surfactant nature and post-synthetic treatments need to be modified in order to obtain the desired mesoporous solid. This could have meant a downturn in the study of these materials, but the development of new synthetic strategies such as EISA⁴³ or nanocasting⁴⁴ led to an increase in non-siliceous mesoporous materials.

Due to their variable composition, non-silica materials can be classified as follows: non-silica oxides, carbons, chalcogens, nitrides, metals and phosphates. In the next sections, advances in each of these groups will be briefly described.

4.2 - Non-silica oxides

Mesoporous oxides include most metals in the periodic table. They are interesting because of their properties and potential (or real) applications in industry. In the following paragraphs, some details concerning the main mesoporous oxides are outlined.

4.2.1 - Alumina

High surface alumina is a good support for various catalytically active phases. It presents high hydrolytic stability, amphoteric character, excellent thermal stability and its range of point zero charge facilitates loading it with different metal species.

The first mesoporous alumina was reported in 1996 by Bagshaw and Pinnavaia³². It was prepared using a nonionic surfactant, and the final material had a surface area of 425-535 m²/g and a wormhole-like structure. Davis and coworkers¹⁸ reported, almost at the same time, a thermally stable alumina with a high surface area

(710 m²/g) and narrow pore size distribution prepared with long-chain carboxylic acids. Soon afterwards, Cabrera et al.⁴⁰ used a cationic surfactant (cetyltrimethylammonium bromide) in a water/ triethanolamine medium. They succeeded in adjusting the pore size from 3-6 nm by modulating the water/triethanolamine ratio, keeping surface areas higher than 250 m²/g in all cases.

Although there were other synthesis methods, which have been previously described, in all cases the mesostructures collapsed after surfactant removal^{41,17,29}. More recently other surfactant (cationic, anionic, nonionic) procedures or the use of the nanocasting method have been considered. These syntheses are based on sol-gel processes in the presence of soft or hard templates.

Most of the reported syntheses lead to disordered mesoporous aluminas, but for applications symmetry is not as important as a narrow pore size distribution and high surface areas. In the words of Cejka⁴⁵ “synthesis carried out with ionic surfactants in aqueous media tend to produce alumina with poorer textural properties than in alcohols solutions, and, in general, higher surface areas are obtained with nonionic as compared to ionic surfactants”.

In general, syntheses are carried out in aqueous media, involving hydrolysis and condensation of monomeric cations as $[Al(H_2O)_6]^{3+}$ or clusters, and working at pH values lower than the isoelectric point of alumina (8-9). However, the wall structure of the obtained materials is amorphous. With the use of block copolymers, it was possible to stabilize γ -Al₂O₃^{14,39,46}. Sánchez and coworkers attribute the ability to stabilize crystalline particles to copolymer stability above the dehydration temperature of the inorganic phase. Besides, using carbons as templates⁴⁷⁻⁴⁹, crystalline γ -Al₂O₃ can also be synthesized.

The evolution from bulk to mesoporous alumina has meant an extension of their properties. There are examples in the literature showing higher activities of heterogeneous catalysts with mesoporous alumina supports compared to conventional alumina. Larger surface areas and volumes enable the incorporation of higher amounts of catalytically active species, and also allow better diffusion through the system which can even be enhanced by tuning the pore size.

4.2.2 - Transition metal oxides

Transition metals have been used in catalysis because of their redox activity. With the development of new templates and techniques, nowadays most of them can be obtained as mesoporous oxides.

4.2.2.1 - Titania

Titania allotropes have been studied because of their electronic and optical properties. Many of their applications (photocatalysis, catalysis, sensors, etc.) strongly depend on the surface structure, crystallization degree and pore size.

The first mesoporous titania was reported by Antonelli's group⁴² in 1995, using tetradecylphosphate as the anionic template. They obtained a material with 200 m²/g, but phosphorus from the template was bound so strongly to titania that it could not be fully removed, limiting its use in catalysis. A few years later, the same group reported a phosphorus free mesoporous titania⁵⁰ using an organic amine as the template. The final amorphous product presented an MCM-41-like structure and a surface area of 710 m²/g. After heat treatment to obtain an anatase phase, a loss of order and surface area is observed.

Yang et al.^{14,39} were the first to prepare mesoporous titania and other metal oxides using amphiphilic block copolymers as a template, through an EISA process. In 2000, Cabrera et al.⁵¹ reported on a cationic surfactant assisted method using triethanolamine as the hydrolysis retarding agent. They obtained a thermally stable titania with a high surface area (606 m²/g).

The aqueous solution approach is usually considered the ideal method due to its reproducibility. Notwithstanding, titania hydrolysis and condensation rates of the titanium precursors are so fast that just a few studies were developed in aqueous media⁵². Some widely used methods are soft-templating synthesis using block copolymers⁵³, and nanocasting using mesoporous silica^{54,55}.

4.2.2.2 - Zirconia

Zirconia is a material with a high thermal stability, high resistance against corrosion and acid-base activity. It can be used in catalysis and photocatalysis, both as a catalyst or as a support.

In 1996 it was obtained as a mesoporous material by Schüth's group⁵⁶ using an alkyltrimethylammonium salt as the surfactant. The method most often used to produce mesoporous zirconia is soft-templating^{56,28,57} with small molecular weight surfactants and block copolymers as templates, although there are also some studies on hard-templating⁵⁸.

4.2.2.3 - Other metal oxides

With regard to the rest of the transition metal oxides, most of them have been synthesized as mesoporous solids. In the following paragraphs they will be classified by groups and briefly commented on.

There are only a few examples of mesoporous vanadium oxide^{59,30} (V_2O_5) because its redox instability makes soft-template removal difficult. Moreover, its solubility in acid and basic media makes it impossible to leach the hard templates without affecting the mesostructure. However, niobium oxide (Nb_2O_5) is much easier to obtain via soft-templating. Both amines³³ and block copolymers^{14,60} have been used as structure directing agents. Similarly, tantalum oxide (Ta_2O_5), widely used as semiconductor, has been obtained⁶¹.

Only a few examples of mesoporous chromium (III) oxide (Cr_2O_3) via soft-templating⁶² are found, since it is difficult to control its hydrolysis and condensation rates. The first mesostructured molybdenum oxide was reported by Antonelli et al.⁶³; it was a mixed valence oxide, but the mesoporous solid was not obtained until 2005 with the use of polyethylene oxide as template⁶⁴. Tungsten oxide (WO_3) is a semiconductor with potential applications in solar energy devices; the mesoporous oxide has been synthesized using block copolymers as templates via EISA³⁹ or nanocasting^{65,10}.

Iron oxides are important because of their applications in magnetic storage, as catalysts or electrodes for lithium-ion batteries. Their syntheses via soft-templating procedures usually results in disordered structures. However, α -Fe₂O₃ and α -FeOOH⁶⁶ films have been prepared via EISA with diblock copolymer, as well as using SBA-15 and KIT-6 as hard templates⁶⁷. However, ruthenium oxide (RuO₂), which is one of the most promising electrode materials for supercapacitors, has seldom been reported in the form of a mesoporous⁶⁸ solid. Cobalt oxide (Co₃O₄) is obtained by hard-templating using SBA-15^{69,70} or KIT-6⁷¹ silica, among others. In fact, it shows the best ordered mesostructures of all nanocasted metal oxide materials. The first mesoporous nickel oxide (NiO) was reported by Banerjee in 2003⁷² using SDS as a template. It is a promising material with a wide range of applications.

Mesoporous copper oxides are expected to be good catalysts for CO oxidation or hydrocarbon combustion. However, due to the low stability of the products, only a few preparations have been reported^{73,74}. Zinc oxide (ZnO) presents a vast spectrum of properties and applications. Soft-templating methods only lead to disordered materials⁷⁵, but ordered solids can be prepared by nanocasting^{76,77}.

Rare earth oxides have interesting properties resulting from their 4f electrons. Using SDS as a template, Yada et al.¹⁹ synthesized a series of oxides including Gd, Tb, Dy, Ho, Er, Tm, Yb and Lu. Morris⁷⁸ used hexadecylamine and obtained mesoporous oxides of La, Pr, Nd, Sm, Gd, Er and Yb. Nanocasting methods have been also explored to obtain rare earth mesoporous oxides^{79,80}.

The most often studied alkaline earth oxides are CaO and MgO. Both can be obtained as disordered mesoporous solids using direct-synthesis^{81,82}. Mesoporous carbons can be used as templates to obtain ordered materials⁸³.

With alkoxide reactivity as a major drawback, the syntheses of mesoporous metal oxides are more complicated than those of silicas. As explained in the preceding paragraphs, by careful selection of the synthesis conditions most of the transition metals have been studied. Mesostructured materials are often obtained, but surfactant elimination is crucial for the stability of the material. With the development of EISA and nanocasting strategies, these syntheses became more widely accessible.

4.3 - Carbon

Porous carbons have been widely used in water and air purification, catalysis, gas storage, and as a template and electrode component. Such diverse applications are related to their physicochemical properties, including their hydrophobic surface, their high resistance to corrosion, great thermic and mechanic stability, high surface area and pore volume and, overall, their low cost⁸⁴.

Conventional porous carbon materials, such as activated carbons or molecular sieves, usually present a broad pore-size distribution, whereas the presence of micropores in their structure limits mass transfer and pore accessibility.

The synthesis of porous carbon materials can be accomplished using different methods such as catalytic activation of carbon precursors⁸⁵, carbonization of polymer blends containing thermally decomposable components⁸⁶, or carbonization of resorcinol-formaldehyde aerogels⁸⁷. In general, these methods yield materials having a broad pore-size distribution. To obtain narrow and controlled pore size distributions, soft and hard-templating strategies are preferred. Schematized in Figure 1 are the main features of both strategies.

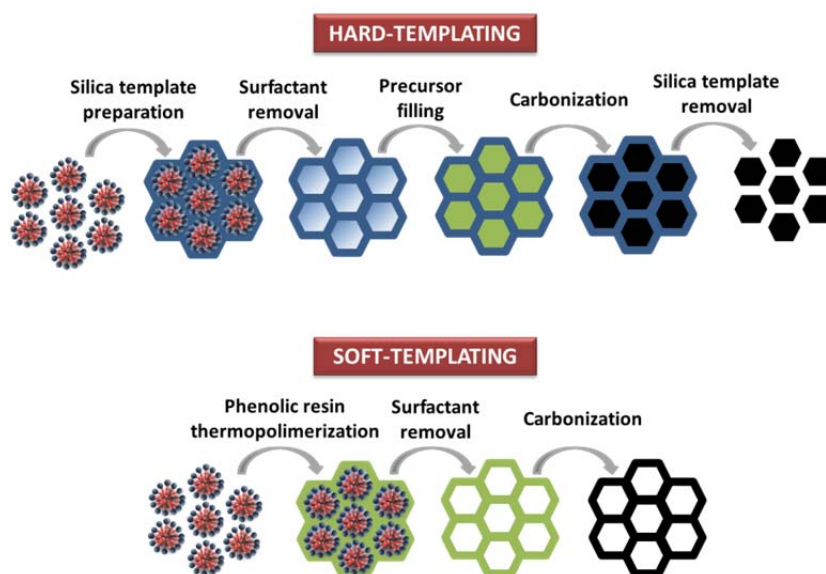


Figure 1. Preparation of ordered mesoporous carbon materials through nanocasting from mesoporous silica hard templates (up) and direct synthesis using soft templates (down).

The first ordered mesoporous carbons (CMK-1) were reported by Ryoo⁴⁴ and Hyeon⁸⁸ in 1999, using MCM-48 as a template. Since then, different silicas (SBA series, MSU-H and HMS) have been used as templates⁸⁹⁻⁹², using carbons precursors such as sucrose, furfuryl alcohol or phenol resin among others. Colloidal silica and silica gel can be used to obtain large-pore materials⁹³.

Gathered in Table 2 are some examples of mesoporous carbons prepared by hard-templating, indicating the precursors and the template employed.

Table 2. Reported mesoporous carbons generated by hard-templating, adapted from reference 94.

Ordered mesoporous carbon	Template	Precursor	Ref.
CMK-1	MCM-48	Sucrose, phenol resin	44
CMK-2	SBA-1	Sucrose	95
CMK-3	SBA-15	Sucrose	89
CMK-3	HMC	Sucrose, phenol resin	92,91,96
CMK-4	MCM-48	Acetylene	95
CMK-5	SBA-15	Furfuryl alcohol	97-99
NCC-1	SBA-15	Furfuryl alcohol	100
N-OMC	SBA-15	Acrylonitrile, pyrrole	101
G-CMK-3	SBA-15	Acenaphthene, benzene, mesophase pitches, pyrrole, poly(vinyl chloride)	102-105
OMC	KIT-6, FDU-5	Sucrose, furfuryl alcohol	106,107
OMC	FDU-12	Sucrose	108
OMC	SBA-16	Sucrose, furfuryl alcohol, acenaphthene	109,110

However, this strategy of synthesis has some limitations. First of all, it entails many steps. Previous synthesis of the silica template is required, followed by carbon precursor impregnation, then later carbonization and template removal. Besides, the pore size distribution of the carbon obtained is wider than that of the silica template. All this makes the synthesis complicated, expensive and very time consuming, which makes large-scale production impractical.

Mesoporous carbons can also be synthesized via soft-templating synthesis, using a block copolymer as a template^{111,112} (Table 3). Materials obtained with this method are more diverse; moreover, their continuous structure makes them more stable. This process is cheap, simple and appropriate for large-scale use.

Table 3. Synthetic conditions for ordered mesoporous carbon materials by the direct strategy, adapted from reference 113.

pH	Precursor	Pathway	Solvent	Catalyst	Template	Ref.
Neutral	Resorcinol	EISA	DMF	Not available	PS-P4VP	114
Neutral	Phenol	EISA	THF	Not available	PEO-PS	115
Neutral	Phenol	EISA	THF	NaOH	PEO-PPMA	116
Neutral	Phenol	EISA	Ethanol	NaOH	P123, P127	117-119
Neutral	Phenol	EISA	Ethanol	NaOH	PPO-PEO-PPO	120
Basic	Phenol	Dilute aqueous	Water	NaOH	P123, P127	121-123
Basic	Phenol	Hydrothermal	Water	NaOH	P123, P127	124,125
Basic	Resorcinol	EISA	Ethanol	NaOH	F108	126
Basic	Resorcinol	Hydrothermal	Water/ethanol	Lysine	F127	127
Acidic	Resorcinol	Hydrothermal	Water/ethanol	HCl	F127	128,129
Acidic	Resorcinol	Hydrothermal	Water/ethanol	Citric acid	F127	130-132
Acidic	Resorcinol	EISA	Ethanol	HCl	F127	133
Acidic	Resorcinol	EISA	Water/ethanol	HCl	F127	111
Acidic	Resorcinol	Phase separation	Water/ethanol	HCl	F127	134-137
Acidic	Resorcinol	Phase separation	Water	Glutamic acid	F127	138
Acidic	Resorcinol/Phloroglucinol	EISA	Water/ethanol	HCl	F127	139-141
Acidic	Phloroglucinol	Phase separation	Water/ethanol	HCl	F127	112,137
Acidic	Phloroglucinol	Phase separation	Water/ethanol	HCl	F127	142

Different approaches can be followed by changing variables such as the synthesis method (EISA, aqueous route, macroscopic phase separation or hydrothermal treatment), precursor (phenol, resorcinol, phloroglucinol), template (F127, F108, P123) or media.

The above mentioned precursors can form single, double or triple hydrogen bonds to the block copolymer chain, being the driving force of the self-assembly. Their reaction and polymerization with formaldehyde involves the protonation of hydrated formaldehyde and electrophilic aromatic substitution reactions of phenols. For this reason, the key factors for the polymerization rate of phenolic resins are the acid concentration and the reactivity of the phenol. As templates, the most utilized are the triblock copolymers; cationic quaternary ammonium surfactants have also been used but are difficult to remove.

The polymerization can be performed in acid or basic conditions, usually using HCl or NaOH as catalysts. Alternative and more environmentally friendly catalysts such as lysine, glutamic acid or citric acid are under study.

As with silica, pore size and morphology can be controlled. Pore size mainly depends on the hydrophobic groups in the surfactants; their size can be increased by enlarging the molecular weight of the hydrophobic blocks. Another way is by the addition of organic swelling agents¹²². As for morphology, carbons synthesized from the EISA method are usually monolithic films, the aqueous route usually generates powder materials, and to obtain carbon fibres it is necessary to grow them within a confined space¹⁴³.

Mesoporous carbons can be functionalized, but their surface inertia and the high temperature required for carbonization can eliminate the added groups if C-X bonds are weak. However, there are some successful metallic and non-metallic modifications.

Nitrogen doped carbons have been synthesized by exposing carbons to a NH_3 flux at a high temperature¹⁴⁴, or by using organic amines in the carbon synthesis¹⁴⁵. These materials have great stability, and can be used in CO_2 ^{146,147} capture with high

selectivity and easy regeneration. Fluorinated carbons have been also prepared by using p-fluorophenol in the synthesis¹⁴⁸. Fluor content does not affect the structure, and these materials present a better electronic transference than pure carbons, favouring their use in electrocatalytic reactions. Moreover, B, P and B-P carbons have been prepared by adding phosphoric or boric acid (or a mixture of them) to the solution¹³⁶. They show better electrochemical performances than pure carbon. Functional groups such as SO₃H- and COOH- can be added by post-functionalization; sulphonated¹⁴⁹ carbons can act as acid catalysts, and acid groups act as anchors for adsorbates such as metallic ions¹⁵⁰.

They can also be doped with metals, usually by co-assembling of the copolymer template, the carbon source and a metallic precursor. Oxides such as CaO¹⁵¹ and MgO¹⁵² give basic properties to the material, enhancing CO₂ adsorption; and, Ni and Fe₂O₃ make materials magnetically separable¹⁵³. The use of other metals such as iridium¹³⁵ or titanium¹⁵⁴ is being studied for their possible catalytic applications.

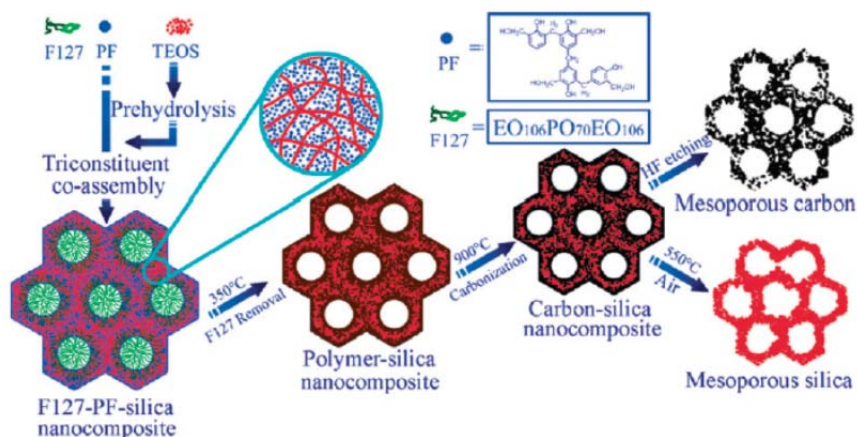


Figure 2. Formation mechanism of ordered polymer-silica and carbon-silica composites.

Although in the above mentioned examples the major component of the matrix is carbon, composites with different silica-carbon ratios also exist. They can be prepared by triconstituent co-assembly of a carbon source, prehydrolyzed silica oligomers and a template¹⁵⁵⁻¹⁵⁸. These materials can be used as supports for noble

metals in catalysis¹⁵⁹. Similarly, a titania and carbon network can be formed¹⁶⁰, with good photocatalytic activity. As shown in Figure 2, removal of silica or titania leads to pure carbons with a hierarchic pore structure^{161,162}.

In the silica-carbon composites there is a high content of oxygen, i.e. the products are actually a mixture of SiC and SiOC. The introduction of a third element in the matrix can affect their performances. For example, silicon oxycarbide and silicon carbonitride show better thermal stability than pure SiC.

As shown in the above paragraphs, there are a lot of studies focused on mesoporous carbons. Their versatility enables modulation of the pore sizes and functionalization. This means an expansion in the application of these materials, particularly for high-value applications related to the energy field, sensing and fine chemical rations. For large volume applications, it is still difficult to compete with the low cost of active carbons

4.4 - Chalcogenide

Metal chalcogenides, including sulphides, selenides and tellurides, form a semiconductor family with excellent electronic, catalytic, semiconducting, optical and magnetic properties¹⁶³⁻¹⁶⁵. Formation of mesoporous materials allow their band gap to be finely adjusted by tuning the thickness of the pore walls. Mesoporous semiconductors with continuous structures are the negative image of quantum dots, known as quantum antidots^{166,167}.

Metal chalcogenides can be divided in two groups, based on the nature of the metals. The first group includes metals that can exist in aqueous solution and can be easily precipitated with S^{2-} , Se^{2-} and Te^{2-} . The second group includes unstable cations that tend to form stable anions ($Mo_7O_{24}^{6-}$). Most of them form anionic metal-chalcogen clusters, which can be used as precursors for the synthesis of mesoporous metal chalcogenides.

4.5 - Nitrides

While the Mobil Corporation's initial patent¹⁶⁸ was very general with regard to elements susceptible to be part of mesoporous structures, surprisingly it did not refer to nitrogen. Nevertheless, a diversity of mesoporous nitrides have been obtained and characterized.

4.5.1 - Silicon nitrides

Silicon nitride composition is diverse, the most important one being Si_3N_4 . These materials have low density, high thermal and fracture resistance, chemical inertia and bio-compatibility among other properties. All this makes them interesting for application in reciprocating engines, bearings, metal cutting and shaping tools, artificial articulations and catalysis. Some of these applications require high surfaces. Thus, mesoporous nitrides have been studied in order to replace dense materials.

They can be produced by pyrolysis of silicon diimide at a high temperature¹⁶⁹. By changing silicon precursors and solvents, the pore size can be controlled¹⁷⁰. But these syntheses are performed in the absence of a surfactant, which leads to disordered mesostructures. Another approach is the carbothermal reduction of silica, using mesoporous organosilica as the precursor¹⁷¹, but only 0.5wt.% of nitrogen is detected in the structure. An increase in the nitrogen content was observed according to the Haskouri method¹⁷², in which MCM-41 was treated with ammonia gas at 950°C. The nitrogen content depends mainly on the treatment temperature; complete conversion can be achieved at above 1400°C. But this temperature is higher than the thermal stability of the mesoporous silica. Therefore, substitution is only partial and leads to mesoporous silicon oxynitrides.

4.5.2 - Carbon nitrides

Carbon nitrides (C_3N_4) present relevant mechanical, conducting, field emission and energy-storage properties¹⁷³⁻¹⁷⁵. They are super-hard diamond-like materials with a variety of technological and biological applications that are conditioned by the particle size, surface area and nitrogen content.

Mesoporous carbon nitrides have been prepared by Vinu et al.¹⁷⁶ by filling SBA-15 with a polymer prepared by refluxing ethylenediamine and carbon tetrachloride with a C/N ratio tunable from 4,5 to 3,5, far from the theoretical one of 0,75. Thomas and coworkers¹⁷⁷ used cyanamide as the precursor and improved the ratio up to 0,72.

These materials can also be used as hard templates to produce metal nitride nanomaterials (TiN, GaN, VN, TaN, Al-Ga-N), heating a metal species loaded sample to 650-800°C under nitrogen atmosphere¹⁷⁸, as shown in Figure 3.

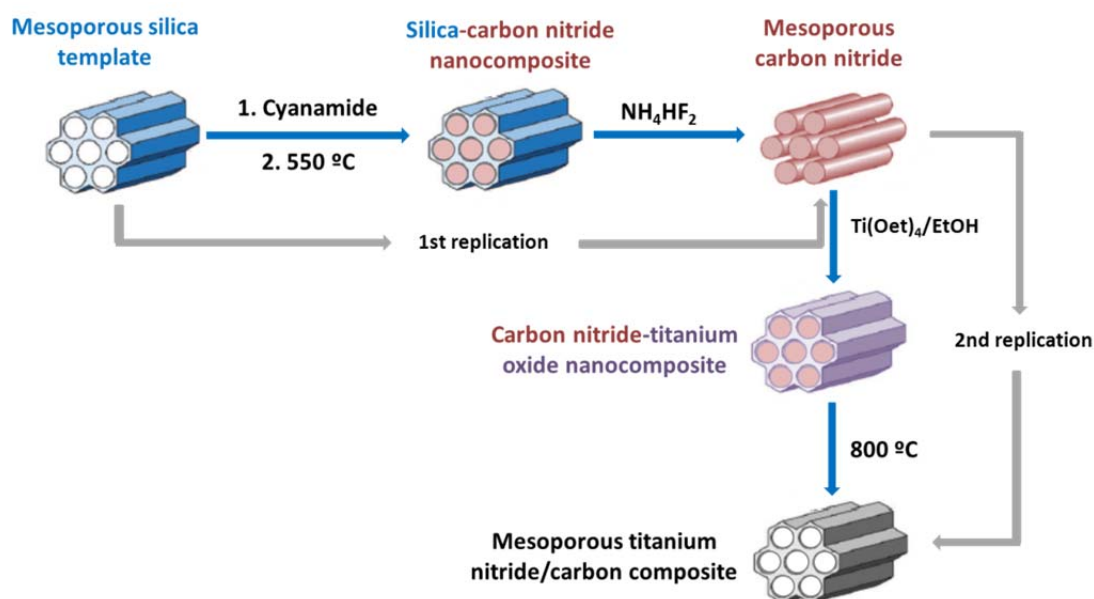


Figure 3. Reaction pathway for the synthesis of mesoporous carbon and metal nitrides.

4.5.3 - Metal nitrides

Metal nitrides can be synthesized via nanocasting using mesoporous silica as a template. Thus, in 1999, Fisher and coworkers¹⁷⁹ reported a gallium nitride in the channels of MCM-41. In 2008, Zhao's group¹⁸⁰ reported they had obtained self-supported mesoporous metal nitrides. By calcination in air, a silica template including a metal precursor is transformed into a mesostructured metal oxide that, in turn, can evolve to nitride by high-temperature ammonia treatment. The silica template can be removed before or after the nitridation process depending on the stability of the desired metal nitride (Figure 4). Since then, different metal nitrides have been prepared and, as mentioned before, carbon nitrides can also be used as templates.

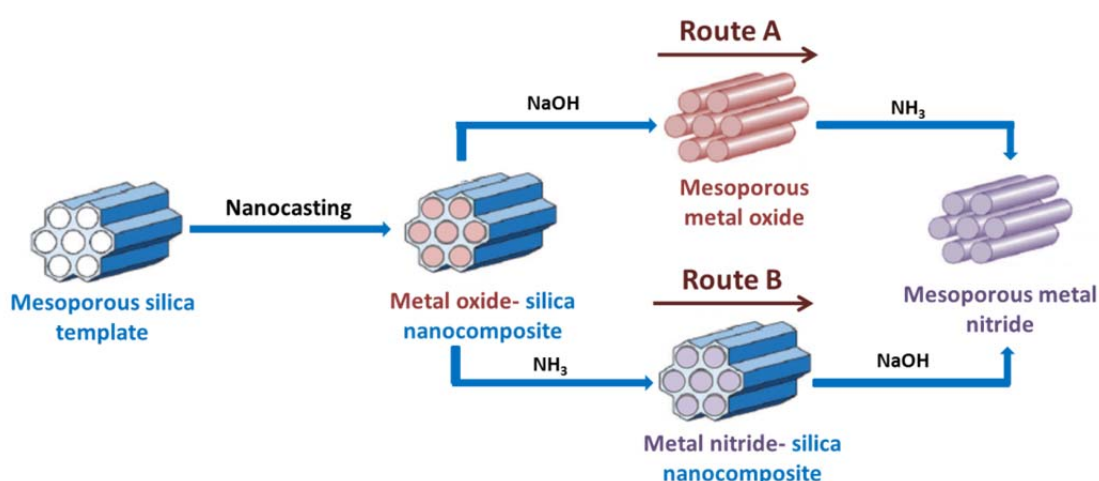


Figure 4. Two pathways for the synthesis of self-supported mesoporous metal nitrides.

4.6 - Metals

Mesoporous metals have many possible applications in areas such as electrochemistry, electronics, magnetics, optics, photonics and catalysis. The synthesis of mesoporous metals is usually difficult; the high surface energy of the metals induces their aggregation into nanoclusters or nanoparticles.

The synthesis of mesoporous metals is usually performed by the chemical or electrochemical reduction of a metal salt in a solution containing a template (Figure 5). They have traditionally been prepared by using silica as the hard template^{44,88} but can also be prepared by direct synthesis from lyotropic liquid crystals (LLC) made of nonionic surfactants in high concentrations^{181,182}. The lyotropic liquid crystals used for this aim consist of short oligomeric $C_n(\text{ethylene oxide})_m$ surfactants. The size of the pore can be controlled by changing the template.

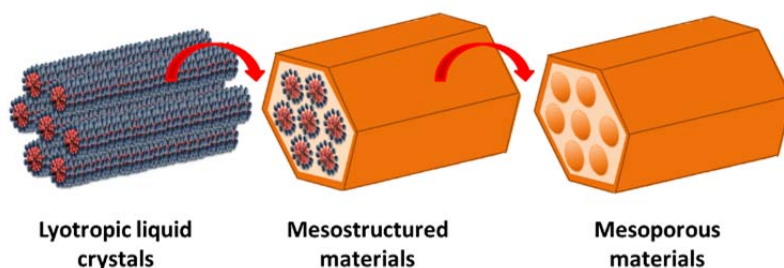


Figure 5. Formation of mesoporous materials from lyotropic liquid crystals.

The first mesoporous metal, Pt microparticles prepared by using a nonionic surfactant, was reported by Attard et al. in 1997¹⁸¹. Since then, many research groups have been working on the application of related procedures to obtain other mesoporous metals. Lyotropic liquid crystals are more versatile than hard templates, making this approach applicable for a wide range of metals which are generally known to be deposited. With this method, it is possible to create different mesostructures by changing the composition of the reaction bath, thus obtaining 2D hexagonal, 3D cubic or nanotubes, nanorods and nanoparticles. Figure 6 shows part of the periodic table, highlighting in red the elements prepared as mesoporous metals or alloys.

									B	C	N	O
									Al	Si	P	S
Ti	V	Cr	Mn	Fe	Co	Ni	Cu	Zn	Ga	Ge	As	Se
Zr	Nb	Mo	Tc	Ru	Rh	Pd	Ag	Cd	In	Sn	Sb	Te
Hf	Ta	W	Re	Os	Ir	Pt	Au	Hg	Tl	Pb	Bi	Po

Figure 6. Part of the periodic table showing the mesoporous metals and alloys prepared in the presence of LLC.

4.7 - Phosphates

Transition metal phosphates have been studied in order to benefit from the redox and/or acid base catalytic properties of the metal. The combination of these properties with easy diffusion makes mesoporous transition metal phosphates an interesting group of materials to be studied.

The best example to understand how these materials evolved from bulk to mesoporous systems is the aluminium phosphate family (ALPOs). Along with zeolites they constitute one of the most important groups of crystalline microporous materials¹⁸³. Since their discovery in 1982¹⁸⁴, their evolution has been similar to that of zeolites. After the development of Mobil mesoporous silicas, the application of their chemistry to ALPOs seemed to be straightforward, due to their electronic and structural similarities. However, the chemical complexity of non-silica materials implies difficulties¹⁵.

Mesoporous ALPOs with different topologies have been synthesized using surfactant assisted methods¹⁸⁵. First attempts to obtain lamellar¹⁸⁶ and hexagonal^{187,188}

MCM-41 type mesostructured ALPOs prepared through surfactant-assisted methods were unsuccessful; the mesostructure collapsed upon surfactant removal. But a few years after, Kuroda and coworkers^{189,190} used a cationic surfactant and isolated mesoporous ALPOs with pore diameters modulated from 1,8-3,9 nm by changing the pore length of the surfactant. In 1999, Cabrera et al.¹⁹¹ prepared thermally stable mesoporous aluminophosphates with adjustable pore sizes by changing the P/Al molar ratio and water content in the reaction mixture.

It is possible to outline some general tendencies that distinguish ALPOs from silica: (1) layered topologies are frequently preferred in ALPOs, (2) ALPOs usually present a poorer structural order than related silicas, and (3) the preparation of mesoporous ALPOs can be seriously limited because of the mesostructure collapse during surfactant removal.

The evolution of these materials, as for zeolites, followed with the incorporation of hetero-elements such as B, Ga, Si, Fe or Ti to the structure^{188,192-195} (MeALPOs), its functionalization with organic groups^{196,197} and the preparation of metal phosphates.

Some examples of transition metal mesoporous phosphates are vanadium phosphate¹⁹⁸, a catalyst in butane to maleic anhydride oxidation; iron phosphate, with great catalytic activity in some oxidation reactions^{199,200}; or zirconium and titanium phosphates, electrocatalysts in an oxygen reduction reaction²⁰¹. In addition, due to their high surface area and their richness in hydroxyl groups, they have been used as adsorbents for radio-nuclear materials²⁰² and heavy metal ions²⁰³.

Preparation of bulk metal phosphates is usually carried out by precipitation of metal inorganic salts with a phosphoric precipitant agent. Mesoporous preparation, as in previous cases, can follow soft or hard-templating routes. However, for tri-elemental systems (M-P-O) auto-assembly is more complex, since two types of precursors are involved. Moreover, hydrolysis and condensation processes are faster for transition metals than for silica, complicating the control of the assembly in a determined morphology. Furthermore, surfactant elimination becomes a problem:

with thermal treatment, structures can be destroyed and, with acid and ethanol extraction, the templates are not always completely removed.

In the following paragraphs some different metal phosphates will be briefly reviewed.

4.7.1 - Zirconium and titanium phosphates

Group IV is one of the most studied groups in the family of transition metal phosphates. Different methods have been used for the fabrication of mesoporous titanium and zirconium phosphates, soft-templating being the most popular.

In the case of zirconium different precursors ($(\text{Zr}(\text{SO}_4))^{204}$, $\text{ZrOCl}_2 \cdot 8\text{H}_2\text{O}^{205}$, $\text{Zr}(\text{OC}_3\text{H}_7)_4^{206}$, $\text{Zr}(\text{OC}_4\text{H}_9)_4^{207}$) and precipitating agents (H_3PO_4 , $\text{NH}_4\text{H}_2\text{PO}_4$, $(\text{NH}_4)_2\text{HPO}_4$, PCl_3), can be used in the presence of a cationic, anionic or non-ionic surfactant. Mesoporous films can also be prepared by spin coating on a silicon substrate²⁰⁸.

Titanium phosphate has been prepared using structure directing agents. Toyota Company Scientists²⁰⁹ claimed that TiCl_4 is a suitable precursor for the synthesis of TiP using anionic surfactants, while Ti-alkoxides are more suitable with cationic surfactants.

4.7.2 - Other compositions

Iron, vanadium and nickel have been studied in heterogeneous catalysis for their redox properties.

Iron phosphate has been explored as a main component of a solid catalyst for selective oxidation reactions^{200,210}, and as a cathode electrode in Li-ion cells²¹¹. The first mesoporous material was reported by Guo et al.²³ using sodium dodecyl sulphate as the surfactant.

Vanadium phosphate is a well-studied catalyst for the oxidation of alkanes¹⁹⁸. There is a linear relationship between butane conversion and the surface area of the catalyst.

Synthesis of mesoporous nickel phosphates is more difficult, given that nickel and phosphorous species are more prone to precipitation. Kandori et al.²¹² have prepared spherical nanoparticles with mesoporosity using sodium dodecyl sulphate.

Syntheses for other transition metals are not common, but there are examples of chromium, niobium, zinc, tantalum and yttrium phosphates.

4.7.3 - Phosphonates

Organically modified mesoporous phosphates are very scarce compared to organosilica²¹³. Organic functional groups can be incorporated by using organophosphorous reagents, extending the applications to fields such as catalysis, molecular sieving and biomedical sciences^{214,215}. The resulting solids can be described as phosphate /phosphonate /diphosphonate materials, with the phosphonate incorporation limited and restricted to the pore surface^{209,216}.

In 2004, El Haskouri et al.²¹⁷ prepared mesoporous aluminium phosphonates and diphosphonates with 100% of organophosphorous groups, using a cationic surfactant and the atrane method.

4.8 - Objectives

Although a variety of materials has been presented in this introduction, their study is still under development. The number of publications on this subject has been increasing over the years, but it is still fairly small compared to those concerning mesoporous silicas. Figure 7 shows the evolution of publications referring to

mesoporous nitrides, phosphates, non-silica oxides and carbons in comparison to silica.

Publications

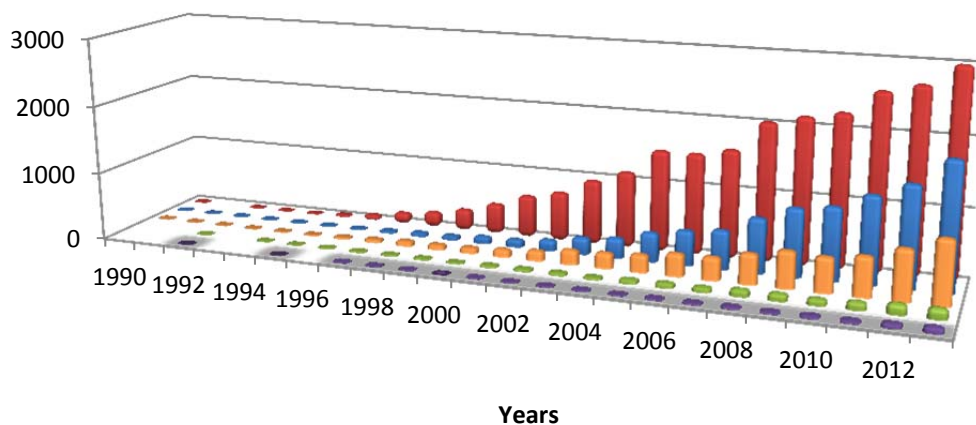


Figure 7. Comparison of the number of publications on mesoporous silica (red), mesoporous carbon (blue), mesoporous non-silica oxides (orange), mesoporous phosphates (green) and mesoporous nitrides (purple). Data from the Web of Science.

The main objective of this chapter is the preparation of non-silica mesoporous materials, in particular, iron phosphates. This kind of material has not been studied in depth and may be of interest for applications such as electrodes, catalysts or adsorbents. Our group has worked on the synthesis of iron phosphates using a cationic surfactant (cetyltrimethylammonium bromide) as the template and triethanolamine as the complexing agent (hydrolysis retarding agent).

In addition, organic modification of the surfaces using phosphonates has been tested. Large surface materials showing disordered pores have been obtained and they are looked at in detail in the next paper.

References

1. Corma, A. *Chemical Reviews* **1997**, *97*, 2373-2419.
2. Davis, M. E. *Nature* **2002**, *417*, 813-821.
3. Taguchi, A.; Schuth, F. *Microporous and Mesoporous Materials* **2005**, *77*, 1-45.
4. Vallet-Regi, M.; Ramila, A.; del Real, R. P.; Perez-Pariente, J. *Chemistry of Materials* **2001**, *13*, 308-311.
5. Lai, C. Y.; Trewyn, B. G.; Jeftinija, D. M.; Jeftinija, K.; Xu, S.; Jeftinija, S.; Lin, V. S. Y. *Journal of the American Chemical Society* **2003**, *125*, 4451-4459.
6. Radu, D. R.; Lai, C. Y.; Jeftinija, K.; Rowe, E. W.; Jeftinija, S.; Lin, V. S. Y. *Journal of the American Chemical Society* **2004**, *126*, 13216-13217.
7. Jiao, F.; Bruce, P. G. *Advanced Materials* **2007**, *19*, 657-+.
8. Shi, Y.; Guo, B.; Corr, S. A.; Shi, Q.; Hu, Y.-S.; Heier, K. R.; Chen, L.; Seshadri, R.; Stucky, G. D. *Nano Letters* **2009**, *9*, 4215-4220.
9. Scott, B. J.; Wirnsberger, G.; Stucky, G. D. *Chemistry of Materials* **2001**, *13*, 3140-3150.
10. Rossinyol, E.; Prim, A.; Pellicer, E.; Arbiol, J.; Hernandez -Ramirez, F.; Peiro, F.; Cornet, A.; Morante, J. R.; Solovyov, L. A.; Tian, B.; Bo, T.; Zhao, D. *Advanced Functional Materials* **2007**, *17*, 1801-1806.
11. Soler-Illia, G.; Scolan, E.; Louis, A.; Albouy, P. A.; Sanchez, C. *New Journal of Chemistry* **2001**, *25*, 156-165.
12. Sanchez, C.; Livage, J.; Henry, M.; Babonneau, F. *Journal of Non-Crystalline Solids* **1988**, *100*, 65-76.
13. Brinker, C. J.; Lu, Y. F.; Sellinger, A.; Fan, H. Y. *Advanced Materials* **1999**, *11*, 579-+.
14. Yang, P. D.; Zhao, D. Y.; Margolese, D. I.; Chmelka, B. F.; Stucky, G. D. *Nature* **1998**, *396*, 152-155.
15. Schuth, F. *Chemistry of Materials* **2001**, *13*, 3184-3195.
16. Soler-illia, G. J. D.; Sanchez, C.; Lebeau, B.; Patarin, J. *Chemical Reviews* **2002**, *102*, 4093-4138.
17. Huo, Q. S.; Margolese, D. I.; Ciesla, U.; Demuth, D. G.; Feng, P. Y.; Gier, T. E.; Sieger, P.; Firouzi, A.; Chmelka, B. F.; Schuth, F.; Stucky, G. D. *Chemistry of Materials* **1994**, *6*, 1176-1191.

18. Vaudry, F.; Khodabandeh, S.; Davis, M. E. *Chemistry of Materials* **1996**, *8*, 1451-1464.
19. Yada, M.; Kitamura, H.; Ichinose, A.; Machida, M.; Kijima, T. *Angewandte Chemie-International Edition* **1999**, *38*, 3506-3510.
20. Chen, F. L.; Liu, M. L. *Chemical Communications* **1999**, 1829-1830.
21. Mamak, M.; Coombs, N.; Ozin, G. *Advanced Materials* **2000**, *12*, 198-+.
22. Michot, L. J.; Mathieu, C.; Bouquet, E. *Comptes Rendus De L Academie Des Sciences Serie Ii Fascicule C-Chimie* **1998**, *1*, 167-174.
23. Guo, X. F.; Ding, W. P.; Wang, X. G.; Yan, Q. J. *Chemical Communications* **2001**, 709-710.
24. Mizuno, N.; Hatayama, H.; Uchida, S.; Taguchi, A. *Chemistry of Materials* **2001**, *13*, 179-184.
25. Abe, T.; Taguchi, A.; Iwamoto, M. *Chemistry of Materials* **1995**, *7*, 1429-1430.
26. Liu, P.; Liu, J.; Sayari, A. *Chemical Communications* **1997**, 577-578.
27. Ciesla, U.; Froba, M.; Stucky, G.; Schuth, F. *Chemistry of Materials* **1999**, *11*, 227-234.
28. Knowles, J. A.; Hudson, M. J. *Journal of the Chemical Society-Chemical Communications* **1995**, 2083-2084.
29. Ciesla, U.; Demuth, D.; Leon, R.; Petroff, P.; Stucky, G.; Unger, K.; Schuth, F. *Journal of the Chemical Society-Chemical Communications* **1994**, 1387-1388.
30. Luca, V.; MacLachlan, D. J.; Hook, J. M.; Withers, R. *Chemistry of Materials* **1995**, *7*, 2220-&.
31. Bagshaw, S. A.; Prouzet, E.; Pinnavaia, T. J. *Science* **1995**, *269*, 1242-1244.
32. Bagshaw, S. A.; Pinnavaia, T. J. *Angewandte Chemie-International Edition in English* **1996**, *35*, 1102-1105.
33. Antonelli, D. M.; Ying, J. Y. *Angewandte Chemie-International Edition in English* **1996**, *35*, 426-430.
34. Stone, V. F.; Davis, R. J. *Chemistry of Materials* **1998**, *10*, 1468-1474.
35. Severin, K. G.; Abdel-Fattah, T. M.; Pinnavaia, T. J. *Chemical Communications* **1998**, 1471-1472.
36. On, D. T. *Langmuir* **1999**, *15*, 8561-8564.
37. Huang, Y. Y.; McCarthy, T. J.; Sachtler, W. M. H. *Applied Catalysis a-General* **1996**, *148*, 135-154.

38. Antonelli, D. M.; Nakahira, A.; Ying, J. Y. *Inorganic Chemistry* **1996**, *35*, 3126-3136.
39. Yang, P. D.; Zhao, D. Y.; Margolese, D. I.; Chmelka, B. F.; Stucky, G. D. *Chemistry of Materials* **1999**, *11*, 2813-2826.
40. Cabrera, S.; El Haskouri, J.; Alamo, J.; Beltran, A.; Beltran, D.; Mendioroz, S.; Marcos, M. D.; Amoros, P. *Advanced Materials* **1999**, *11*, 379-381.
41. Huo, Q. S.; Margolese, D. I.; Ciesla, U.; Feng, P. Y.; Gier, T. E.; Sieger, P.; Leon, R.; Petroff, P. M.; Schuth, F.; Stucky, G. D. *Nature* **1994**, *368*, 317-321.
42. Antonelli, D. M.; Ying, J. Y. *Angewandte Chemie-International Edition in English* **1995**, *34*, 2014-2017.
43. Lu, Y. F.; Ganguli, R.; Drewien, C. A.; Anderson, M. T.; Brinker, C. J.; Gong, W. L.; Guo, Y. X.; Soyez, H.; Dunn, B.; Huang, M. H.; Zink, J. I. *Nature* **1997**, *389*, 364-368.
44. Ryoo, R.; Joo, S. H.; Jun, S. *Journal of Physical Chemistry B* **1999**, *103*, 7743-7746.
45. Marquez-Alvarez, C.; Zilkova, N.; Perez-Pariente, J.; Cejka, J. *Catalysis Reviews-Science and Engineering* **2008**, *50*, 222-286.
46. Kuemmel, M.; Grosso, D.; Boissiere, U.; Smarsly, B.; Brezesinski, T.; Albouy, P. A.; Amenitsch, H.; Sanchez, C. *Angewandte Chemie-International Edition* **2005**, *44*, 4589-4592.
47. Li, W. C.; Lu, A. H.; Schmidt, W.; Schuth, F. *Chemistry-a European Journal* **2005**, *11*, 1658-1664.
48. Liu, Q.; Wang, A.; Wang, X.; Zhang, T. *Chemistry of Materials* **2006**, *18*, 5153-5155.
49. Wu, Z.; Li, Q.; Peng, D.; Webley, P. A.; Zhao, D. *Journal of the American Chemical Society* **2010**, *132*, 12042-12050.
50. Antonelli, D. M. *Microporous and Mesoporous Materials* **1999**, *30*, 315-319.
51. Cabrera, S.; El Haskouri, J.; Beltran-Porter, A.; Beltran-Porter, D.; Marcos, M. D.; Amoros, P. *Solid State Sciences* **2000**, *2*, 513-518.
52. Grosso, D.; Illia, G.; Crepaldi, E. L.; Charleux, B.; Sanchez, C. *Advanced Functional Materials* **2003**, *13*, 37-42.
53. Zhang, J.; Deng, Y.; Gu, D.; Wang, S.; She, L.; Che, R.; Wang, Z.-S.; Tu, B.; Xie, S.; Zhao, D. *Advanced Energy Materials* **2011**, *1*, 241-248.

54. Kim, S. S.; Lee, H. I.; Shon, J. K.; Hur, J. Y.; Kang, M. S.; Park, S. S.; Kong, S. S.; Yu, J. A.; Seo, M.; Li, D.; Thakur, S. S.; Kim, J. M. *Chemistry Letters* **2008**, *37*, 140-141.
55. Yue, W.; Randorn, C.; Attidekou, P. S.; Su, Z.; Irvine, J. T. S.; Zhou, W. *Advanced Functional Materials* **2009**, *19*, 2826-2833.
56. Ciesla, U.; Schacht, S.; Stucky, G. D.; Unger, K. K.; Schuth, F. *Angewandte Chemie-International Edition in English* **1996**, *35*, 541-543.
57. Hudson, M. J.; Knowles, J. A. *Journal of Materials Chemistry* **1996**, *6*, 89-95.
58. Liu, B.; Baker, R. T. *Journal of Materials Chemistry* **2008**, *18*, 5200-5207.
59. Li, Z. F.; Ruckenstein, E. *Langmuir* **2002**, *18*, 6956-6961.
60. Lee, J.; Orilall, M. C.; Warren, S. C.; Kamperman, M.; Disalvo, F. J.; Wiesner, U. *Nature Materials* **2008**, *7*, 222-228.
61. Antonelli, D. M.; Ying, J. Y. *Chemistry of Materials* **1996**, *8*, 874-881.
62. Sinha, A. K.; Suzuki, K. *Journal of Physical Chemistry B* **2005**, *109*, 1708-1714.
63. Antonelli, D. M.; Trudeau, M. *Angewandte Chemie-International Edition* **1999**, *38*, 1471-1475.
64. Chen, J. L.; Burger, C.; Krishnan, C. V.; Chu, B. *Journal of the American Chemical Society* **2005**, *127*, 14140-14141.
65. Zhou, L.; Ren, Q.; Zhou, X.; Tang, J.; Chen, Z.; Yu, C. *Microporous and Mesoporous Materials* **2008**, *109*, 248-257.
66. Brezesinski, T.; Groenewolt, M.; Antonietti, M.; Smarsly, B. *Angewandte Chemie-International Edition* **2006**, *45*, 781-784.
67. Jiao, F.; Jumas, J.-C.; Womes, M.; Chadwick, A. V.; Harrison, A.; Bruce, P. G. *Journal of the American Chemical Society* **2006**, *128*, 12905-12909.
68. Subramanian, V.; Hall, S. C.; Smith, P. H.; Rambabu, B. *Solid State Ionics* **2004**, *175*, 511-515.
69. Tian, B. Z.; Liu, X. Y.; Yang, H. F.; Xie, S. H.; Yu, C. Z.; Tu, B.; Zhao, D. Y. *Advanced Materials* **2003**, *15*, 1370-+.
70. Tueysuez, H.; Comotti, M.; Schueth, F. *Chemical Communications* **2008**, 4022-4024.
71. Dickinson, C.; Zhou, W.; Hodgkins, R. P.; Shi, Y.; Zhao, D.; He, H. *Chemistry of Materials* **2006**, *18*, 3088-3095.
72. Banerjee, S.; Santhanam, A.; Dhathathreyan, A.; Rao, P. M. *Langmuir* **2003**, *19*, 5522-5525.

73. Lai, X.; Li, X.; Geng, W.; Tu, J.; Li, J.; Qiu, S. *Angewandte Chemie-International Edition* **2007**, *46*, 738-741.
74. Luo, H. M.; Zhang, J. F.; Yan, Y. S. *Chemistry of Materials* **2003**, *15*, 3769-3773.
75. Pauporte, T.; Rathousky, J. *Journal of Physical Chemistry C* **2007**, *111*, 7639-7644.
76. Polarz, S.; Orlov, A. V.; Schueth, F.; Lu, A.-H. *Chemistry-a European Journal* **2007**, *13*, 592-597.
77. Wagner, T.; Waitz, T.; Roggenbuck, J.; Froba, M.; Kohl, C. D.; Tiemann, M. *Thin Solid Films* **2007**, *515*, 8360-8363.
78. Lyons, D. M.; Harman, L. P.; Morris, M. A. *Journal of Materials Chemistry* **2004**, *14*, 1976-1981.
79. Laha, S. C.; Ryoo, R. *Chemical Communications* **2003**, 2138-2139.
80. Shen, W. H.; Dong, X. P.; Zhu, Y. F.; Chen, H. R.; Shi, J. L. *Microporous and Mesoporous Materials* **2005**, *85*, 157-162.
81. Liu, C.; Zhang, L.; Deng, J.; Mu, Q.; Dai, H.; He, H. *Journal of Physical Chemistry C* **2008**, *112*, 19248-19256.
82. Li, H.; Zhang, L.; Dai, H.; He, H. *Inorganic Chemistry* **2009**, *48*, 4421-4434.
83. Roggenbuck, J.; Tiemann, M. *Journal of the American Chemical Society* **2005**, *127*, 1096-1097.
84. Stein, A.; Wang, Z.; Fierke, M. A. *Advanced Materials* **2009**, *21*, 265-293.
85. Oya, A.; Yoshida, S.; Alcanizmonge, J.; Linaressolano, A. *Carbon* **1995**, *33*, 1085-1090.
86. Ozaki, J.; Endo, N.; Ohizumi, W.; Igarashi, K.; Nakahara, M.; Oya, A.; Yoshida, S.; Iizuka, T. *Carbon* **1997**, *35*, 1031-1033.
87. Biener, J.; Stadermann, M.; Suss, M.; Worsley, M. A.; Biener, M. M.; Rose, K. A.; Baumann, T. F. *Energy & Environmental Science* **2011**, *4*, 656-667.
88. Lee, J.; Yoon, S.; Hyeon, T.; Oh, S. M.; Kim, K. B. *Chemical Communications* **1999**, 2177-2178.
89. Jun, S.; Joo, S. H.; Ryoo, R.; Kruk, M.; Jaroniec, M.; Liu, Z.; Ohsuna, T.; Terasaki, O. *Journal of the American Chemical Society* **2000**, *122*, 10712-10713.
90. Li, H.; Sakamoto, Y.; Li, Y.; Terasaki, O.; Thommes, M.; Che, S. *Microporous and Mesoporous Materials* **2006**, *95*, 193-199.
91. Kim, S. S.; Pinnavaia, T. J. *Chemical Communications* **2001**, 2418-2419.

92. Lee, J.; Yoon, S.; Oh, S. M.; Shin, C. H.; Hyeon, T. *Advanced Materials* **2000**, *12*, 359-+.
93. Han, S.; Lee, K. T.; Oh, S. M.; Hyeon, T. *Carbon* **2003**, *41*, 1049-1056.
94. Lu, A.-H.; Schueth, F. *Advanced Materials* **2006**, *18*, 1793-1805.
95. Ryoo, R.; Joo, S. H.; Jun, S.; Tsubakiyama, T.; Terasaki, O. *Studies in Surface Science and Catalysis* **2001**, *135*, 150.
96. Lee, J. S.; Joo, S. H.; Ryoo, R. *Journal of the American Chemical Society* **2002**, *124*, 1156-1157.
97. Joo, S. H.; Choi, S. J.; Oh, I.; Kwak, J.; Liu, Z.; Terasaki, O.; Ryoo, R. *Nature* **2001**, *412*, 169-172.
98. Che, S. N.; Lund, K.; Tatsumi, T.; Iijima, S.; Joo, S. H.; Ryoo, R.; Terasaki, O. *Angewandte Chemie-International Edition* **2003**, *42*, 2182-2185.
99. Kruk, M.; Jaroniec, M.; Kim, T. W.; Ryoo, R. *Chemistry of Materials* **2003**, *15*, 2815-2823.
100. Lu, A. H.; Schmidt, W.; Spliethoff, B.; Schuth, F. *Advanced Materials* **2003**, *15*, 1602-+.
101. Yang, C. M.; Weidenthaler, C.; Spliethoff, B.; Mayanna, M.; Schuth, F. *Chemistry of Materials* **2005**, *17*, 355-358.
102. Kim, T. W.; Park, I. S.; Ryoo, R. *Angewandte Chemie-International Edition* **2003**, *42*, 4375-4379.
103. Yang, H. F.; Yan, Y.; Liu, Y.; Zhang, F. Q.; Zhang, R. Y.; Meng, Y.; Li, M.; Xie, S. H.; Tu, B.; Zhao, D. Y. *Journal of Physical Chemistry B* **2004**, *108*, 17320-17328.
104. Fuertes, A. B.; Centeno, T. A. *Journal of Materials Chemistry* **2005**, *15*, 1079-1083.
105. Fuertes, A. B.; Alvarez, S. *Carbon* **2004**, *42*, 3049-3055.
106. Che, S. N.; Garcia-Bennett, A. E.; Liu, X. Y.; Hodgkins, R. P.; Wright, P. A.; Zhao, D. Y.; Terasaki, O.; Tatsumi, T. *Angewandte Chemie-International Edition* **2003**, *42*, 3930-3934.
107. Kleitz, F.; Choi, S. H.; Ryoo, R. *Chemical Communications* **2003**, 2136-2137.
108. Fan, J.; Yu, C. Z.; Gao, T.; Lei, J.; Tian, B. Z.; Wang, L. M.; Luo, Q.; Tu, B.; Zhou, W. Z.; Zhao, D. Y. *Angewandte Chemie-International Edition* **2003**, *42*, 3146-3150.
109. Guo, W. P.; Su, F. B.; Zhao, X. S. *Carbon* **2005**, *43*, 2423-2426.
110. Kim, T. W.; Ryoo, R.; Gierszal, K. P.; Jaroniec, M.; Solovyov, L. A.; Sakamoto, Y.; Terasaki, O. *Journal of Materials Chemistry* **2005**, *15*, 1560-1571.

111. Tanaka, S.; Nishiyama, N.; Egashira, Y.; Ueyama, K. *Chemical Communications* **2005**, 2125-2127.
112. Liang, C. D.; Dai, S. *Journal of the American Chemical Society* **2006**, *128*, 5316-5317.
113. Ma, T.-Y.; Liu, L.; Yuan, Z.-Y. *Chemical Society Reviews* **2013**, *42*, 3977-4003.
114. Liang, C. D.; Hong, K. L.; Guiochon, G. A.; Mays, J. W.; Dai, S. *Angewandte Chemie-International Edition* **2004**, *43*, 5785-5789.
115. Deng, Y.; Yu, T.; Wan, Y.; Shi, Y.; Meng, Y.; Gu, D.; Zhang, L.; Huang, Y.; Liu, C.; Wu, X.; Zhao, D. *Journal of the American Chemical Society* **2007**, *129*, 1690-1697.
116. Deng, Y.; Liu, C.; Gu, D.; Yu, T.; Tu, B.; Zhao, D. *Journal of Materials Chemistry* **2008**, *18*, 91-97.
117. Meng, Y.; Gu, D.; Zhang, F. Q.; Shi, Y. F.; Yang, H. F.; Li, Z.; Yu, C. Z.; Tu, B.; Zhao, D. Y. *Angewandte Chemie-International Edition* **2005**, *44*, 7053-7059.
118. Meng, Y.; Gu, D.; Zhang, F.; Shi, Y.; Cheng, L.; Feng, D.; Wu, Z.; Chen, Z.; Wan, Y.; Stein, A.; Zhao, D. *Chemistry of Materials* **2006**, *18*, 4447-4464.
119. Florent, M.; Xue, C.; Zhao, D.; Goldfarb, D. *Chemistry of Materials* **2012**, *24*, 383-392.
120. Huang, Y.; Cai, H.; Yu, T.; Zhang, F.; Zhang, F.; Meng, Y.; Gu, D.; Wan, Y.; Sun, X.; Tu, B.; Zhao, D. *Angewandte Chemie-International Edition* **2007**, *46*, 1089-1093.
121. Zhang, F. Q.; Meng, Y.; Gu, D.; Yan, Y.; Yu, C. Z.; Tu, B.; Zhao, D. Y. *Journal of the American Chemical Society* **2005**, *127*, 13508-13509.
122. Zhang, F.; Meng, Y.; Gu, D.; Yan, Y.; Chen, Z.; Tu, B.; Zhao, D. *Chemistry of Materials* **2006**, *18*, 5279-5288.
123. Zhang, F.; Gu, D.; Yu, T.; Zhang, F.; Xie, S.; Zhang, L.; Deng, Y.; Wan, Y.; Tu, B.; Zhao, D. *Journal of the American Chemical Society* **2007**, *129*, 7746-+.
124. Huang, Y.; Cai, H.; Feng, D.; Gu, D.; Deng, Y.; Tu, B.; Wang, H.; Webley, P. A.; Zhao, D. *Chemical Communications* **2008**, 2641-2643.
125. Fang, Y.; Gu, D.; Zou, Y.; Wu, Z.; Li, F.; Che, R.; Deng, Y.; Tu, B.; Zhao, D. *Angewandte Chemie-International Edition* **2010**, *49*, 7987-7991.
126. Liu, C.; Li, L.; Song, H.; Chen, X. *Chemical Communications* **2007**, 757-759.
127. Hao, G.-P.; Li, W.-C.; Wang, S.; Wang, G.-H.; Qi, L.; Lu, A.-H. *Carbon* **2011**, *49*, 3762-3772.
128. Liu, L.; Wang, F.-Y.; Shao, G.-S.; Yuan, Z.-Y. *Carbon* **2010**, *48*, 2089-2099.

129. Liu, L.; Deng, Q.-F.; Agula, B.; Zhao, X.; Ren, T.-Z.; Yuan, Z.-Y. *Chemical Communications* **2011**, *47*, 8334-8336.
130. Liu, L.; Deng, Q.-F.; Agula, B.; Ren, T.-Z.; Liu, Y.-P.; Zhaorigetu, B.; Yuan, Z.-Y. *Catalysis Today* **2012**, *186*, 35-41.
131. Liu, L.; Deng, Q.-F.; Liu, Y.-P.; Ren, T.-Z.; Yuan, Z.-Y. *Catalysis Communications* **2011**, *16*, 81-85.
132. Liu, L.; Deng, Q.-F.; Ma, T.-Y.; Lin, X.-Z.; Hou, X.-X.; Liu, Y.-P.; Yuan, Z.-Y. *Journal of Materials Chemistry* **2011**, *21*, 16001-16009.
133. Long, D.; Lu, F.; Zhang, R.; Qiao, W.; Zhan, L.; Liang, X.; Ling, L. *Chemical Communications* **2008**, 2647-2649.
134. Wang, X.; Liang, C.; Dai, S. *Langmuir* **2008**, *24*, 7500-7505.
135. Gao, P.; Wang, A.; Wang, X.; Zhang, T. *Chemistry of Materials* **2008**, *20*, 1881-1888.
136. Zhao, X.; Wang, A.; Yan, J.; Sun, G.; Sun, L.; Zhang, T. *Chemistry of Materials* **2010**, *22*, 5463-5473.
137. Tsouris, C.; Mayes, R.; Kiggans, J.; Sharma, K.; Yiacoumi, S.; DePaoli, D.; Dai, S. *Environmental Science & Technology* **2011**, *45*, 10243-10249.
138. Lu, A.-H.; Spliethoff, B.; Schueth, F. *Chemistry of Materials* **2008**, *20*, 5314-5319.
139. Tanaka, S.; Nakatani, N.; Doi, A.; Miyake, Y. *Carbon* **2011**, *49*, 3184-3189.
140. Tanaka, S.; Doi, A.; Nakatani, N.; Katayama, Y.; Miyake, Y. *Carbon* **2009**, *47*, 2688-2698.
141. Tanaka, S.; Katayama, Y.; Tate, M. P.; Hillhouse, H. W.; Miyake, Y. *Journal of Materials Chemistry* **2007**, *17*, 3639-3645.
142. Mayes, R. T.; Tsouris, C.; Kiggans, J. O., Jr.; Mahurin, S. M.; DePaoli, D. W.; Dai, S. *Journal of Materials Chemistry* **2010**, *20*, 8674-8678.
143. Rodriguez, A. T.; Chen, M.; Chen, Z.; Brinker, C. J.; Fan, H. *Journal of the American Chemical Society* **2006**, *128*, 9276-9277.
144. Mangun, C. L.; Benak, K. R.; Economy, J.; Foster, K. L. *Carbon* **2001**, *39*, 1809-1820.
145. Hao, G.-P.; Li, W.-C.; Qian, D.; Wang, G.-H.; Zhang, W.-P.; Zhang, T.; Wang, A.-Q.; Schueth, F.; Bongard, H.-J.; Lu, A.-H. *Journal of the American Chemical Society* **2011**, *133*, 11378-11388.
146. Soutullo, M. D.; Odom, C. I.; Wicker, B. F.; Henderson, C. N.; Stenson, A. C.; Davis, J. H., Jr. *Chemistry of Materials* **2007**, *19*, 3581-3583.

147. Bagreev, A.; Menendez, J. A.; Dukhno, I.; Tarasenko, Y.; Bandosz, T. J. *Carbon* **2004**, *42*, 469-476.
148. Wan, Y.; Qian, X.; Jia, N.; Wang, Z.; Li, H.; Zhao, D. *Chemistry of Materials* **2008**, *20*, 1012-1018.
149. Liu, L.; Sun, G.; Wang, C.; Yang, J.; Xiao, C.; Wang, H.; Ma, D.; Kou, Y. *Catalysis Today* **2012**, *183*, 136-142.
150. Wu, Z.; Webley, P. A.; Zhao, D. *Langmuir* **2010**, *26*, 10277-10286.
151. Wu, Z.; Hao, N.; Xiao, G.; Liu, L.; Webley, P.; Zhao, D. *Physical Chemistry Chemical Physics* **2011**, *13*, 2495-2503.
152. She, L.; Li, J.; Wan, Y.; Yao, X.; Tu, B.; Zhao, D. *Journal of Materials Chemistry* **2011**, *21*, 795-800.
153. Zhai, Y.; Dou, Y.; Liu, X.; Tu, B.; Zhao, D. *Journal of Materials Chemistry* **2009**, *19*, 3292-3300.
154. Yu, T.; Deng, Y.; Wang, L.; Liu, R.; Zhang, L.; Tu, B.; Zhao, D. *Advanced Materials* **2007**, *19*, 2301-+.
155. Wei, H.; Lv, Y.; Han, L.; Tu, B.; Zhao, D. *Chemistry of Materials* **2011**, *23*, 2353-2360.
156. liu, Y. *Journal of Porous Materials* **2011**, *18*, 597-605.
157. Ma, Y.; Cui, L.; He, J.; Wang, T.; Guo, Y.; Tang, J.; Li, G.; Hu, Y.; Xue, H.; Liu, M.; Sun, X. *Electrochimica Acta* **2012**, *63*, 318-322.
158. Liu, R.; Shi, Y.; Wan, Y.; Meng, Y.; Zhang, F.; Gu, D.; Chen, Z.; Tu, B.; Zhao, D. *Journal of the American Chemical Society* **2006**, *128*, 11652-11662.
159. Wan, Y.; Wang, H.; Zhao, Q.; Klingstedt, M.; Terasaki, O.; Zhao, D. *Journal of the American Chemical Society* **2009**, *131*, 4541-4550.
160. Liu, R.; Ren, Y.; Shi, Y.; Zhang, F.; Zhang, L.; Tu, B.; Zhao, D. *Chemistry of Materials* **2008**, *20*, 1140-1146.
161. Krawiec, P.; Kockrick, E.; Borchardt, L.; Geiger, D.; Corma, A.; Kaskel, S. *Journal of Physical Chemistry C* **2009**, *113*, 7755-7761.
162. Kockrick, E.; Schrage, C.; Borchardt, L.; Klein, N.; Rose, M.; Senkovska, I.; Kaskel, S. *Carbon* **2010**, *48*, 1707-1717.
163. Alivisatos, A. P. *Science* **1996**, *271*, 933-937.
164. Repins, I.; Contreras, M. A.; Egaas, B.; DeHart, C.; Scharf, J.; Perkins, C. L.; To, B.; Noufi, R. *Progress in Photovoltaics* **2008**, *16*, 235-239.
165. Harman, T. C.; Walsh, M. P.; Laforge, B. E.; Turner, G. W. *Journal of Electronic Materials* **2005**, *34*, L19-L22.

166. Weiss, D.; Roukes, M. L.; Menschig, A.; Grambow, P.; Vonklitzing, K.; Weimann, G. *Physical Review Letters* **1991**, *66*, 2790-2793.
167. Stupp, S. I.; Braun, P. V. *Science* **1997**, *277*, 1242-1248.
168. Kresge, C. T.; Leonowicz, M. E.; Roth, W. J.; Schmitt, K. D.; Vartuli, J. C. In *Google patents*, 1993.
169. Kaskel, S.; Schlichte, K. *Journal of Catalysis* **2001**, *201*, 270-274.
170. Kaskel, S.; Schlichte, K.; Zibrowius, B. *Physical Chemistry Chemical Physics* **2002**, *4*, 1675-1681.
171. Kapoor, M. P.; Inagaki, S. *Chemistry Letters* **2003**, *32*, 94-95.
172. El Haskouri, J.; Cabrera, S.; Sapina, F.; Latorre, J.; Guillem, C.; Beltran-Porter, A.; Beltran-Porter, D.; Marcos, M. D.; Amoros, P. *Advanced Materials* **2001**, *13*, 192-195.
173. Huynh, M. H. V.; Hiskey, M. A.; Archuleta, J. G.; Roemer, E. L. *Angewandte Chemie-International Edition* **2005**, *44*, 737-739.
174. Hellgren, N.; Guo, J. H.; Luo, Y.; Sathe, C.; Agui, A.; Kashtanov, S.; Nordgren, J.; Agren, H.; Sundgren, J. E. *Thin Solid Films* **2005**, *471*, 19-34.
175. Thomas, A.; Goettmann, F.; Antonietti, M. *Chemistry of Materials* **2008**, *20*, 738-755.
176. Vinu, A.; Ariga, K.; Mori, T.; Nakanishi, T.; Hishita, S.; Golberg, D.; Bando, Y. *Advanced Materials* **2005**, *17*, 1648-+.
177. Jun, Y.-S.; Hong, W. H.; Antonietti, M.; Thomas, A. *Advanced Materials* **2009**, *21*, 4270-+.
178. Fischer, A.; Antonietti, M.; Thomas, A. *Advanced Materials* **2007**, *19*, 264-+.
179. Winkler, H.; Birkner, A.; Hagen, V.; Wolf, I.; Schmechel, R.; von Seggern, H.; Fischer, R. A. *Advanced Materials* **1999**, *11*, 1444-1448.
180. Shi, Y.; Wan, Y.; Zhang, R.; Zhao, D. *Advanced Functional Materials* **2008**, *18*, 2436-2443.
181. Attard, G. S.; Goltner, C. G.; Corker, J. M.; Henke, S.; Templer, R. H. *Angewandte Chemie-International Edition in English* **1997**, *36*, 1315-1317.
182. Attard, G. S.; Bartlett, P. N.; Coleman, N. R. B.; Elliott, J. M.; Owen, J. R.; Wang, J. H. *Science* **1997**, *278*, 838-840.
183. Yu, J. H.; Xu, R. R. *Accounts of Chemical Research* **2003**, *36*, 481-490.
184. Wilson, S. T.; Lok, B. M.; Messina, C. A.; Cannan, T. R.; Flanigen, E. M. *Abstracts of Papers of the American Chemical Society* **1982**, *184*, 6-INOR.

185. Tiemann, M.; Froba, M. *Chemistry of Materials* **2001**, *13*, 3211-3217.
186. Sayari, A.; Karra, V. R.; Reddy, J. S.; Moudrakovski, I. L. *Chemical Communications* **1996**, 411-412.
187. Feng, P. Y.; Xia, Y.; Feng, J. L.; Bu, X. H.; Stucky, G. D. *Chemical Communications* **1997**, 949-950.
188. Holland, B. T.; Isbester, P. K.; Blanford, C. F.; Munson, E. J.; Stein, A. *Journal of the American Chemical Society* **1997**, *119*, 6796-6803.
189. Kimura, T.; Sugahara, Y.; Kuroda, K. *Microporous and Mesoporous Materials* **1998**, *22*, 115-126.
190. Kimura, T.; Sugahara, Y.; Kuroda, K. *Chemical Communications* **1998**, 559-560.
191. Cabrera, S.; El Haskouri, J.; Guillem, C.; Beltran-Porter, A.; Beltran-Porter, D.; Mendioroz, S.; Marcos, M. D.; Amoros, P. *Chemical Communications* **1999**, 333-334.
192. Zhao, X. S.; Lu, G. Q.; Whittaker, A. K.; Drennan, J.; Xu, H. *Microporous and Mesoporous Materials* **2002**, *55*, 51-62.
193. Khimyak, Y. Z.; Klinowski, J. *Physical Chemistry Chemical Physics* **2000**, *2*, 5275-5285.
194. Gianotti, E.; Oliveira, E. C.; Coluccia, S.; Pastore, H. O.; Marchese, L. *Inorganica Chimica Acta* **2003**, *349*, 259-264.
195. Wang, L. M.; Tian, B. Z.; Fan, J.; Liu, X. Y.; Yang, H. F.; Yu, C. Z.; Tu, B.; Zhao, D. Y. *Microporous and Mesoporous Materials* **2004**, *67*, 123-133.
196. Kimura, T. *Journal of Materials Chemistry* **2003**, *13*, 3072-3078.
197. Kimura, T. *Chemistry Letters* **2002**, 770-771.
198. Hutchings, G. J. *Journal of Materials Chemistry* **2004**, *14*, 3385-3395.
199. Lin, R.; Ding, Y.; Gong, L.; Dong, W.; Wang, J.; Zhang, T. *Journal of Catalysis* **2010**, *272*, 65-73.
200. Wang, Y.; Wang, X. X.; Su, Z.; Guo, Q.; Tang, Q. H.; Zhang, Q. H.; Wan, H. L. *Catalysis Today* **2004**, *93-5*, 155-161.
201. Tian, X.; He, W.; Cui, J.; Zhang, X.; Zhou, W.; Yan, S.; Sun, X.; Han, X.; Han, S.; Yue, Y. *Journal of Colloid and Interface Science* **2010**, *343*, 344-349.
202. Li, X. S.; Courtney, A. R.; Yantasee, W.; Mattigod, S. V.; Fryxell, G. E. *Inorganic Chemistry Communications* **2006**, *9*, 293-295.
203. Dutta, A.; Patra, A. K.; Bhaumik, A. *Microporous and Mesoporous Materials* **2012**, *155*, 208-214.

204. Kleitz, F.; Thomson, S. J.; Liu, Z.; Terasaki, O.; Schuth, F. *Chemistry of Materials* **2002**, *14*, 4134-4144.
205. Sun, Y.; Afanasiev, P.; Vrinat, M.; Coudurier, G. *Journal of Materials Chemistry* **2000**, *10*, 2320-2324.
206. Yuan, Z. Y.; Ren, T. Z.; Azioune, A.; Pireaux, J. J.; Su, B. L. *Catalysis Today* **2005**, *105*, 647-654.
207. Sahu, A. K.; Pitchumani, S.; Sridhar, P.; Shukla, A. K. *Fuel Cells* **2009**, *9*, 139-147.
208. Nishiyama, Y.; Tanaka, S.; Hillhouse, H. W.; Nishiyama, N.; Egashira, Y.; Ueyama, K. *Langmuir* **2006**, *22*, 9469-9472.
209. Bhaumik, A.; Inagaki, S. *Journal of the American Chemical Society* **2001**, *123*, 691-696.
210. Muneyama, E.; Kunishige, A.; Ohdan, K.; Ai, M. *Journal of Catalysis* **1996**, *158*, 378-384.
211. Padhi, A. K.; Nanjundaswamy, K. S.; Masquelier, C.; Okada, S.; Goodenough, J. B. *Journal of the Electrochemical Society* **1997**, *144*, 1609-1613.
212. Kandori, K.; Nakashima, H.; Ishikawa, T. *Journal of Colloid and Interface Science* **1993**, *160*, 499-501.
213. Sayari, A.; Hamoudi, S. *Chemistry of Materials* **2001**, *13*, 3151-3168.
214. Rocha, C. O.; Rocha, J.; Lin, Z. *Catalysis Letters* **2003**, *89*, 69-74.
215. Michel, R.; Lussi, J. W.; Csucs, G.; Reviakine, I.; Danuser, G.; Ketterer, B.; Hubbell, J. A.; Textor, M.; Spencer, N. D. *Langmuir* **2002**, *18*, 3281-3287.
216. Ren, N.; Tang, Y.; Wang, Y. J.; Hu, S. H.; Dong, A. G.; Hua, W. M.; Yue, H. H.; Shen, J. Y. *Chemistry Letters* **2002**, 1036-1037.
217. El Haskouri, J.; Guillem, C.; Latorre, J.; Beltran, A.; Beltran, D.; Amoros, P. *European Journal of Inorganic Chemistry* **2004**, 1804-1807.

Mesoporous iron phosphate/phosphonate hybrid materials

Jamal El Haskouri^{a,b}, Alaina Moragues^a, Aurelio Beltrán^a, Sonia Murcia-Mascarós^{a,b}, Fernando Plazaola^c, Estibaliz Legarra^c, Adela Mauri-Aucejo^d, Mauro Brotons-Gisbert^a, Juan F. Sánchez-Royo^a, Daniel Beltrán^a and Pedro Amorós^a

^a Institut de Ciència dels Materials, Universitat de València, 46071 Valencia, Spain.

^b Fundació General, Universitat de València, 46071 Valencia, Spain

^c Departamento de Electricidad y Electrónica, Facultad de Ciencia y Tecnología, Universidad del País Vasco/EHU, 48080 Bilbao, Spain

^d Departament de Química Analítica. Facultat de Química. Universitat de València, 46100 Burjassot, València, Spain

Received 24th June 2013, Accepted 9th December 2013

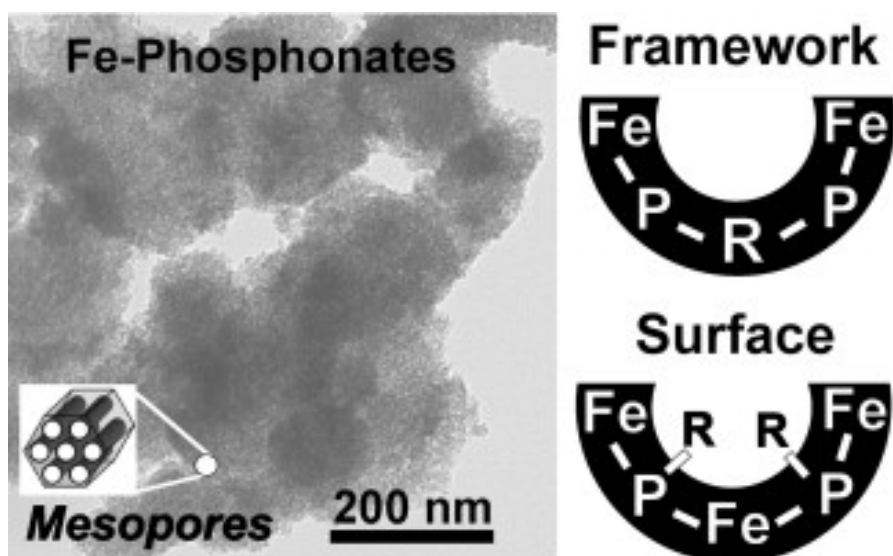
Published online 19th December 2013

Microporous and Mesoporous Materials 187 (2014) 14–22

DOI: 10.1016/j.micromeso.2013.12.015

Abstract

Relatively high surface area pure mesoporous iron-phosphorous oxide-based derivatives have been synthesized through an S^+I^- surfactant-assisted cooperative mechanism by means of a one-pot preparative procedure from aqueous solution and starting from iron atrane complexes and phosphoric and phosphonic acids. A soft chemical extraction procedure allows opening the pore system of the parent as-prepared materials by exchanging the surfactant without mesostructure collapse. The nature of the pore wall can be modulated from iron phosphate up to hybrids involving approximately 30% of organophosphorous entities (phosphonates or diphosphonates). X-ray powder diffraction, transmission electron microscopy and surface analysis techniques show that these hybrid materials present regular unimodal disordered pore systems. Spectroscopic results (Fe-57 Mössbauer, XPS, UV-Vis, FTIR and RAMAN) not only confirm the incorporation of organophosphorous entities into the framework of these materials but also provide us useful information to elucidate both the mechanism through which they are formed, and some details on their specific local structures.



Introduction

Nature created a diversity of open-framework inorganic materials with regular pore architectures^{1,2}. Crystalline aluminosilicate zeolites were the first type of microporous materials to be recognized³. Academic and industrial interest in zeolites steadily progressed as chemists learned to synthesize them in the laboratory^{3,4}. All known zeolite frameworks are based upon vertex-sharing (SiO_4) and (AlO_4) tetrahedra, which delimit interconnected channels or cages^{4,2,3}. Because of their wide-ranging applications in fields where molecular recognition is needed³, the attention paid to three-dimensional open-frameworks led to the search for new material families. Efforts were successful in the early 1980s, when investigations at Union Carbide yielded a new class of crystalline molecular sieves, the aluminophosphates (ALPOs)⁵. With neutral tetra-connected frameworks (alternating $[\text{PO}_4]$ and $[\text{AlO}_4]$ units) closely related to those adopted by zeolites⁶, ALPOs quickly stirred interest looking for expanding micropores availability. Due to their significant electronic and structural similarities, ALPOs chemistry evolved through similar ways to that of zeolites and tackling also questions as, among others, the chemical modification (“functionalization”) of the material walls or the “expansion” of the pore sizes⁷.

In the broad sense, ALPOs chemistry has proven to be more complex (or versatile) than that of silica-based materials. So, ALPOs formally allow even a complete exchange of aluminum atoms or phosphate groups by other metal atoms or phosphate-related entities, respectively. In fact, a diversity of new inorganic open-framework aluminum-free phosphates was characterized during the 1990s². The well-known structure-directing effect due to small organic molecules was key for synthesizing such porous materials, although collapse of the inorganic framework after “template” removal often occurred². At the same time, replacement of phosphate groups by other tetrahedral or pseudotetrahedral entities was explored for preparing new open structures, what also made possible the obtaining of inorganic-organic hybrid skeletons (looking for overcome limitations imposed by the relatively small sizes of the polyhedral centers and their connectivity in purely inorganic systems). With regard to the “expansion” of the pore sizes (in the search for efficiency in treatments

of bulky substrates), the Mobil' synthesis of the M41S silicas by using surfactants as "supramolecular templates" constituted a milestone in the field by offering a way for expanding the typical pore sizes in zeotypes to the mesopore range⁸⁻⁹. Such strategy was quickly adapted for synthesizing also non silica-based materials, although it met with limited success¹⁰. In that concerning ALPOs and related phosphates, to imitate the chemistry of mesostructured/mesoporous zeolites did not resulted as straightforward as initially might be thought precisely because of the relative chemical versatility of non-silica materials¹¹. In practice, concerning phosphate chemistry, the area most widely explored in last decades has been, very likely, that dealing with organically modified inorganic open-frameworks^{2,12-14}. In order to get open skeletons, phosphate-like moieties have been replaced (totally or in part) by more complex related organic species (mono or diphosphonates, functionalized monophosphonates, mixed phosphate-oxalate groups, and so on). It does not seem hasty to state that in the many and ingenious work devoted to these hybrid materials lays the genesis of the nowadays exciting metal-organic frameworks (MOFs). The state of the art of phosphonate-based MOFs (including also non-crystalline or unconventional UMOF materials) has been recently revised by Clearfield and coworkers¹⁵.

In previous publications, our group reported on the synthesis of organically modified pure mesoporous ALPOs¹⁶⁻¹⁹. Together with Al, the preparation of micro or mesoporous phosphate-phosphonate hybrid materials is well documented for Ti and Zr, and there is also information concerning related materials including a diversity of metals (like Ga, In, Sn, V, Mo, Fe, Co and Zn)^{2,11}. In particular, iron phosphates have aroused interest because of both their very rich crystal chemistry and traditional or novel (based on surface and diffusion phenomena) practical applications²⁰⁻²³. In fact, there is a large variety of naturally occurring iron phosphate materials, which includes many structurally diverse examples of both open and dense octahedral-tetrahedral frameworks^{20,24}. The mineral cacoxenite, $[\text{AlFe}_{24}(\text{OH})_{12}(\text{PO}_4)_{17}(\text{H}_2\text{O})_{24}]\cdot 51\text{H}_2\text{O}$, constitutes a beautiful example of how nature constructs stable microporous solids: built up from isotropic Fe^{3+} cations in $\text{Fe}_4(\text{OH})_2^{\text{q+}}$ clusters and $\text{PF}_{26}\text{O}_{28}^{\text{q-}}$ Keggin-like blocks, it contains relatively large cylindrical channels (free diameter size of 1.42 nm) filled with delocalized water molecules²⁵. Looking to imitate nature, the application of

hydrothermal techniques and the generalization of the use of small molecules as structural directing agents, allowed preparing a wide set of layered and open structures based on iron phosphate frameworks^{2,20}. However, as suggested above, utilization of micelles as “supramolecular templates” for obtaining high surface mesoporous iron phosphates has not resulted so satisfactory because of the intermediate formation of lamellar or other unstable phases, which readily collapse by elimination of the surfactant. Thus, the only apparently successful synthesis reported until now is based on using an anionic surfactant (dodecyl sulfate) as template under the obligatory assistance of HF^{26,27}. In the self-assembling processes leading to the mesostructured intermediate, the dodecyl sulfate portions should be able to match with fluoride-linked iron-phosphate cationic clusters, and subsequent surfactant removal occurs without collapse of the mesophase. Also, a related dodecyl sulfate directed procedure (excluding HF) allowed obtaining a hybrid mesoporous iron oxophenyl-phosphate material under hydrothermal conditions²⁸, although the P:Fe molar ratio of 0.47 in this solid is far from that corresponding to the 1:1 ideal stoichiometry. In contrast, as far as we know, all attempts based on using surfactants of different nature (including cationic ones) only have rendered mesostructured solids which do not resist template elimination²⁹.

In this paper, we report on a detailed study of the one-pot surfactant-assisted procedure that has allowed us to prepare for the first time mesoporous iron phosphates with organically modified surfaces and/or frameworks by using a cationic surfactant as template. This simple and reproducible method yields pure large surface area mesoporous materials displaying high chemical homogeneity as well as good dispersion of the organic groups. On the basis of spectroscopic results, we analyze the iron-oxygen and phosphorus-oxygen local environments and, additionally, we present here a reasonable proposal accounting for the self-assembly mechanism of formation of these hybrid materials.

Experimental Section

Chemicals

All the synthesis reagents are analytically pure and were used as received from Aldrich ($\text{FeCl}_2 \cdot 4\text{H}_2\text{O}$, triethanolamine $[\text{N}(\text{CH}_2\text{-CH}_2\text{-OH})_3$, hereinafter TEA], cetyltrimethylammonium bromide (CTMABr), and phosphoric acid) and Fluka (methylphosphonic acid, 1,2-ethylenediphosphonic acid)

Preparative Procedure

The method is based on the use of a cationic surfactant (CTMABr) as supramolecular template and porogen agent (after template removal), and a hydroalcoholic reaction medium (water: TEA). As commented below, the presence of the complexing polyalcohol is basic in order to harmonize the rates of the hydrolytic reactions of the iron species in water-phosphoric acid media and the subsequent processes of self-assembling among the resulting inorganic polyanions and the surfactant aggregates.

In a typical synthesis leading to sample 3 (a mixed phosphate-phosphonate iron mesoporous material), $\text{FeCl}_2 \cdot 4\text{H}_2\text{O}$ (1.23g) was slowly added at 60° C to a mixture of TEA (33mL) and NaOH (0.56g). The resulting solution was heated under air at 120 °C, and CTMABr (2.25g) was added and solved without apparent alteration. After cooling this solution until 60 °C, it was mixed with methylphosphonic acid (5.80 gr) and water (100 mL). The color of the surfactant-containing solution evolved from green to red as the formation of iron-pseudoatranine complexes (Fe(III) compounds containing TEA-based ligands) advanced³⁰. Finally, H_3PO_4 (5%) was added drop by drop with the help of a burette while controlling the apparent pH value. The solution was gradually decolorized, and we stopped the addition of H_3PO_4 (12.1 mL) as soon as some turbidity was observed (apparent pH value slightly below 6). After a few minutes, a beige colored solid appeared. The resulting suspension was aged at room temperature for 12 h, filtered off, washed with water and ethanol and air dried. The surfactant was chemically extracted from the mesostructured powder with an acetic acid/ethanol solution (*ca.* 1g of powder, 16 mL of acetic acid and 130 mL of ethanol; *t* = 24h, at

room temperature). The final mesoporous material was separated by filtration, washed with ethanol and air dried. A completely equivalent procedure was followed for obtaining solids containing terminal (methylphosphonate) or bridging phosphonates (1,2-ethylenediphosphonic acid). In all cases, the molar ratio of the reagents was adjusted to 0.2 Fe: 7.7 P (H_3PO_4 + Phosphonic acid): 7 TEA: 0.5 NaOH: 0.22 CTMABr: 180 H_2O .

Summarized in Table 1 are the main synthesis variables and physical data concerning the materials prepared in this way: pure iron phosphate (sample 1), mixed iron phosphate-monophosphonate solids (samples 2 to 4), and mixed iron phosphate-diphosphonate derivatives (samples 5 to 7).

Table 1. Selected synthetic and physical data

Sample	Phosphonic acid ^a	Nominal ^b (%)	Real ^c (%)	P/Fe ^d (molar rat.)	d_{100} ^e (nm)	S_{BET} (m^2/g)	BJH pore (nm)	Pore Vol. ^f (cm^3/g)
1	-	0	0	1.37	4.91	377.0	3.18	0.40
2	M	12	15	1.20	5.17	358.9	3.22	0.53
3	M	25	29	1.30	5.29	417.3	3.28	0.56
4	M	75	28	1.31	5.28	459.6	3.30	0.57
5	D	10	15	1.13	5.10	347.3	3.58	0.41
6	D	25	30	1.38	5.22	350.3	3.67	0.50
7	D	50	27	1.30	5.35	306.7	3.94	0.49

^a M = methylphosphonic acid, and D = 1,2-ethylenediphosphonic acid. ^b % of phosphonic acid respect to total P in the mother liquor. ^c % of phosphonate groups respect to total P in the mesoporous solids estimated from CHN analysis. ^d P/Fe molar ratio values from EPMA. ^e d-spacing values from XRD data. ^f Pore size and volume values calculated by using the BJH model on the adsorption branch of the isotherms.

Physical Measurements

All solids were characterized by elemental CNH analysis and electron probe microanalysis (EPMA) using a Philips SEM-515 instrument (to determine Fe and P). P/Fe molar ratio values averaged from EPMA data corresponding to *ca.* 30 different particles of each sample are summarized in Table 1. X-Ray powder diffraction (XRD)

data were recorded on a Seifert 3000TT θ - θ diffractometer using $\text{CuK}\alpha$ radiation. Patterns were collected in steps of $0.02^\circ(2\theta)$ over the angular range 1 - $10^\circ(2\theta)$ for 25 s per step. In order to detect the presence of some crystalline bulk phase, additional patterns were recorded with a larger scanning step ($0.05^\circ(2\theta)$) over the angular range 10 - $60^\circ(2\theta)$ for 10 s per step. TEM images were recorded with a JEOL-JEM-1010 electron microscope operating at 100kV and equipped with digital camera MegaView III and "ANALYSIS" software. Surface area and pore size values were calculated from nitrogen adsorption-desorption isotherms (-196°C) recorded on a Micromeritics ASAP-2020 automated instrument. Porous samples were degassed at 100°C and 10^{-6} Torr prior to analysis. Surface areas were estimated according to the BET model, and pore size dimensions were calculated by using the BJH method. Values obtained are shown in Table 1. Fe-57 Mössbauer spectra were recorded at room temperature in a transmission geometry using a 25 mCi Co-57 source in a Rh matrix in a constant acceleration mode. All the isomer shifts are given relative to metallic Fe. X-ray photoelectron spectra (XPS) were recorded with an Omicron spectrometer equipped with an EA-125 hemispherical electron multichannel analyzer and an unmonochromatized Mg $\text{K}\alpha$ X-ray source having radiation energy of 1253.6 eV. The samples (0.2 mg) were slightly pressed into a small pellet of 15 mm diameter and then mounted on the sample holder. Every sample was introduced into the chamber where they were dried and degassed for 4 h, in order to achieve a dynamic vacuum below 10^{-8} Pa prior to analysis. Spectra of the sample were registered at 300 W and pass energy of 20 eV. Diffuse reflectance (UV-Vis) spectra were measured at room temperature using a Shimadzu UV-Vis 2501PC instrument equipped with an integrated sphere. FTIR spectra were collected on a Nicolet 4700 spectrometer (200 scans with a resolution of 4 cm^{-1}) using self-disks of 1% sample in KBr. Micro-Raman spectra were obtained by means of a HORIBA Jobin Yvon iHR320 spectrometer with Peltier-cooled CCD and a 532 nm doubled YAG laser as excitation. The samples were measured in backscattering geometry at room temperature. A 50x microscope objective was used to focus the excitation laser on the sample and collect the scattered light to the spectrometer. In order to prevent local heating and transformation, laser power varied from 1 to 3 mW. Recording times ranged from 30 to 300 seconds, with 2-10

accumulation scans, depending on the sample. Measurements were carried out directly on the sample with no previous preparation of any kind. The Raman spectra have been corrected for background fluorescence and the base line is shifted for clarity.

Results and Discussion

Synthesis

Difficulties for obtaining iron phosphate related materials in the form of large surface mesoporous solids have been emphasized in previous publications²⁶⁻²⁹. This has also been our experience. Indeed, in view of the potential applicability of such materials^{27,31,32} and the chemical relationships between iron and aluminum, we considered the viability of synthesizing the iron-containing materials by using the same procedure which allowed us to prepare mesoporous ALPO derivatives (from phosphite to phosphate or silico-phosphates and phosphonates, as well as hybrid materials)^{19,18,17,16}. However, when we applied the so-called “atrane route” under the optimized conditions which enabled us to obtain the aluminum derivatives, we failed to synthesize analogous mesoporous iron compounds. After non-negligible effort, we fixed the general experimental conditions as described in the experimental section.

In practice, despite the procedural changes imposed by the nature of the metal, the preparative method reported here retains the main features of the “atrane route”, a simple technique whose details have been discussed elsewhere³³. Thus, together with the participation of a cationic surfactant as template and porogen, the synthetic method implies modulating the hydrolytic reactivity of iron species by the presence of TEA. However, while TEA typically acts as a “hydrolysis-retarding agent” of the metal species owing to the inertness of unstable atrane-complexes^{33,18}, the modulation of the hydrolytic reactivity of iron species has not only a kinetic but also mainly thermodynamic ground. Let us see. TEA displays a great affinity towards Fe(III). Incidentally, it should be noted that in alkaline medium, in the presence of an excess of TEA, the Fe(III)-TEA/Fe(II)-TEA redox couple is strongly reducing³⁴. A variety of truly tripodal (i.e. tetradentate) TEA-based Fe(III) derivatives (ferratranes, from monomers

to clusters) has been isolated and characterized when working in essentially non-aqueous reaction media³⁵⁻³⁸. Also, a Fe(III):TEA=1:2 solid was isolated from stoichiometric amounts of FeCl₃.6H₂O and TEA in water³⁰, although, very likely, the ligand in the resulting solid is not tetradentate³⁹⁻⁴¹. Almost certainly, both the composition and the characteristics of the metal to ligand bonds in the Fe(III)-TEA complex species in aqueous solution can vary with the TEA : Fe(III) ratio. However, even the 1:1 complex (whose formation is highly favored in basic medium) has a stability constant as high as 10^{41.2} 42. This elevated thermodynamic stability explains the well-known use of TEA to mask iron in a diversity of complexometric or gravimetric titrations^{43,44}.

Our preparative procedure starts from non-aqueous alkalinized solutions of Fe(II) in excess of TEA, which are heated under air. Under these conditions, iron species must be readily oxidized without oxide formation, which is consistent with all our experimental results (see below). In any case, whatever is the ultimate nature of the so-formed reactive iron species, the resulting clear solution (in absence of water) will contain, in all likelihood, some type of ferratrane complex. As usual, these solutions are unstable but inert towards hydrolysis. After adding water (in the presence of surfactant), they remain clear but their color progressively turns reddish. At this point lies the main difference with regard to the syntheses of the related aluminum derivatives. In the aluminum case, the addition of aqueous solutions containing the adequate amounts of the H₃PO₄ + phosphonic acid reagent provokes the immediate precipitation of the corresponding mesostructured solid (apparent pH *ca.* 8). In contrast, in the iron case, the oxophosphate species cannot fully displace TEA-like ligands from the comparatively more stable pseudoatrane intermediate^{30,39-41} until “blocking” (protonation) the TEA coordinating ability. Thus, mesostructured solids formation is not observed until apparent pH values slightly lower than 6. Moreover, addition of H₃PO₄ should be done very carefully: once turbidity is appreciated in solution, small excesses of H₃PO₄ cause the complete redissolution of the mesostructured solid (very likely because of the formation of very stable anionic species like [Fe(PO₄)₃]⁶⁻ or [Fe(HPO₄)₃]³⁻)⁴⁵. On the other hand, the fact that the course of the synthesis, on the whole, is largely orchestrated by the organizing function of the

surfactant is evident from the intermediate formation of the mesostructured solids. Furthermore, preparations comparable to those here described carried out in absence of TEA systematically yield non-porous amorphous irrelevant solids. One more time, we can reasonably conclude that the presence of TEA (its capability for giving atrane and/or pseudoatrane complexes) is basic in order to harmonize the rates of the hydrolytic reactions of the metal species and the subsequent processes of self-assembling among the resulting inorganic polyanions and the surfactant aggregates.

In short, TEA initially inhibits the typical hydrolytic reactions of Fe(III), this avoiding the precipitation of oxo-hydroxide solids or the formation of polymeric hexacoordinated $\text{Fe}(\text{O}, \text{OH}, \text{H}_2\text{O})_6$ cationic specie. When acidifying, oxophosphate species⁴⁶ can compete for Fe(III) coordination sites⁴⁵. The dominant oxophosphate species in these conditions in rich aqueous media are $\text{H}_2\text{PO}_4^-/\text{HPO}_4^{2-}$ and $\text{RPO}_3^{2-}/\text{RP}(\text{OH})\text{O}_2^-$. In the presence of a great excess of oxophosphorus-reagents, the formation of iron phosphate and/or iron phosphonate complex anions involving, very likely, the presence of terminal or iron-bridging hydroxyl groups should be favored over the direct condensation of Fe^{3+} ions through hydroxo or oxo bridges⁴⁶. Mesostructure formation, which finally is observed at apparent pH values around 6, should occur when the advance of the anionic condensation yield Fe-phosphate/phosphonate oligomers adequate (similar charge density distribution) for matching with CTMA^+ micellar aggregates.

Characterization

We have used EPMA to check the chemical homogeneity of the resulting solids. Summarized in Table 1 are the corresponding P:Fe molar ratio values (averaged from data of *ca.* 30 different particles). EPMA shows that all samples are chemically homogeneous at micrometric level (spot area *ca.* $1\mu\text{m}$) with a constant and well-defined composition. In all cases, the solids present P:Fe molar ratio values (*ca.* 1.30 ± 0.10) somewhat higher than the 1:1 typical of stoichiometric ALPOs. Notwithstanding, the relatively low deviation from such idealized composition suggests that all these solids may be basically regarded as iron-phosphate/phosphonate derivatives rather than consisting, to a significant degree, of FeO_x oxidic domains connected through

phosphate or organophosphorus moieties (as might suggest the above mentioned result [P:Fe=0.47] referred to the dodecyl templated oxophenyl-phosphate material)²⁸. On the other hand, the iron defective compositions must be consistent with the need for a certain net negative charge on the material pore walls in order to allow an adequate matching with cationic surfactant portions yielding the intermediate mesostructured nets. In any case, both the high-angle XRD patterns and spectroscopic results in this work (see below) clearly show that there is no segregation of crystalline or amorphous bulk phases (FeO_x domains) in our materials. From these observations, together with the impossibility to condense phosphate, phosphonate and/or diphosphonate groups among them (originating P-O-P links) in aqueous media, it seems reasonable to propose that all the synthesized mesoporous materials display regular distributions of the Fe and P atoms along the pore walls at micrometric level.

Elemental CNH analysis results reveal that all the mesoporous solids are exempt from nitrogen, which confirms the efficiency of the surfactant extraction soft-procedure we have used. Therefore, CNH analysis allows estimating unambiguously the content of organophosphorus groups in the final mesoporous materials (see Table 1). The phosphonate: phosphate stoichiometric-ratio in the final materials (whether they contain terminal phosphonates or bridging diphosphonate species) only is close to that present in the mother liquor for nominal proportions of organic-phosphorus reagents around 25% (samples 3 and 6). As can be noted, with regard to the reagent proportions, the real phosphonate incorporation to the mesostructure increases for organic-phosphorus reagent contents lower than 25% (samples 2 and 5), while the contrary occurs when the organic reagent proportion exceeds such 25% value (samples 4 and 7). In practice, the real phosphonate incorporation to the mesostructure seems to be limited at values around 30% (what occurs even starting from nominal phosphonate: phosphate proportions as high as 50% -sample 7- or 75% -sample 4-). In contrast to that observed for organically modified mesoporous ALPOs (which showed a clear preference for phosphate vs. phosphonate incorporation when monophosphonate groups were involved)^{17,18}, in the present case we cannot appreciate any significant difference concerning phosphonate incorporation related to its functionality (mono or diphosphonate species). Also, in the case of the iron

derivatives we are dealing with, it has been not possible obtaining pure mesoporous mono or diphosphonates (i.e. only the pure phosphate or hybrid phosphate-phosphonate materials result). It seems reasonable to assume that such differences should be accounted for based on the different chemistry of the concerned metals (Fe vs. Al). Now, taking into account the synthetic route (cationic template, comparatively low apparent pH values) and the stoichiometric restrictions (according to the analytical results) for achieving the necessary electroneutrality in the intermediate mesostructures, all indicates that iron exhibits an ability lower than aluminum for constructing (in a cooperative way with phosphonate entities) negatively-charged networks capable of coupling with positively-charged surfactant aggregates. In practice, in the case of ALPOs, both phosphate (with variable proportions of protonated and unprotonated units) and OH^- groups can modulate the charge on aluminum centers allowing further phosphonate incoming to yield anionic skeletons^{18,17}. As we shall comment, it is the participation of OH^- ligands which seems to be restricted for the iron derivatives under our experimental conditions, which, in turn, reduces the chances for compensating the charge of the iron centers.

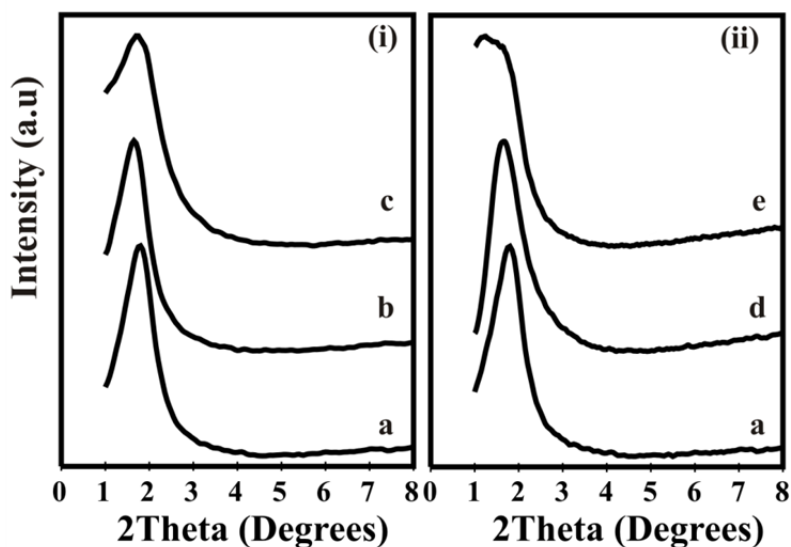


Figure 1. XRD patterns of selected mesostructured (i) and mesoporous (ii) samples: (a) Sample 1, (b) Sample 3 and (c) Sample 6.

Shown in Figure 1 is the evolution of the low-angle XRD patterns with the phosphonate or diphosphonate content in the solids. All solids display XRD patterns with only a single and strong diffraction peak, which is typical of mesostructured/mesoporous materials prepared through surfactant-assisted procedures⁹. This peak is usually associated with the (100) reflection when a MCM-41-like lattice is assumed^{9,8}. The absence of additional signals indicates that ordered domains are not present. These features are characteristic of disordered hexagonal (H_d) or wormhole-like pore systems. Also, the d_{100} reticular distance (and consequently the a_0 cell parameter) slightly increases with the phosphonate or diphosphonate content (see Table 1). This is not a surprising result. In fact, as phosphate/phosphonate substitution progress, one obtains a larger molecular volume and a smaller net connectivity, both factors favoring a lower density of the substituted material. The experimentally observed smooth variation of the broadness and position of the peak, in both series of materials, allows a certain character of “solid solutions” to be recognized in them in the 0-30% content range.

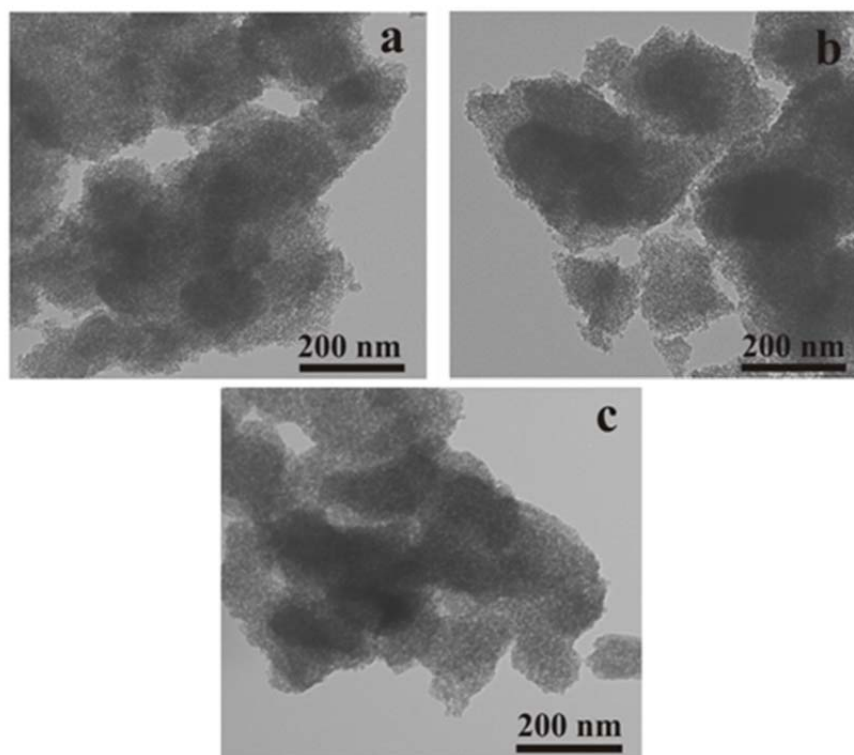


Figure 2. Representative TEM images of mesoporous materials: (a) Sample 1, (b) Sample 3 and (c) Sample 6.

The information from TEM images fully correlates with XRD observations (Figure 2). A similar morphology of aggregates of mesoporous particles (with sizes in the 0.1-0.2 μm range) is observed regardless the phosphate/phosphonate proportion or phosphonate type. The observation in all cases of a dominant (single-type) particle morphology (with highly disordered hexagonal or wormhole-like intra-particle mesopore system arrays) supports the monophasic nature of the final solids, and allows discarding phase-segregation processes.

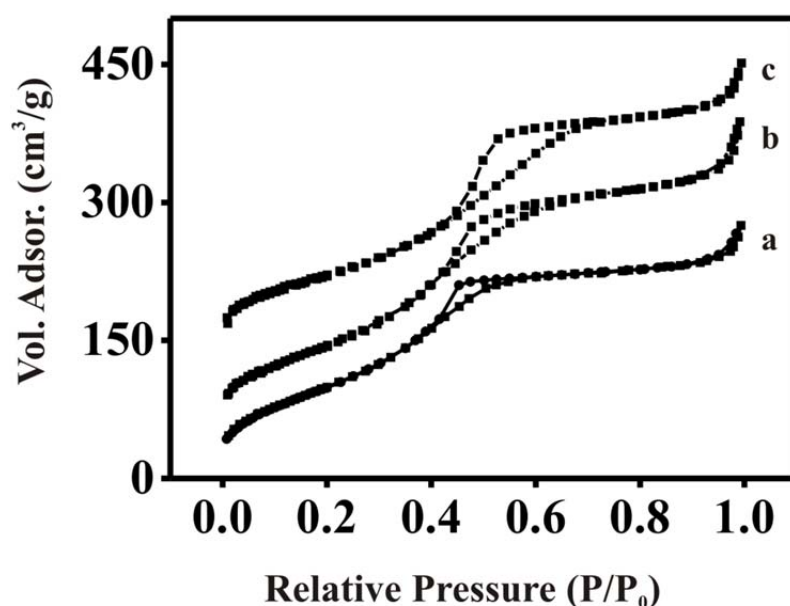


Figure 3. N_2 adsorption-desorption isotherms of (a) Sample 1, (b) Sample 3 and (c) Sample 6.

Mesoporosity is further illustrated by the N_2 adsorption-desorption isotherms (Figure 3). In all cases, the curves show one well-defined step at intermediate partial pressures ($0.3 < P/P_0 < 0.8$) characteristic of type IV isotherms with an H1 small hysteresis loop (as defined by the IUPAC). This adsorption should be due to the capillary condensation of N_2 inside the intra-particle mesopores. Moreover, the sharpness of this step indicates the uniformity of the mesopores (see Table 1; the BJH pore size distribution curves -centered at around 3-4 nm- expand from *ca.* 2.5-4.5 nm, and t-plot analyses also are consistent with the practical absence of micropores). In

addition, all isotherms display a second (and relatively small) adsorption effect at higher relative partial pressures which should be associated to the filling of the large textural inter-particle voids. The progressive incorporation of phosphonate groups does not modify drastically the BET surface area values (see Table 1). Also, the pore sizes and volumes (estimated by using the absorption branch of the isotherms and applying the BJH model) only grow smoothly with the phosphonate inclusion (see Table 1).

In short, dealing with the mesoscale architecture, the TEA induced preparation of pure iron phosphate yields a material displaying BET area and BJH pore size and volume values larger than those previously reported for analogous solids synthesized through other surfactant assisted procedures²⁶⁻²⁸. A similar comment can be made with regard to the hybrid phosphate/phosphonate derivatives. Moreover, in these last cases, the P:Fe molar ratios (iron defective) do not substantially diverge from the 1:1 ideal stoichiometry, which supports the idea of a good dispersion of P and Fe sites along the mesopore walls.

It has been previously noted that final performance of mesoporous iron phosphate derivatives in a variety of processes should be attributed to not only their morphological features but also their specific local structures²⁷. So, we have applied a diversity of techniques looking for gain insight about the short range iron-oxygen and phosphorus-oxygen environments in these almost amorphous materials. ⁵⁷Fe Mössbauer spectroscopy offers us relevant information concerning the metal sites. Shown in Figure 4 are the room-temperature spectra corresponding to some selected samples.

The results of fitting the spectra using the NORMOS software are gathered in Table 2. Discrimination between octahedral and tetrahedral iron environments can be achieved on the basis of the isomer shift (IS) values. Thus, at room temperature, a IS value of 0.3 mm/s is accepted as frontier between tetrahedral (IS < 0.3 mm/s) and octahedral (IS > 0.3 mm/s) geometries⁴⁷. In the case we are dealing with, regardless the type of phosphonate or its proportion, the spectra of all samples can be fitted with two doublets. First at all, the values of the isomer shift (IS) and the relatively narrow quadrupolar splitting (QS) values are indicative of the presence of only Fe³⁺ in these

samples^{47,48}. There is no hint of Fe²⁺. Also, in all cases, the respective isomer shift values obtained for the two doublets are slightly lower than 0.3 and 0.5 mm/s. According to the above, this suggests the coexistence of both tetrahedral and octahedral iron environments. On the other hand, the results of fitting show that octahedral sites seem to be slightly dominant in all samples, with relative proportions in the *ca.* 54-64% range. In addition, the relative great width (Γ) of the spectra, larger than the instrumental one (0.28 mm/s), indicates that iron atoms are located in distorted positions that vary from position to position. A priori, this might be a predictable outcome taking into account the amorphous nature of the mesopore walls.

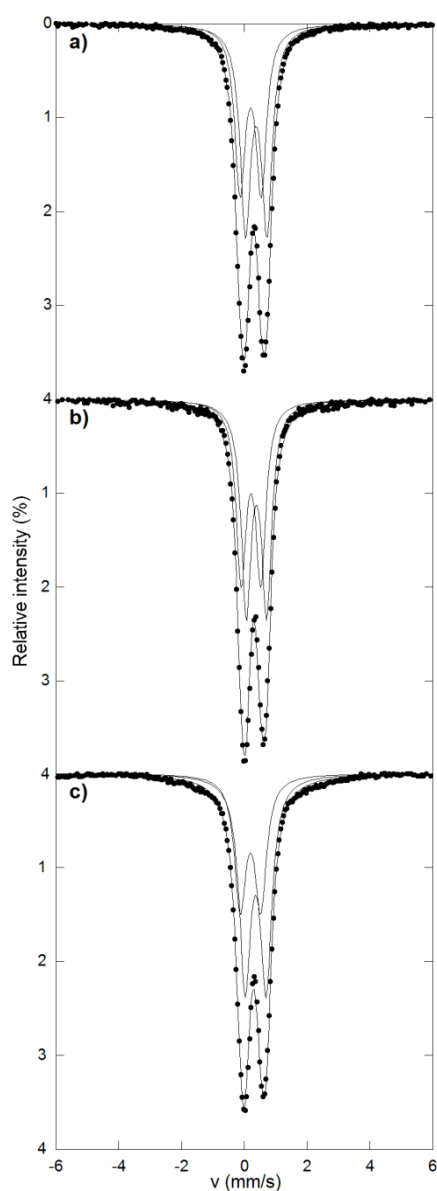


Figure 4. Fitted Mössbauer spectra of (a) Sample 1, (b) Sample 3 and (c) Sample 6.

Table 2. Hyperfine parameters of the measured samples: full width at half maximum (Γ), isomer shift (δ), quadrupolar splitting (Δ) and relative area (A).

Sample	Tetrahedral Fe ³⁺				Octahedral Fe ³⁺		
	Γ (mm/s)	δ (mm/s)	Δ (mm/s)	Area (%)	δ (mm/s)	Δ (mm/s)	Area (%)
1	0.40±0.01	0.31±0.01	0.67±0.01	45±1	0.49±0.01	0.68±0.01	55±1
2	0.40±0.01	0.28±0.01	0.65±0.01	36±1	0.47±0.01	0.69±0.01	64±1
3	0.38±0.01	0.32±0.01	0.63±0.01	46±1	0.49±0.01	0.65±0.01	54±1
5	0.41±0.01	0.29±0.01	0.67±0.01	39±1	0.48±0.01	0.68±0.01	61±1
6	0.43±0.01	0.30±0.01	0.65±0.01	39±1	0.47±0.01	0.67±0.01	61±1

The presence of both tetrahedral and octahedral iron sites is further illustrated by UV-Vis spectroscopy (see Supplementary information) and XPS measurements (see Figure 5). The Fe 2p spectra measured by XPS in these samples show a spin-orbit doublet characteristic of oxidized Fe, in which the more prominent feature, the $J = 3/2$ component (being J the total angular momentum) appears at binding energies of 712.5 ± 0.2 eV irrespective of the sample, accompanied with a $J=1/2$ component with a spin-orbit splitting of 13.9 eV^{49,50}. The characteristic satellite of the $2p_{3/2}$ peak around 718 eV is not well resolved due to the main peaks broadening, as expected because of the amorphous nature of the pore walls. No appreciable differences are observed in the spectra of any of the final mesoporous materials (pure phosphate and mixed phosphate-phosphonates). The experimental binding energy values are very close to those previously reported for iron phosphates and oxides combining different proportions of tetrahedral and octahedral Fe³⁺ environments^{49,27}. In contrast, the center of gravity of the Fe $2p_{3/2}$ signal appears shifted to binding energy values slightly lower than those reported for materials including only octahedral Fe-environments (BE of 712.3 eV)⁴⁸. In addition, the low intensity of the $2p_{3/2}$ satellite peak also supports the presence of Fe³⁺ tetrahedral environments^{49,50}.

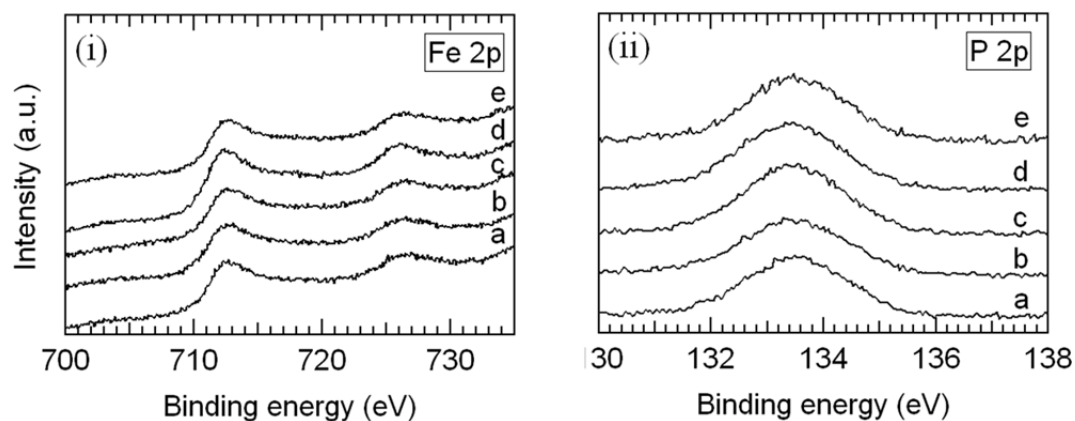


Figure 5. XPS spectra of (i) Fe2p and (ii) P2p. (a) Sample 1, (b) Sample 2, (c) Sample 3, (d) Sample 5, and (e) Sample 6.

The presence of paramagnetic iron species hinders using NMR techniques, which were extremely useful for characterizing the local structure at the anionic counterparts (phosphate and phosphonate moieties) in the case of the related organically modified pure mesoporous ALPOs^{19,18,17}. Then, besides XPS, we have resorted to other spectroscopic techniques (IR, Raman) for better understanding of the nature and organization of the anionic portions (i.e. the local structure around phosphorus atoms). Figure 5 shows the P 2p XPS spectra of some selected samples. The P 2p spectra measured by XPS show a broad peak centered at 133.5 eV in all samples. Spin-orbit deconvolution of these peaks (not shown) indicates that the P 2p spectra appear to be composed by a unique spin-orbit doublet whose $J=3/2$ component is located at 133.1 ± 0.1 eV and the $J=1/2$ component at 134.1 ± 0.1 eV, with an intensity ratio given by the relative $2J+1$ degeneracy of the states. It has to be noted that, although the P 2p signal really consist of a doublet with $2p_{1/2}$ and $2p_{3/2}$ components, the low energy separation between them often leads to consider the P 2p signal as a single peak⁴⁹. The binding energy of P 2p in iron phosphates is usually centered at 134.1 eV⁴⁹. In comparison, the phosphorus peak corresponding to our mesoporous materials shifts to a lower energy (*ca.* 133.5 eV) (Table 3). According to the literature data^{51,27,52}, such a lowering of the binding energy of P 2p can be attributed to the effective presence in the materials of a certain proportion of HPO₄²⁻

sites. On the other hand, the analysis of the O 1s XPS peaks provides additional information useful for discriminating P-O-Fe and P-OH species⁴⁹.

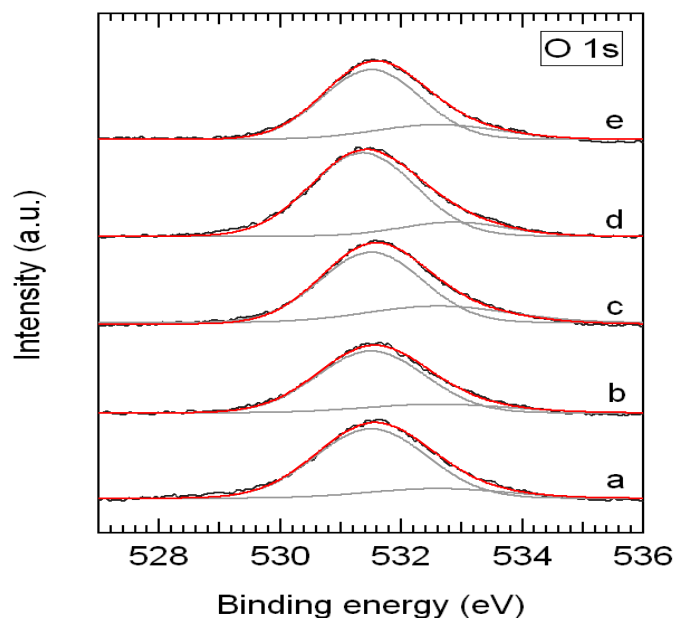


Figure 6. XPS spectra of O1s. (a) Sample 1, (b) Sample 2, (c) Sample 3, (d) Sample 5, and (e) Sample 6.

Figure 6 displays the XPS spectra of the O 1s region for some selected samples. The binding energies of P-O-Fe or Fe-OH, and P-OH species typically appear in the 531.3-532.1 and 532.6-533.6 eV ranges, respectively⁴⁹. Regardless the proportion and/or nature of the phosphonate entities, the O 1s spectra measured by XPS appear to be composed by a singlet located at 531.5 ± 0.1 eV accompanied with a less intense peak located at 532.6 ± 0.1 eV. Therefore, the fitting of our spectra have been carried out with two peaks: 531.5 eV (attributed to P-O-Fe and Fe-OH entities), and 532.6 eV (P-OH). The absence of signals at around 530 eV provides additional evidence over the nonexistence of segregated FeO_x domains⁴⁹. The area of the P-OH signal at 532.6 eV slightly increases with the phosphonate content, but in a rough way, a relative average area of *ca.* 19% (of the total signal) is computed in all the spectra (i.e. the weighted relationship between the 531.5 and 532.6 eV signals is nearly constant in all cases and close to *ca.* 4.25). In absence of water molecules (precluded by the high vacuum conditions during the measurements), and assuming that to ensure network connectivity only one oxygen atom (at most) per phosphate group might be

protonated (i. e. contributing to the 532.6 eV signal), it is straightforward to infer (apart from Fe-OH, contributions to the 531.5 eV signal should come from three P-O-Fe bonds per each P-OH unit plus four or three P-O-Fe bonds per each unprotonated-phosphate or phosphonate group, respectively) that the *ca.* 4.25 weighted relationship between the signal areas would correspond to a $\text{HPO}_4^{2-}/(\text{PO}_4^{3-} + \text{phosphonate})$ minimum proportion of *ca.* 3:2 in all our materials. IR and Raman spectroscopies offer additional evidences confirming the presence of protonated HPO_4^{2-} species in the mesoporous material frameworks (see Supplementary information).

Table 3. O1s XPS spectra deconvolution data.

Sample	Signal at 531.5±0.1 eV Intensity (%)	Signal at 532.6±0.1 eV Intensity (%)
1	85	15
2	83	17
3	77	23
5	86	14
6	80	20

Having reached this point, gathering all the available information (from the analytical data to the results obtained from the different structural techniques applied), we have considered interesting to make a reasonable proposal dealing with the approximate nominal “stoichiometries” in this family of iron mesoporous phosphate/phosphonate hybrid materials. With this aim, it is mandatory not only to preserve the analytical data but calculations also have to be based on the need to achieve the network electroneutrality. Actually, dealing with anhydrous samples, all our above considerations would finally fit with the following “ideal stoichiometric” formulations: 1) $[\text{Fe}_{\text{Td}}]_{0.4}[(\text{Fe}_{\text{Oh}})_{0.6}(\text{OH})_x][(\text{HPO}_4)_{0.75+x}(\text{PO}_4)_{0.5-x}]$ ($x \leq 0.15$) for the pure phosphate (sample 1); 2) $[\text{Fe}_{\text{Td}}]_{0.4}[(\text{Fe}_{\text{Oh}})_{0.6}(\text{OH})_x][(\text{HPO}_4)_{1-y}(\text{CH}_3\text{PO}_3)_y]_{0.75+x}(\text{PO}_4)_{0.5-x}]$ ($x \leq 0.15$; $y \leq 0.50$) for hybrid materials containing terminal monophosphonate entities (samples 2-4); and 3) $[\text{Fe}_{\text{Td}}]_{0.4}[(\text{Fe}_{\text{Oh}})_{0.6}(\text{OH})_x][(\text{HPO}_4)_{1-2y}(\text{O}_3\text{P-CH}_2\text{-CH}_2\text{-PO}_3)_y]_{0.75+x}(\text{PO}_4)_{0.5-x}]$ ($x \leq 0.15$; $y \leq 0.25$) for solids containing diphosphonate groups (samples 5-7). Taking into account that ensuring network connectivity would preferably favor the location of hydrogenphosphate, phosphonate and hydroxide groups on the material surface (with OH and R groups oriented towards the pore voids), such idealized formula should be

consistent with core walls of these materials built up mainly from 3D alternating Fe_{Td} and phosphate groups (i.e. our materials might be thought of as consisting of verlinite-type cores extending to the surface through Fe_{Oh} species).

Formation mechanism

In the absence of ion mediated species at the surfactant-iron phosphate/phosphonate interface (EDAX results show that no chlorine ions are incorporated to the materials), the mesostructured parent-solids of this family of mesoporous hybrids constitute an example of surfactant-templated materials formed through an S^+I^- ionic mechanism¹⁰. The charge matching at the interface must occur between cationic surfactant aggregates and anionic Fe-phosphate and/or Fe-phosphate/phosphonate based moieties. Thus, the Fe-phosphate/phosphonate walls must retain a certain negative net-charge allowing the assembly of the intermediate mesostructured materials. On the basis of the data already discussed, it seems reasonable to propose that the Fe-phosphate/phosphonate walls are able to compensate the positive surfactant charge through two cooperative mechanisms implying formal deprotonation of hydrogenphosphate and hydroxide groups. The presence of $\equiv\text{P-O}^-$ units (connected to iron atoms) and Fe-O^- entities (corresponding to octahedral iron sites at the wall surface) would allow neutralizing the charge of one CTMA^+ cation per each $\equiv\text{P-O}^-$ or Fe-O^- group. The surfactant evolution, through chemical exchange under acid conditions (CTMA^+/H^+), would subsequently result in the protonation of these sites in the final mesoporous materials.

Up to now, there is nothing in the proposed mechanism different from that assumed for explaining the formation of analogous mesoporous ALPO_5 ^{19,18,17}. However, in the case of ALPO_5 , it was found that formal replacement of phosphate by phosphonate groups can progress in a continuous way until completion (100%), that is to say until yielding pure mesoporous aluminum phosphonates (whereas maximum phosphonate incorporation into the iron derivatives we are dealing with only attains a *ca.* 30%). What happens in the case of aluminum is that the progressive replacement of phosphate groups (which occurs in moderately basic media) is accompanied by a simultaneous increase of the proportion of octahedral vs. tetrahedral Al sites (*ca.* 90%

in the pure phosphonates). Thus, although hydrogenphosphate groups (and consequently $\equiv\text{P-O}^-$ units) are not available in phosphonates, the charge matching with surfactant aggregates is accounted for at expense from the increase in Al-O $^-$ groups (Al-octahedral sites). Herein lies the main difference with the case at hand: the Fe_{Oh}:Fe_{Td} ratio in the iron derivatives remains practically constant (around 60:40%; with a relatively low proportion of Fe-OH units) regardless the phosphonate group content. This observation very likely is in the origin of the limited phosphonate incorporation to the mesostructures. In fact, hypothetically higher proportions of phosphonate units could lead to low-charged hybrid oligomers inadequate for matching with the surfactant micelles. The small proportions of octahedral sites (in comparison with the aluminum case) and, even more, Fe-OH units might be explained on the basis of the need for attaining relatively acid media in which the phosphate/phosponate groups can advantageously compete with TEA-like ligands. In turn, in these conditions (low OH $^-$ availability), the ready coordination of iron by phosphate-type groups would seriously limit the efficacy of OH species as ligands.

Concluding remarks

In conclusion, high surface area mesoporous iron phosphate and phosphate/phosphonate hybrid materials have been synthesized through a generalized one-pot procedure by using a cationic surfactant as co-assembling template. All our experimental results indicate that the final solids possess a well-established oxo-phosphate-based mesostructure, without segregation of metal oxide domains. The seemingly favored verlinite-like arrangement in the mesostructure core hinders the obtaining of pure phosphonate materials analogous to those previously synthesized by the atrane route in the aluminium case.

Acknowledgment

This research was supported by the Ministerio de Economía y Competitividad (MAT2009-14564-C04-04, MAT2010-20129-C02-02 and MAT2012-38429-C04-03) and the Generalitat Valenciana (PROMETEO/2009/108). Financial support from the Spanish CICYT and Basque Government under Grants MAT2012-37923 and IT-443-40 is appreciated. J.E.H. and S.M.M. thank the Fundació General de la Universitat de València for financial support. A.M. thanks MEC for a FPI fellowship. M. B.-G. thanks Generalitat Valenciana for financial support. Authors thank Val-Space Consortium the use of their installations at the Valencia University.

Appendix A. Supplementary data

Supplementary data associated with this article can be found, in the online version, at <http://dx.doi.org/10.1016/j.micromeso.2013.12.015>.

References

1. Tanev, P. T.; Butruille, J. R.; Pinnavaia, T. J. *Chemistry of Advanced Materials* **1998**, 329-388.
2. Cheetham, A. K.; Ferey, G.; Loiseau, T. *Angewandte Chemie-International Edition* **1999**, 38, 3268-3292.
3. Breck, D. W. *Zeolite Molecular Sieves: Structure, Chemistry and Use*: New York, 1973.
4. Wang, Z.; Yu, J.; Xu, R. *Chemical Society Reviews* **2012**, 41, 1729-1741.
5. Wilson, S. T.; Lok, B. M.; Messina, C. A.; Cannan, T. R.; Flanigen, E. M. *Abstracts of Papers of the American Chemical Society* **1982**, 184, 6-INOR.
6. Yu, J. H.; Xu, R. R. *Accounts of Chemical Research* **2003**, 36, 481-490.
7. Hartmann, M.; Kevan, L. *Chemical Reviews* **1999**, 99, 635-663.
8. Kresge, C. T.; Leonowicz, M. E.; Roth, W. J.; Vartuli, J. C.; Beck, J. S. *Nature* **1992**, 359, 710-712.
9. Kresge, C. T.; Roth, W. J. *Chemical Society Reviews* **2013**, 42, 3663-3670.
10. Soler-illia, G. J. D.; Sanchez, C.; Lebeau, B.; Patarin, J. *Chemical Reviews* **2002**, 102, 4093-4138.
11. Schuth, F. *Chemistry of Materials* **2001**, 13, 3184-3195.
12. Rojo, T.; Luis Mesa, J.; Lago, J.; Bazan, B.; Luis Pizarro, J.; Isabel Arriortua, M. *Journal of Materials Chemistry* **2009**, 19, 3793-3818.
13. Shimizu, G. K. H.; Vaidyanathan, R.; Taylor, J. M. *Chemical Society Reviews* **2009**, 38, 1430-1449.
14. Ma, T.-Y.; Yuan, Z.-Y. *ChemSuschem* **2011**, 4, 1407-1419.
15. Gagnon, K. J.; Perry, H. P.; Clearfield, A. *Chemical Reviews* **2012**, 112, 1034-1054.
16. Cabrera, S.; El Haskouri, J.; Guillem, C.; Beltran-Porter, A.; Beltran-Porter, D.; Mendioroz, S.; Marcos, M. D.; Amoros, P. *Chemical Communications* **1999**, 333-334.
17. El Haskouri, J.; Guillem, C.; Latorre, J.; Beltran, A.; Beltran, D.; Amoros, P. *European Journal of Inorganic Chemistry* **2004**, 1804-1807.
18. El Haskouri, J.; Guillem, C.; Latorre, J.; Beltran, A.; Beltran, D.; Amoros, P. *Chemistry of Materials* **2004**, 16, 4359-4372.
19. El Haskouri, J.; Perez-Cabero, M.; Guillem, C.; Latorre, J.; Beltran, A.; Beltran, D.; Amoros, P. *Journal of Solid State Chemistry* **2009**, 182, 2122-2129.
20. Lii, K. H.; Huang, Y. F.; Zima, V.; Huang, C. Y.; Lin, H. M.; Jiang, Y. C.; Liao, F. L.; Wang, S. L. *Chemistry of Materials* **1998**, 10, 2599-2609.
21. Song, Y. N.; Zavalij, P. Y.; Suzuki, M.; Whittingham, M. S. *Inorganic Chemistry* **2002**, 41, 5778-5786.
22. Kang, B.; Ceder, G. *Nature* **2009**, 458, 190-193.

23. Zhang, T.; Lu, Y.; Luo, G. *Industrial & Engineering Chemistry Research* **2013**, *52*, 6962-6968.
24. Moore, P. B. *American Mineralogist* **1970**, *55*, 135-169.
25. Moore, P. B.; Shen, J. *Nature* **1983**, *306*, 356-358.
26. Guo, X. F.; Ding, W. P.; Wang, X. G.; Yan, Q. J. *Chemical Communications* **2001**, 709-710.
27. Yu, D.; Wu, C.; Kong, Y.; Xue, N.; Guo, X.; Ding, W. *Journal of Physical Chemistry C* **2007**, *111*, 14394-14399.
28. Mal, N. K.; Bhaumik, A.; Matsukata, M.; Fujiwara, M. *Industrial & Engineering Chemistry Research* **2006**, *45*, 7748-7751.
29. Zhu, S. M.; Zhou, H. S.; Hibino, M.; Honma, I. *Chemistry Letters* **2004**, *33*, 774-775.
30. Naiini, A. A.; Young, V.; Verkade, J. G. *Polyhedron* **1995**, *14*, 393-400.
31. Pillai, U. R.; Sahle-Demessie, E. *Chemical Communications* **2004**, 826-827.
32. Zhang, X.-X.; Tang, S.-S.; Chen, M.-L.; Wang, J.-H. *Journal of Analytical Atomic Spectrometry* **2012**, *27*, 466-472.
33. Cabrera, S.; El Haskouri, J.; Guillem, C.; Latorre, J.; Beltran-Porter, A.; Beltran-Porter, D.; Marcos, M. D.; Amoros, P. *Solid State Sciences* **2000**, *2*, 405-420.
34. Wen, Y. H.; Zhang, H. M.; Qian, P.; Zhou, H. T.; Zhao, P.; Yi, B. L.; Yang, Y. S. *Electrochimica Acta* **2006**, *51*, 3769-3775.
35. Saalfrank, R. W.; Bernt, I.; Uller, E.; Hampel, F. *Angewandte Chemie-International Edition in English* **1997**, *36*, 2482-2485.
36. Ali, A. E. *Egyptian Journal of Chemistry* **2005**, *48*, 121-127.
37. Jones, L. F.; Jensen, P.; Moubaraki, B.; Berry, K. J.; Boas, J. F.; Pilbrow, J. R.; Murray, K. S. *Journal of Materials Chemistry* **2006**, *16*, 2690-2697.
38. Panapoy, M.; Duangdee, C.; Laobuthee, A.; Ksapabutr, B. *Songklanakarin Journal of Science and Technology* **2009**, *31*, 541-545.
39. Sen, B.; Dotson, R. L. *Journal of Inorganic & Nuclear Chemistry* **1970**, *32*, 2707-&.
40. Icbudak, H.; Yilmaz, V. T.; Howie, R. A.; Andac, O.; Olmez, H. *Acta Crystallographica Section C-Crystal Structure Communications* **1995**, *51*, 1759-1761.
41. Icbudak, H.; Yilmaz, V. T.; Olmez, H. *Thermochimica Acta* **1996**, *289*, 23-32.
42. Ringbom, A. **Complexation in Analytical Chemistry. A Guide for the Critical Selection of Analytical Methods Based on Complexation Reactions**; Interscience Publishers, a Division of John Wiley & Sons: New York-London, 1963.
43. Laitinen, H. A.; Harris, W. E. *Chemical Analysis*, second ed. ed., 1975.
44. Harris, D. C. *Quantitative Chemical Analysis*, seventh ed. ed.: New York, 2007.
45. Nicholls, D.; Press, P. Ed.: Oxford, 1973.
46. Flynn, C. M. *Chemical Reviews* **1984**, *84*, 31-41.

47. Tuel, A.; Arcon, I.; Millet, J. M. M. *Journal of the Chemical Society-Faraday Transactions* **1998**, *94*, 3501-3510.
48. Raj, A.; Sivasanker, S.; Lazar, K. *Journal of Catalysis* **1994**, *147*, 207-213.
49. Daou, T. J.; Begin-Colin, S.; Greneche, J. M.; Thomas, F.; Derory, A.; Bernhardt, P.; Legare, P.; Pourroy, G. *Chemistry of Materials* **2007**, *19*, 4494-4505.
50. Yamashita, T.; Hayes, P. *Applied Surface Science* **2008**, *254*, 2441-2449.
51. Fujii, T.; de Groot, F. M. F.; Sawatzky, G. A.; Voogt, F. C.; Hibma, T.; Okada, K. *Physical Review B* **1999**, *59*, 3195-3202.
52. Annapragada, A. V.; Gulari, E. *Journal of Catalysis* **1990**, *123*, 130-146.

Mesoporous iron phosphate/phosphonate hybrid materials

Supplementary Information

Jamal El Haskouri, Alaina Moragues, Aurelio Beltrán, Sonia Murcia-Mascarós,
Fernando Plazaola, Estibaliz Legarra, Adela Mauri-Aucejo, Mauro Brotons-
Gisbert, Juan F. Sánchez-Royo, Daniel Beltrán and Pedro Amorós

Materials characterization: UV-Vis spectroscopy

Shown in Figure S1 are the UV-Vis spectra of some selected samples. In all cases, the spectra of the final mesoporous materials show intense bands in the UV region (in the 250-300 nm range), this accounting for the Laporte allowed ligand-to-metal charge-transfer transitions ($t_1 \rightarrow t_2$ and $t_1 \rightarrow e$) involving Fe^{3+} in $[\text{FeO}_4]$ pseudo-tetrahedral topologies¹. Moreover, the significant adsorption tail in the 300-350 nm range is also indicative of the presence of quasi-octahedral iron environments². At this point, it has to be noted that none of the samples originate appreciable absorption at $\lambda > 350$ nm, this sustaining again that all the samples are exempt from extra-framework FeO_x domains³.

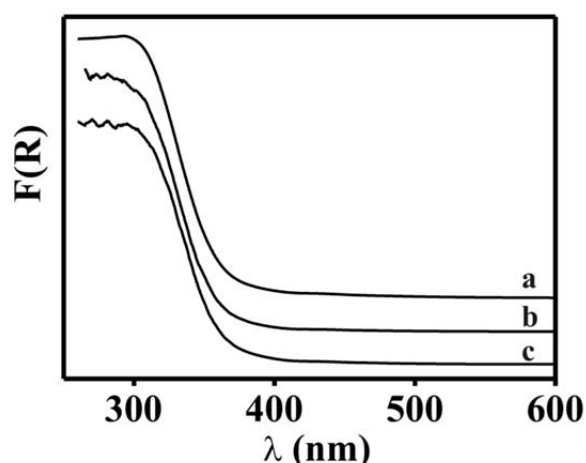


Figure S1. UV-Vis Spectra of (a) Sample 1, (b) Sample 3 and (c) Sample 6.

Materials characterization: FT-IR and RAMAN spectroscopy

Shown in Figure S2 are the FT-IR spectra of some selected samples. Regardless the type and content of phosphonate entities, all spectra display an intense and broad band centered at *ca.* 1059 cm^{-1} which has a clear shoulder at *ca.* 900 cm^{-1} . Such an intense band and the shoulder can be assigned to symmetric P-O stretching modes from PO_4^{3-} and HPO_4^{2-} groups, respectively⁴. The band tail at *ca.* $1150\text{-}1200\text{ cm}^{-1}$ could

be attributed to the OH in plane deformation of HPO_4^{2-} groups^{4,5}. The incorporation of phosphonate entities (samples 2 to 7) is evident from the high energy zone of the IR spectra. Thus, the spectra show now two characteristic (although weak) bands at *ca.* 2868 and 2926 cm^{-1} associable to C-H stretching vibration modes. As expected, the structure of the bands in the OH stretching spectral region (typically 3500-3200 cm^{-1}) is very complex, but the effect appearing around 3436 cm^{-1} has been previously attributed to P-OH stretching vibrations in related mesoporous iron phosphates⁶. In a similar way, the Raman spectra show an intense and broad band centered at *ca.* 1010 cm^{-1} , with two shoulders at 890 and 1175 cm^{-1} . These bands can be assigned to P-O stretching vibrations of PO_4^{3-} and HPO_4^{2-} groups^{4,7,8}. In fact, our Raman spectra are very similar to that previously reported in the reference 9⁹ for a related mesoporous iron phosphate, compound for which the authors concluded the presence of HPO_4^{2-} groups as majority anionic species.

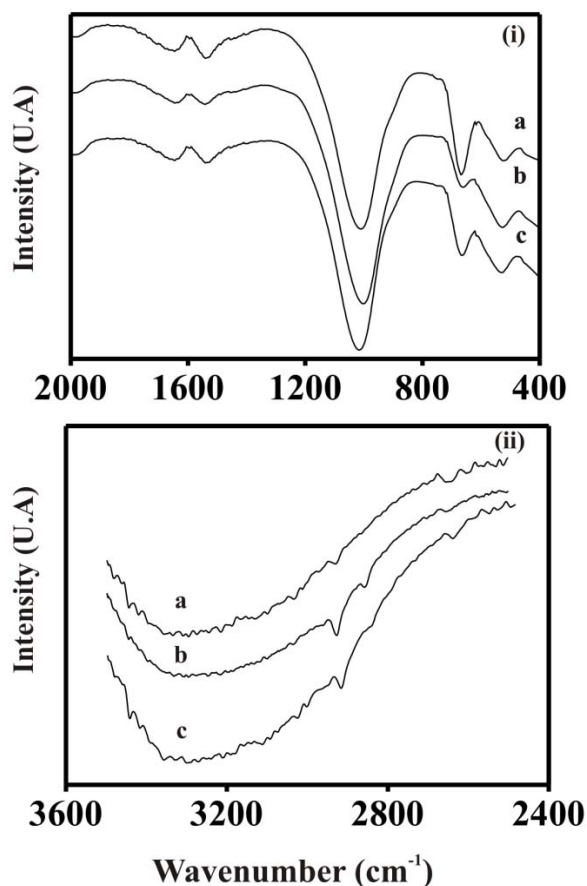


Figure S2. FT-IR spectra of (a) Sample 1, (b) Sample 3 and (c) Sample 6.

References

1. Selvam, P.; Mohapatra, S. K. *Journal of Catalysis* **2006**, *238*, 88-99.
2. Samanta, S.; Giri, S.; Sastry, P. U.; Mal, N. K.; Manna, A.; Bhaumik, A. *Industrial & Engineering Chemistry Research* **2003**, *42*, 3012-3018.
3. Gurgul, J.; Latka, K.; Hnat, I.; Rynkowski, J.; Dzwigaj, S. *Microporous and Mesoporous Materials* **2013**, *168*, 1-6.
4. Frost, R. L.; Xi, Y.; Pogson, R. E.; Millar, G. J.; Tan, K.; Palmer, S. J. *Journal of Raman Spectroscopy* **2012**, *43*, 571-576.
5. Farmer, V. C. ***Mineralogical Society Monograph 4: The Infrared Spectra of Minerals***, 1974.
6. Mal, N. K.; Bhaumik, A.; Matsukata, M.; Fujiwara, M. *Industrial & Engineering Chemistry Research* **2006**, *45*, 7748-7751.
7. Frost, R. L.; Xi, Y.; Palmer, S. J.; Tan, K.; Millar, G. J. *Journal of Molecular Structure* **2012**, *1011*, 128-133.
8. Frost, R. L.; Palmer, S. J.; Pogson, R. E. *Spectrochimica Acta Part a-Molecular and Biomolecular Spectroscopy* **2011**, *79*, 1149-1153.
9. Yu, D.; Wu, C.; Kong, Y.; Xue, N.; Guo, X.; Ding, W. *Journal of Physical Chemistry C* **2007**, *111*, 14394-14399.

5. Conclusions and perspectives

There is no doubt that TEM images of surfactant-assisted mesostructures can be fascinating. In any case, the variety of applications (real and/or potential) of mesoporous silica and non-silica materials in hot research subjects is impressive. But at the same time, impressive images, sophisticated characterization techniques and spectacular properties can often overshadow the equally appealing chemistry involved in the synthesis of these kinds of materials. So, it is not unusual to find interesting papers in high impact journals in which chemistry has been set aside, deserving only a few words in the experimental section or short comments in the discussion or results sections.

During the development of this PhD Thesis, a significant part of the effort has been focused on the rationalization of the chemistry involved in the synthetic procedures. This is essential to achieve high chemical reproducibility, pure materials and high reaction yields. Somehow, apart from the use of surfactants as template agents (obvious nexus given the role played by micelles in this research area), the rationalization of the chemistry could be considered as the leitmotiv of the work collected here. In this context, as the final organic-inorganic self-assembly processes usually occur in aqueous or hydro-alcoholic reaction media, it is necessary to consider the hydrolysis and condensation of the different inorganic precursors (in our case atrane complexes) to understand the consolidation of the inorganic network (the pore walls).

In the chapter focused on UVM-7 silica (Chapter 2), high temperature reactions (growth of gold nanoparticles and carbon nano-objects) have been used in order to elucidate the internal organization of the intra-particle mesopore system of this material. Together with the electron tomography experiments these reactions, which can be considered as typical in solid state chemistry (in our case, inside confined spaces: the mesopores), have been decisive to help determine the interconnected nature of the UVM-7 intra-particle pore system. This connectivity is probably the key to understanding the enhanced mass transfer kinetics of NBS solids when compared to other micrometric mesoporous silicas. The second part of the Chapter 2 is devoted to mesopore size expansion by using alkanes as swelling agents. After careful re-reading of the classic bibliography on the chemistry of colloids, we have found in the

experiences and ideas of Windsor a plausible explanation for the three-phase nature of the resulting reaction media in alkane/surfactant/water mixtures, and its effect on the incorporation of swelling agents. The relatively low increase in the mesopore size observed is due to the limited incorporation of alkane molecules inside the micelles. In addition, for the first time, we have determined the alkane and surfactant amounts really incorporated on the siliceous net through chemical analysis. Hence, classical ideas of colloid chemistry have been our guide to understanding and conducting our mesopore expansion in UVM-7 silicas. With these contributions, we have probably completed our story with this material.

Chapter 3 is developed from the isolation of gold-containing porous silica nanocomposites. Two aspects seem to be the determining factors in the performance of these materials: the dispersion of the gold nanoparticles, and the interaction between the gold species and the supports. We have designed our preparative strategy following these principles. The adjustment of pH conditions used for gold impregnation must be combined with a judicious selection of the different oxidic nanodomains that can be inserted in/on the silica walls. In any case, the pH must be lower than the isoelectric points on the non-silica oxidic domains. These MO_x domains have been formed via two different methods: “one-pot” co-condensation and post-impregnation.

The first method implies the use of the atrane route. This is a chemical strategy developed within our group, which is based on the use of triethanolamine complexes as inorganic precursors. The alternative route involves a typical impregnation strategy using acetylacetonate complexes as precursors. These complexes melt before degrading, thus favouring a good, homogeneous dispersion of the MO_x domains on the silica walls after thermal treatment of the composites. Regardless of the preparative route, the gold species preferably interact with the surface of the MO_x domains, with the subsequent growth of the gold species on the MO_x sites. The amorphous or crystalline nature of these domains depends on which route has been adopted: the one-pot (atrane) route leads to amorphous MO_x sites, while slightly larger, crystalline domains are obtained through impregnation. The interaction with gold seems to be stronger in the case of crystalline oxides, probably because of a certain epitaxial

growth of the gold particles on crystalline supports. Thus, depending on the nature of the support, soft or strong anchoring can be achieved. Hence, impregnation must be selected when the working conditions of the composites imply high temperatures. In contrast, for catalytic reactions carried out under mild conditions, both of the strategies work. Furthermore, we have observed that the nature of the MO_x domains also affects the thermal stability of the support itself. The crystalline domains induce supplementary stability in the composites, acting as a scaffold that hinders the complete collapse of the structure at high temperatures. This advantage has not been observed for composites with amorphous domains.

In short, some basic principles of coordination, colloidal and solid state chemistry have been combined for the synthesis of nanocomposites.

Finally, the isolation of iron phosphates and hybrid phosphonates (Chapter 4) is based on a competition between two typical iron complexes with ligands derived from triethanolamine and phosphate. Both of these have been traditionally used in analytical chemistry for the determination of iron content under different specific methods. In our case, the hydrolytic attack on the Fe-atrane complexes in the presence of phosphate-type anions in the media is the key point for the formation of mesostructured and mesoporous iron phosphate and phosphonate derivatives.

There comes a time when you need to stop and write the Thesis. This time can also be seen as a time for reflection; to think about the future and aspects of the work that are worth pursuing.

As mentioned above, it is difficult to think of additional modifications for the UVM-7 architecture. Some work has been done including additional co-solvents; this leads to significant changes in the reaction media and an evolution from Winsor III to Winsor IV is observed. However, this also implies a substantial change in the material architecture from NBS type (UVM-7) to core-shell particles.

As for MO_x domains, the possible combinations (including chemical composition and reactivity, amorphous or crystalline nature or dispersion) as well as changes in gold incorporation offer a wide variety of variables that can be adapted for

specific applications. At this point, we have initiated the generalization of the use of acetylacetonate complexes to form other MO_x nanodomains with the double role of anchors and scaffolds. Moreover, some of these composites have been tested as catalysts for carbon-carbon coupling reactions. Specifically, for the addition of boronic acids to 2-cyclohexen-1-one, a reaction that is usually carried out using rhodium based catalysts.

In a certain sense, non-silica based mesoporous materials such as metal phosphates can be seen as amorphous mesoporous MOFs. This family of materials has enjoyed huge expansion in recent years in terms of possible compositions, pore organization and applications. Thus, this is a fully open field for the development of new materials.

In any case, a change of interest during the post-doctoral period would not be a problem since, now, I feel open-minded and ready to learn more about the Chemistry involved in different processes.

